Seismic studies of gas hydrate in the Ulleung Basin, East Sea, offshore Korea

by

Iulia Stoian

BSc, Jacobs University Bremen, formerly International University Bremen, Germany, 2006

A Thesis Submitted in Partial Fulfillment of the
Requirements for the Degree of

MASTER OF SCIENCE

in the

School of Earth and Ocean Sciences

Seismic studies of gas hydrate in the Ulleung Basin, East Sea, offshore Korea

by

Iulia Stoian

BSc, Jacobs University Bremen, formerly International University Bremen, Germany, 2006

Supervisory Committee

Dr. Roy D. Hyndman, Supervisor (School of Earth and Ocean Sciences)

Dr. George D. Spence, Co-Supervisor (School of Earth and Ocean Sciences)

Dr. Ross N. Chapman, Departmental Member (School of Earth and Ocean Sciences)

Dr. R. Ross Haacke, Additional Member (Geological Survey of Canada, Pacific Geoscience Centre)

Dr. Michael Riedel, Additional Member (Department of Earth and Planetary Sciences, McGill University)

Dr. Douglas R. Schmitt, External Examiner (Department of Physics, University of Alberta)

Supervisory Committee

Dr. Roy D. Hyndman, Supervisor (School of Earth and Ocean Sciences)

Dr. George D. Spence, Co-Supervisor (School of Earth and Ocean Sciences)

Dr. Ross N. Chapman, Departmental Member (School of Earth and Ocean Sciences)

Dr. R. Ross Haacke, Additional Member (Geological Survey of Canada, Pacific Geoscience Centre)

Dr. Michael Riedel, Additional Member (Department of Earth and Planetary Sciences, McGill University)

Dr. Douglas R. Schmitt, External Examiner (Department of Physics, University of Alberta)

Abstract

This thesis work is directed at estimating gas hydrate and free gas distribution and saturation in local structures in the Ulleung Basin, East Sea offshore Korea. The estimates are obtained from a 2-D multi-channel seismic (MCS) reflection profile from the basin. Firstly, structures of locally focused upwelling fluid and gas flow were imaged using time-migrated sections and seismic attributes, and secondly seismic velocities were obtained to estimate gas hydrate and free gas saturations. The structures investigated are up to 1 km across, and are characterized by reduced reflectivity ('blank zones') and pulled-up sediment reflectors on the seismic sections. Throughout the study, a comparison is made between the blank zones and areas outside them where

not much gas hydrate or gas is expected, to examine their peculiar characteristics as related to the formation of gas hydrate and underlying free gas. The regional depth of possible occurrence of gas hydrate and free gas is determined by predicting the base of the gas hydrate stability zone (BGHSZ) from sediment properties and heat flow estimates calibrated by a few bottom-simulating reflectors (BSRs) from outside the analyzed seismic section.

A large number of normal moveout (stacking) velocity profiles were obtained within and outside the blank zones. Interval velocities were then derived by applying the commonly used unconstrained Dix equation as well as by applying constraints to inversion using regularized linear inversion and non-linear Bayesian inversion. The latter method fully explores the uncertainty of the interval velocity estimates. Compared to areas outside the blank zones, the velocities within the blank zones are up to 30% larger at about 30 m above the BGHSZ and up to 65% smaller immediately below the BGHSZ. The velocity increase implies a gas hydrate saturation of 10-40% of the pore space. The velocity decrease implies a free gas saturation of 1-4% of the pore space. Their detailed distribution within individual structures cannot be resolved. Reflector pull-up in time sections in the hydrate zone allows an independent velocity estimate, assuming the pull-up is solely a velocity effect. The implied velocity is much higher than the interval velocity estimates, so there also must be physical deformation. The heat flow estimated depth of the BGHSZ is in good agreement with the transition from gas hydrate to free gas as inferred from seismic velocities.

The general conclusion of the thesis work is that a variety of careful analyses of MCS data that characterize the seismic signal and estimate the seismic velocity structure can provide insight into gas hydrate and free gas occurrences. The large amounts of gas hydrate and free gas associated with the blank zones inferred by this study should draw special attention to future energy and climate effects in this area and other similar regions.

Table of Contents

List of Tables

List of Figures

Acknowledgements

Many thanks to Roy Hyndman for sharing his extensive knowledge providing simple explanations, for his encouragement for me to keep an open-mind and reach higher, for his patience, and for supporting my decisions. Many thanks to all my committee members, George Spence, Ross Chapman, Michael Riedel, Ross Haacke for their guidance and useful advice. I would like to thank Ulrike Schmidt for the help with seismic processing, Stan Dosso, for the excellent lectures which advanced my knowledge and the discussions on my research, Mike Wilmut for help with some inversion work and Kelin Wang for insightful lectures.

I appreciate all opportunities I had during my MSc, such as participating in cruises and conferences. I had the great opportunity as a student to be part of the 2-month drilling expedition for gas hydrate offshore Korea in fall 2007. For this I would like to thank Roy and George for their support and encouragement, Michael, Keun-Pil Park, Gary Humphrey and Peter Schultheiss for making it happen. I would like to thank Ele Willoughby and the other participants of the gas hydrate cruise on CCGS J.P. Tully offshore Vancouver Island in the summer of 2006 for the great experience.

I would like to thank my colleagues and friends in Victoria, Ranjan, Angela, Lionel, Leah, Mae, Ikuko, Sabine, Natalie, Sheri, Yan, Lucinda, Evan for the good times, help and support.

Last but not least, special thanks to my parents for supporting me in all my endevours.

Chapter 1

Introduction

1.1 Overview and Objectives

The main objectives of this thesis are: a) to locate and quantify gas hydrate and free gas accumulations in the Ulleung Basin, southern East Sea, offshore Korea, using 2-D multi-channel seismic (MCS) reflection data, and b) to understand the geologic controls on the formation and distribution of natural gas hydrate.

A series of analyses have been carried out on a dataset collected in 2005 by the Korean Institute of Geosciences and Mineral Resources (KIGAM). The interpretation of the results is based on the influence of gas hydrate and gas on the physical properties of the bulk sediments. Gas hydrate increases the seismic velocity and free gas decreases the seismic velocity. Both hydrate and gas may cause seismic attenuation, the amount dependent on their concentration and distribution.

Throughout the study, the primary comparison is made between blank zones, also known as chimneys or vents, that contain high concentrations of gas hydrate and outside more uniform areas with low concentrations of gas hydrate. This comparison

should aid the understanding of the controls and mechanisms of hydrate formation and fluid and gas migration in such vent features, which are believed to host large accumulations of gas hydrate. The work entailed different independent analyses to map the gas hydrate and free gas occurrences. Most effort was dedicated to careful analysis of MCS data, by using different approaches to obtain accurate velocities and estimate their uncertainties.

Chapter 1 presents an overview of natural gas hydrate occurrence, stability and main physical properties, as well as a geological introduction to the area of study. The main physical property investigated is the seismic velocity of sediments that contain gas hydrate. Seismic velocity is the primary control on reflection amplitudes in the seabed, since density changes are generally small and do not affect the acoustic impedance much. The MCS data are processed with the main objective to determine the presence and size of seismic velocity anomalies compared to hydrate-free and gas-free sediments that may provide evidence of hydrate and gas. The results are presented in Chapter 2. Different ways to determine interval velocities are investigated in Chapter 3. Anomalous interval velocities characterizing the local structures are used to derive gas hydrate and free gas saturations in Chapter 4. In addition to detecting the presence of gas hydrate and gas, interval velocities are used to predict the base of gas hydrate stability zone (BGHSZ) in Chapter 5. Chapter 6 focuses on the interpretation of the seismic profiles, using the reflectivity image and special processing using complex seismic attributes. The results are summarized and discussed in Chapter 7.

The author participated in the KIGAM drilling expedition in the Ulleung Basin

in fall of 2007, with Dr. Michael Riedel as Co-Chief Scientist. Local structures containing hydrate were logged and cored. However, the drilling data have not yet been released publically and are not included in the thesis. Initial reports indicate that substantial hydrate was encountered (*Park* 2008, *Park et al.* 2008, *Kim et al.* 2008a, *Holland et al.* 2008).

1.2 Gas Hydrate: Importance, Stability, Distribution

Natural gas hydrates are clathrates, crystalline solids where molecules of gas, mostly methane, are encaged by molecules of water. Because of the crystalline structure, the gas is concentrated by up to a factor of 164 compared to a gas phase under standard pressure and temperature conditions. Gas hydrate is found under land in Arctic and Antarctic permafrost regions and in thermodynamically stable regions of the oceans beneath continental slopes. Gas hydrates are found at shallow depths compared to conventional hydrocarbons, up to 1000 m in permafrost areas and up to a few hundred meters beneath the seafloor in marine settings.

Global estimates of hydrate-bound gas have decreased from 10^{18}-10^{17} m^3 at STP in 1970s-early 1980s to 10^{14}-10^{15} [3] m^3 at present as a result of the improved knowledge of the distribution and concentration of gas hydrates (*Milkov* 2004). Gas hydrate concentrates natural gas significantly, which generates less carbon dioxide (CO_2) upon combustion than either coal or oil, and thus it may provide a large new source of cleaner energy that can offset the declining supplies of conventional energy. It could also provide energy security for countries such as Korea, Japan and India, that have limited conventional fossil fuel domestic resources. However, only the gas hydrate

fraction found in concentrated rather than dispersed accumulations may become a gas reserve (e.g., *Milkov* 2004) because the production technology is only currently being developed.

Gas hydrate also may be involved in past and present changes in climate (e.g., *Kennet et al.* 2003), since methane is 20 times more potent as a greenhouse gas than CO_2 in causing global warming and can be released into the oceans if the hydrate melts. Hydrate dissociation can also result in geological hazards such as seafloor landslides, or can pose a hazard to drilling and seabed installations (e.g., *Hovland and Gudmestad* 2001).

Figure 1.1a is a schematic representation of the gas hydrate phase stability in an oceanic environment. Gas hydrate is stable at pressure and temperature conditions given by the intersection of the gas hydrate phase boundary with the ocean and seabed geothermal gradients. Gas hydrate can form in the ocean above the seafloor, but is not stable, because methane is lost by diffusion and oxidation to the ocean water and hydrate floats to the surface due to its lower density.

Simple one-dimensional models for hydrate formation (e.g., *Hyndman and Davis* 1992, *Davie and Buffett* 2001) assume a stratified view of hydrate systems (as shown in Fig. 1.1a). In this case, hydrate precipitates from regional rising methane-saturated water or from rising free gas within the hydrate stability zone when the concentration of methane is higher than indicated by the solubility curve (Fig. 1.1b). The regional formation of high velocity gas hydrate and underlying low velocity free gas is concluded to be the cause of wide-spread bottom-simulating reflectors (BSRs) (*MacKay et al.* 1994). The regional hydrate and free gas that form BSRs usually appear to be

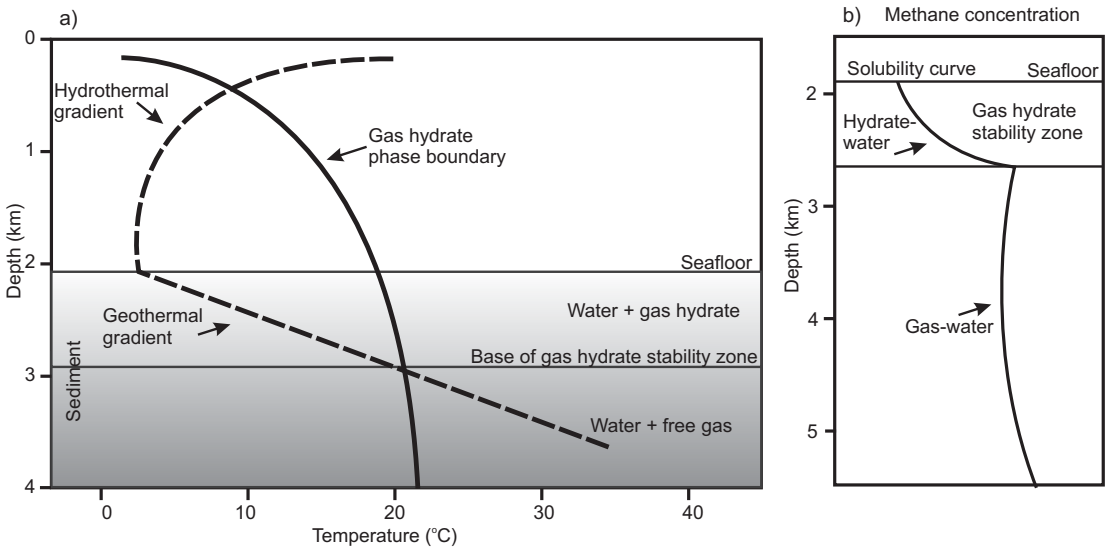

Figure 1.1: a) Schematic representation of the marine gas hydrate stability zone; b) methane solubility curves in the hydrate stability zone and below.

of low concentration, with free gas that may be immobile.

The most important factor controlling the formation of gas hydrate is the availability of natural gas, which can have thermogenic or biogenic origin. In areas with a high sedimentation rate containing significant organic carbon, gas hydrates from biogenic gases form in situ, as organic matter is biologically converted to methane (i.e., organic diagenesis) at low-temperatures. This gas can form either in the hydrate stability zone or can migrate from below. Thermogenic gases, formed at temperatures higher than about 100^o C, commonly migrate from deeper sources to the hydrate stability zone through faults and permeable channels. This usually results in a more localized distribution of gas hydrate. The thermogenic and biogenic gases can be distinguished by analyzing δ^{13}C isotopes, ^{18}O isotope and hydrocarbon gas ratios (*Sloan* 1998).

Recent work has focused on localized occurrences of concentrated hydrate due to

local concentrations of rising fluid and gas (e.g., *Liu and Flemings* 2007). In such places gas hydrate can form quickly from local rising gas that becomes mobile when its concentration exceeds a critical value. The rate and duration of the upward delivery of deep subsurface fluids and gases through faults and channels towards the seafloor determines the amounts and locations of localized hydrate deposits (*Liu and Flemings* 2007) and the geological response at the seafloor (e.g., *Roberts* 2001).

1.3 Gas Hydrate and Free Gas Identification

The presence of gas hydrate in sediments can be detected directly in cores, or indirectly by pore-water geochemistry and geophysical methods.

Upon formation, gas hydrates exclude the chloride ions from the water with which they form, leaving the water around enriched in salt which then difusses away to leave normal salinity levels plus hydrate in pore space. If hydrate dissociates upon core retrieval, its presence is indicated by a number of factors: a) low interstitial-water chlorinity due to the water freshening as the hydrates dissociate; b) large gas exsolution seen as gas voids; c) high methane sediment concentration; d) low core temperature as hydrate dissociation is an endothermic reaction (*Sloan* 1998).

When no hydrate cores are available, the presence of gas hydrate and free gas in sediments is commonly detected from seismic data. In marine settings, the most common seismic indicator is the BSR, imaged at frequencies below a few hundred Hz (e.g., *Shipley et al.* 1979, *Hyndman and Davis* 1992, *Chapman et al.* 2002). It has opposite polarity and parallels the seafloor. The BSR has been commonly thought to represent the interface between overlying high velocity gas hydrate sediments and

underlying low velocity free gas accumulations at the BGHSZ (e.g., *Hyndman and Spence* 1992). Most recent detailed studies conclude that the BSR is mainly a result of the underlying low velocity free gas accumulations, and the generally small hydrate quantities above it contribute less to the impedance contrast (e.g., *Singh et al.* 1993, *MacKay et al.* 1994, *Minshull et al.* 1994, *Holbrook et al.* 1996). Hydrates have been found in many areas without a BSR, such as in the Ulleung Basin offshore Korea (*Park et al.* 2008), Gulf of Mexico (*Cooper and Hart* 2003), on the Blake Ridge, offshore South Carolina (*Holbrook et al.* 1996).

The BSR represents the BGHSZ, which is mainly controlled by pressure and temperature conditions, and to a lesser extent by salinity and gas composition. Since the temperature gradient (heat flow) normally varies slowly horizontally, the temperature at the depth of the BGHSZ is almost constant, fluctuating slightly due to the changes in water depth which result in different pressures. Thus, if there are no lateral heat flow variations, the regional BGHSZ runs nearly parallel to the seafloor, shallowing toward shallower water depth.

Free gas accumulations beneath the GHSZ that produce a BSR are mainly a result of the following mechanisms: hydrate recycling (e.g. *Kvenvolden and Barnard* 1983) and the solubility-curvature mechanisms (*Haacke et al.* 2007, 2008). When hydrate is pushed downward through the BGHSZ due to for example, sedimentation, it dissociates. The resulting free gas, if in large enough quantities, migrates upward to form hydrate again. This process, called hydrate recycling, is dominant at high rates of upward fluid flow on active margins (*Haacke et al.* 2007, 2008). On the other hand, the solubility-curvature mechanism can explain the formation of low concentrations of

free gas in thick layers seen especially on passive margins at low rates of upward fluid flow. Gas hydrate exists just above the BGHSZ, from which dissolved gas diffuses downwards; this diffusion and the upward movement of advecting fluids result in a steady-state profile of dissolved gas. Free gas is produced below the BGHSZ as the dissolved gas exceeds the gas-water solubility (*Haacke et al.* 2007, 2008).

The concentration of free gas below the BSR is generally less than a few percent by pore volume (e.g., *MacKay et al.* 1994, *Holbrook et al.* 1996). Because of this low concentration, unlike conventional gas reservoirs, the gas is probably distributed as bubbles trapped in the sediment matrix, rather than a semi-continuous buoyant volume (*Schowalter* 1979). In most cases, there is no reflection from the base of the gas zone, implying a downward decreasing gas concentration (e.g., *Singh et al.* 1993, *Chapman et al.* 2002).

1.3.1 Gas Hydrate in Acoustically Blanked Zones

Large gas hydrate concentrations, sometimes associated with free gas escaping at the seafloor, have been found at the location of acoustically blanked zones, referred to as chimneys or vents (*Paull et al.* 1995, *Sassen et al.* 2001, *Heeschen et al.* 2003). For example, at Bullseye vent offshore Vancouver Island, massive hydrate was found in the top 40 m below the seafloor (*Riedel et al.* 2006a). Such features are important because they allow methane to escape at the seafloor (e.g., *Pecher* 2002) and strong upward gas expulsion can reach the atmosphere to affect the global climate. Additionally, they are likely the best prospects for developing hydrate as an energy resource since they contain high concentrations of hydrate near the seabed.

The vent features are associated with localized channelling of gas rich fluids and/or free gas from below the BGHSZ, which can sometimes pass through the GHSZ. *Liu and Flemings* (2007) describe the existence of three-phase chimneys (where gas, water and gas hydrate co-exist) extending up to or near the seafloor because of increased pore fluid salinities that result from salt exclusion during hydrate formation. If the methane flux is high, free gas initially forms hydrate and increases the salinity up to a point when it is too saline for further hydrate to form. Because of the effect of salinity on hydrate stability, gaseous methane is then able to bypass the GHSZ without forming hydrate. In this high flux system, hydrate concentration increases upward from the base of the regional hydrate stability zone because at shallower depths free gas can form increasing amounts of hydrate until salinities are too high for further hydrate formation. A peak in hydrate concentration can be found closer to the seafloor as salinity anomalies are reduced by upward diffusion into the seawater, enabling more hydrate to form. This situation was encountered at the South Hydrate Ridge, where gas, water and hydrate were detected at in situ conditions, with highly saline pore water (*Mikov et al.* 2004). Higher than seawater salinities were also encountered in the Krishna-Godavari Basin offshore India (*Kastner et al.* 2008) and at Bullseye vent in Northern Cascadia (*Riedel et al.* 2006a). Free gas could also co-exist with water and hydrate in the GHSZ if it is trapped inside hydrate-coated fractures that do not allow the inflow of water (*Riedel et al.* 2006b).

If the upward migrating fluids are warm, they could result in local lateral variations in the BGHSZ, which is shallowed (*Wood et al.* 2002). This may cause the deeper gas hydrate to become unstable. *Taylor et al.* (2000) report a study at the Blake Ridge

Diapir, where the BGHSZ, defined by the BSR, is shallowed by about 100 m over the center of a diapir. The diapir causes faults to form, which are a pathway for migration of gas and fluids to the seafloor. In this case, the increased heat flow is likely a result of the high thermal conductivity of the underlying salt, in addition to the advective heat flow transported by fluids. Abnormal heat flow was also detected offshore Ireland in the Porcupine Basin (*Henriet et al.* 2001) and in the Baikal Rift zone (*Vanneste et al.* 2001). At vents like the ones at Blake Ridge there is no shallowing of the BGHSZ below seafloor vents, only a slight disruption of the BSR (*Gorman et al.* 2002). No heat flow anomaly was detected at the Bullseye vent on the Cascadia margin (*Riedel et al.* 2006b), which argues against the model of *Wood et al.* (2002).

When the expulsion of fluids, gas and sediments is fast, the vents are associated with pockmarks and mud volcanoes (e.g., *Roberts* 2001). Mud volcanoes can be imaged as low seafloor reflectivity because of 'softer' disturbed sediments (*Roberts et al.* 2006). In low flux environments, seafloor lithification occurs by mineral precipitation, as the methane dissolved in pore waters is consumed by sulfate reduction. Authigenic carbonates are the most common products and are sometimes associated with chemo-synthetic communties. Their presence results in a strong seafloor reflectivity. An intermediate flux supports gas hydrate formation at or near the seafloor. Many chemosynthetic communities are found in areas of lithified seafloor, resulting in a highly variable seafloor reflectivity (*Roberts et al.* 2006).

1.3.2 Seismic Attributes as Hydrate and Free Gas Indicators

Both gas hydrate and free gas-bearing sediments can either attenuate or enhance seismic energy (e.g., *Holbrook et al.* 2002). This probably depends on the concentration and distribution of gas hydrate and free gas and also on the types of host sediments. Attenuation of hydrate-bearing sediments also appears to be frequency-dependent (e.g., *Matsushima* 2006). Gas highly attenuates energy in the seismic frequency range (30-110 Hz) while hydrate does not significantly attenuate energy at seismic frequencies, but it does at sonic frequencies (10-20 kHz) (*Matsushima* 2006). The attenuation may result from intrinsic attenuation which measures the irreversible removal of seismic energy due to conversion to heat and attenuation due to scattering from velocity and density heterogenetities.

The attenuation of seismic waves by gas hydrate is not well understood. Gas hydrate reduces porosity and increases the elastic moduli of the solid frame, making the rock stiffer, implying less elastic energy losses, so expected less attenuation. In hydrate-free sediments *Klimentos and McCann* (1990) show that attenuation increases with increasing porosity and clay content, while velocity decreases, as expected. However, unexpectedly, low-amplitude reflectors above some BSRs have been observed (*Shipley et al.* 1979) and many cases of large seismic attenuation by sediments containing hydrate have been reported (e.g., *Sakai* 1999, *Wood et al.* 2000, *Guerin and Goldberg* 2002, *Pratt et al.* 2003). Some explanations for reduced amplitudes are summarized below.

Lee et al. (1993) suggest that the preference for high velocity gas hydrate to form in

high-porosity, low-velocity sediments increases the velocity of the host sediments and results in a reduction of the velocity contrast between the porous sediments hosting the gas hydrate and the adjacent less porous sediments. This reduction in impedance contrasts between high- and low-porosity sediments may result in a decrease of the reflection amplitude of the hydrate-bearing sediment sections at saturations lower than 25% pore space, as higher saturations will result in enhanced reflections (*Holbrook et al.* 2002). An alternative explanation for the low reflectivity on the Blake Ridge based on VSP data is the presence of a uniform sedimentary layer above highly reflective free gas-containing layers (*Holbrook* 2001).

Dvorkin and Uden (2004) attribute the attenuation in gas hydrate sediments to elastic heterogeneity, which results in pore-fluid crossflow between stiff and soft domains of the rock as the waves pass. The presence of hydrate increases the elastic moduli of the rock, and its patchy distribution results in elastic heterogeneity. The attenuation is thus a result of the viscous energy losses, due to the wave-induced fluid crossflow. Attenuation could also result from energy scattering due to small scale elastic heterogeneity (e.g., *Huang et al.* 2008). *Chand and Minshull* (2004) concluded that the permeability contrast between the host sediments and hydrate attenuates energy in hydrate-sediments due to fluid flow, mainly at frequencies above 200 Hz.

The presence of free gas and gas hydrate in the sediments can sometimes be identified from displays of complex seismic attributes, especially instantaneous amplitude and instantaneous frequency. Depending on the concentrations of gas hydrate and free gas, the instantaneous amplitude may be either increased (bright spots or enhanced reflections) or decreased (wipeout zones). Bright spots mark accumulations of free

gas below the BGHSZ, which have a lower impedance due to the low seismic velocity of free gas. Enhanced reflectors can also result from the presence of gas hydrate above the BGHSZ. At Blake Ridge, bright spots associated with high velocities inside chimneys indicate the presence of gas hydrate (*Gorman et al.* 2002). At Nankai trough, bright reflectors above the BSR are associated with hydrate-concentrated zones (*Saeki et al.* 2008).

A decrease in the instantaneous frequency is common immediately below a gas reservoir (*Taner et al.* 1979). *Taylor et al.* (2000) report a case at the Blake Ridge of a low-frequency anomaly over the center of a diapir above the BSR. This is associated with high reflection strength anomalies at fault locations, interpreted to be the result of fluid migration along faults. At Vestnesa Ridge offshore W-Svalbard, high amplitude reflections and the attenuation of higher frequencies below the BSR indicate free gas (*Petersen et al.* 2008).

1.4 Gas Hydrate Properties

The formation of gas hydrate in marine sediments changes the physical properties of the bulk sediment, and in particular it increases its velocity and electrical resistivity. The degree to which the sediment structure or volume is changed, thus the influence on bulk sediment properties, depends on how and where in the sediment the hydrate forms. Two limiting configurations are that the hydrate forms in the pore fluid between the grains of the sediments or it can displace the sediments, and does not occupy pore volume. In the former case there is little change to the sediment volume, as rising methane reacts with the sediment pore fluid, while in the latter case there is

a volume change as hydrate forms from rising gas rich fluids. When hydrate replaces the pore fluid, it could cement the grains (e.g., *Dvorkin and Nur* 1993, *Lee et al.* 1993). Pore-filling gas hydrate is mainly found in coarser grained more permeable sediments such as silts and sands (e.g., *Holland et al.* 2008). On the other hand, grain displacing hydrate is mainly found in less permeable finer grained sediments as lenses, veins and nodules of pure gas hydrate of centimeters to even meters in size. The veins cross-cutting sedimentary layers are likely formed by fracturing of the sediments (e.g., *Holland et al.* 2008). Considering these different types of hydrate morphology, careful analysis of the model converting measurements of seismic velocity anomalies to gas hydrate saturations is required.

The velocity of solid gas hydrate is about 3.65 km/s (*Waite et al.* 2000). To a first approximation, gas hydrate has similar high velocity and resistivity as the grains forming the sediment matrix, and very different velocity and resistivity to the pore fluid.

1.4.1 Seismic Velocity, Gas Hydrate and Free Gas Saturation

Gas hydrate and free gas saturations can be derived from velocity measurements, compared to a no-hydrate, no-free gas reference. The seismic velocity wavelength and resolution are about three orders of magnitude larger than the size of nodules, veins and fractures in which hydrates have been commonly detected. This means that the velocity measurement is only a weighted average of elastic properties of gas hydrate small-scale occurrences and adjacent sediments. Therefore, the gas hydrate saturation is an estimate of the total amount of gas hydrate present, with no information on the

nature of small scale distribution.

Free gas is modeled to occur in pore space, with no effect on sediment rigidity (*Gassmann* 1951). Usually, the S-wave velocity is nearly unchanged, because the density of the gas-water mixture is close to that of the original pore water if gas saturations are low. Free gas saturations can be estimated using the Biot-Gassmann theory (e.g., *Desmons* 1996) and includes the effect of pressure and temperature on gas compressibility.

The most common approaches to estimate gas hydrate saturations from seismic velocity are summarized below.

Effective Porosity Reduction Model

The porosity-reduction model assumes that gas hydrate replaces the pore fluid, reducing the sediment effective porosity with a substance much like the grains themselves (e.g., *Hyndman et al.* 1993, *Yuan et al.* 1996). The underlying assumption is that the P-wave velocity of pure gas hydrate is similar to that of the sediment matrix. In this model, bulk sediment density usually is not greatly affected by gas hydrate, because hydrate density is similar to that of the pore fluid. Borehole density logs can thus be used to compute a no-hydrate velocity and resistivity reference measurement. Any bulk sediment velocity measurement can be converted to porosity using empirical porosity-velocity relations. *Hyndman et al.* (1993) derived such a relationship from porosity and velocity measurements on core samples from the Nankai accretionary prism from well below the BGHSZ, to exclude the influence from gas hydrate or free gas:

$$\phi = -1.180 + \frac{8.607}{v} - \frac{17.89}{v^2} + \frac{13.94}{v^3}, \tag{1.1}$$

where ϕ is porosity and v is velocity in km/s. The measured velocities are on the range 1.6-2.2 km/s and the porosities 35-60%.

The decrease in porosity resulting from an increase in velocity due to hydrate formation relative to a reference porosity can be translated into hydrate saturation:

$$S_h = \frac{\phi_{ref} - \phi_{gh}}{\phi_{ref}}, \tag{1.2}$$

where S_h is the hydrate saturation, ϕ_{ref} is the reference porosity and ϕ_{gh} is the hydrated sediment velocity.

Errors may arise from using the effective porosity reduction model because of the use of a velocity-porosity trend for homogeneous sediments, since for example, sands and clays have different porosity-velocity relations. Furthermore, this model includes hydrate in the rock frame without allowing it to modify the elastic properties of the frame. Recent observation from scientific drilling indicate that this is not usually an accurate reflection of how hydrate forms in porous media.

Time-Averaging Equations

Time-averaging equations are founded on the simple physical assumption that the total traveltime through the bulk sediment is approximately equal to the average traveltime through each component, weighted by the volume fraction of the component.

The first time-averaging equation to estimate sediment porosity from bulk sediment velocity and fluid and matrix velocities for consolidated sediments was introduced by *Wyllie et al.* (1958). The two-phase system Wyllie equation was extended to a three-phase system equation that includes gas hydrate by *Pearson et al.* (1983):

$$\frac{1}{V_1} = \frac{\phi(1-S_h)}{V_w} + \frac{\phi S_h}{V_h} + \frac{1-\phi}{V_m}, \tag{1.3}$$

where V_1 is the Wyllie velocity, V_w is the pore fluid velocity, and V_m is the sediment matrix velocity, V_h is the velocity of pure hydrate and S_h is the gas hydrate saturation.

The time-averaging equation gives inaccurate results for some sediments, especially in the case of unconsolidated sediments. *Wood* (1941) introduced an equation useful for particles in suspension (i.e., very high porosity). *Lee et al.* (1996b) extended the Wood equation to a three-phase system with gas hydrate.

$$\frac{1}{\rho_b V_2^2} = \frac{\phi(1-S_h)}{\rho_w V_w^2} + \frac{\phi S_h}{\rho_h V_h^2} + \frac{1-\phi}{\rho_m V_m^2}, \tag{1.4}$$

where V_2 is the Wood velocity, ρ_b, ρ_w and ρ_m are the bulk, fluid and matrix densities, respectively, and ρ_h is the density of pure hydrate.

A good estimate of bulk sediment velocities for unconsolidated marine sediments with gas hydrate can be obtained by combining the low-porosity Wyllie equation (Eq. 1.3) with the high-porosity Wood equation (Eq. 1.4) *Lee et al.* (1996b):

$$\frac{1}{V_{lee}} = \frac{W\phi(1-S_h)}{V_2} + \frac{1-W\phi(1-S_h)}{V_1}, \tag{1.5}$$

where W is an arbitrary weighting factor that gives more importance to either Wyllie or Wood velocity, depending on the sediment porosity.

To determine hydrate saturation, the following quantities need to be estimated: the velocity and density of the formation constituents (e.g., water, hydrate and matrix), those of the bulk sediment and sediment porosity.

The time-averaging approach introduces uncertainty through the weighting factor W, which weights the Wyllie or Wood velocity relations for high porosity and low porosity sediments, respectively. Gas hydrate found in high porosity sediments has low effective porosity and consolidates the formation, so the Wyllie relation should be favoured rather than the Wood equation. The weighting factor W is thus dependant on the gas hydrate saturation, is not a constant and its uncertainty can be a source of error.

Rock Physics Model

Helgerud et al. (1999), *Helgerud* (2001) use rock physics to build an effective medium model for the elastic moduli of high porosity marine sediments containing gas hydrate or free gas. The model requires knowledge of the porosity and the elastic moduli of the sediment constituents (gas hydrate, free gas, pore water and sediment grains). A baseline model for fully water-saturated sediments (*Dvorkin et al.* 1999) is used to calculate a no-hydrate velocity depth profile, from a porosity-depth profile. Elastic properties of effective media containing gas hydrate or free gas can be calculated under different assumptions on their formation mechanisms. Gas hydrate can be part of the pore fluid or of the load-bearing sediment matrix. When pore-filling,

the gas hydrate does not add stiffness to the sediment frame, slightly increasing the P-wave velocity and barely affecting the S-wave (shear) velocity. On the other hand, if the gas hydrate is load-bearing, the sediment frame is stiffer, increasing the P-wave velocity and only slightly the S-wave velocity. If the gas hydrate cements the grain contacts, both the P- and S-wave are further increased (e.g., *Dvorkin and Nur* 1993).

1.5 Gas Hydrate Offshore Korea

The seismic data used in this study are from the Ulleung Basin, East Sea, offshore Korea.

1.5.1 Tectonic and Geologic Setting of the East Sea (Sea of Japan)

The East Sea is a back-arc basin situated on the eastern side of the Eurasian plate, bordering the Philippine and the Pacific plates (Fig. 1.2). Three deep basins, Japan, Yamato and Ulleung, are part of the East Sea. They are separated by the Korea Plateau, Oki Bank, Yamato Ridge and Kita-Yamato Ridge, which represent rifted continental remnants. The Ulleung Interplain Gap separates the Ulleung Basin from the Japan Basin. The formation of the East Sea is generally thought to result mainly from the divergent motions of the Pacific and Eurasian plates (e.g., *Lallemand and Jolivet* 1985, *Tamaki et al.* 1992). Active slow convergence is taking place today along the eastern margin of the East Sea, while the Philippine and Pacific plates are subducting under the adjacent Japan Arc.

Several modes of opening have been proposed for the East Sea. The evolution of the basin is constrained by onland deformations, offshore crustal structure and timing of volcanic activity. *Otofuji et al.* (1991) argue for fan shaped opening of the East Sea

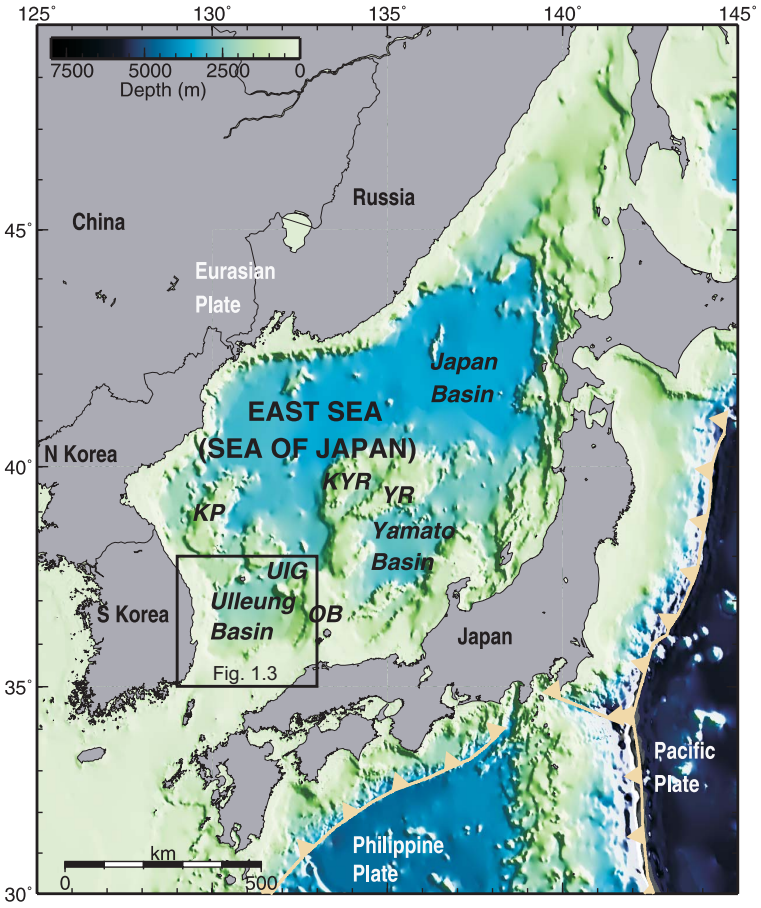

Figure 1.2: Map with the location and bathymetry of the East Sea (Sea of Japan) and its deep basins, Japan, Yamato and Ulleung Basin; OB: Oki Bank, YR: Yamato Ridge, KYR: Kita-Yamato Ridge, KP: Korea Plateau, UIG: Ulleung Intraplain Gap.

with differential rotation of the Japanese Islands, as supported by paleomagnetic data. Another view argues for a linear pull-apart opening along two major shear zones on the margins of the sea (*Lallemand and Jolivet* 1985). A more recent model proposing the formation of the East Sea as a pull-apart basin, with the opening accommodated by differential rotation of the Japanese Islands is based on the results of ODP Legs 127 and 128 (*Jolivet and Tamaki* 1992). The model is supported by the ages of the oceanic basement and the different sediment lithologies and magnetic anomaly lineations from the Japan Basin. This model suggests that the evolution of the

northern and southern parts is very different. At 25 Ma the Japan arc was straight and no ocean spreading was taking place in the back-arc. The East Sea started opening in the early Miocene (∼20 Ma), which is the period of maximum spreading and extension and is associated with large amounts of volcanics. Crustal thinning resulted in the break-up of the lithosphere, followed by seafloor spreading whereby oceanic crust was emplaced in the Japan Basin. Rifting and seafloor spreading of thinned crust in the north was concurrent with the eastward drift and rotation of the Japanese Islands in the southern East Sea. The latter processes resulted in the formation of the Ulleung and Yamato basins as pull-apart basins around Late Early Miocene (15 Ma). The motion of the Philippine plate gradually changed the back-arc extensional regime into a compression around 8-10 Ma. Slow subduction along the eastern margin of the East Sea near the coast of Japan was initiated at 1.8 Ma and lead to the reactivation of normal faults into thrust faults, that is still going on at present. This recent tectonic shortening may have been an important factor in the sediment compression and fluid expulsion that resulted in gas hydrate formation.

1.5.2 Tectonic and Geologic Setting of the Ulleung Basin

The Ulleung Basin is situated in the southwest part of the East Sea (Figs. 1.2, 1.3). It has a rhomboidal shape and is enclosed by the continental slope of Korea on the east and by Japan on the west and south. The submarine topographic highs Korea Plateau and Oki Bank bound the basin on north and east. The basin has steep margins in the north and west (slope gradient of 4-6^o) which exhibit slope-failure scars, slumps and debris flow deposits. The gentle slopes in the east and south (1-2^o) also

show the presence of scarp features resulting from slumps and slides (*Chough et al.* 2000).

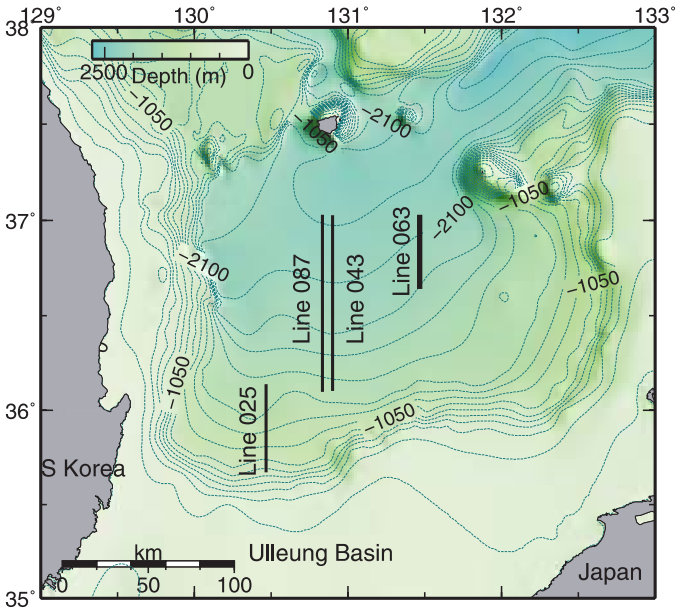

Figure 1.3: Bathymetry of Ulleung Basin with the location of the seismic line 063 analyzed in this study and lines with BSRs (025, 087, 043) used to calibrate heat flow and BGHSZ calculations.

Yoon and Chough (1995) propose a model for the formation of Ulleung Basin as a pull-apart basin based on the interpretation of seismic reflection profiles, paleomagnetic, and structural data, starting from the East Sea opening model of *Jolivet and Tamaki* (1992). The evolution of the Ulleung Basin has three stages: 1. pull-apart opening from late Oligocene to early Miocene; 2. rotational opening associated with differential rotation of the Japanese Arc from early to middle Miocene and 3. initiation of back-arc closing since late Miocene ($\sim$ 12 Ma) until present as a result of the collision of the Bonin Arc with central Japan.

The Ulleung Basin and the Korea Plateau are characterized by many mass failure and mass flow features. During the initial stage of back-arc opening of the East Sea,

rapid subsidence, structural movements and slope instability were associated with slope failure and mass deposits alternating with volcanic sills and flows. Active uplift and compressional deformation led to mass flow deposits in the basin during the transition from extension to compression at late middle Miocene. The Ulleung Basin underwent rapid subsidence during the late Miocene associated with normal to strike-slip faults. Intense compressional deformation during the early Pliocene resulted in anticlinal folds and unconformities mainly in the western margin of Ulleung Basin; the next phase of compressional deformation in the middle Pliocene produced large scale folds and faults in the Ulleung Basin. The tectonic deformation events from Miocene and Pliocene led to further large-scale mass failure and mass flow events. Since middle Pliocene, the East Sea was tectonically quiescent; however, the Ulleung Basin was affected by mass failure, possibly a result of sea level fluctuations, climate change, seismic events or gas hydrate dissociation (*Kwon and Bahk* 2006).

1.5.3 Seismic Stratigraphy of the Ulleung Basin

Four seismic sequence units can be identified in the Ulleung Basin based on the interpretation of multi-channel seismic profiles (*Lee* 1992, *Chough and Lee* 1992, *Chough et al.* 2000). The oldest unit is interpreted to be rifting extension volcanic flows and sills intercalated with sediments and bedded clastic and volcanoclastic debris. The second is middle Miocene marine shale on the basin plain and mass flow deposits on the western and north-eastern basin margins. The next younger unit is composed of marine shale interbedded with thin sandstone and siltstone beds on the basin plain. The youngest top unit consists of Pliocene-Quaternary turbidites and hemipelagic

sediments in the central part of the basin, debris flow deposits along the basin margin up to the middle slope region, and slump/slide deposits on the upper slope.

Lee and Suk (1998) subdivide the 0.5 s thick (TWT) upper Pliocene-Quaternary sequence in five units. The gas hydrate is mainly contained in the shallower units. These units are separated by relatively continuous reflectors and delimit different facies, distinguished on the basis of reflector character and geometry. The different facies and their seismic character are briefly described below. They will be later identified on the seismic sections analyzed in the current work, rather than completely describe their distribution in the whole Ulleung Basin, which can be found in *Lee and Suk* (1998). Turbidites and hemipelagic sediments are identified as a well-stratified facies having continuous reflectors and uniform seismic character. Mass transport complexes resulting from various types of mass flows (slides/slumps, debris flows, unchannelized high-density turbidity currents) have a structureless to chaotic character and show randomly oriented low to moderate short reflectors and near-transparent zones. Debris flow deposits have a similar internal character as mass transport complexes, and have a wedge-shape external form. The slide/slump deposits comprise irregular, blocky masses bounded upslope by scars. Mixed turbidites/hemipelagic sediments and mass transport complexes represent a weakly to moderately stratified facies that shows subparallel to parallel, variable amplitude reflectors with moderate continuity and locally transparent and/or chaotic zones. *Chough et al.* (1997) classified the uppermost (∼50-70 m) sedimentary sequence into different echo types based on high resolution reflection profiles throughout the basin, and their description is also useful in identifying the units in the current work.

The distribution of mass flow deposits in the Ulleung Basin follows the depth contours. Slides and slump deposits are found on the upper to lower slope areas at water depths of 300-1500 with individual sheets reaching up to 50 m in thickness. Debris flows are found in water depths of 1100-2100 m and represent the transition between the slide/slump deposits on the basin slopes and turbidites in the basin plain. The turbidite sequences are mainly found at water depths greater than 2000 m (*Lee et al.* 1996a). This distribution suggests that mass-flow processes were activated at the upper slope, and this resulted progressively in debris flows and turbidity currents in the deeper basin (*Chough et al.* 1997).

Slumping and sliding represent the movement of a mass of semi-consolidated sediment along external shear planes with relatively minor internal flow accommodated by discrete internal shear planes (*Fraser* 1989, *Hallam* 1981). Debris flows and turbidity currents represent fluid or fluidlike flow that takes place internally in response to the movement. Turbidity currents have a greater fluid content than debris flows. The debris flows behave like plastics and generally have a laminar flow. They can transport a wide range of grain sizes as a result of their cohesive nature and great viscosity of the material. Turbidity flows are formed when two fluids of unequal density are side by side and flow together. Density differences in turbidity currents result from the presence of suspended particles in the flow and when these differences are eliminated, the flow stops. The sediments deposited by a turbidity flow generally reflect the deceleration of the flow: the basal units are coarser and the overlying ones are finer grained.

The Ulleung Basin sediments are also characterized by several tephra layers (*Chun*

et al. 1997). The ash layers found around 1-2 m below the seafloor resulted from the Ulleung-Oki eruption (9.3 ka BP).

1.5.4 Gas Hydrate Exploration in the Ulleung Basin

The Ulleung Basin contains gas hydrate where it is stable in water deeper than about 1000 m, as inferred from geophysical, geological and geochemical studies. Initial gas hydrate research was conducted offshore Korea between 1996-2004, and a 10 year National Gas Hydrate Development Program was established in 2004 with the aim to identify the gas hydrate occurrences and estimate the potential reserves for future production (*Park et al.* 2008). Extensive 2D and 3D seismic surveys, OBS data collection, deep coring, piston coring, heat flow measurements and drilling were conducted in the East Sea.

There is both direct and indirect evidence for the presence of gas hydrate in the Ulleung Basin. The seismic indicators of gas hydrate are acoustic blank zones with pulled-up reflectors in time sections, BSRs, and the indicators of gas are seafloor pockmarks and enhanced reflection amplitudes below the BSR (*Lee et al.*, 2005, *Horozal et al.*, submitted, *Park*, 2008, *Kang et al.*, 2008). BSRs are well developed on the continental slope, but very weak or absent in the basin plain (*Kang et al.* 2008). Subsurface depths to the BSR range between 210 ms and 240 ms in TWT (*Yoo et al.* 2008). Heat flow values derived from the depth of the BSR in the Ulleung Basin are between 65 and 115 mW/m^2, comparable to those from ocean probe measurements (*Horozal et al.*, submitted). The high heat flow values in the northern part of the basin are related to the younger and hotter lithosphere and the distribution of

presumed incipient oceanic crust.

High seismic velocities imply high concentrations of gas hydrate in acoustically blanked chimney structures (e.g., *Lee et al.* 2005). There are numerous such features with a width of 0.2 km to 1.5 km in the northeastern part of the Ulleung Basin (*Kang et al.* 2008, *Yoo et al.* 2008). The features are seen entirely or only half-way through the GHSZ which extends to about 200-250 m below the seafloor. Some chimney structures extend well below the stability zone. Some of the features that extend close to the seafloor have surface expression of gas escape, such as pockmarks and mounds. There are also many gas seepage indications not associated with the chimney structures, predominantly on the continental slope where debris flow deposits are found (*Kang et al.* 2008). Gas seepages on the continental slope are more often associated with dome structures of about 100-500 m in diameter and 15 m in height. Enhanced reflections below the BSR are seen in the western slope of the area. The gas is thought to pass through the more permeable debris flow deposits. In addition, high total organic carbon concentrations (more than 0.5%) and high sedimentation rates of 60-280 m per million years (*Kwon et al.* 2006) derived from piston cores, could explain gas hydrate formation by organic diagenesis.

Gas hydrate in the Ulleung Basin was recovered for the first time in 2007 by piston cores in a blank zone structure (*Park* 2008). The hydrate samples were 2-5 cm in diameter massive hydrate found 3-8 m below the seafloor. The samples represent structure I hydrate containing more than 99% methane (*Park* 2008). More gas hydrate was recovered in fall 2007 from similar structures, during the drilling and coring expedition, where Logging While Drilling (LWD) data indicated high velocities

and resistivities (*Park et al.* 2008). Gas hydrate was found up to 150 m below the seafloor (bsf) at water depths between 1800 and 2100 m. The dominant sediments are fine-grained siliceous and calcareous clays with a terrigeneous and pelagic source. Coarser-grained sediments were also found as sand and silt beds, centimeters to meters in thickness, formed by debris flows and turbidity currents. Gas hydrate was found in clay, as veins and layers with thickness of a few centimeters, and as pore-filling material within the silt and sand layers. Thick intervals (130 m and 100 m) of gas hydrate-bearing sediments of interbedded clays and sands were discovered. Pore-filling hydrate in coarser-grained sediments and grain-displacing hydrate in finer-grained sediments were also discovered in the Krishna-Godavari Basin offshore India (*Collett et al.* 2008) and at the Cascadia Margin offshore Vancouver Island (*Riedel et al.* 2006a).

Chapter 2

Stacking Velocity from Processing of MCS Data

Seismic velocities are the primary focus of this study because of their importance for: a) obtaining a good reflectivity image from a multi-channel stack and migrated section; and b) identifying anomalous velocity values which can be related to physical properties of subsurface sediments, in particular the presence of high-velocity gas hydrate and low-velocity free gas. The main analysis uses conventional moveout velocities, i.e., stacking velocities obtained from semblance spectra. Accurate and detailed velocities are obtained with considerable effort.

The work is focused on a single line, 063, shot in the eastern side of the Ulleung Basin, where there are a series of prominent blanking zones that may contain large hydrate concentrations. The 34 km long line is largely on the basin plain in water depths of about 2000 m in a direction of 45^o to the depth contours (Fig. 1.3).

2.1 Processing of MCS Data

The multi-channel seismic reflection data were acquired as part of the 2005 Gas Hydrates 2-D Data Acquisition from the KIGAM seismic survey vessel Tamhae II using an airgun array source of 1035 in^3 and a single streamer with 240 recording channels (*Kang et al.* 2008). The near offset is 161 m and the far offset 3149 m, with receiver spacing of 12.5 m. The distance between shots is 25 m, resulting in a common depth point (CDP) spacing of 6.25 m. The sampling rate is 1 ms and the data contain power up to 400 Hz (Fig. 2.1). The dominant frequency is 70 Hz, which for a sediment velocity of 1600 m/s results in a dominant wavelength of 23 m. The maximum vertical resolution is between one quarter and one eighth of the dominant wavelength of the pulse (*Yilmaz* 2001), which in this study is 3-6 m. The horizontal resolution of the unmigrated seismic data given by the Fresnel zone is about 350 m at a depth of 2.5 km. Both the vertical and horizontal resolution decrease with increasing depth.

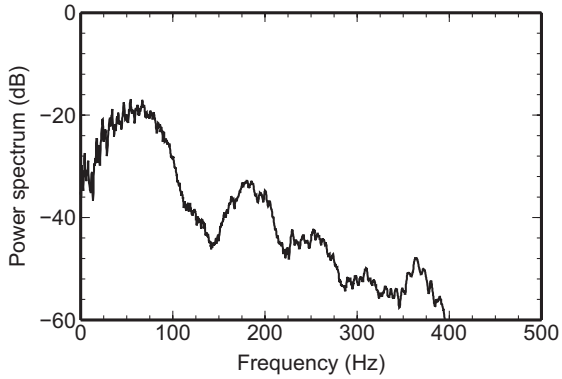

Figure 2.1: Power spectrum from all traces in a shot gather from 2.8 to 5.0 s TWT.

The seismic processing was done using the Globe Claritas software from Geological

and Nuclear Services Inc., New Zealand, using the following sequence (some of the more important steps are described in detail afterwards):

- zero phase bandpass Butterworth filter with corner frequencies: 5-15-150-250 Hz
- minimum phase bandpass Butterworth filter (5-15-150-250 Hz)
- predictive deconvolution on shot gathers: operator length = 200 ms, gap length = 12 ms
- zero phase bandpass Butterworth filter (5-15-150-250 Hz)
- coarse stacking velocity analysis using semblance spectra
- spherical divergence correction of $(V_{RMS}^2 \cdot TWT)$
- dip moveout (DMO) using 60 offset planes to correct for reflector dip
- detailed velocity analysis using semblance spectra, with velocity quality check: constant velocity gathers (CVG) and constant velocity stacks (CVS)
- normal moveout (NMO) correction with detailed stacking velocities and stack
- interval velocities derived from smoothed stacking velocities using Dix equation
- finite difference time-migration
- stacks and migrated sections repeated at different offsets

2.1.1 Predictive Deconvolution

Deconvolution increases the vertical (temporal) resolution by compressing the seismic wavelet produced by the airgun array. It is an important step that sharpens the processed image and improves the accuracy of the velocity analysis. Predictive deconvolution is chosen over source signature deconvolution because the source signature was not available. Predictive deconvolution with an operator length of 200 ms and a gap length of 12 ms is applied on shot gathers. There is no reverberation on the autocorrelation function or shot gathers, and the length of the operator and gap should not introduce too much noise and at the same time compress the seismic wavelet. The filter is designed on a time window between 2.75 and 5.50 s, which is the traveltime between the seafloor and the first water multiple. The filter is applied on the whole length of the trace. Since the deconvolution filter assumes that both the seismic wavelet and the earth impulse response are minimum phase, a minimum phase bandpass Butterworth filter (5-15-150-250 Hz) is applied prior to deconvolution. The choice of corner frequencies of the filter emphasizes the dominant frequency of the source signal, excluding very low and high frequencies, where noise is expected to dominate. To convert the data to minimum phase, one could also apply a filter designed to convert the source wavelet to a minimum phase wavelet. This is not done because the source wavelet is not available so this could introduce a significant error. After deconvolution, a zero phase bandpass Butterworth filter (5-15-150-250 Hz) is applied to the data.

2.1.2 Stacking Velocity Analysis

Stacking velocities have been estimated by moveout analysis on CDP gathers using semblance as a coherence measure. Stacking velocities are used to approximate RMS velocities from the sea surface (source and receiver) to the reflector (*Al-Chalabi* 1974). A stacking velocity function is picked for each CDP, by identifying the velocity corresponding to the maximum semblance on velocity spectra plots. The semblance is a measure of signal coherency along the NMO trajectory over the entire spread length of the CDP gather that allows optimal stacking. The velocity analysis is done with the Constant Velocity Analysis (CVA) application of Globe Claritas. The application requires an initial brute stack that is obtained from a few velocity profiles with values characteristic of marine sediments. Semblance is calculated using a weighted average of 5 neighbouring CDP's, with weights 0.3, 0.5 for the neighbouring CDPs and 1 for the central CDP.

An initial velocity analysis was carried out on line 063 every 300 CDPs (1875 m) and a more detailed analysis after the DMO (see Sec. 2.1.3) every 50 CDPs (313 m) outside the blank zones and every 10 CDPs (63 m) inside the blank zones. A total of 151 velocity profiles were calculated, where 40 are inside the blank zones and 111 are outside the blank zones. The velocity spectrum is computed along hyperbolic paths for a velocity range of 1450 to 2020 m/s in increments of 1 m/s from 2.7 s to 4.5 s. The amplitudes below 4.5 s ($\sim$1.8 s bsf) generally were found to be too weak for useful velocity analysis. In order to identify the velocity corresponding to maximum semblance, the colour range of the semblance spectra was modified several times when

picking velocities in one panel because the auto-picking feature was not working.

2.1.3 Dip Moveout (DMO) Correction and New Velocity Analysis

The DMO correction improves the accuracy of stacking velocity estimation, by removing the effect of reflector dip on the moveout velocity and reducing dip conflict in the stack (*Hale* 1984), especially at the location of blank zones, which have pulled-up reflectors. DMO correction is applied after the first rough velocity profiles are picked. The data are first sorted from CDP to common offset planes. The 240 offset planes are distributed between CDP's such that neighbouring CDP's have different offsets, with a pattern that is repeated every 4 CDP's, which means that a certain offset is present once every 4 neighbouring CDPs. The DMO routine requires fully populated offset planes before the traces are added. The offsets are first regularized, which reduces the number of offset planes from 240 to 60, with offsets at a spacing of 50 m instead of 12.5 m, resulting in every set of 4 neighbouring CDP's having the same offsets. After the data are regularized, forward NMO is applied, followed by the DMO routine, and inverse NMO. The NMO routine uses a 2-D horizontally and vertically smoothed velocity function of the initial velocity picks, such that the DMO is not influenced by laterally varying velocities. The velocities are adjusted after DMO analysis on the existing grid and more velocity profiles are added. As expected, the largest changes from the previous velocity-traveltime functions are in the blank zones, which have the largest reflector dips, up to $\sim 5^0$.

2.2 Stacking Velocity Analysis Results

2.2.1 Velocity Profiles and Stack

A new stack image is created using the velocity picks after DMO correction (Fig. 2.2). The 34-km-long profile is shown between CDP 1633 and 7035. The stacking velocities picked at the seafloor are shown above the stack. A high amplitude reflector is seen from CDP 2400 to CDP 6200 at about 3.3 s. Several blank zones that are 40-100 CDPs (250-625 m) wide can be identified on the stack between 2.8 and 3.0 s. The features centered at CDP 2020 and 3380 have reduced reflection amplitudes both above and below the BGHSZ, whereas the features centered at CDP 3550 and 6080 have reduced amplitudes above and clear and strong reflectors below the BGHSZ, particularly beneath CDP 3550 between 3.0 and 3.1 s. Although reflection amplitudes are reduced within these features above the BGHSZ, some reflectors can still be identified although they are not very clear. The reflectors inside the blank zone centered at CDP 3380 appear bowed downwards and the ones in the blank zones centered at CDP 2020 and CDP 3550 are bowed upwards (Figs. 2.3, 2.4). The direction of the bend of the reflectors in the blank zone centered at CDP 6080 is not very clear (Fig. 2.5). The reflectors below the BGHSZ are relatively flat and do not follow the bowing-up or bowing-down of the shallower reflectors. A narrower feature 50 CDP wide with pulled-up reflectors partway through the GHSZ is seen at CDP 2400, but the amplitudes are only slightly reduced. Very short features with pulled-up reflectors around CDP 2400 are seen protruding just around the BGHSZ. Narrow features with pulled-up reflectors from above the BGHSZ mid-way to the seafloor are

seen at CDP 3200 and 5400. Some of these features have reduced amplitudes also below the BGHSZ.

The seafloor stacking velocity represents the effective average water velocity. A slight decrease is noted from the north to the south of the profile, as the traveltime to the seafloor decreases by 0.05 s. The average of all picks across the profile is 1471 m/s, with a standard deviation of 2.4 m/s.

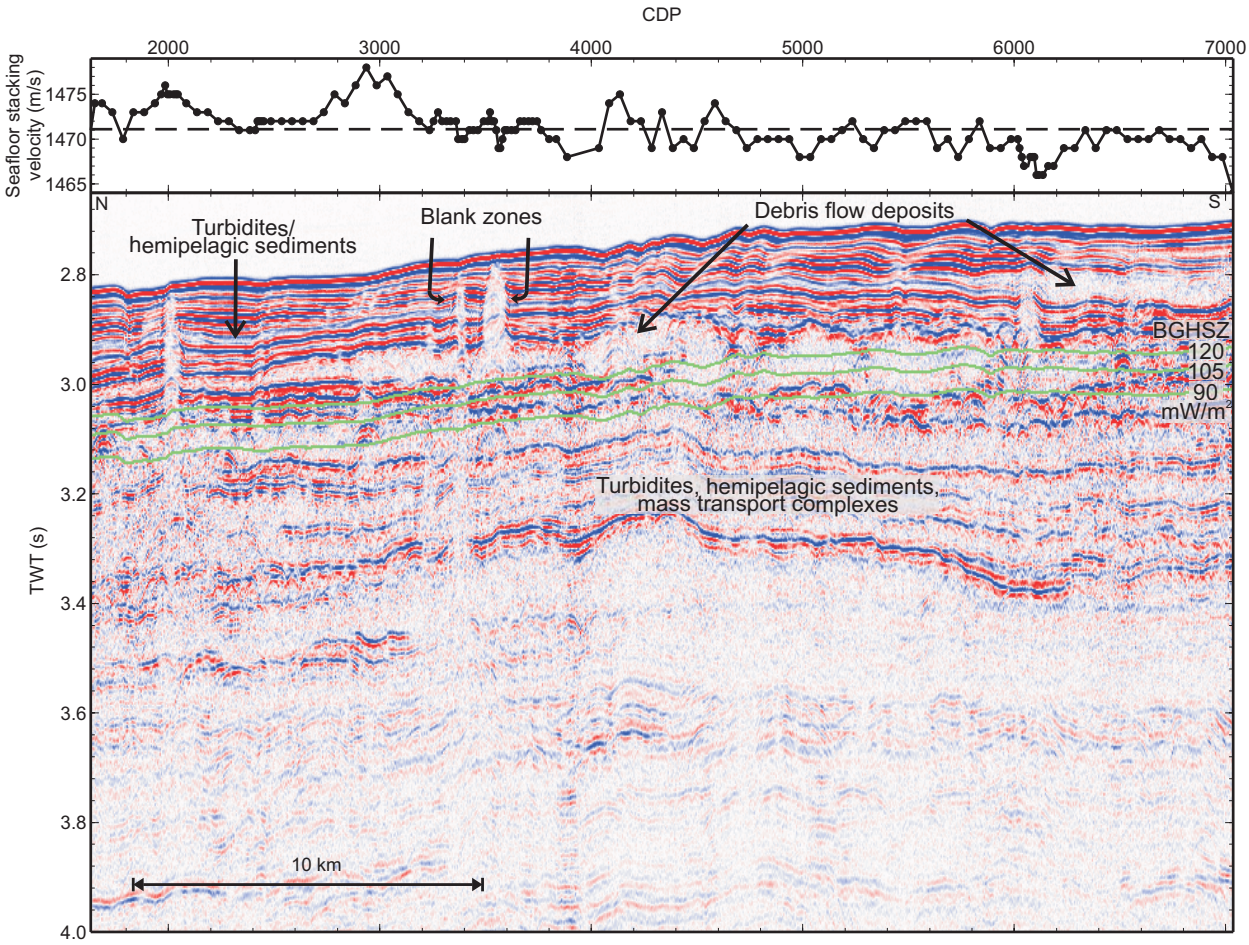

Figure 2.2: Stack after DMO indicating the predicted BGHSZ with three different constant values of heat flow along the line.

On Figs. 2.3, 2.4 and 2.5, the black diamonds indicate the location of the velocity picks at the given CDP locations. The velocity spectra at these CDP gathers are

shown together with the velocity picks at maximum semblance. More velocity profiles were analyzed than shown in the figures. The predicted BGHSZ for constant heat flow values of 105 and 120 mW/m^2 (Chapter 5) is shown by the green curves on the stack and by the black dashed lines on the velocity spectra figures.

Stacking velocity profiles inside the blank zones are compared to those outside the blank zones, where it is assumed that there is little gas hydrate or free gas. The differences between these areas can aid in the understanding of the nature of the pull-up/pull-down, blanking and how these features are formed. The stacking velocity outside the blank zones generally increases by about 10 m/s from the seafloor to the BGHSZ (e.g., CDP 2485 in Fig. 2.3, CDP 5985 in Fig. 2.5). Very few profiles show a continuous decrease in velocity over the same depth range (e.g., CDP 2085, CDP 2135 in Fig. 2.3). The velocity decreases by about 10-20 m/s around the BGHSZ at some locations (e.g., CDP 1965, CDP 2085 in Fig. 2.3, CDP 3622 in Fig. 2.4, CDP 6160, CDP 6185 in Fig. 2.5). Inside the blank zones, the velocity shows very different trends than outside. In most cases, the velocity both increases and decreases above the BGHSZ (e.g., CDP 2045 in Fig. 2.3, CDP 3370, CDP 3390, CDP 3550, CDP 3580 in Fig. 2.4, CDP 6045 in Fig. 2.5). Most of the profiles show a velocity decrease around the BGHSZ by an average 15-30 m/s, which is larger than the decrease outside the blank zones at the same depth (e.g. CDP 2005, CDP 2025 in Fig. 2.3, CDP 3360, CDP 3540 in Fig. 2.4, CDP 6055, CDP 6085 in Fig. 2.5).

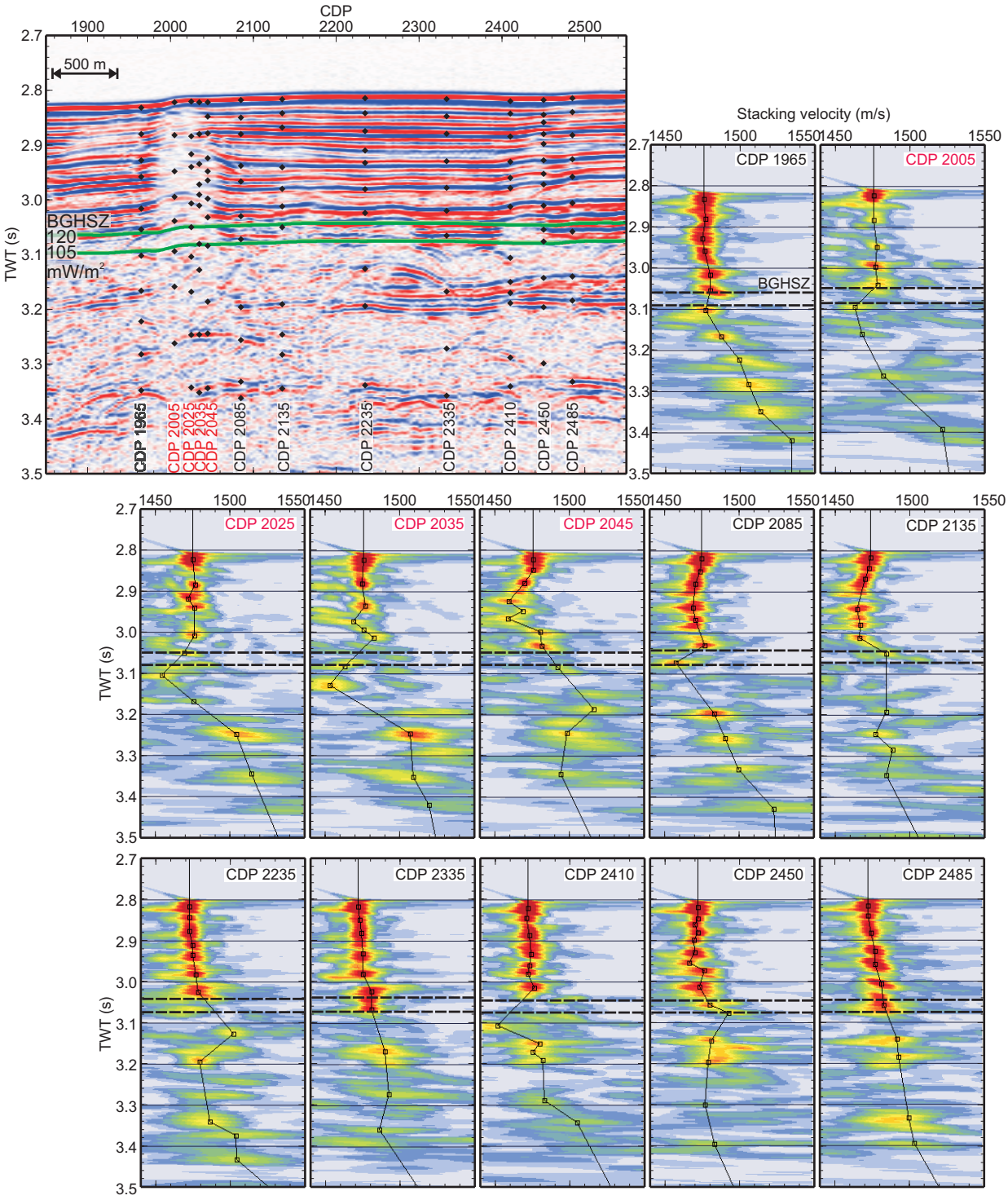

Figure 2.3: Stack between CDP 1850 and 2550 showing the location of the central CDPs used for the semblance calculations.

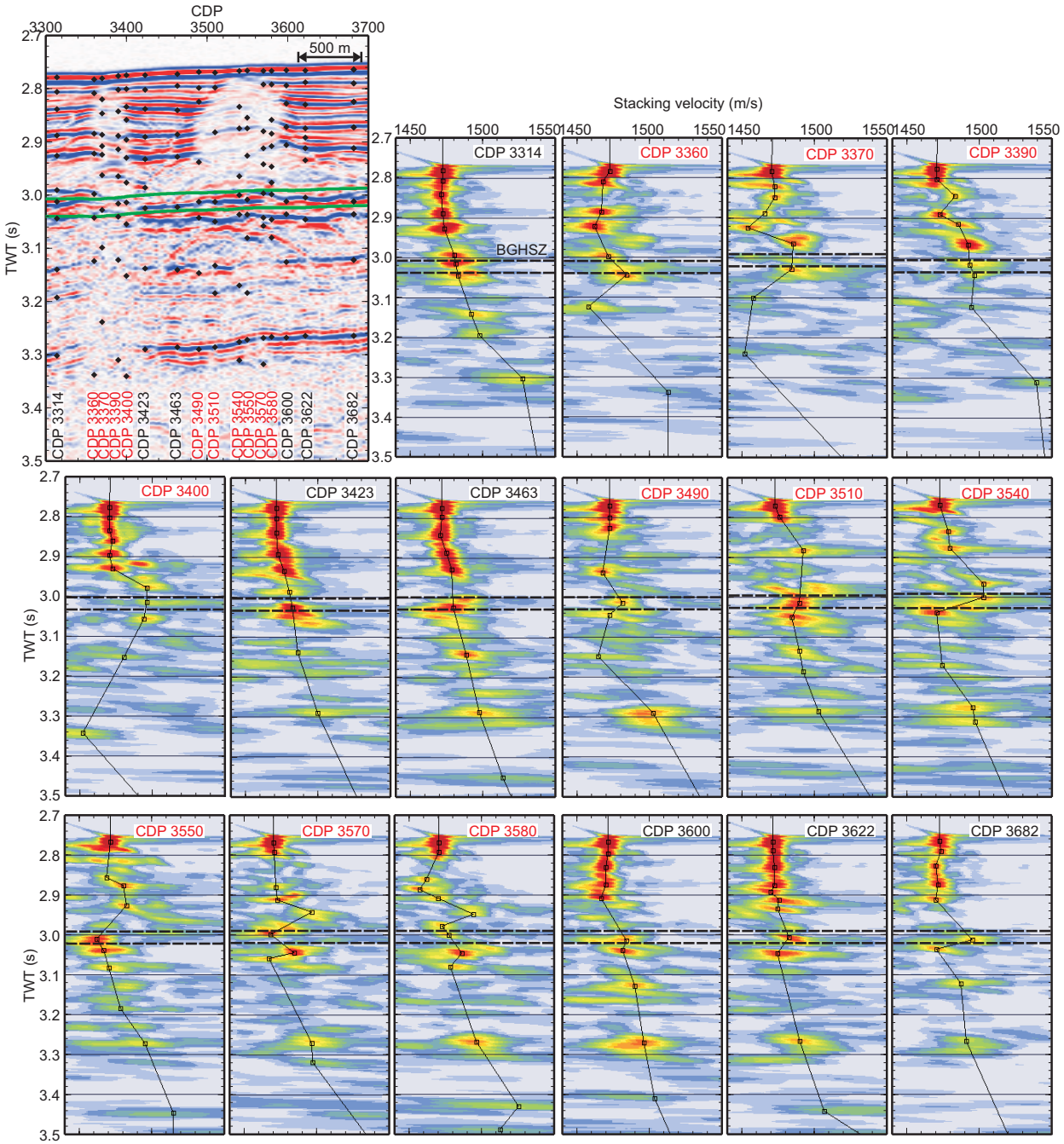

Figure 2.4: Stack between 3300 and 3700 showing the location of the central CDPs used for the semblance calculations.

2.2.2 Velocity Quality Check: CVG and CVS

The velocity model from semblance analysis can be checked and improved by visually analyzing CVG and CVS. The correct velocity at a certain depth is the

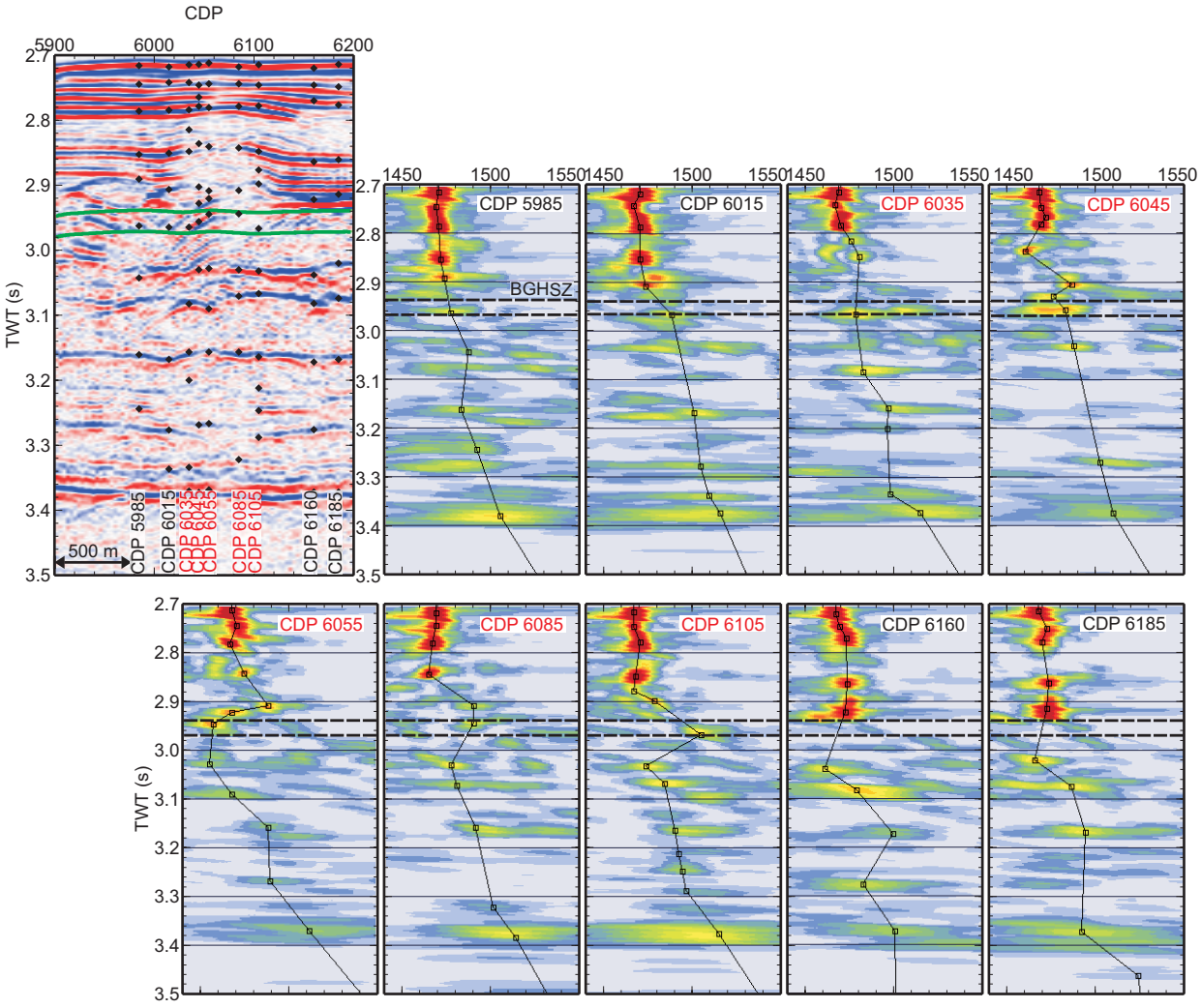

Figure 2.5: Stack between 5900 and 6200 showing the location of the central CDPs used for the semblance calculations.

one that flattens a reflector in a CVG and the one that gives the best stacked event amplitude and continuity in CVS. This process is rather time-consuming but increases the confidence that picked velocities correspond to coherent events. The velocities are used to correct the arrivals in a CDP gather for NMO, and the traces are then stacked.

Fig. 2.6 shows two CDP gathers which have been NMO-corrected repeatedly using constant velocities between 1450 and 1500 m/s every 10 m/s. The far right panel

shows the gather moved out using the velocity function picked from the semblance spectrum and the flattened events. An averaged instantaneous amplitude is plotted on top of the moved out gathers to show the main reflection events (curves also shown in Figs. 6.6 and 6.7). The CDP gather 3463 (Fig. 2.6a) is from an area outside the blank zone and CDP gather 3550 (Fig. 2.6b) is from inside a blank zone. The CDP gather 3463 has higher amplitude and more coherent reflectors, especially above 3.0 s. This can also be seen in the instantaneous amplitude curve shown in white in the rightmost panel which is averaged over CDP 3420-3471. The lower reflection amplitudes inside the blank zone can be easily seen on the CDP gathers 3550 and in the instantaneous amplitude curve, which is averaged over CDPs 3490-3582. The seafloor, and the reflectors at 3.0 s and 3.3 s are the most prominent ones.

Some of the shallower reflectors appear curved or the arrivals do not align properly after the NMO correction. Very often a reflector is only coherent in the near offset traces, and sometimes in the far offset traces or the middle offset traces. The curved or mis-aligned reflectors could be a result of an improper NMO correction, that assumes a hyperbolic fit to the arrivals from a reflector. A disrupted structure can also affect the coherence across the gather. Random noise from the streamer movement and coherent noise such as multiples are additional factors. Improper DMO correction at the location of the blank zones would result in the velocity being overestimated. The dip effect can be better removed by repeating the DMO correction. The curved, mis-aligned and non-continuous reflectors make it more difficult to identify the most accurate velocity from a constant velocity gather. Generally, only the most coherent part of the reflector from a CDP gather is used when analyzing the flattened reflectors

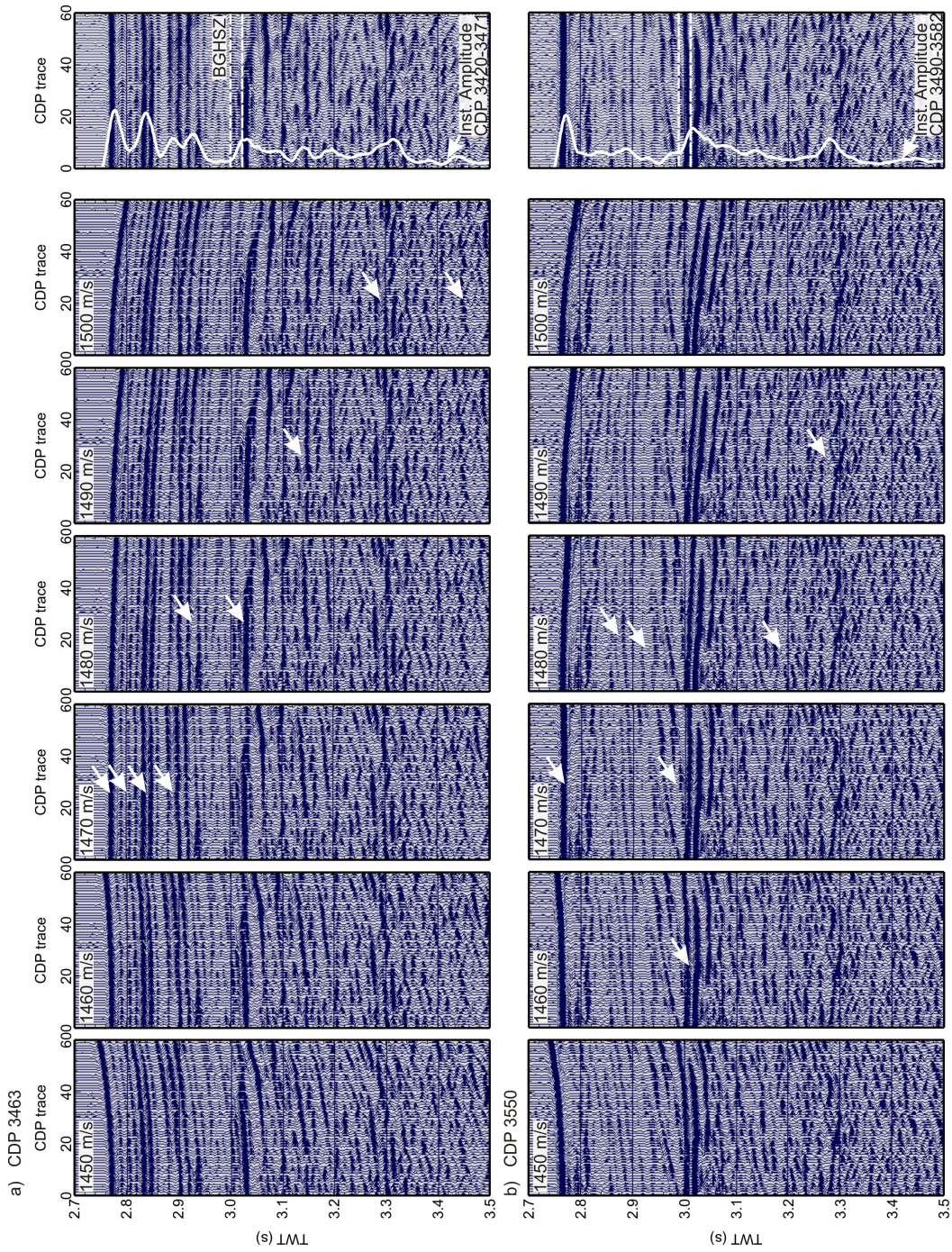

Figure 2.6: Constant velocity gathers (CVG) for a) CDP 3463 and b) CDP 3550 using a velocity range of 1450-1500 m/s every 10 m/s shown at the top of each panel. The arrows indicate the event that is flattened by the constant velocity. The far right panel is the same CDP gather with a different NMO applied to each reflector.

in CVG for moveout velocity; the data from such reflectors may have significantly higher uncertainty.

An example of CVS (Fig. 2.7) is shown on data between CDP 3300 and 3700, which are stacked with a range of constant velocities between 1450 m/s and 1500 m/s, every 10 m/s. Any event corrected with the right velocity shows increased amplitude and continuity. These reflectors can be identified in the stack obtained with a varying velocity function shown in Fig. 2.4. The seafloor and reflector at 3.3 s give the best stack response for velocities of 1470 m/s and 1500 m/s, respectively. The pulled-down reflectors above and below 2.9 s around CDP 3380 are best imaged with a velocity of 1460 m/s and 1450 m/s, respectively. These stacking velocities 'picked' from the CVS agree with those derived from semblance spectra. The reflectors immediately below 3.0 s show bright sections for all velocity scans, so there is not a single velocity that can improve the stack. This observation agrees with the wide range of velocities identified for these reflectors from semblance plots.

2.2.3 1D Velocity Profiles

The velocity profiles between CDP 1985-2045, CDP 2410-2450, CDP 3360-3400, CDP 3490-3600, CDP 6015-6115 are treated separately from the rest of the profiles, as they appear acoustically blanked and have pulled-up reflectors. The distinction between these areas and those outside is made in all plots by red and black symbols and lines, respectively.

The seafloor is adjusted to zero depth by subtracting the seafloor traveltime at each CDP from the later traveltimes. All picks within each of the two regions are

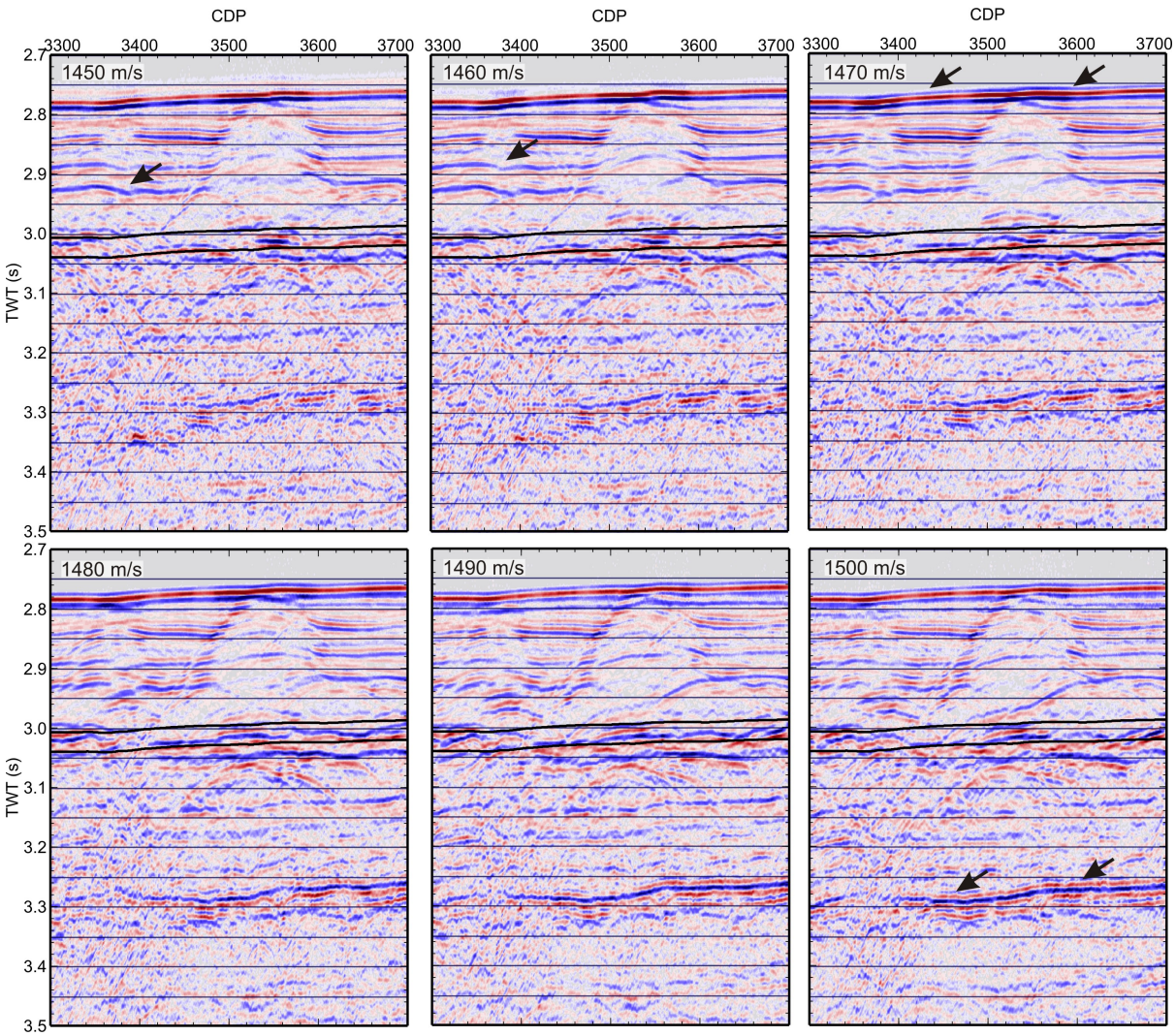

Figure 2.7: Constant velocity stacks (CVS) using a velocity range of 1450-1500 m/s every 10 m/s. The correct velocity corresponds to the maximum amplitude and continuity for a certain event and can be compared to that picked from semblance plots.

shown in Fig. 2.8a, with the uppermost 0.5 s TWT shown in Fig. 2.9a. The picks from inside the blank zones are shown in red and those from outside the blank zones are shown in black. The running mean of each dataset is calculated every 5 ms in running windows of 50 ms. The velocities larger or smaller than 2 standard deviations away from the mean, indicated by the dashed lines, are excluded from further calculations, assuming that they are an error due to structural complexities or other problems.

Under the assumption that the data are normally distributed, 95.5% of the data points should lie within 2 standard deviations from the mean. This is approximately the case for our data, where 5.8% of the initial velocities outside the blank zones and 3.4% velocities inside the blank zones are excluded. The distribution of velocities inside the blank zones deviates from a normal distribution, especially at depths close to the BGHSZ.

To define the general velocity variation with depth, quadratic trends are fit through the two datasets with outliers excluded, as indicated by the dashed lines. Also, the picks are averaged in time every 5 ms using a 50 ms long running window. The running mean is shown in Figs. 2.8b and 2.9b, with the corresponding standard deviation in Figs. 2.8c and 2.9c and the number of picks in each window in Figs. 2.8d and 2.9d.

The mean stacking velocity outside the blank zones increases only slowly with depth at shallow depths, from 1471 m/s at the seafloor to 1478 m/s at 250 ms bsf, corresponding to the approximate depth of the BGHSZ. The mean velocity inside the blank zones is 1-3 m/s lower than outside between 100 and 160 ms bsf, 3-6 m/s higher between 220 and 290 ms, and again lower by 4-9 m/s between 300 and 350 ms. There is clearly a larger variability in velocities inside the blank zones and the anomalies have been analyzed considering the sources of errors, presented in more detail in Sec. 2.2.6. One way is to look at the standard deviation and data count, which quantify the random errors. The standard deviation is larger for velocities inside the blank zones; this could result from the reduced reflection amplitudes in these features, from the reduced number of velocity picks, which is about half that from outside and possibly due to the larger dips which have not been adequately corrected for. In addition, the

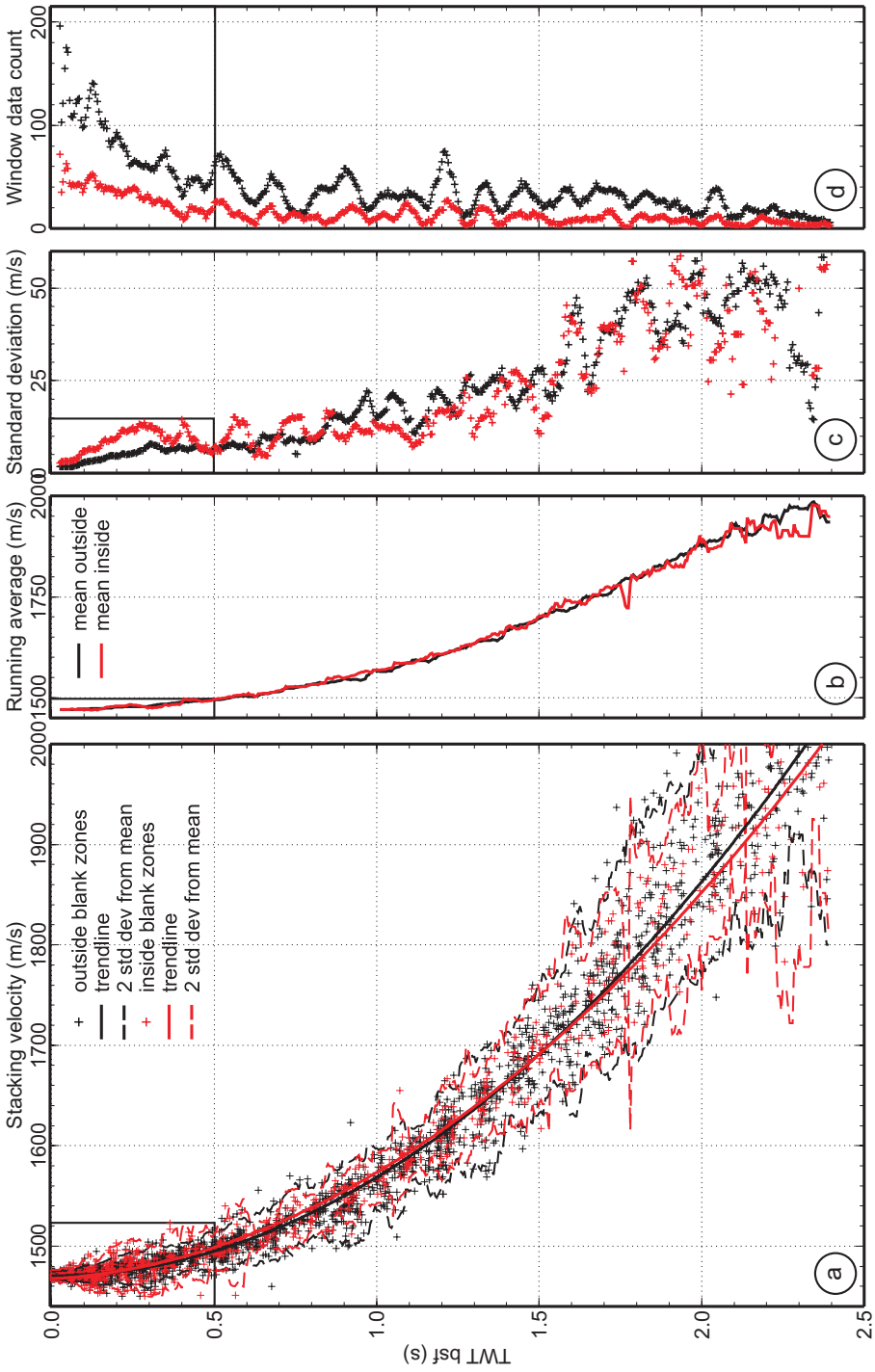

Figure 2.8: a) Stacking velocity to a reflection depth of 2.5 s bsf (∼3000 m bsf) outside and inside blank zones in black and red, respectively, fit by quadratic trendlines; velocities larger than two standard deviations are excluded from further calculations; b) running mean every 5 ms in 50 ms long windows; c) standard deviation; d) window data count.

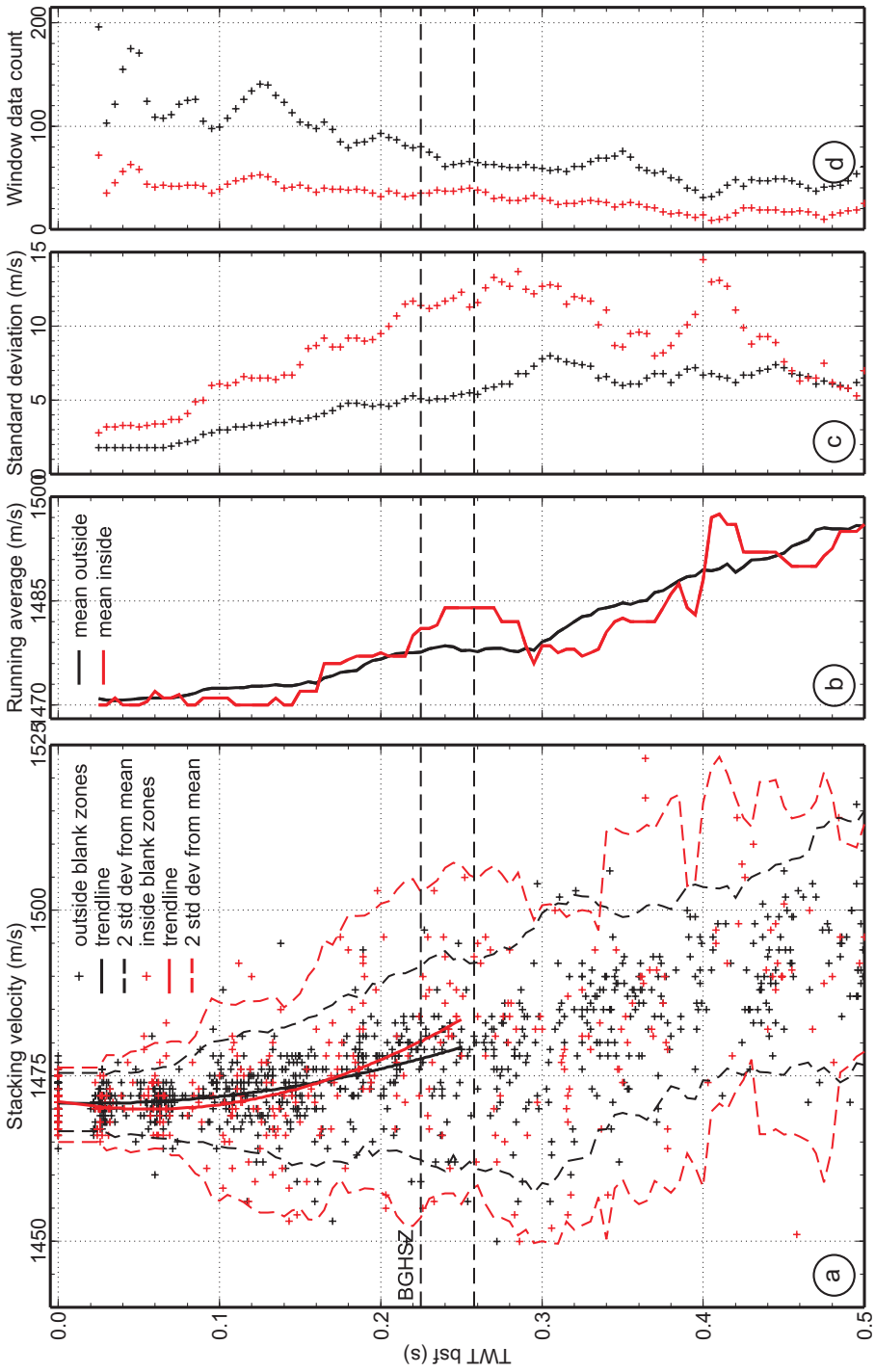

Figure 2.9: Enlargement of Fig. 2.8 up to 0.5 s bsf, where hydrate and gas is expected. a) Stacking velocity up to 0.25 s outside and inside blank zones in black and red, respectively, fit by quadratic trendlines; velocities larger than two standard deviations are excluded from further calculations; b) running mean every 5 ms in 50 ms long windows; c) standard deviation; d) window data count.

larger standard deviation likely reflects real velocity variations (e.g., gas hydrate and structure). The standard deviation increases approximately linearly from 2 m/s at the seafloor to 10 m/s and 13 m/s at 300 ms bsf for areas outside and inside the blank zones, respectively. Below this depth, the standard deviation oscillates greatly, which is reflected by the reduced number and larger variations in the velocity picks. The standard deviation reaches about 25 m/s at 1.5 s bsf and 50 m/s below 1.6 s. The standard error of the mean (Fig. 2.10), representing an estimate of the uncertainty in the mean, is calculated to provide an indication of the size of the uncertainty of this estimate. The standard error of the mean outside the blank zones is 0.1 m/s just below the seafloor, 0.3 m/s at 0.1 s, 0.7 m/s at 0.25 s at the BGHSZ, and 0.8 m/s at 0.5 s. The standard error inside the blank zones is 0.3 m/s immediately below the seafloor, 1 m/s at 0.1 s, 2 m/s at 0.25 s, 2.5 m/s below the BGHSZ, and 1.4 m/s at 0.5 s. The difference of the mean inside the blank zones as compared to outside the blank zones is significant, as the value of the mean plus one standard error inside the blank zones does not intersect with that from outside the blank zones.

The stacking velocities up to 0.25 s and up to 2.50 s are fit separately by quadratic polynomials for areas outside and inside the blank zones. The form of the general second degree equation is given below:

$$V = a + bt + ct^2 \tag{2.1}$$

where V is the stacking velocity in m/s, t is the TWT bsf in s and the coefficients a, b and c are given in Table 2.1.

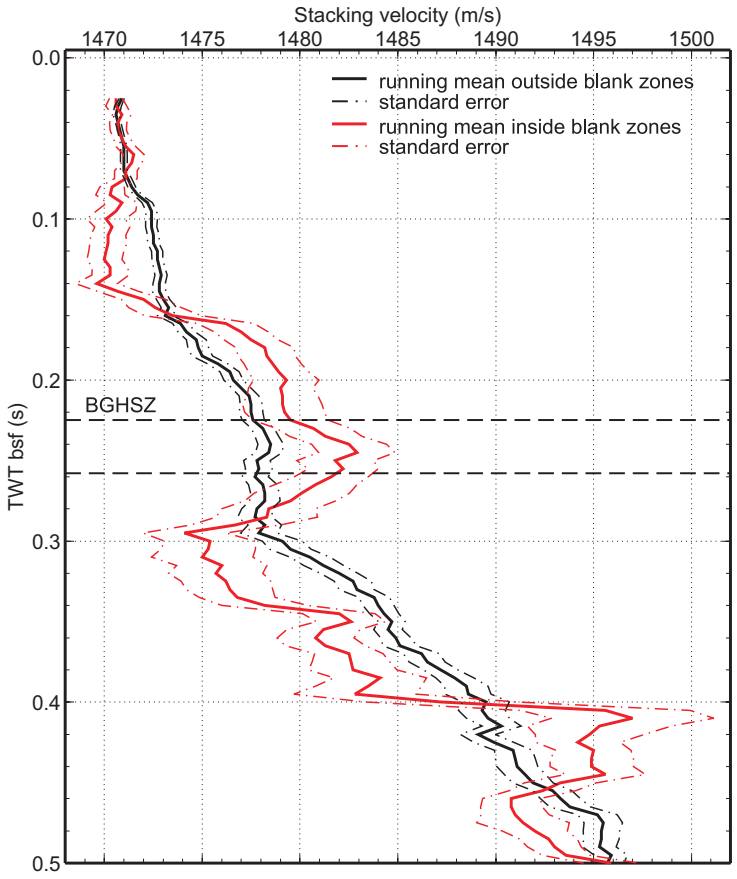

Figure 2.10: Stacking velocity running mean and standard error outside and inside the blank zones shown in black and red.

	Shallow 0.25 s bsf		Deep 2.5 s bsf	
	out	in	out	in
a	1470.92	1471.09	1470.58	1467.40
b	6.55	40.51	0.26	19.62
c	160.46	360.27	98.24	86.36

Table 2.1: Coefficients a, b, and c from the stacking velocity polynomial of the form given by Eq. 2.1. Different polynomials are fit to the velocity data and to the running median up to 0.25 s bsf and 2.5 s TWT bsf, outside and inside the blank zones.

2.2.4 2D Velocity Grid

Fig. 2.11 shows a gridded surface of the picked stacking velocities produced using the near-neighbour algorithm. The locations of the picks are marked by crosses. The locations of the blank zones centered at CDP 2020, 2430, 3380, 3550 and 6080

are indicated by the black dashed lines. The velocities generally increase from 1470 m/s at the seafloor to 1510 m/s at about 0.5 s bsf. Stacking velocity characterizes the interval from the sea surface to a certain reflector. Therefore, a lower or higher stacking velocity at one point should be associated with a lower or higher velocity in the interval bounded at the bottom by the respective pick and at the top by the closest pick. In this respect, the interpolation used to produce Fig. 2.11 is misleading because it shows an anomaly both above and below a pick.

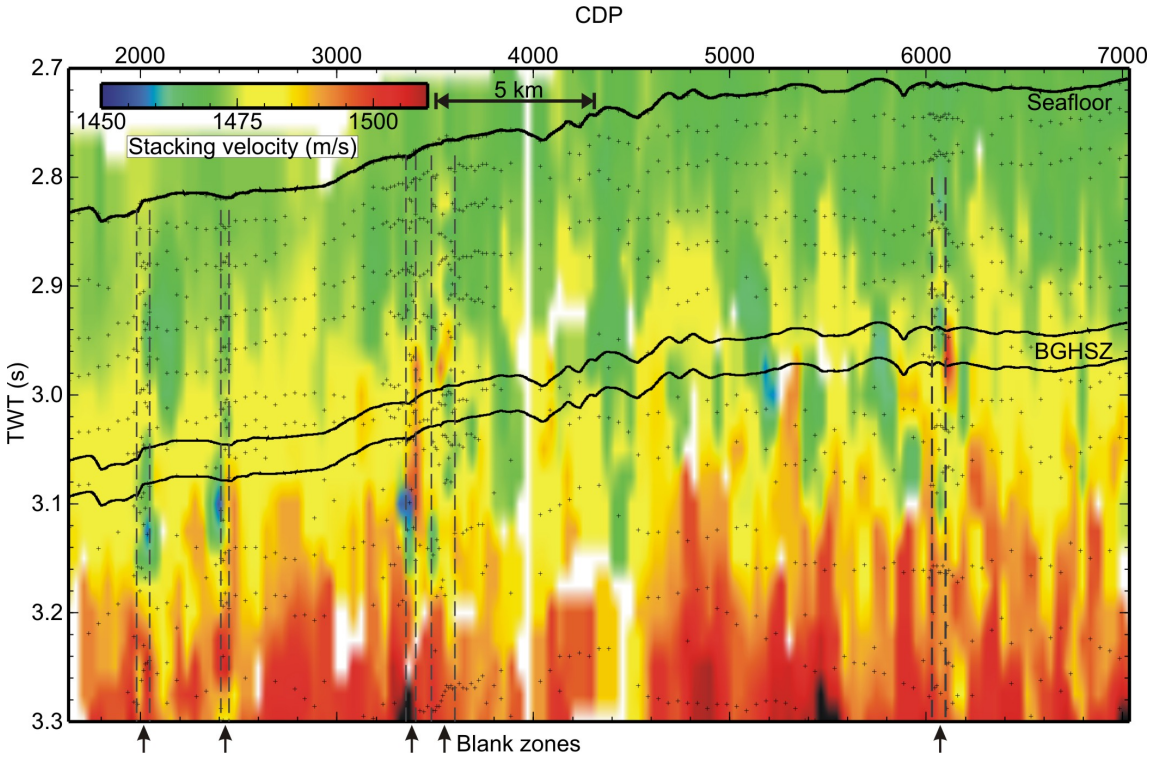

Figure 2.11: Gridded plot of stacking velocities on line 063 using the near-neighbour interpolation algorithm. The velocity picks are indicated by crosses. The approximate extent of the blank zones is indicated by the dashed lines. The seafloor and BGHSZ are indicated by the solid black curves, where the BGHSZ is calculated for constant heat flow of 105 and 120 mW/m^2.

2.2.5 2D Velocity Anomalies

Stacking velocity anomalies (Figs. 2.12, 2.13) represent the deviation of each velocity from the running mean of velocity picks outside the blank zones calculated every 1 ms in 50 ms long windows. All calculations exclude picks that lie beyond 2 standard deviations from the mean. This velocity mean outside the blank zones is taken to be representative of normal sediments in the area.

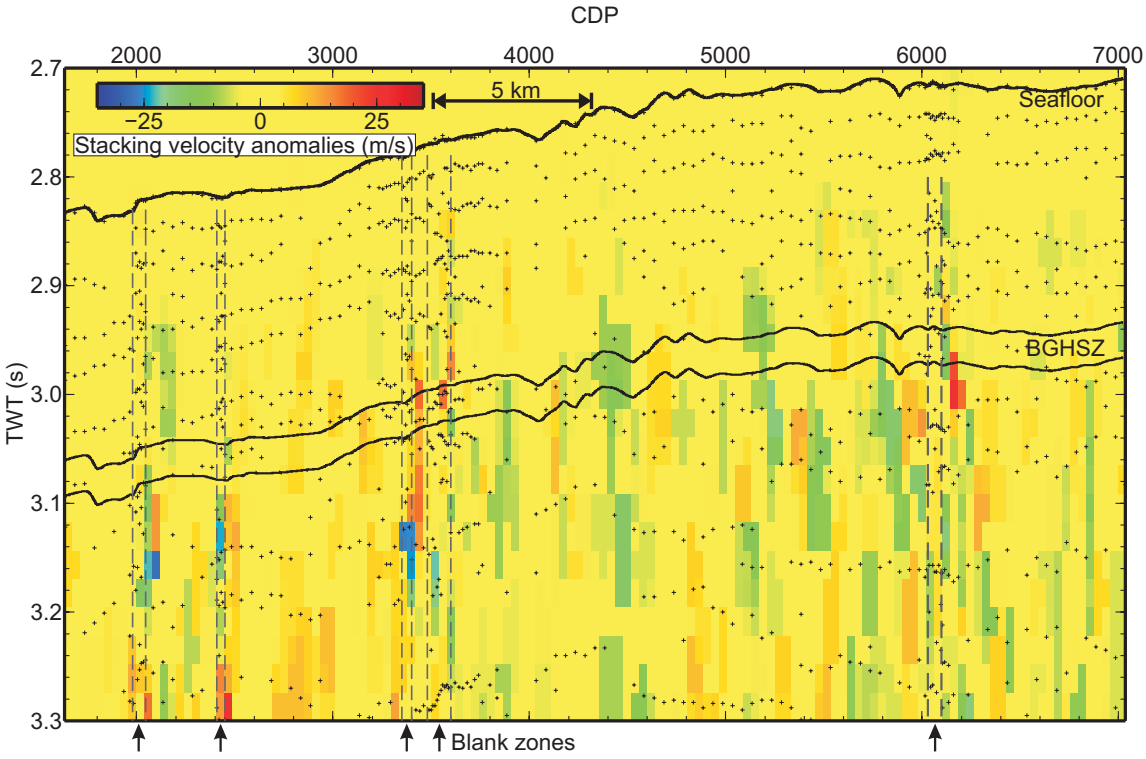

Figure 2.12: Gridded plot with stacking velocity anomalies derived by subtracting a running mean calculated every 1 ms in 50 ms long windows from each velocity pick shown in Fig. 2.11.

There are velocity anomalies associated with the blank zones, but very careful analysis is required to assess whether they are significant to be associated with physical changes in sediments. The blank zone at CDP 2020 and the area immediately next to it show a negative stacking velocity anomaly of about 10-15 m/s above the BGHSZ

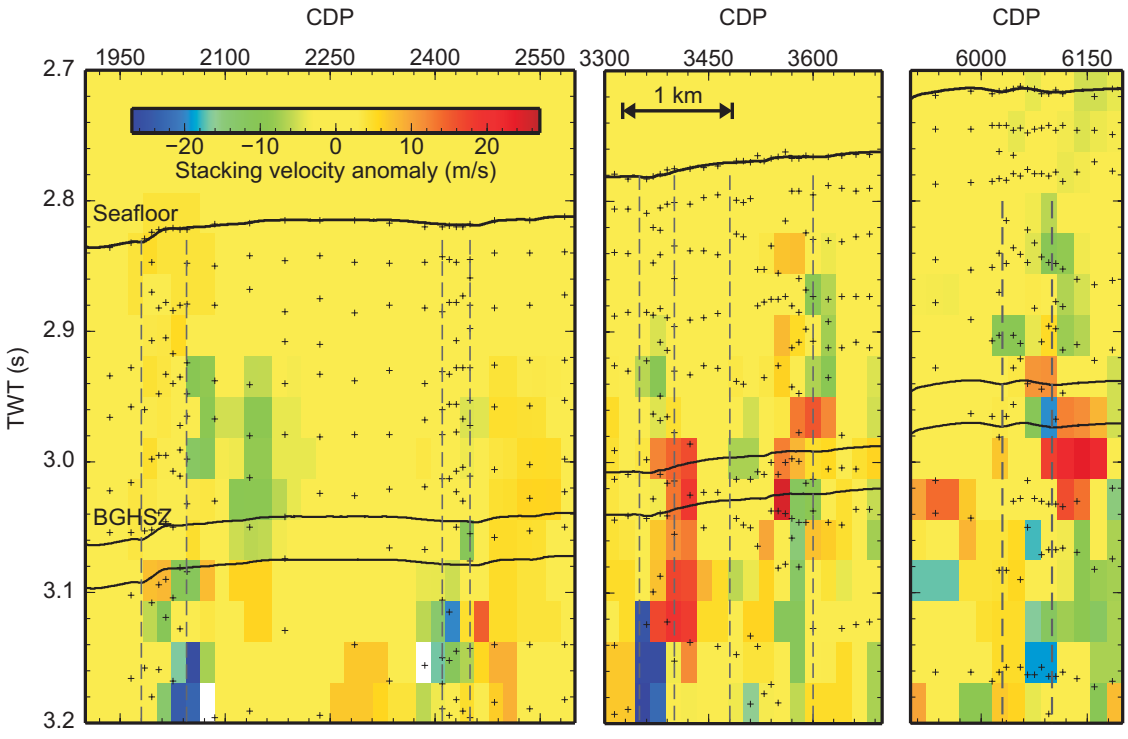

Figure 2.13: Gridded stacking velocity anomalies associated with the blank zones and areas next to them.

and of about 20-25 m/s around and below the BGHSZ. These velocity anomalies are also noted in the discussion of Fig. 2.3. The blank zone at CDP 3380 shows a few locations above the BGHSZ around 2.92 s with a velocity decrease of about 10 m/s, but shows an increase of about 15 m/s above and around the depth of the BGHSZ, also noted from the velocity spectra in Fig. 2.4. The blank zone at CDP 3550 shows positive anomalies of 10 m/s at 2.84 s, and of 25 m/s around 2.98 s. There are some smaller negative anomalies of 10-15 m/s around 2.85 s and 3.0 s. Negative velocity anomalies of 15-25 m/s lower than the mean are seen below the BGHSZ. The blank zone at CDP 6080 shows negative anomalies of 10-15 m/s above the BGHSZ, but also a few positive anomalies of 20 m/s around the depth of the BGHSZ. A patchy distribution of negative anomalies of about 20 m/s is seen around and below the BGHSZ

from CDP 3600 to CDP 7000.

2.2.6 Error Sources in Estimating Stacking Velocity

The most important factors that limit the accuracy and resolution of the velocity estimates are: the spread length, the signal-to-noise ratio, the deviation from hyperbolic moveout, the limited bandwidth of the data and the effect of reflector dip (*Yilmaz* 2001). The hyperbolic approximation and dip effects introduce systematic errors and the others random errors. Lack of large offset information corresponds with a lack of significant moveout for discrimination of velocity, which results in a loss of sharpness of the peaks in the velocity spectra. The large offsets in the recorded data in this study (161 m - 3149 m) allow accuracy of stacking velocities. The incidence angle of rays reflecting from ∼200 m bsf recorded at the far offset is 35^0 degrees, which is close to optimum for good accuracy of stacking velocities. These offsets likely avoid the high sensitivity to seafloor topography and water column velocity variations characteristic for even larger offsets. The quality of the velocity spectrum is reduced when the signal-to-noise ratio is reduced. The error in the stacking velocity in the presence of random noise is proportional to the magnitude of the stacking velocity, the standard deviation of the time shifts of reflection wavelets along the velocity moveout curve, and inversely proportional to the fold of coverage and the moveout time at maximum offset (*Al-Chalabi* 1974). The stacking velocity measurement method used here employs a hyperbolic approximation for the velocity moveout curve. This assumes horizontal layers and zero-offset reflections. The stacking velocity is obtained using a hyperbolic approximation across the entire spread length, which can devi-

ate from the NMO velocity, which results by fitting a hyperbola through the nearest offsets only. The difference between the stacking velocity and the NMO velocity is called the spread length bias (*Al-Chalabi* 1974, *Hubral and Krey* 1980). The incidence angles at short offsets are closer to the vertical, such that rays do not refract much through the overburden and are thus closer to the straight-ray geometry required for hyperbolic moveouts. One further implication of this is that the hyperbolic approximation is more accurate at greater depths, where the angle of incidence decreases. However, at greater depths, the accuracy is lower because of the smaller moveout. The resolution in velocity picking also depends on the signal bandwidth, where a more compact wavelet along the reflection traveltime trajectory in the CMP gather results in a more accurate velocity pick. At greater depths, due to the attenuation of higher frequencies and the decrease in signal-to-noise ratio, the semblance peaks become wider, decreasing the accuracy of the velocity pick. The deconvolution prior to velocity analysis is used to compress the source wavelet and improve the velocity resolution.

The picking error is estimated to be approximately 1-2 m/s for the reflectors closer to the seafloor and 2-4 m/s for the reflectors closer to the BGHSZ in areas where the reflectors are coherent and have stronger amplitudes. In the blank zones, where the reflectors are less coherent and have reduced amplitudes and larger dips, the picking error is 1-2 m/s higher for reflectors down to the BGHSZ. The error in picking the velocity from the velocity spectrum increases considerably with depth, which is a consequence of many of the factors listed above. The hyperbolic approximation would introduce a small systematic deviation from the true velocity, which is likely

embedded in the random noise quantified by the standard deviation. It is very likely that a significant percentage of the standard deviation is also a result of a real lateral variation of velocity due to changes in physical properties of the sediments. Also, some of the factors mentioned above have effects on stacking velocity errors that partially cancel each other. In view of all these, it is very difficult to quantify individually the error from each factor, therefore, the error sources are only separated into data scatter as given by the standard deviation and systematic error. The picking error, which contributes largely to the standard deviation, can be estimated by looking at the sharpness of the velocity spectra and analyzing CVG panels: the error increases as the range of velocities that can flatten a particular reflector increases.

The total error in stacking velocity from different sources is estimated for reflectors up to ∼0.25 s bsf for an area inside and outside the blank zone centered at CDP 3550. The total error outside the blank zone has a standard deviation of 4 m/s near the seafloor and increases to 8 m/s at the depth of the BGHSZ, and inside the blank zone it varies from 5 m/s to 14 m/s. The reflectors for which the errors are estimated are traced by the blue curves in Fig. 2.14. The two major components of the errors in stacking velocities and time are shown in Table 2.2, where the cumulative velocity and traveltime standard deviations, σ_v and σ_t, are used to estimate interval velocity errors in Sec. 3.1.3. The errors inside the blank zone are slightly larger, as a result of the decreased amplitude and coherence of the reflectors. The blank zone also has large reflector dips, up to 5^0, which could introduce larger errors in velocities and traveltime from the DMO correction and time-migration, respectively. The migration process (Sec. 6.1) attempts to position the reflectors at their true position; this process is

very sensitive to the velocity field used. Therefore, the traveltime error inside the blank zones is probably larger than outside, due to the larger dip of reflectors before migration and heterogeneity of the velocity field.

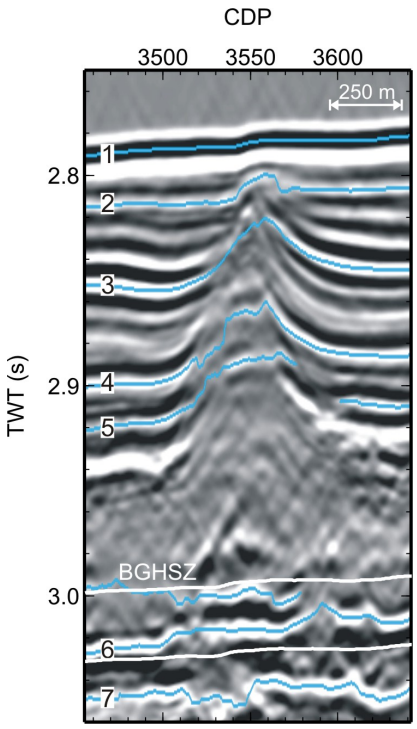

Figure 2.14: Reflectors (blue curves) inside and outside the blank zone centered at CDP 3550 after migration. The estimated standard deviations of the traveltime and velocity error at each reflector are given in Table 2.2.

2.2.7 Discussion

The processing of the MCS data was made with the main focus to derive stacking velocities. In Chapter 3 these are converted to interval velocities, which are used to estimate gas hydrate and free gas saturations in Chapter 4. The velocity is used for the finite-difference migration in Chapter 6 to obtain a good subsurface reflectivity image. The velocity analysis inside the blank zones was carried out on a more detailed grid. These velocities were analyzed in comparison with areas surrounding them.

Reflector	Stacking velocity standard deviation σ_v (m/s)						Traveltime σ_t (ms)	
	Random		Systematic		Total		Picking	
	Inside	Outside	Inside	Outside	Inside	Outside	Inside	Outside
1	3.0	2.0	2.0	2.0	5.0	4.0	2.0	2.0
2		2.0		2.0		4.0		2.0
3		3.0		2.0		5.0		3.0
4	4.0	3.0	2.0	2.0	6.0	5.0	3.0	3.0
5	6.0	4.0	2.0	2.0	8.0	6.0	4.0	4.0
6	10.0	5.0	2.0	2.0	12.0	7.0	5.0	4.0
7	12.0	6.0	2.0	2.0	14.0	8.0	6.0	5.0

Table 2.2: Estimated standard deviation of the errors for stacking velocities and reflection time outside and inside the blank zone centered at CDP 3550, for reflectors shown in Fig. 2.14.

The stacking velocities outside the blank zones show an average uniform increase of about 10 m/s from the seafloor to the BGHSZ. On the other hand, the velocities inside the blank zones show both positive and negative anomalies above the BGHSZ. A critical issue in this study is to distinguish which of these variations are real and which are due to noise. The reduction of velocity below the BGHSZ is sometimes seen at locations outside the blank zones, and very often inside the blank zones, indicating the potential presence of free gas. Sometimes anomalies can be identified for neighbouring CDPs, but generally they are seen at distinctive CDPs. The velocity pick is a weighted average velocity over a large distance of 33 m (5 CDPs), so even one anomalous velocity pick is thought to be significant if larger than the error limit. Reduced velocities are often seen below the BGHSZ in areas where the reflectors have reduced coherence, interpreted to be debris flow deposits. Thus, if free gas causes the reduction in velocity, it could be that it prefers to accumulate or percolate through these deposits if they are more porous and permeable.

The stacking velocity anomalies are calculated by subtracting an average velocity from outside the blank zones from each velocity pick, which represents the degree of downward compaction in the area. The random errors across the line are quantified by the standard deviation from the mean of all picks adjusted below the seafloor, calculated with a vertical running window from seafloor downwards. The standard deviation includes picking errors, noise, data bandwidth and streamer length errors, and real velocity variations. The systematic error results from the assumption of hyperbolic moveout and possibly from the dependance of velocity on reflector dip that is not completely removed by the DMO correction. The velocity anomalies are estimated to be significant if larger than 4-5 m/s outside the blank zones, if larger than 6-7 m/s inside the blank zones above the BGHSZ, and if larger than about 10 m/s immediately below the BGHSZ.

Chapter 3

Interval Velocity

Seismic velocity anomalies compared to a reference velocity at the same depth are the most important quantitative indicators of gas hydrate and free gas. In this chapter interval velocities are converted from RMS velocities using the Dix equation (*Dix* 1955), where the RMS velocities are approximated by stacking velocities derived from dip-moveout corrected data from seismic line 063. This is the most common way to obtain interval velocities from seismic data. The Dix equation is valid for a horizontally layered earth with constant layer velocities and small offsets, or near-normal-incident rays. Thus, the difference between RMS and stacking velocities depends on the degree of subsurface velocity heterogeneity, on the spread length (*Al-Chalabi* 1974) and on the dip of the reflectors (*Hubral* 1976). Here, the dip effect is removed to a first approximation through the DMO correction.

The Dix equation gives unrealistic values and uncertainties for small variations in the RMS velocities and for very thin intervals compared to the depth over which the RMS velocities are determined. In particular, when the velocity decreases with

depth, the interval velocity estimate is biased towards small velocities because of the non-linear relation between RMS velocity and interval velocity expressed through the Dix equation.

Interval velocity is first determined directly from the Dix equation with no constraints (Section 3.1). Before inverting the real stacking velocities from line 063, synthetic cases are used to demonstrate how problems are generated by the straightforward use of the Dix equation, how to avoid some of them, and how the results from the real data should be interpreted. To overcome the large oscillations in the interval velocity and the bias towards negative velocities, regularized linear inversion is applied to derive interval velocities under different constraints (Section 3.2). Using interval velocities outside the blank zones as a reference velocity, interval velocities inside the blank zones are also derived from reflector pull-up assuming the pull-up is only a velocity effect (Section 3.3). Interval velocity and an accurate estimate of its uncertainty are obtained by applying non-linear Bayesian inversion. The performance of the regularized linear inversion and non-linear inversion is also first exemplified by synthetic models.

The uncertainty in the derived velocities using the Dix equation is analytically calculated from the uncertainty in RMS velocities and in traveltime (Section 3.1.3), and from the uncertainty in RMS velocities using the model covariance matrix. The uncertainty in interval velocity is numerically derived from the uncertainty in both RMS velocity and traveltime using non-linear Bayesian inversion (Section 3.2.2).

3.1 Interval Velocity from Unconstrained Dix Inversion

For a continuous velocity function, the RMS velocities, V, are related to interval velocities, v, by the equation:

$$V^2(t) = \int_0^T v^2\, dt \;/\; \int_0^T dt\,. \tag{3.1}$$

Since RMS velocities are only determined at discrete times t, the above equation can be re-written as:

$$V^2(t) = \frac{1}{t}\sum_{j=1}^{N} v_j^2 \Delta t_j, \tag{3.2}$$

where t is the traveltime corresponding to the RMS velocity V after propagation through N layers:

$$t = \sum_{i=1}^{N} \Delta t_i. \tag{3.3}$$

The analytic inverse of Eq. 3.2 is the Dix equation (Eq. 3.4). It expresses the interval velocity of any interval as a function of RMS velocity and traveltime at the top and bottom on the interval considered (V_n, t_n, and V_{n-1}, t_{n-1}, respectively).

$$v_n = \left(\frac{V_n^2 t_n - V_{n-1}^2 t_{n-1}}{t_n - t_{n-1}}\right)^{1/2}. \tag{3.4}$$

The equation is based on the assumptions that the layers are flat and the offsets are small. The RMS velocities assume straight vertical rays, with no bending at layer

boundaries.

The Dix equation for a velocity profile can be expressed as a system of equations in vector notation:

$$\mathbf{Am} = \mathbf{d}, \tag{3.5}$$

where $\mathbf{A}$ is the sensitivity matrix representing traveltime information, $\mathbf{m}$ is the model vector whose component values represent squared interval velocities, v_i^2, and $\mathbf{d}$ is the data vector whose component values contain squared RMS velocities, V_i^2, where i=1:N, with N the number of layers. Since the number of data equals that of model parameters, the problem is even-determined and the solution does not depend on the data covariance and can be written as:

$$\mathbf{m} = \mathbf{A}^{-1}\mathbf{d}. \tag{3.6}$$

The model, representing squared interval velocity is from now on called the Dix model and its square root, the Dix interval velocity. The posterior uncertainty of the model is given by the model covariance matrix:

$$\mathbf{C}^{(m)} = \mathbf{A}^T\mathbf{C}^{(d)}\mathbf{A}^{T-1}, \tag{3.7}$$

where $\mathbf{C}^{(d)}$ is the data covariance matrix, whose diagonal elements represent the squared standard deviation of data, and the other elements are taken to be zero, assuming independent errors. The data standard deviation is calculated from the

RMS velocity standard deviation using the relative error of a product:

$$\sigma_{V^2} = 2V\sigma_V, \tag{3.8}$$

where σ_{V^2} is the standard deviation of the squared RMS velocity (data) and σ_V is the standard deviation of the RMS velocity. For the real data inversion, an estimate of the standard deviation of the RMS velocity as a function of depth can be derived from the scatter of stacking velocities adjusted below the seafloor from all CDP profiles analyzed along the line (Fig. 2.8). Most of the scatter in the stacking velocity is interpreted to be a result of zero-mean Gaussian-distributed random noise and some of the scatter as a result of lateral physical variability in sediments.

The standard deviation of the model is calculated as the square root of the diagonal elements of the model covariance matrix $\mathbf{C}^{(m)}$. The off-diagonal elements of the model covariance matrix $\mathbf{C}^{(m)}$ represent correlations between parameters and are not analyzed with this method, but will be in Section 3.2.2. The standard deviation of the interval velocity is calculated using the relative error equation for a division:

$$\sigma_v = \sigma_{v^2}/2v, \tag{3.9}$$

where σ_v is the standard deviation of the interval velocity and σ_{v^2} is the standard deviation of the model, which is squared interval velocity.

Both the interval velocity and its standard deviation can alternatively be estimated numerically using a Monte Carlo approach. This is done by taking the calculated model as the mean of a distribution with standard deviation calculated from the model

covariance matrix and then drawing a large number of models from that distribution. The interval velocity is then calculated as the mean of the square root of all models, and the standard deviation characterizes the width of the distribution.

3.1.1 Synthetic Studies

A theoretical case is studied to determine interval velocities from noisy RMS velocities using the Dix equation. The true interval velocity is chosen to be continuously increasing with depth (black line in Fig. 3.1c) and to have positive and negative anomalies (Fig. 3.2c). Such anomalies would result if gas hydrate and gas, respectively, were present in the sediments. The true RMS velocity is calculated from the true interval velocity using Eq. 3.5, and shown in Figs. 3.1a and 3.2a. Different realizations of random noise with increasing standard deviation with depth are added to the RMS velocity. A realistic standard deviation of the random noise variable is 2 m/s at the seafloor, increasing to 15 m/s at 1 s bsf. These values are estimated from the scatter of ∼100 velocity profiles calculated along line 063, as discussed in Section 2.2.3 (Fig. 2.8c black crosses). Squared interval velocities and interval velocities are derived from 100 noisy RMS velocity profiles (Figs. 3.1b,c, 3.2b,c). The mean of the velocity squared and velocity for each layer is shown by the green lines.

Very often when the RMS velocity decreases with depth, the squared interval velocity is negative. In such cases, the interval velocity is taken to be the negative square root of the absolute value of the squared interval velocity. Even though a negative interval velocity has no physical meaning, such values should not be excluded individually because they are negatively correlated with a neighbouring interval ve-

locity with which they have in common an RMS velocity, as shown later in Section 3.2.2.

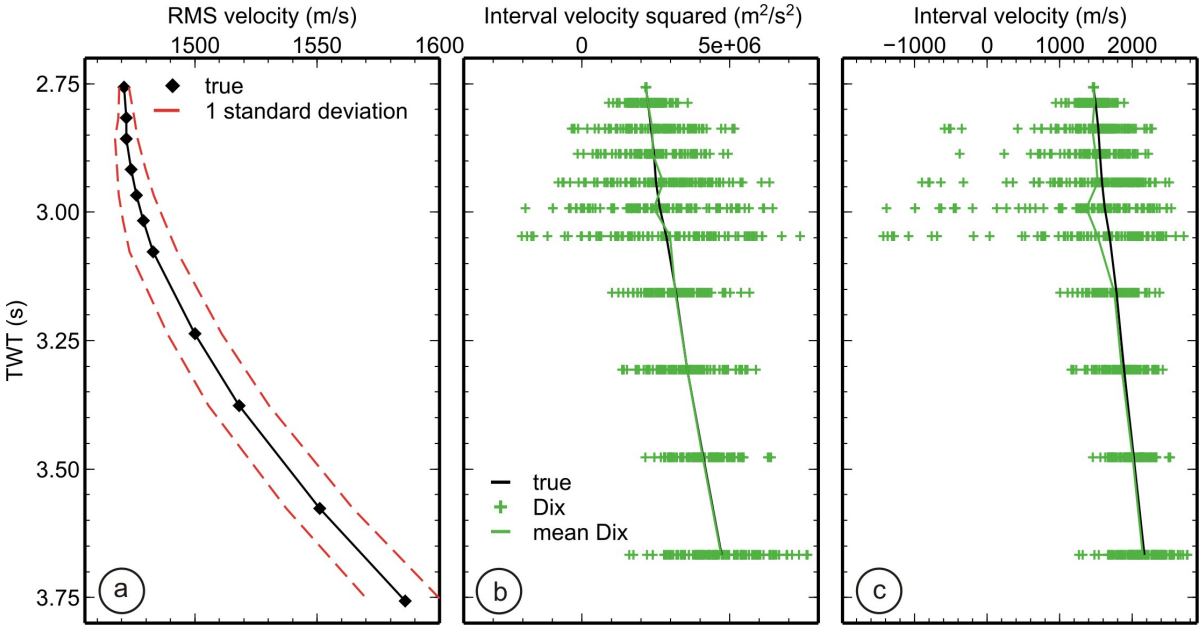

Figure 3.1: Synthetic true RMS velocity (black diamonds) to which noise with standard deviation shown by the red dashed line is added; b) Dix interval velocity squared (green crosses) inverted from 100 noisy RMS velocity profiles and the mean of all points (green line) compared to true profile (black line); cs) Dix interval velocity (green crosses).

The distribution of interval velocities deviates from a normal distribution with a longer tail towards lower velocities, unlike the distribution of squared interval velocities. This is because the relationship between the RMS velocity and interval velocity is non-linear while that between the squares of the RMS velocity and interval velocity is linear. A bias from the true velocity can be seen in the shallower part of the profile in Fig. 3.1c, and where the RMS velocity decreases with depth in Fig. 3.2c. In the case shown in Fig. 3.1, considering the size of the error on the true RMS velocity profile, there is a larger probability of velocity reversals with depth in the shallower part of the profile where the RMS velocity gradient is steepest. These result in too

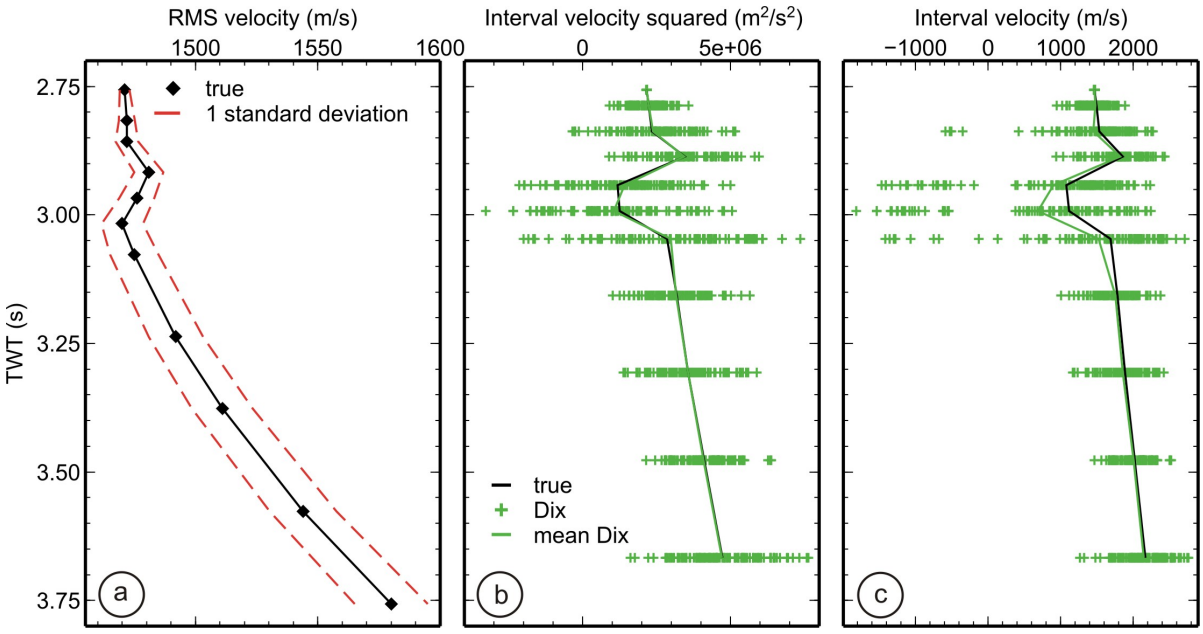

Figure 3.2: a) Synthetic true RMS velocity (black diamonds) to which noise with standard deviation shown by the red dashed line is added; b) Dix interval velocity squared (green crosses) inverted from 100 noisy RMS velocity profiles and the mean of all points (green line) compared to true profile (black line); b) Dix interval velocity (green crosses).

low interval velocities and the mean of all interval velocity profiles (green line) for these layers is thus biased. The interval velocity is no longer biased at greater depths, where there are fewer velocity reversals and the intervals are thicker. The maximum probability of the interval velocity distribution (i.e., the mode) is a better estimate of the true value than the mean. In the Ulleung Basin dataset discussed in Section 3.1.2, there are not as many data points in a vertical time window as shown in the synthetic case, which does not result in a well-defined peak of the distribution. Therefore, taking the peak of a distribution introduces likely as large an error as taking the mean of the distribution.

If one is interested in the mean of a number of interval velocity profiles, a more accurate estimate than the one discussed above can be calculated if the squared

interval velocity profiles are first added to calculate their mean, followed by taking the square root. If enough velocity profiles are added, the squared interval velocity mean is less likely to be negative and is closer to the true value. Thus, one avoids taking the square root of negative numbers which results in a large bias in the interval velocities. A quantitative proof of these observations is given by calculating the cross-correlation and semblance between the true interval velocity and: i) the mean of an increasing number of velocity profiles; ii) the square root of the mean of an increasing number of squared interval velocity profiles. The results are shown in Fig. 3.3a and b, respectively, for the two different models presented in Fig. 3.1, and Fig. 3.2. It can be noted that, irrespective of the number of data inversions, the mean of the interval velocity does not get close to the true velocity profile (i.e., green curves do not approach the value of 1), as the mean is not the best measure of a non-normal distribution due to the non-linear relation between RMS velocity and interval velocity. On the other hand, the square root of the mean of at least 10 squared interval velocity profiles gets close to the true velocity profile (i.e., blue curves approach 1). A larger number of velocity profiles, around 15-20, should be added together in a real case because the intervals are no longer at the same depth for different profiles, and also because the number of intervals varies from profile to profile. Both cross-correlation and semblance are calculated as the former is a measure of the phase match whereas the latter is a measure of both phase and amplitude match.

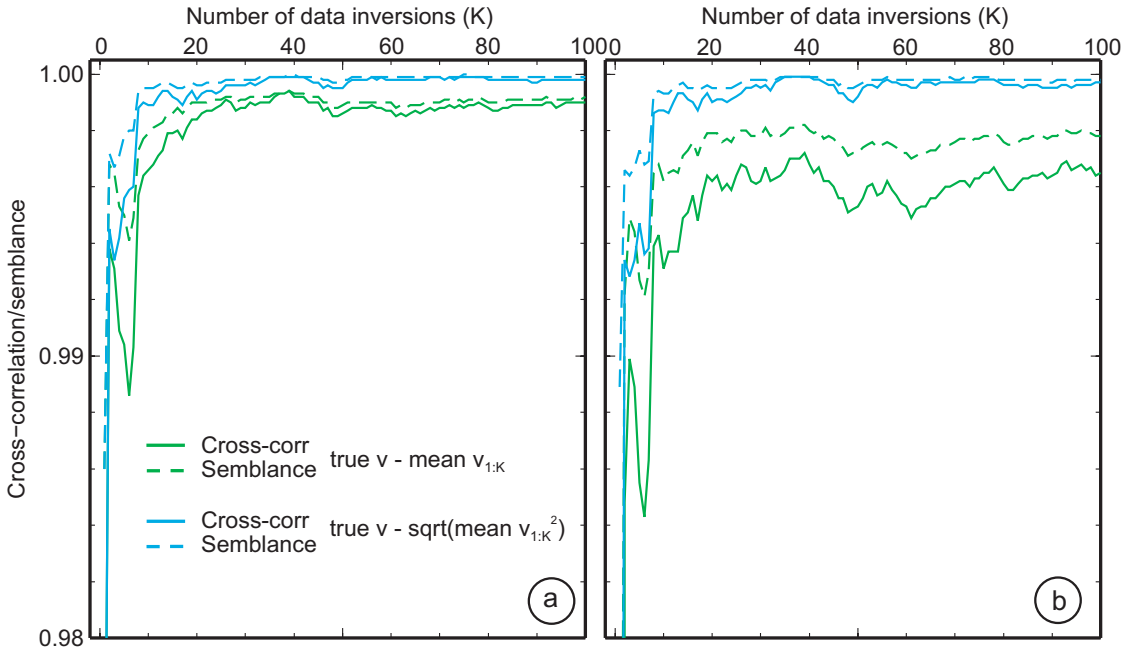

Figure 3.3: Cross-correlation (continuous line) and semblance (dashed line) between the true interval velocity profile and: i) the cumulative mean of interval velocity profiles (green line) and ii) the square root of the cumulative mean of squared interval velocity profiles, where the number of profiles added K is given by the number of data inversions, for the results shown in a) Fig. 3.1 and b) Fig. 3.2.

3.1.2 Inversion of Ulleung Basin Data

In this section interval velocities are calculated from stacking velocities from line 063 using the unconstrained Dix equation. First, the choice of seafloor stacking velocities is analyzed. Interval velocities are presented in a 1-D profile and in a 2-D grid, and velocity anomalies are then calculated.

The stacking velocity pick at the seafloor shown in the top panel of Fig. 3.4 represents the water velocity. The water velocity is a function of pressure, density and temperature and is expected to vary laterally by only small amounts. The mean of the seafloor picks over the section is 1471 m/s. The standard deviation of the picks is 2.4 m/s, which is close to the picking uncertainty. The values decrease somewhat

from CDP 1633 towards CDP 7035, probably representing a regional trend. The two most pronounced positive velocity anomalies in seafloor stacking velocity are seen around CDP 2000 and CDP 3000 and a negative anomaly around CDP 6200. They may represent real velocity variations in the water column or may be artifacts of small changes in hydrophone and airgun array depths or geometry that are not completely accounted for.

Since the water velocity is expected to be nearly constant over the distance of the study area (34 km), without much scatter and anomalies, two cases with different water velocities are considered when calculating interval velocities. First, a constant velocity of 1471 m/s, which represents the average of all stacking velocity picks for the study survey line (top panel in Fig. 3.4), is used to derive interval velocities. The interval velocities of the first interval below the seafloor are indicated by the blue line in the middle panel in Fig. 3.4. In the second case, interval velocities are derived using the stacking velocity picks for each CDP, and the interval velocities of the first interval below the seafloor are shown by the black line in Fig. 3.4 middle panel. The seafloor and center of the first interval traveltime are shown in the bottom panel in Fig. 3.4. The interval velocity is expected to be relatively constant, if the sediment geology does not vary much laterally, which is the case here. The velocity of the first interval oscillates more laterally when a constant stacking velocity of 1471 m/s is used. If the seafloor stacking velocity pick is larger than 1471 m/s, the corresponding interval velocity is lower, and if the seafloor stacking velocity pick is smaller than 1471 m/s, the interval velocity is higher. This relation between the stacking velocity and interval velocity is noted for the entire line, and suggests that if the stacking velocity

is higher or lower at the seafloor, the deeper stacking velocities must be also higher or lower. This is also seen by inspection of the stacking velocity profiles. The RMS velocity is expected to vary at all depths in a similar way as at the surface, resulting from either a real water velocity variation or from errors introduced from the source-receiver geometry or ship navigation. Therefore, in either case, one minimizes the effect of this error on interval velocities at all depths by using a seafloor stacking which has the same amount of error as the deeper values. Without any further quantitative analysis to relate the percentage increase or decrease in stacking velocity to that in interval velocity, the stacking velocity picks at the seafloor are used in all of the following calculations.

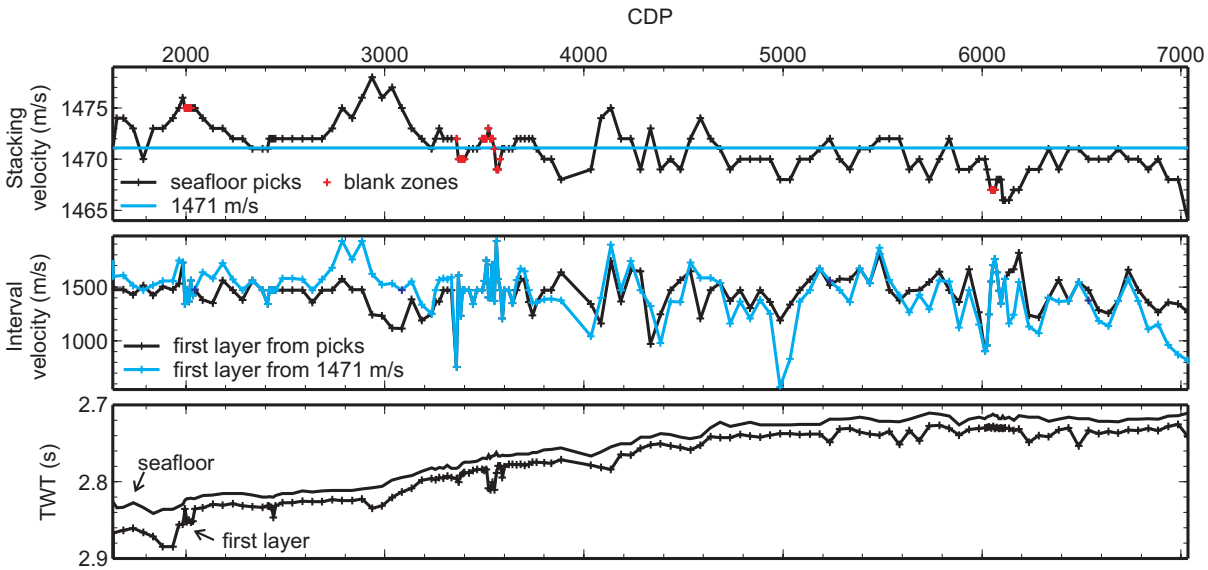

Figure 3.4: Top: stacking velocity picks at the seafloor, with an average velocity of 1471 m/s. Middle: interval velocity in the first layer below the seafloor calculated using seafloor velocity picks and the constant value of 1471 m/s. Bottom: seafloor traveltime from the stacking velocity picks and traveltime at the middle of the first interval corresponding to the interval velocities.

1D Velocity Profiles

Interval velocities were first compiled to 2.5 s to examine the effect of compaction with depth. The shallower data up to 0.5 s are shown separately, because this is where velocity variations due to gas hydrate and free gas are expected.

The interval velocity statistical measures shown in Fig. 3.5 and Fig. 3.6 (trend-line, mean, median and standard deviation) are calculated from interval velocities within two standard deviations from the mean. It is recognized that very few high velocity values associated with hydrate or free gas may be excluded. They are shown separately for inside all 5 blank zones and outside the blank zones. The interval velocities outside greater than two standard deviations from the mean represent 5.0% of initial data points outside the blank zones, and 4.8% inside the blank zones. The results are shown separately for blank zones and areas outside them, indicated by the black and red colours, respectively. Interval velocities are adjusted to zero depth, and plotted at the middle of the interval as black and red crosses for areas outside and inside the blank zones, respectively in Figs. 3.5a and 3.6a. The high velocity zone above and low velocity below the BGHSZ are clear in the average (Figs. 3.5b and 3.6b), although it may not be clear in individual velocity-depth estimates (Figs. 3.5a and 3.6a). As a reference-velocity depth to highlight local velocity anomalies, a linear trend given by Eq. 3.10 is fit through the interval velocities up to 0.25 s (Fig. 3.6a) and a quadratic trend through velocities up to 2.5 s (Fig. 3.5a). The shallower velocities are fit separately so that the deeper data do not control the shallow data, which appears to have a slightly different velocity-depth gradient. The coefficients

of the polynomials that fit these data are given in Table 3.1, where a and b are the coefficients of a first degree polynomial of the form given in Eq. 3.10 that fits the shallower data, and a, b and c are the coefficients of a second degree polynomial of the form given in Eq. 2.1 that fits all data.

$$v = a + bt, \tag{3.10}$$

where t is TWT bsf in s.

	Shallow 0.25 s bsf		Deep 2.5 s bsf	
	out	in	out	in
a	1448.97	1436.93	1457.72	1414.35
b	846.11	957.08	603.56	611.57
c	-		140.25	137.19

Table 3.1: Coefficients for the first and second degree polynomials (general form given by Eqs. 3.10 and 2.1) used to fit interval velocity data shown in Fig. 3.5a up to 2.5 s and 3.6b up to 0.25 s using interval velocities within two standard deviations away from the mean of all picks shown.

The interval velocity running mean and median are quite similar for areas outside the blank zones up to 0.25 s bsf, unlike those for areas inside the blank zones (Fig. 3.6b). This is the result of the larger number of interval velocity outliers inside the blank zones. The mean interval velocity outside the blank zones increases from 1466 m/s for sediments close to the seafloor to 1625 m/s at 0.18 s, followed by a slight decrease around the BGHSZ, and continues to increase to 1700 m/s at 0.5 s bsf. The mean interval velocity between 0.05 and 0.1 s inside the blank zones is slightly lower, up to 300 m/s higher between 0.12 s and 0.18 s, and up to 300 and 700 m/s lower between 0.2 s and 0.32 s as compared to areas outside the blank zones.

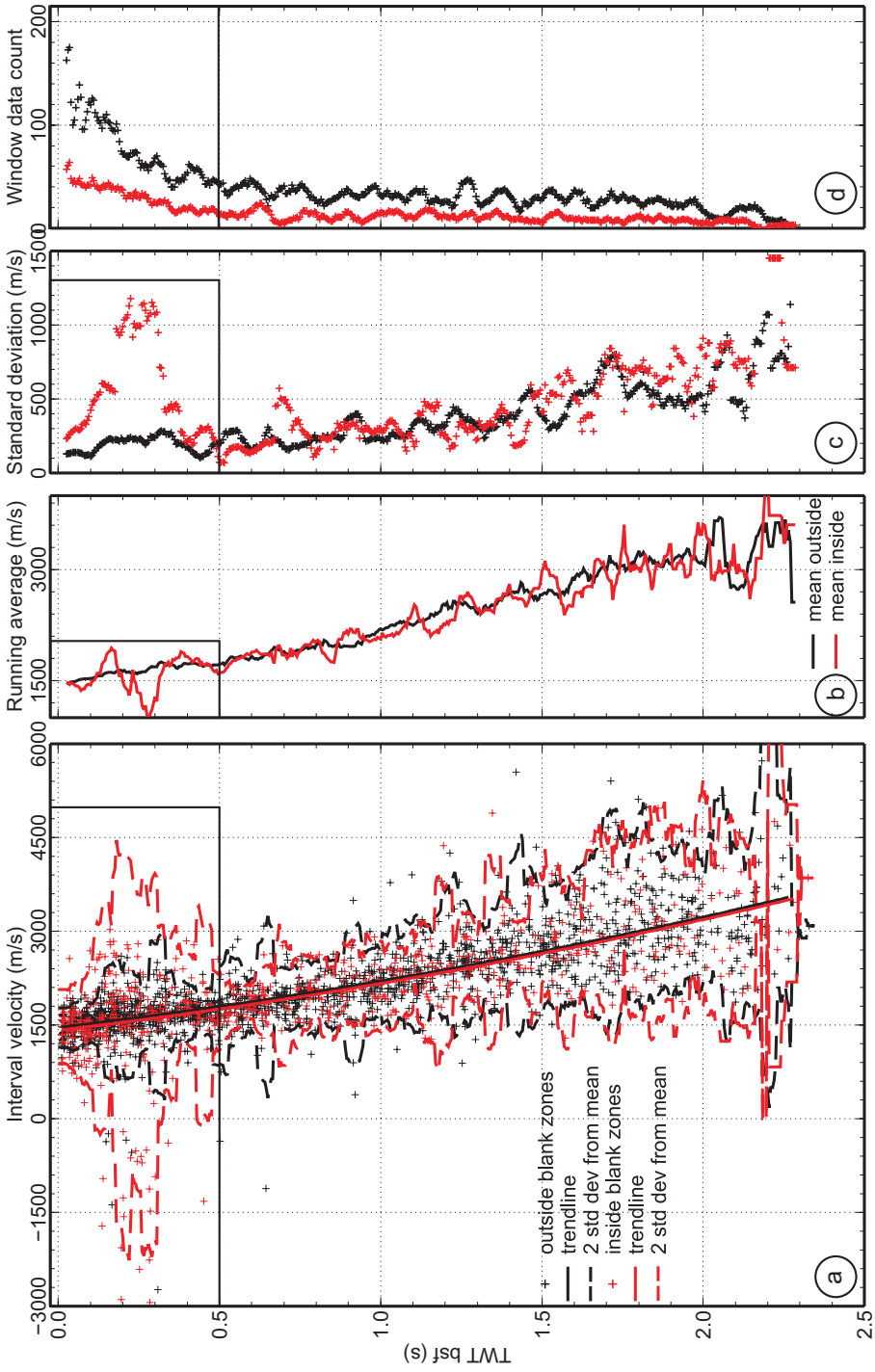

Figure 3.5: a) Interval velocity calculated from stacking velocity shown in Fig. 2.8 outside and inside the blank zones in black and red, respectively, fit by quadratic trendlines; velocities larger than two standard deviations are excluded for further calculations, as indicated by the dashed lines; b) running mean and median every 5 ms in 50 ms long windows; c) standard deviation; d) window data count.

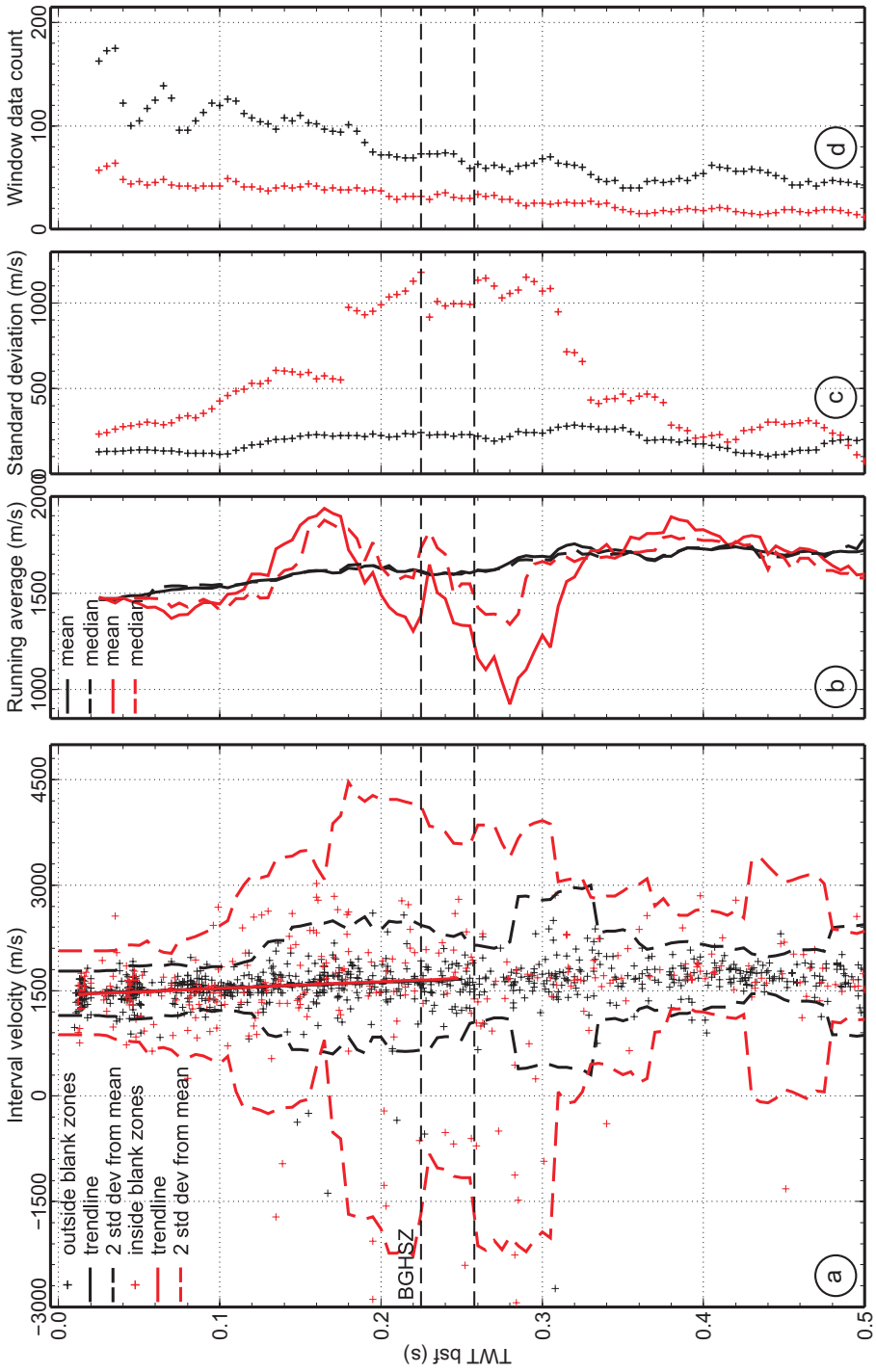

Figure 3.6: Enlargement of Fig. 3.5 up to 0.5 s; a) interval velocity outside and inside the blank zones in black and red, fit by linear trendlines; b) running mean and median every 5 ms in 50 ms long windows; c) standard deviation; d) window data count.

The standard deviation outside the blank zones varies from about 150 m/s close to the seafloor to 350 m/s around the depth of the BGHSZ (Fig. 3.6c). Where no velocity anomalies are detected inside the blank zones, the standard deviation is about 150 m/s larger. The standard deviation reaches up to 1100 m/s above and below the BGHSZ, where velocity anomalies are seen inside the blank zones. Therefore, the standard deviation inside the blank zones represents an overestimate of the velocity uncertainty around the BGHSZ, where gas hydrate and gas are expected.

The mean and its standard error are shown in Fig. 3.7 up to 0.5 s. The standard error of the mean of velocities outside the blank zones (black curves) increases from 10 m/s just below the seafloor to 28 m/s at 0.25 s around the BGHSZ. Inside the 5 blank zones, the standard error is 30 m/s below the seafloor and increases to 180 m/s at 0.25 s, where it is the largest. The anomalous values of the mean velocity inside the blank zones are quite significant, considering the standard error.

The bias towards negative velocities should be accounted for when interpreting the interval velocity mean. The bias is larger where the velocity decreases with depth. The negative anomalies in the mean inside the blank zones are likely biased by $\sim$300 m/s to lower values (as seen in the synthetic cases). The positive anomaly above the BGHSZ may be slightly biased to lower velocities because some velocity profiles with a decrease in velocity with depth contributed to the mean. The mean outside the blank zones may as well be slightly biased to lower velocities, less than the mean inside the blank zones, where more velocity profiles show a velocity decrease with depth.

An interval velocity trend is also calculated directly from the quadratic polynomial

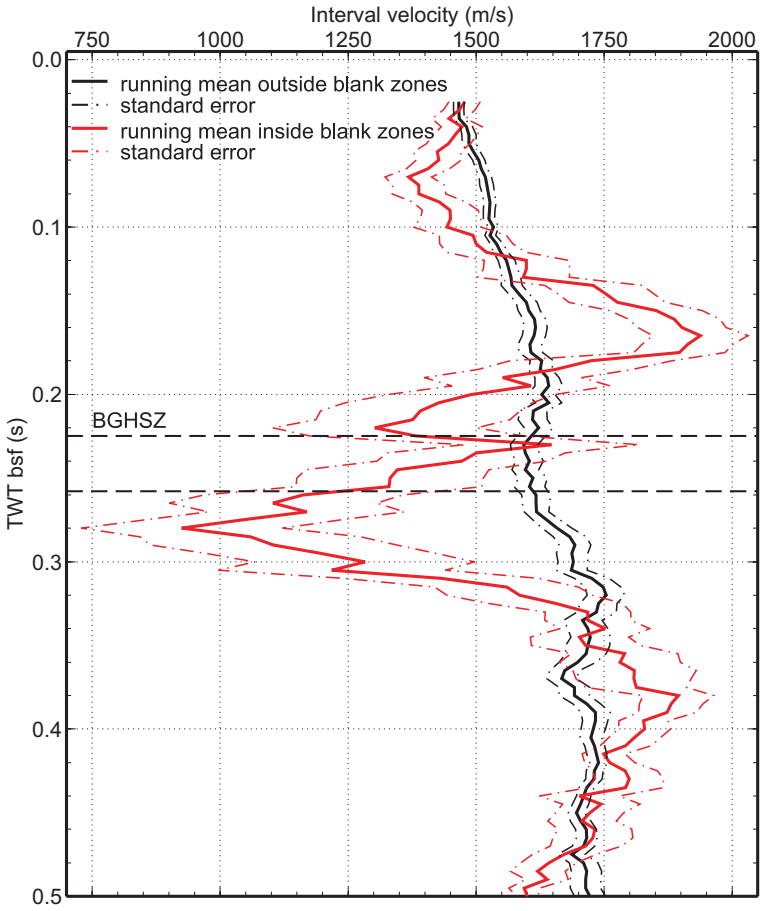

Figure 3.7: Interval velocity running mean and standard error outside and inside the blank zones shown in black and red. As noted in text, the standard error in the blank zones is an overestimate.

that best fits RMS velocities (Section 2.2.3). Different trends are calculated separately from data up to 2.5 s bsf (Fig. 3.8a) and up to 0.25 s bsf (Fig. 3.8b). Each of the stacking velocity trends (Fig. 3.8 panel I) is sampled every 50 ms and these data points are used to derive interval velocities with the Dix equation (Fig. 3.8 panel II). The interval velocities are fit by a first degree polynomial of the form given by Eq. 3.10. The coefficients a and b given in Table 3.2 are derived separately for shallow sediments up to 0.25 s bsf and for deep sediments up to 2.5 s bsf and also for areas outside and inside the blank zones. The interval velocities derived from the

stacking velocity trends are increasing with depth, when the latter are increasing. The stacking velocity trend inside the blank zones up to 0.25 s bsf shows a decrease from the seafloor to 0.075 s bsf, resulting in an interval velocity of 1420 m/s in the upper 0.05 s bsf. The interval velocities inside the blank zones are 40-100 m/s higher from 0.1 to 0.25 s bsf than outside.

	Shallow 0.25 s bsf		Deep 2.5 s bsf	
	Trend picks		Trend picks	
	out	in	out	in
a	1450.64	1357.39	1471.27	1520.54
b	934.77	2001.77	544.21	505.58
c	-		167.97	152.51

Table 3.2: Coefficients of the first and second degree polynomial that defines the interval velocity trend calculated from stacking velocity trends separately for areas outside and inside the blank zones and up to 0.25 s and 2.5 s, shown in Fig. 3.8.

2D Velocity Grid

Interval velocities derived from each stacking velocity profile using the unconstrained inversion are shown as a gridded plot in Fig. 3.9. The areas indicated by the boxes are enlarged and shown in Fig. 3.10.

The blank zones show both positive and negative anomalies, compared to the outside reference. Although the data are scattered, most intervals have higher velocities of 2000-3000 m/s above the BGHSZ, and lower velocities of 500-1000 m/s around the BGHSZ and below. Velocities lower than the average of 1500 m/s are also seen in a few intervals above the high velocity zone in the GHSZ.

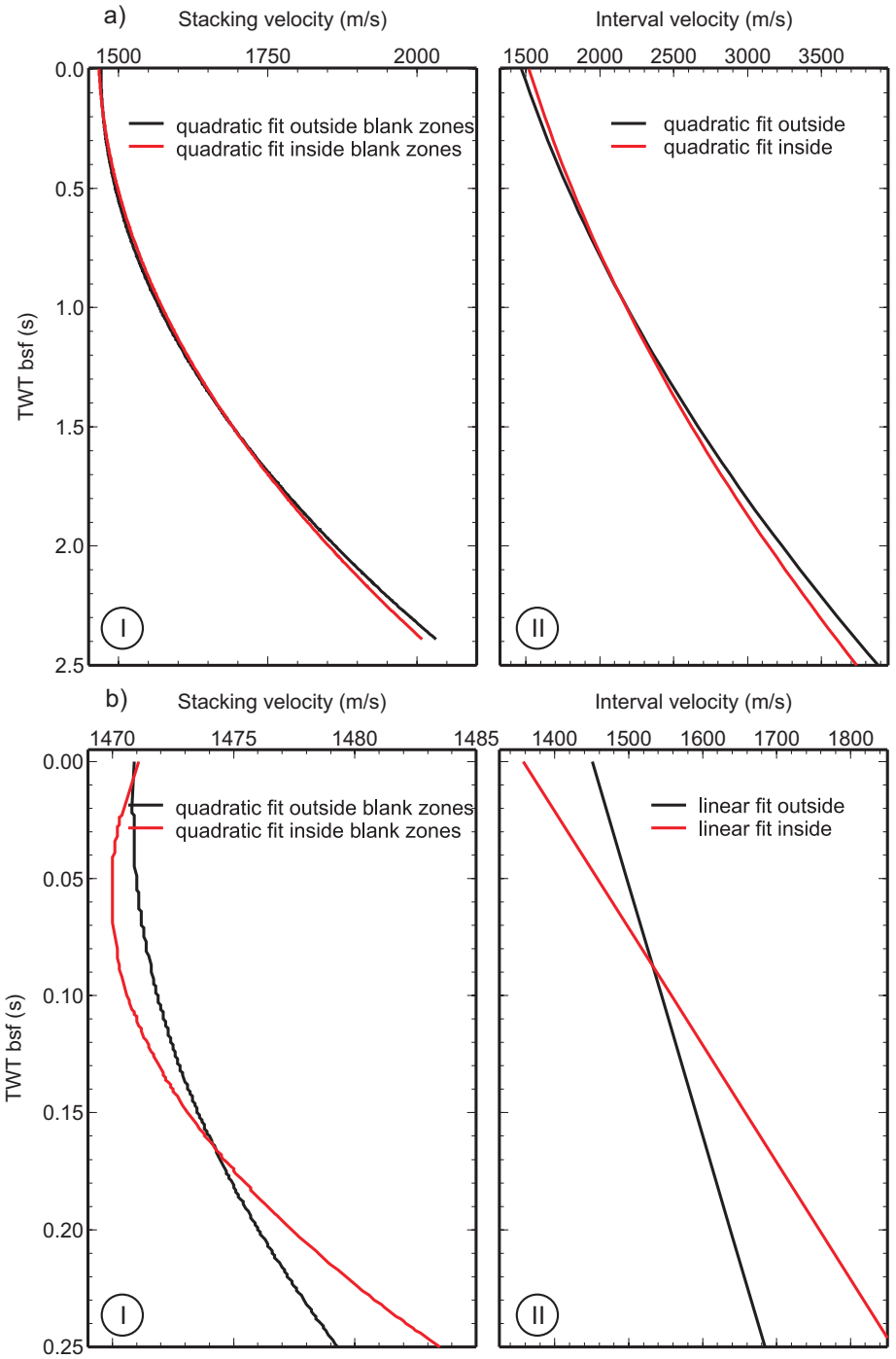

Figure 3.8: Stacking and interval velocity trends for depths up to a) 2.5 s TWT bsf and b) 0.25 s TWT bsf. The velocities outside and inside the blank zones are given by the black and red curves, respectively. The coefficients that define a first degree polynomial that fits the interval velocities are given in Table 3.2.

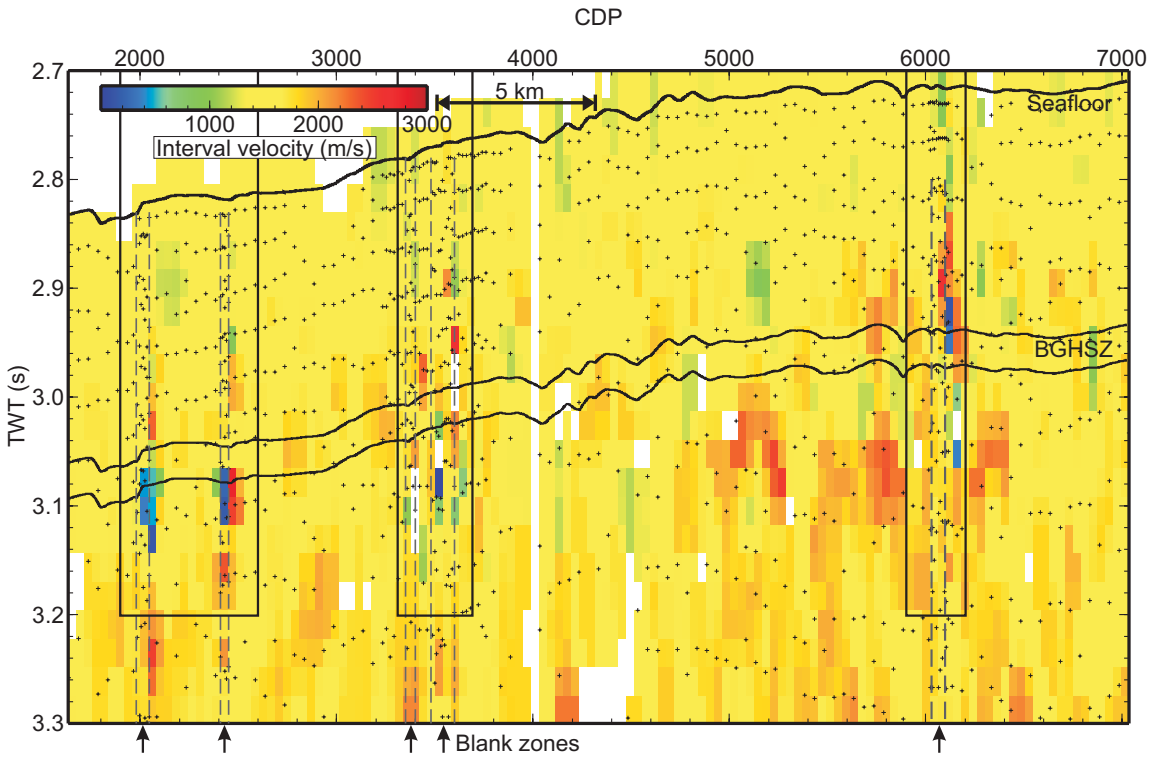

Figure 3.9: Gridded interval velocities from the unconstrained Dix inversion showing the location of the blank zones and the zones that are enlarged and shown in Fig. 3.10.

2D Velocity Anomalies

Interval velocity anomalies are derived by subtracting a reference velocity given by the running velocity mean from areas outside the blank zones from each interval velocity datum. There are barely significant high velocities above the BGHSZ and low velocities below the BGHSZ in the mean outside the blank zones (Fig. 3.7). This suggests that there may be a small bias in using the areas outside the blank zones as a no-hydrate, no-gas reference velocity-depth. The regularized solution presented in Section 3.2.1 is a better estimate of this reference profile. The gridded velocity plot is shown in Fig. 3.11. The anomalies associated with the blank zones mentioned earlier can be identified. As well, both positive and negative anomalies larger than 500 m/s

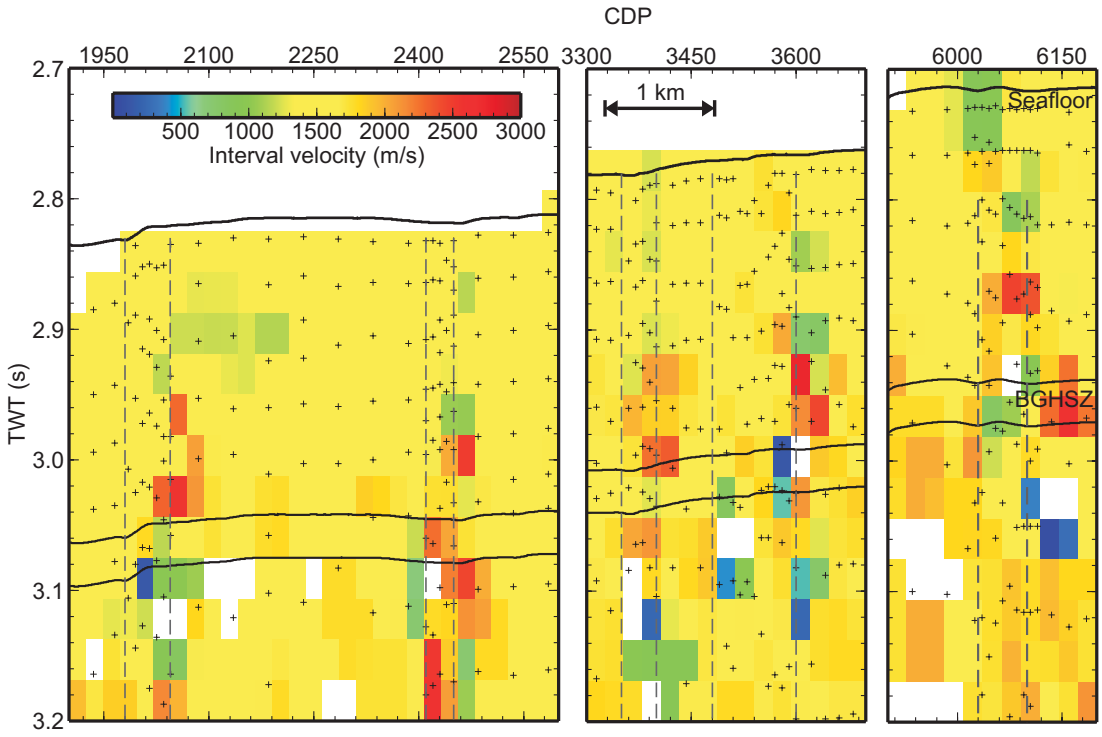

Figure 3.10: Gridded interval velocities around the blank zones, enlarged from Fig. 3.9. The difference in colour as compared to Fig. 3.9 arises from the different interpolation parameters used.

are noted below the BGHSZ between CDP 3800 and CDP 6200.

3.1.3 Analytical Error Analysis

The errors involved in deriving interval velocities from RMS velocities using the Dix equation are large and extremely sensitive to interval thickness and depth in addition to small fluctuations in stacking velocities. In this section the errors are calculated analytically from the Dix equation. A numerical solution is derived from the non-linear Bayesian inversion in Section 3.2.2.

The exact first order equation takes into account both the uncertainty in traveltime and in RMS velocity, as given below (*Hajnal and Sereda* 1981):

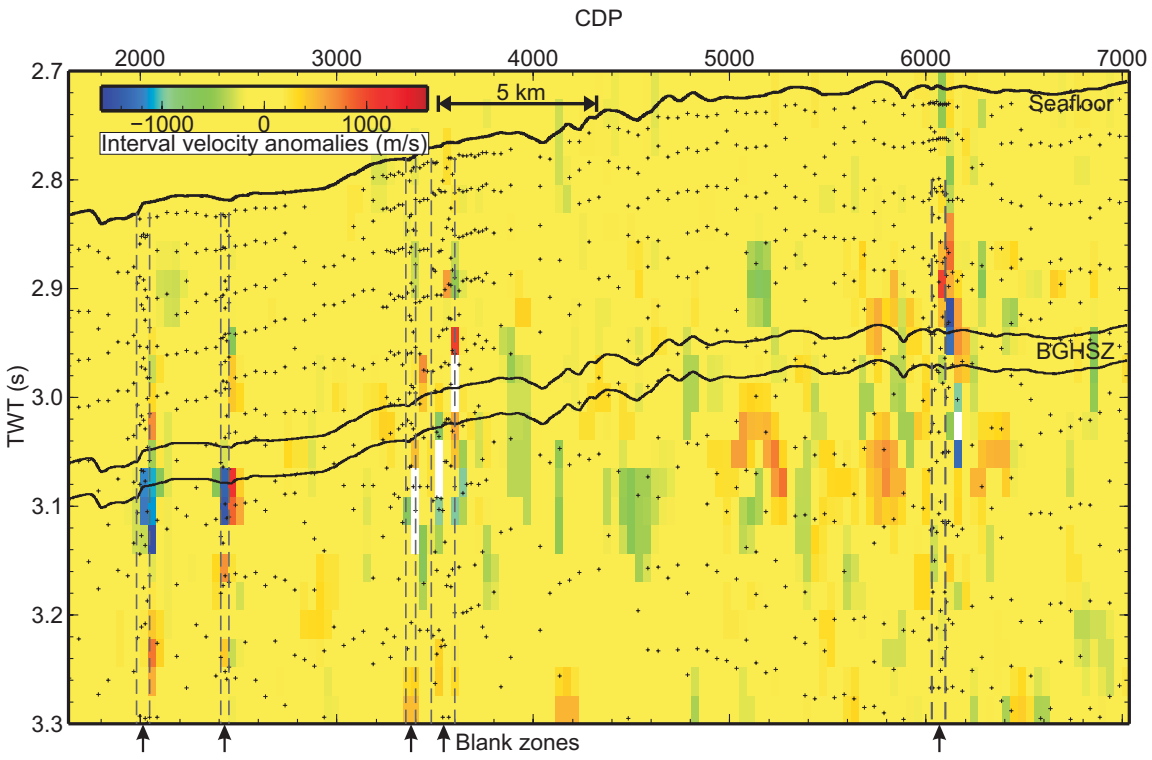

Figure 3.11: Interval velocity anomalies.

$$\Delta v_{I,n} = \left(\frac{1}{ac}\right)^{0.5} (v_n t_n \Delta v_n + v_{n-1} t_{n-1} \Delta v_{n-1}) + 0.5 \left(\frac{b^2}{a^3 c}\right)^{0.5} (t_n \Delta t_{n-1} + t_{n-1} \Delta t_n), \tag{3.11}$$

where Δv and ΔV are the interval and stacking velocity errors, Δt is the traveltime error, t_{n-1} and t_n are the TWT at the top and bottom of the layer where interval velocity is evaluated, and

$$a = t_n - t_{n-1}, b = v_n^2 - v_{n-1}^2, c = v_n^2 t_n - v_{n-1}^2 t_{n-1} \tag{3.12}$$

The commonly used simplification of the exact equation (Eq. 3.13) uses the assumption that the error resulting from the traveltime is very small and that the

errors from the stacking velocity at the top and bottom of any layer are equal (*Hajnal and Sereda* 1981). The interval velocity error increases with depth and RMS velocity and thinner intervals, as given by the equation:

$$\Delta v_{I,n} = 2\frac{t_{n-1}}{t_n - t_{n-1}}\Delta V_{n-1}. \tag{3.13}$$

The interval velocity error estimates are calculated for interval velocities inside and outside the blank zone centered at CDP 3550 using Eq. 3.11 and the total RMS velocity and traveltime errors from Table 2.2. The results are given in Table 3.3, including the separate components from RMS velocity and traveltime at the top and bottom of the interval under consideration. The error resulting from the reflection times is insignificant compared to that from stacking velocities.

Interval	Error from v_{n+1}		Error from v_n		Error from t_{n+1}		Error from t_n		Total error (m/s)	
	Inside	Outside	Inside	Outside	Inside	Outside	Inside	Outside	Inside	Outside
1	206	377	100	320	1	0	1	0	308	697
2		324		280		4		5		615
3		224		220		11		11		466
4	547	480	403	380	110	35	146	46	1206	940
5	257	177	163	121	2	3	2	3	424	303
6	-	1553	-	1351		101	-	126	-	3130

Table 3.3: Errors for interval velocity in m/s outside and inside the blank zones, showing the separate components from RMS velocity error and traveltime error at the bottom (v_{n+1}, t_{n+1}) and top (v_n, t_n) of the interval considered.

Interval velocity and its uncertainty are calculated for two CDP profiles, at CDP 3540 from a blank zone and at CDP 3463 from outside (Fig. 3.12). The noise of the data is calculated as a function of traveltime, where the standard deviation of the noise on the stacking velocities increases from 2 m/s at the seafloor to 15 m/s at 1 s

bsf at CDP 3463 (outside the blank zone) and from 3 m/s at the seafloor to 20 m/s at 1 s bsf at CDP 3540 (inside the blank zone) and the standard deviation of the traveltime increases from 2 m/s at the seafloor to 20 ms at 1 s bsf. The velocity and its uncertainty for layer 4 at CDP 3540 cannot be determined. A solution for this case can be found using the non-linear approach (Section 3.2.2). As expected, the deep thin layer at CDP 3540 has a very high uncertainty.

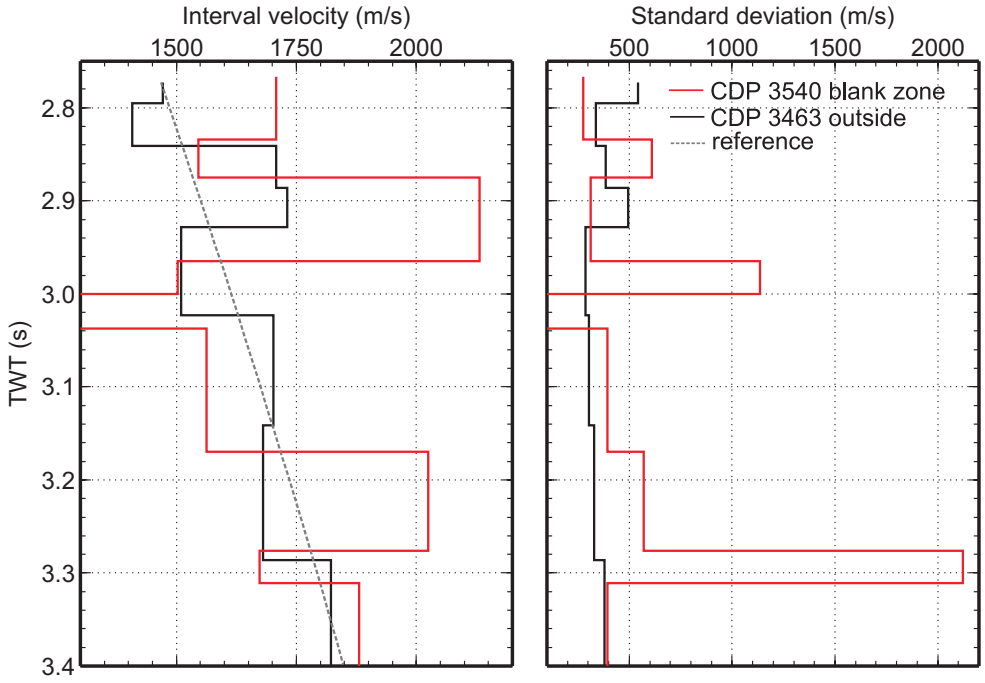

Figure 3.12: Interval velocity and uncertainty calculated using Eq. 3.11 from stacking velocities at CDP 3540 from inside a blank zone and CDP 3463 from outside the blank zone.

3.2 Constrained Dix Inversion

The Dix equation (Eq. 3.1 or Eq. 3.2) is a nonlinear mapping between RMS velocities and interval velocities, but a linear mapping between the squared RMS velocities and squared interval velocities. The solution gives nonrealistic and highly oscillating values, even for small variations in RMS velocities and where the intervals

are thin. The uncertainties are generally very large, they increase with depth, are inversely proportional to layer thickness, and cannot be determined where the velocity decreases too much with depth (*Hajnal and Sereda* 1981). As noted in Section 3.1.1, the velocities are biased towards negative velocities when the RMS velocity decreases with depth.

Considering the uncertainties in the interval velocities derived with the Dix equation, two different approaches are taken in this study, both of which introduce additional constraints to the inversion. The Dix equation is solved linearly by regularized inversion to obtain minimum structure velocities and non-linearly by Bayesian inversion.

3.2.1 Regularized Linear Inversion

The solution of the regularized linear inversion approach is determined by constraining the model to be small, flat or smooth, in addition to minimizing the data misfit, where the Dix equation fits the data exactly. The uncertainty of the solution is determined from the uncertainty in the stacking velocity.

Oldenburg et al. (1984) derive interval velocities by minimizing the gradient of the squared velocity to obtain a flat model using L1 and L2 norms. *Dubose* (1988) constrains the model, represented by squared interval velocities, to be smooth. *Clapp et al.* (1998) determine smooth and blocky models in a similar way. *Harlan* (1999) uses damped least squares and linearizes the relationship and solves it using a Gauss-Newton iteration. If one wants smooth velocities while preserving sharp geologic interval contrasts, an edge-preserving form of model regularization can be applied

(*Valenciano et al.* 2004).

The regularized solution is obtained by minimizing an objective function ϕ with respect to all model parameters, i.e.,

$$\frac{\partial \phi}{\partial \mathbf{m}} = 0, \tag{3.14}$$

where the objective function is:

$$\phi = |\mathbf{S}(\mathbf{Am} - \mathbf{d})|^2 + \mu |\mathbf{H}(\mathbf{m} - \hat{\mathbf{m}})|^2. \tag{3.15}$$

The first term represents the χ^2 data misfit, where $\mathbf{S}$ is a weighting matrix defined by Eq. 3.16 and the second term is a regularization term, where μ is the trade-off parameter, $\mathbf{H}$ is the regularization weighting matrix and $\hat{\mathbf{m}}$ is the prior estimate.

$\mathbf{S}$ is the upper-triangular Cholesky decomposition of the data covariance matrix $\mathbf{C}^{(d)-1}$:

$$\mathbf{S} = diag \left\{ \frac{1}{\sigma_{V_1^2}}, \frac{1}{\sigma_{V_2^2}}, \ldots, \frac{1}{\sigma_{V_N^2}} \right\}, \tag{3.16}$$

where σ_V is the standard deviation corresponding to N RMS squared velocities, where N is the number of data.

The trade-off parameter μ controls the relative importance of data and prior information: a very large μ results in a model that applies the prior information with little regard to data, and a very small μ gives the least squares solution.

The general regularized solution is given by:

$$\mathbf{m} = \hat{\mathbf{m}} + [\mathbf{A}^T\mathbf{C}^{(d)-1}\mathbf{A} + \mu\mathbf{H}^T\mathbf{H}]^{-1}\mathbf{A}^T\mathbf{C}^{(d)-1}[\mathbf{d} - \mathbf{A}\hat{\mathbf{m}}]. \tag{3.17}$$

In this study, no prior estimate is available, so $\hat{\mathbf{m}}$ is taken to be zero. A good source for a prior estimate would be sonic logs or velocity from VSP.

The uncertainty of the regularized solution is quantified by the standard deviation which is the square root of the diagonal elements of the model covariance matrix, defined as:

$$\mathbf{C}^{(m)} = [\mathbf{A}^T\mathbf{C}^{(d)-1}\mathbf{A} + \mu\mathbf{H}^T\mathbf{H}]^{-1}. \tag{3.18}$$

Different types of regularization can be applied, depending on the type of solution desired, by using a different regularization matrix $\mathbf{H}$. The smallest model, also called zeroth order regularization, is obtained by setting $\mathbf{H}$ equal to the identity matrix. For a model that represents a discretized function of time, $\mathbf{m}(\mathrm{t})$, the matrix $\mathbf{H}$ for the flattest model is:

$$\mathbf{H} = bidiag\left\{-\frac{1}{t_{i+1} - t_i}, \frac{1}{t_{i+1} - t_i}\right\}, \tag{3.19}$$

where the last row of the matrix has zeros. The flattest model remains as constant as possible by minimizing model gradients.

To obtain a smooth model, the matrix $\mathbf{H}$ is designed as a discrete 2^{nd} derivative operator:

$$\mathbf{H} = tridiag\left\{-\frac{1}{(t_{i+1}-t_i)^2}, \frac{t_{i+2}-t_i}{(t_{i+2}-t_{i+1})(t_{i+1}-t_i)^2}, -\frac{1}{(t_{i+2}-t_{i+1})(t_{i+1}-t_i)}\right\}, \tag{3.20}$$

where the last two rows of the matrix are zero. The model has minimum curvature or roughness.

Synthetic Studies

Different synthetic examples are shown in this section, to compare the solution of the unconstrained inversion with that from the constrained inversion (smallest, flattest and smoothest model regularization) using different parameters. The parameters that recover best the expected velocity trends are used for inverting data from line 063 in the next section.

Two synthetic models that characterize the data are tested: i) a model with a linear increase in velocity with depth; ii) a model with a velocity increase in the shallower part of the model that would result from gas hydrate, and a velocity decrease below the gas hydrate stability that would result from free gas. The comparison between the performance of the calculated models (Dix and regularized) is useful in understanding the results of the inversion of stacking velocities from line 063. Different regularization parameters that correspond to different misfits (χ^2) between the observed and calculated data are tested. Models with different numbers of layers are considered to select an optimum length for the real dataset to invert. Also, synthetic datasets with noise with different standard deviation-depth functions are

inverted.

In the following synthetic cases, 100 noisy datasets are inverted for the Dix and regularized solution. Noise added to a true RMS velocity profile is represented by zero-mean random variables with standard deviation increasing from 2 m/s for the first layer up to 15 m/s at 1 s bsf. This amount of noise approximately characterizes our data from line 063.

A comparison between the interval velocity squared (the model) and the interval velocity (the square root of the model) from both the unconstrained and constrained inversion is shown in Fig. 3.13. The true model (black line) has a one-layer positive anomaly above a two-layer negative anomaly. The distribution of squared Dix interval velocities (green crosses) for each layer is normal, with the mean of 100 models (green line) being very close to the true model (Fig. 3.13a). However, the Dix interval velocity distribution for each layer is not normal, having a longer tail of small velocities in the shallower layers (Fig. 3.13b). Therefore, the mean of the interval velocity distribution for each layer no longer matches the true model, being biased towards lower velocities. This occurs because of the non-linear relation between the RMS velocity and the interval velocity. Therefore, to estimate an unbiased mean velocity, one can take the square root of the mean of squared Dix interval velocities, as shown by the dashed blue line in Fig. 3.13b. The regularized solutions (red crosses) correspond to a smooth model calculated for a misfit χ^2=N (N=11). This model cannot recover well the anomalies.

Different true velocity profiles and their recovery by each of the regularization models (smooth, flat, small), as compared to the Dix model, are shown in Figs. 3.14,

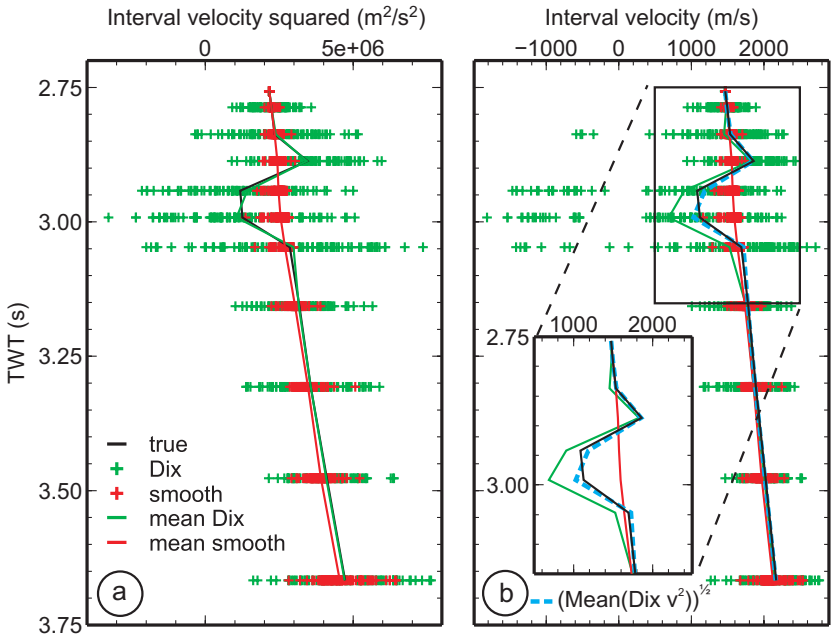

Figure 3.13: Dix solutions (green crosses) and regularized solutions (red crosses) obtained by inverting 100 noisy datasets; their mean for each layer (green and red lines), and true values (black line) for a) interval velocity squared (model), and b) interval velocity; the square root of the mean of squared interval velocities shown in b) by the blue dashed line.

3.15 and 3.16. Fig. 3.14 corresponds to a true model that has in the shallower part one layer with a positive anomaly above two layers with negative anomaly. A model with one layer having lower than average velocity is considered in Fig. 3.15 and a model with a uniform increase in velocity with depth is shown in Fig. 3.16. The data inverted have noise with a standard deviation increasing from 2 m/s for the first layer to 15 m/s for the last layer and the models are derived for a misfit of χ^2=N (N=11).

For all cases, the distribution of regularized interval velocities (red crosses) is much narrower than that of the Dix interval velocities (green crosses), especially in the shallower part. The anomalous parts of the models (Figs. 3.14 and 3.15) are not very well recovered by the regularized models, but the values do not oscillate as much as the Dix velocities. The mean of the smallest velocities is closer to the true

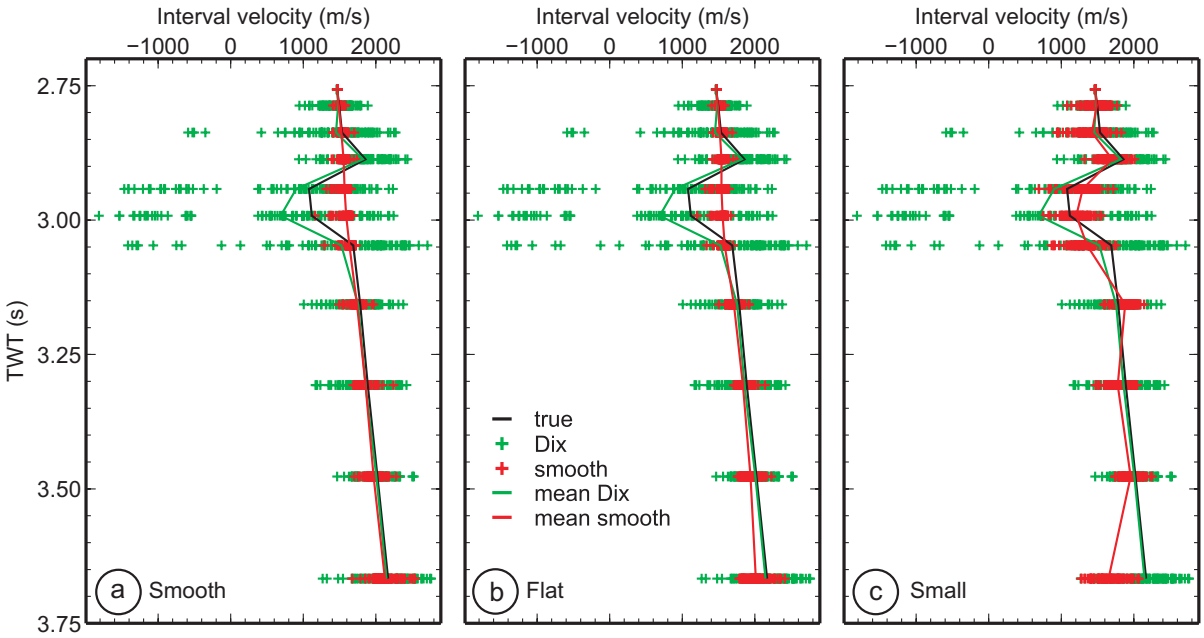

Figure 3.14: Comparison between the Dix interval velocities (green crosses) and the regularized interval velocities (red crosses) calculated for the a) smoothest, b) flattest, and c) smallest regularization models. The mean of the velocities for each layer is shown by the green and red lines for the Dix and regularized velocities, respectively and the true model is indicated by the black line. In this model, velocities have both positive and negative anomalies.

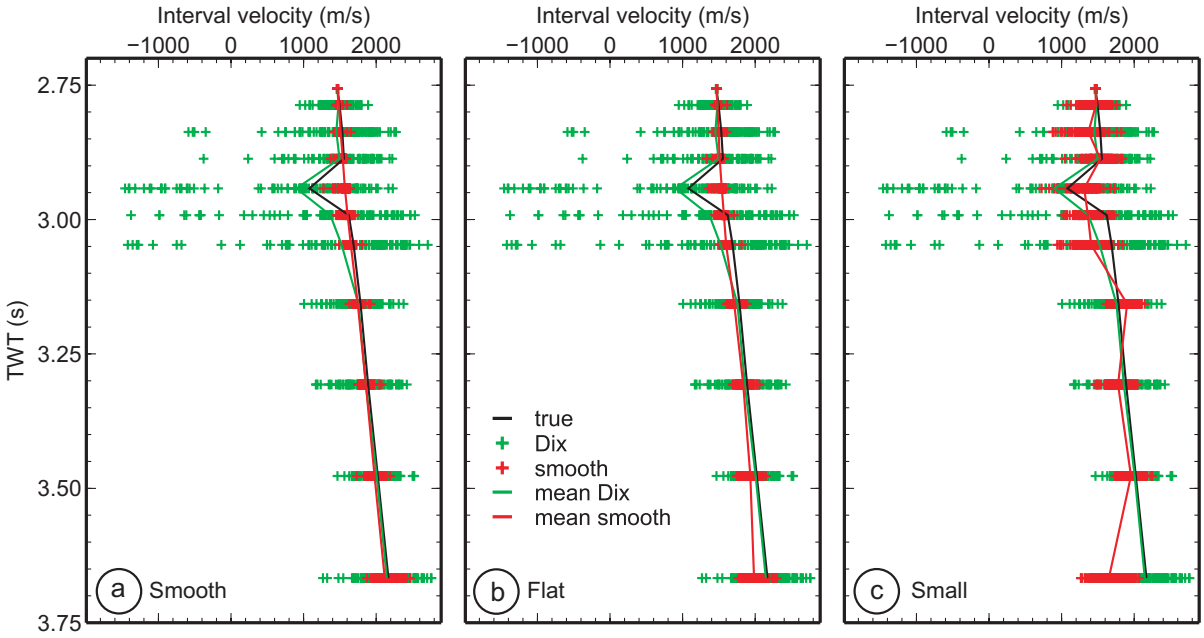

Figure 3.15: Same as Fig. 3.14; in this model, velocities have only a negatative anomaly.

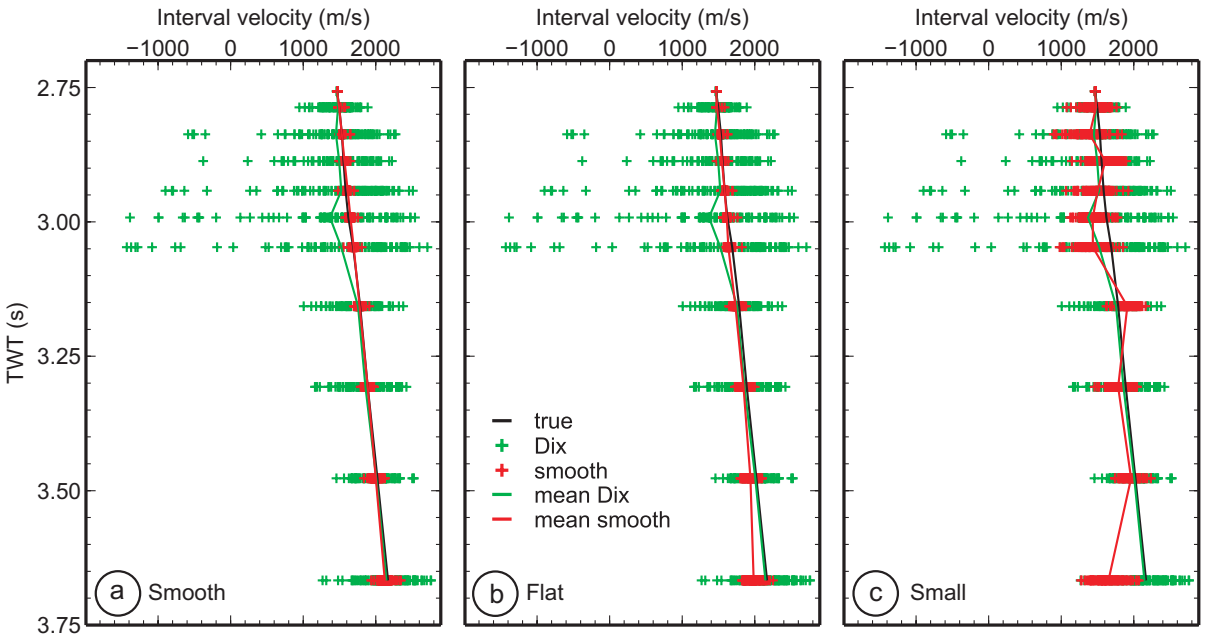

Figure 3.16: Same as Fig. 3.14, different true profile; in this model, the velocity increases uniformly with depth.

velocity for the anomalous layers, but the distribution of velocities is much wider. The mean of all Dix velocities resembles well the true value, except for the layers with the negative anomaly, where the Dix velocity mean is biased towards smaller velocities. However, the velocity distribution is very large, with unrealistic values. At greater depths below the anomalous velocities as well as for the model with constant velocity increase with depth (Fig. 3.16), the smoothest model resembles best the true velocity as compared to the flattest model where velocities try to keep a constant gradient and smallest model where velocities become too small. It can be thus concluded that the Dix interval velocities are unrealistic if taken from individual profiles, but their mean recovers positive anomalies well and negative anomalies that are biased. The smooth model performs the best for deeper velocities that increase uniformly with depth, and the distribution of velocities is overall narrower. The individual velocity

profiles for these deeper layers are much closer to the true profiles, as compared to the Dix velocities. Also, the smoothest velocities are slightly closer to the true ones as compared to the flattest velocities. The smallest model recovers more of the anomalous velocities, but individual profiles deviate largely from the true profile, and only the mean is significant in the shallower part.

One way to quantify the quality of individual Dix and regularized velocity profiles and the mean of a number of velocity profiles is using cross-correlation and semblance. The cross-correlation and semblance shown in Fig. 3.17 are calculated between the true model and the mean of an increasing number of calculated velocity profiles from Fig. 3.16. It can be noted that in the case of a smooth and flat model (Fig. 3.17a,b), one interval velocity profile by itself is closer to the true profile than one Dix profile. About 20 Dix velocity profiles need to be added before their mean is closer to the true value. Because of the large bias in the Dix interval velocity, the cross-correlation and semblance are lower than for the regularized smooth and flat models. The cross-correlation and semblance for the small model (Fig. 3.17c) are much lower than the Dix because of the decrease in velocity for the deeper layers imposed by this type of constraint. If the velocities of the deepest layers of the small solution are excluded, the cross-correlation and semblance improve significantly. This example shows that the inversions of one velocity profile with Dix equation deviate too much from the true model to be analyzed individually; rather, the mean of about 20 velocity profiles is needed for useful accuracy. Conversely, the regularized smooth and flat velocity can be analyzed individually; however, the anomalies are heavily smoothed. It should be noted that this example corresponds to a true continuously increasing velocity with

depth, and the cross-correlation and semblance change for the different models shown in Figs. 3.14 and 3.15.

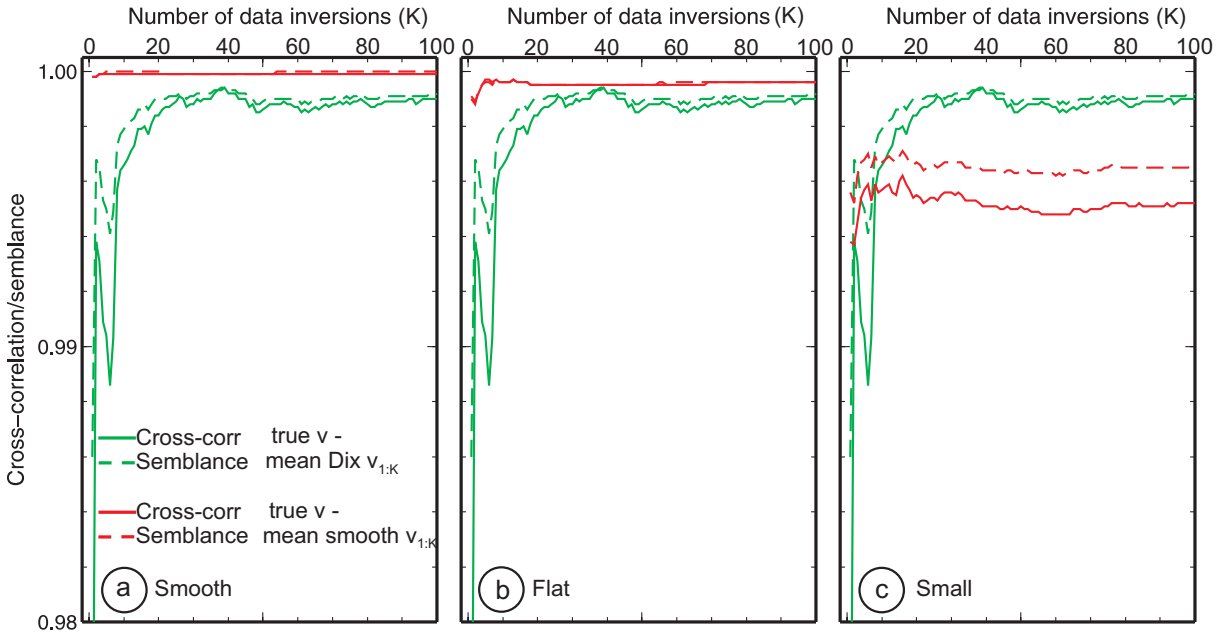

Figure 3.17: Cross-correlation/semblance between the true interval velocity and the cumulative mean of interval velocity profiles shown in Fig. 3.16, where the number of profiles added is given by the number of data inversions.

Interval velocities inverted from RMS velocities with different standard deviations of zero-mean noise are shown in Fig. 3.18. The regularized solution for a smooth model is calculated for a misfit of $\chi^2 = \mathrm{N}$. The interval velocities shown in Fig. 3.18a are calculated from RMS velocities with noise with standard deviation of 2 m/s at the seafloor incresing linearly to 15 m/s at 1 s bsf. Two other cases of interval velocities derived from RMS velocities with errors with standard deviation half and a quarter of those mentioned above are shown in Fig. 3.18b and 3.18c. Both the Dix interval velocity and the regularized interval velocity improve as the error on RMS velocity decreases: the width of the distribution of the Dix interval velocities decreases considerably, and the regularized interval velocities get closer to the true

anomalous values.

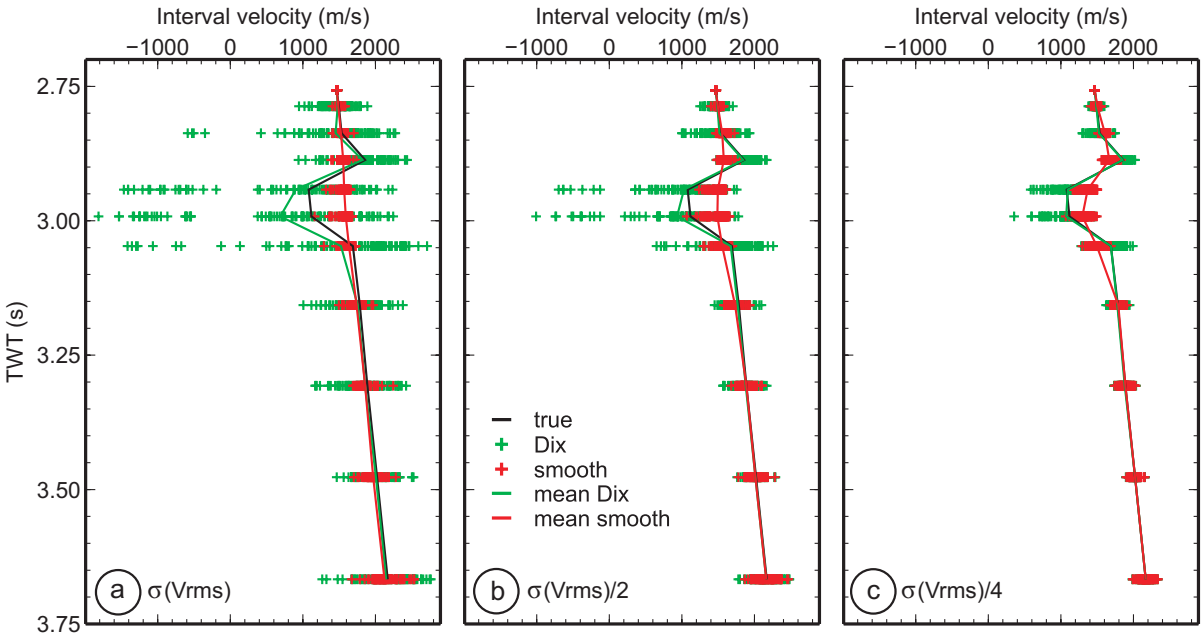

Figure 3.18: Comparison between the Dix interval velocity (green crosses) and smooth interval velocity (red crosses) from RMS velocities with different standard deviations σ_{Vrms}: a) 2-15 m/s, b) 1-7.5 m/s, c) 0.5-3.7 m/s. The ranges correspond to first and last RMS velocity, between which σ_{Vrms} increases linearly.

Regularized models are calculated for different trade-off parameters μ, chosen for different misfits to data. For N data with Gaussian errors, the expected value for the data misfit is $\chi^2 = \mathrm{N}$, such that observations are fit within a degree justified by their error. Three cases where the regularized solution is calculated for different values of χ^2 are shown in Fig. 3.19. The distribution of the regularized interval velocities becomes much wider as the misfit decreases, since the data are overfit by fitting the noise. By decreasing the misfit, the regularized solution approaches the Dix solution, for which data are fit exactly. Thus, the smaller the misfit, the more noise artifacts are introduced. If the misfit were larger than N (not shown here), the data would be fit too poorly and information contained in the data would be discarded.

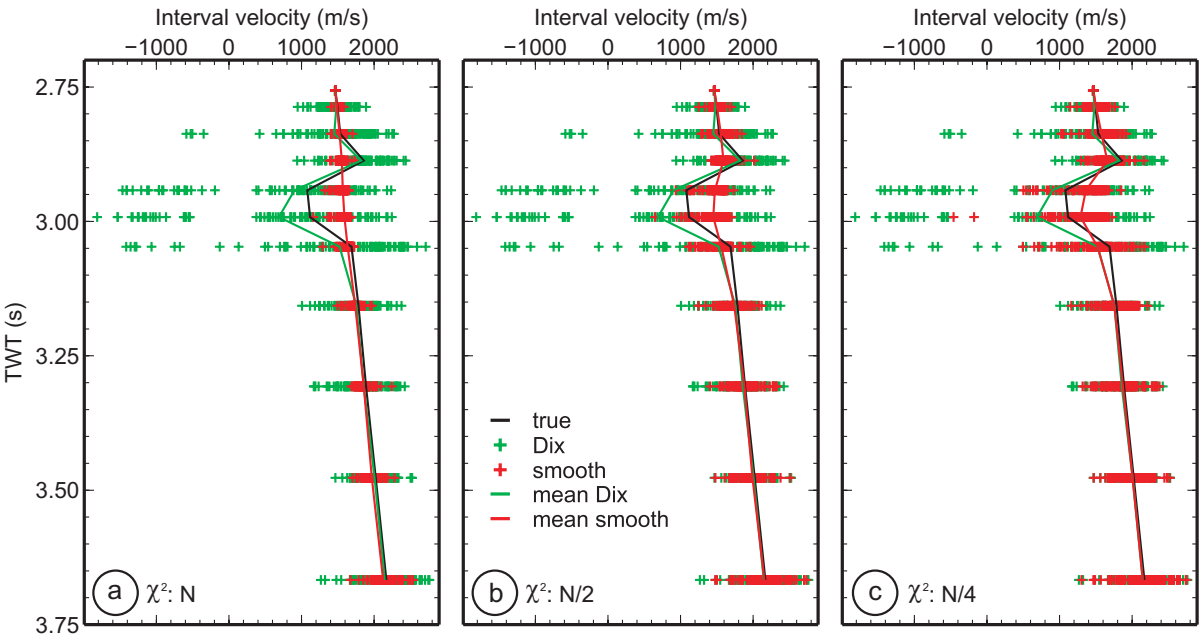

Figure 3.19: Comparison between the Dix interval velocity (green crosses) and smooth interval velocity (red crosses) calculated for different misfits to data: a) χ^2=N, b) χ^2=N/2, c) χ^2=N/4, with N=11.

A comparison between a profile 1 s long and one 0.5 s long, with anomalies in the shallower part is shown in Fig. 3.20. The regularized interval velocities in the layers with anomalies are slightly closer to the true values for the case in Fig. 3.20b, although still not a good representation of the true model. This happens because the shallower values are not controlled by the deeper layers like in the case in Fig. 3.20a. Therefore, if there are RMS velocity anomalies in the shallower part of the section, the regularized interval velocity should be calculated from the shallower RMS velocities. In the dataset from line 063, many positive and negative velocity anomalies are seen in the blank zones, and sometimes negative anomalies outside the blank zones. To recover these anomalies better, only the shallower part of the section should be inverted.

In summary, the results from the synthetic cases have shown that the uncon-

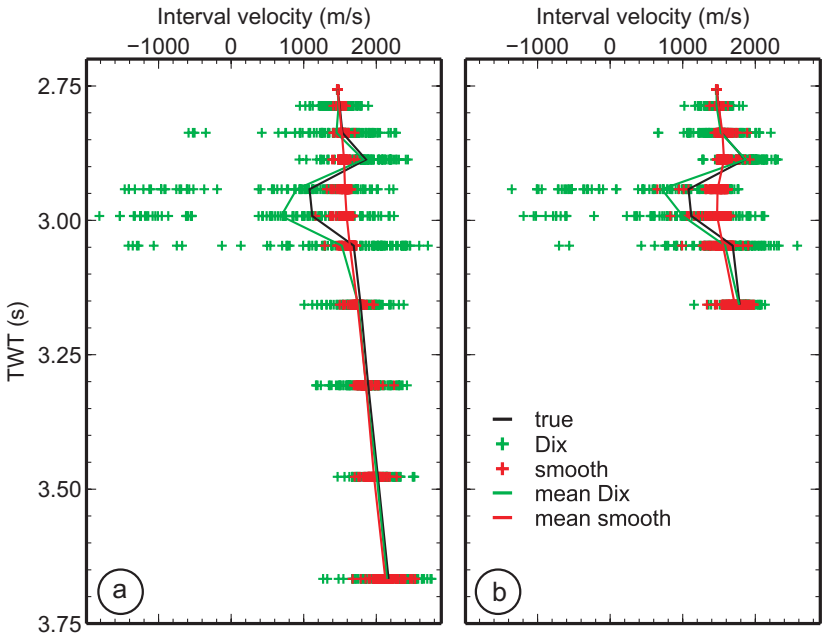

Figure 3.20: Comparison between the regularized interval velocity for a profile up to a) 1 s bsf and b) 0.5 s bsf.

strained interval velocity estimates from individual velocity profiles have too large uncertainties. This problem can be overcome by applying constraints to the inversion. Furthermore, when averaging across a number of velocity profiles, the mean estimate from the unconstrained Dix inversion for layers where the velocity decreases with depth is biased to low velocities. An unbiased estimate can be determined from at least 15 profiles by first averaging squared interval velocities and then taking their square root. The regularized inversion does not recover well velocity anomalies, but works very well for a velocity that is uniformly increasing with depth, by reducing the uncertainty. The regularized velocities are best determined using a smoothness constraint by fitting data to a statistical level consistent with their uncertainties and using only the shallower data for inversion.

Inversion of Ulleung Basin Data

The stacking velocity data from outside and inside the blank zones are inverted separately because of the different levels of noise on the two datasets. The standard deviation of the noise on the squared stacking velocities, which forms the data covariance matrix, is used to calculate the regularized solution, its uncertainty (model covariance matrix) and the uncertainty of the Dix solution. The standard deviation of the random noise on the stacking velocities is approximated to be increasing linearly from 2 m/s at the seafloor to 7.5 m/s at 0.5 s bsf outside the blank zones. Two cases with different noise on stacking velocities inside the blank zones are considered. The first case (Case I) assumes that the random noise on the data corresponds exactly to the scatter in the stacking velocities, which has a standard deviation of 3 m/s at the seafloor increasing to 12.5 m/s at 0.28 s bsf and decreasing to 5.5 m/s to 0.5 s bsf. The second case (Case II) assumes that the error increases linearly with depth from 3 m/s at the seafloor to 9 m/s at 0.5 s bsf. Two cases are considered because the regularized solution, its uncertainty and the uncertainty in the Dix solution depend on the data error, and therefore the confidence in the interval velocity results is reflected by the degree to which the stacking velocity errors are trusted. The choice of errors in the second case, where the noise has a smaller standard deviation than that of the scatter, implies that the data have real anomalies that should not be considered as a contribution to the random noise. An approximately linear increase in standard deviation with depth is also implied if a trend is extrapolated from greater depth. Anomalies in the stacking velocities are expected, which makes the solution of Case

II preferred.

In the cases shown below, the regularized interval velocity is calculated for a smooth model with a data misfit of $\chi^2 = N$. The regularized velocities are shown by the red crosses in Fig. 3.21a outside the blank zones and in Figs. 3.22a and 3.23a inside the blank zones for the two cases described above. The Dix solution shown by the green crosses is also plotted for comparison.

As required by the smooth model, the regularized interval velocities have a much narrower distribution than the Dix velocities. Many of the features seen in the mean of Dix velocities are removed (Figs. 3.21b, 3.22b, 3.23b). Outside the blank zones (Fig. 3.21b), the regularized mean is slightly larger than the Dix mean, as a result of the bias in Dix velocities noted in the synthetic cases. The regularized mean in the blank zones (Figs. 3.22b, 3.23b) does not show the same large positive and negative anomalies as the Dix mean. For case I, where the stacking velocities have maximum possible uncertainty, the regularized solution reflects this by showing no anomaly, as any anomaly in stacking velocity is not significant considering its error. The regularized solution for case II is no longer continously increasing with depth, showing slight deviations around the BGHSZ as compared to the velocity mean outside the blank zones. The standard deviation indicated by crosses in Figs. 3.21c, 3.22c and 3.23c is calculated for individual profiles from the model covariance matrix and thus represents the uncertainty of the velocity estimate. The standard deviation indicated by the continuous lines quantifies the scatter of velocities in each running window; thus, it is an estimate of the lateral variation in velocity along the profile.

A direct comparison between the running mean of interval velocities from the

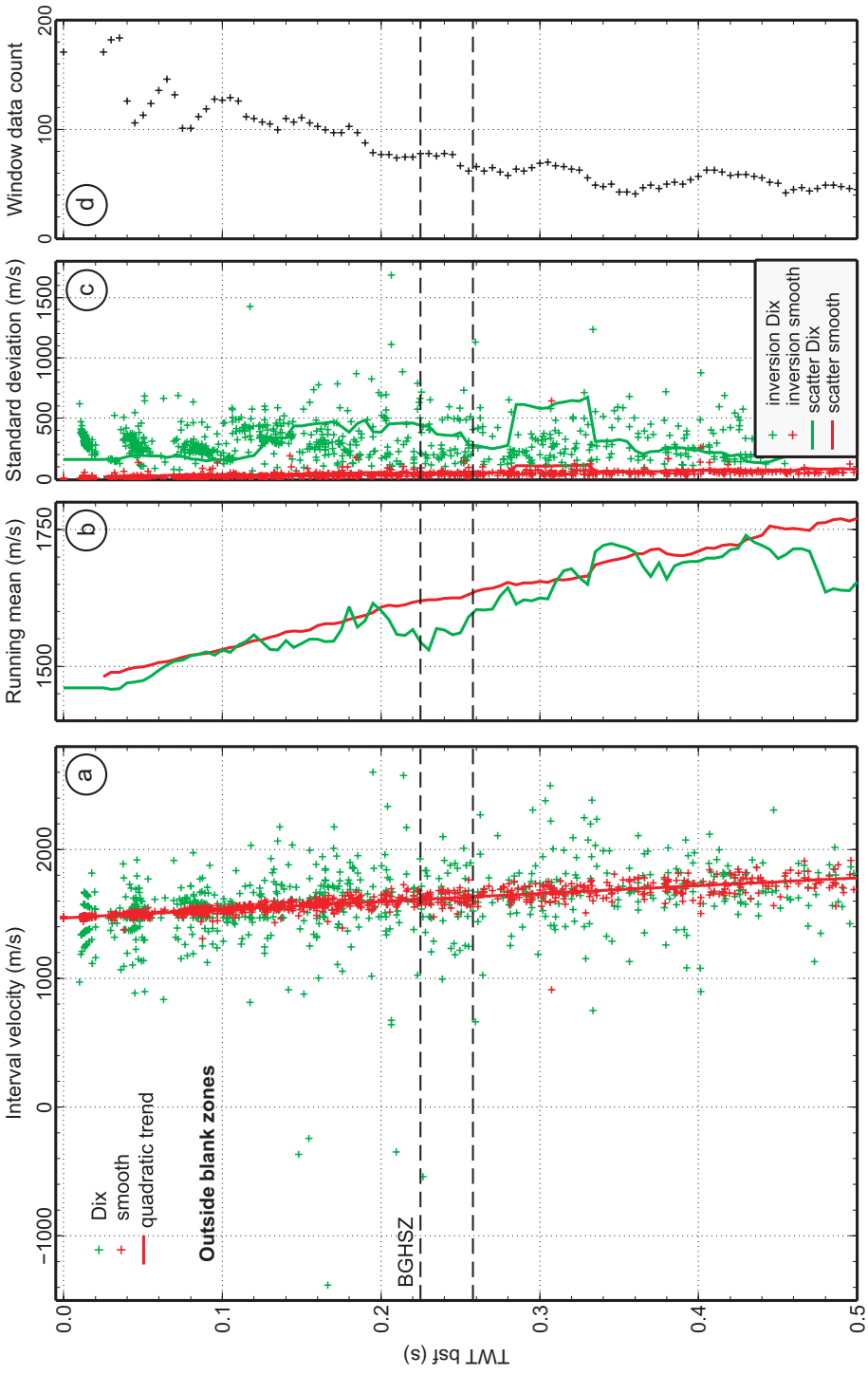

Figure 3.21: a) Comparison between interval velocity from the Dix (green crosses) and smooth model (red crosses) outside the blank zones, with a quadratic trendline through the latter; b) running mean of the interval velocities in 50 ms long windows calculated every 5 ms; c) standard deviation from the inversion of each velocity profile shown by the crosses; standard deviation of the interval velocity distribution for the running windows with mean shown in b) indicated by the continuous lines; d) window data count.

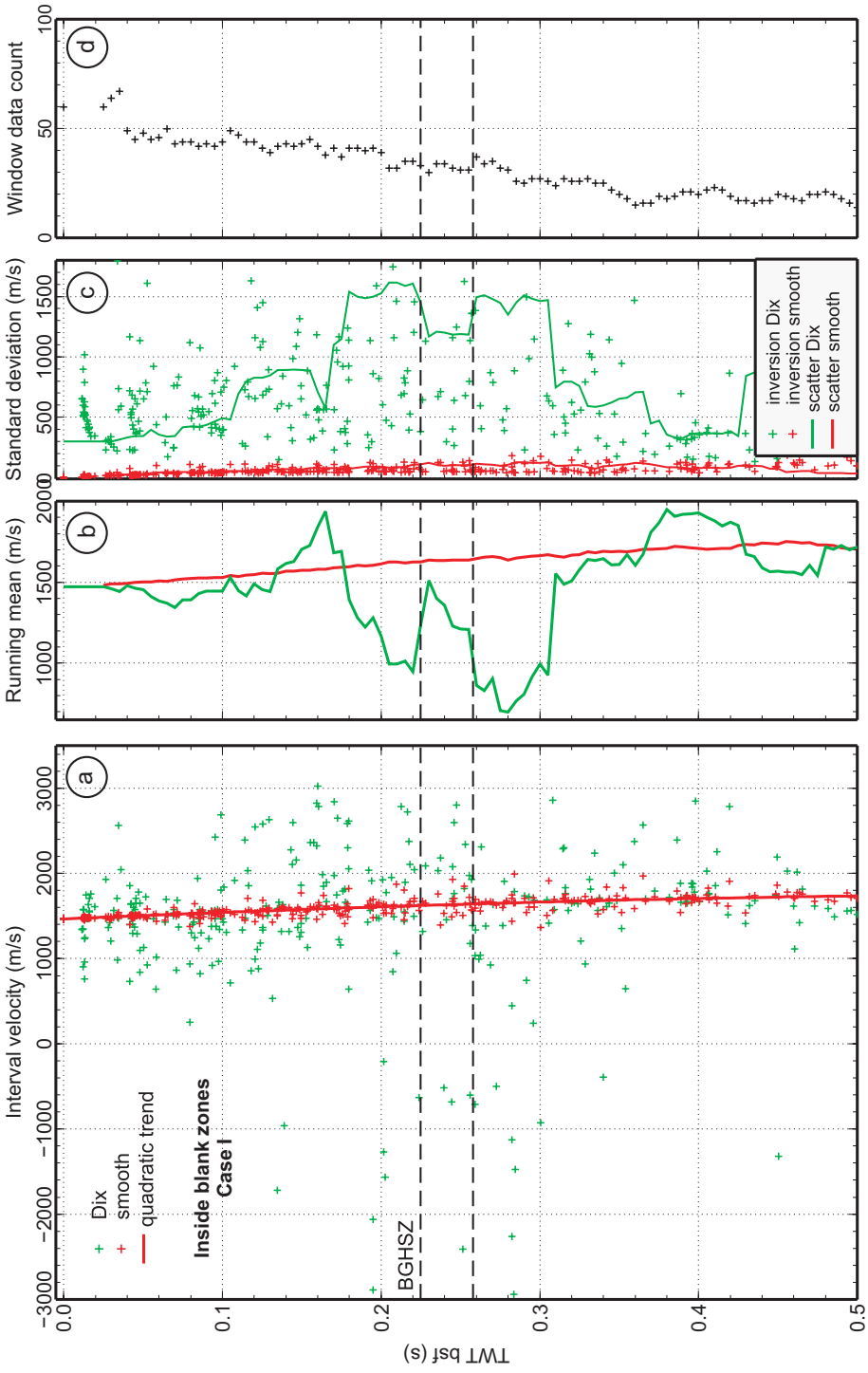

Figure 3.22: a) Comparison between interval velocity from the Dix (green crosses) and smooth model (red crosses) inside the blank zones (Case I, see text for details), with a quadratic trendline through the latter; b) running mean of the interval velocities in 50 ms long windows calculated every 5 ms; c) standard deviation from the inversion of each velocity profile shown by the crosses; standard deviation of the interval velocity distribution for the running windows with mean shown in b) indicated by the continuous lines; d) window data count.

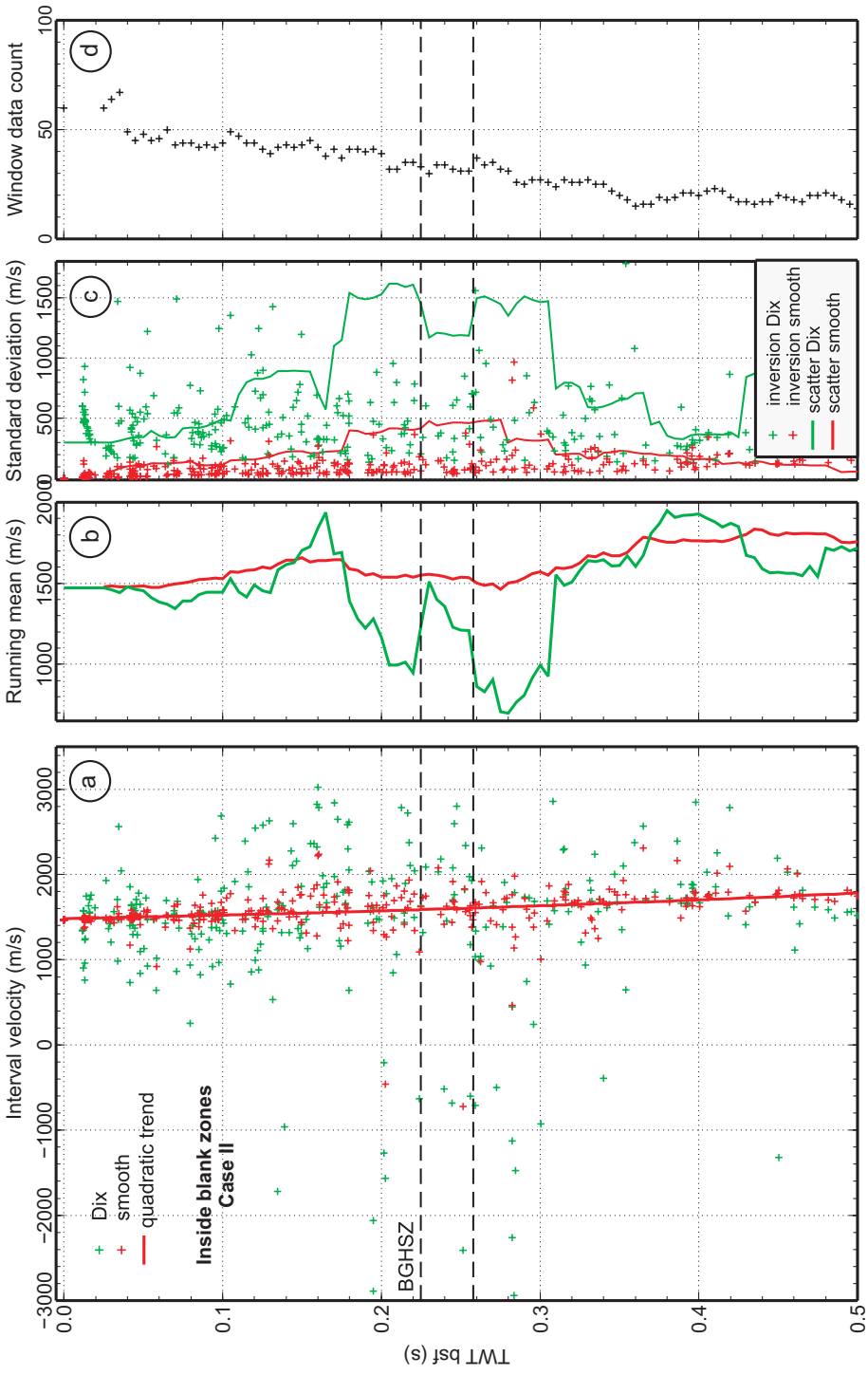

Figure 3.23: a) Comparison between interval velocity from the Dix (green crosses) and smooth model (red crosses) inside the blank zones (Case II, see text for details), with a quadratic trendline through the latter; b) running mean of the interval velocities in 50 ms long windows calculated every 5 ms; c) standard deviation from the inversion of each velocity profile shown by the crosses; standard deviation of the interval velocity distribution for the running windows with mean shown in b) indicated by the continuous lines; d) window data count.

unconstrained Dix equation (green and blue curves) corresponding to the mean of interval velocities and the square root of the mean of squared interval velocities, respectively, and the regularized smooth solution (red curve) from inside and outside the blank zones is shown in Fig. 3.24. By taking the square root of the squared interval velocity mean, one avoids taking the square root of negative and very small squared interval velocities, which biases the mean of interval velocities towards small values. The bias is easily noted as the green line always indicates smaller values than the blue line. As expected, the smooth velocity is a minimum-structure representation of the other two curves. All curves inside the blank zones show a positive anomaly at ∼0.16 s, followed by two peaks of negative anomalies at ∼0.21 s and ∼0.28 s. The curves outside the blank zones show a small positive anomaly at ∼0.2 s followed by a small negative anomaly at ∼0.23 s.

A comparison between the mean inside and outside the blank zones from each method, and one standard error away from the mean is shown in Fig. 3.25. The largest positive anomaly of interval velocity inside the blank zones above the BGHSZ at ∼0.16 s is 420 m/s (Fig. 3.25b), followed by 390 m/s (Fig. 3.25a) and 65 m/s (Fig. 3.25c). The largest negative anomaly right above the BGHSZ is 590 m/s (Fig. 3.25a), followed by 360 m/s (Fig. 3.25a) and 70 m/s (Fig. 3.25c). The second peak of the negative anomaly below the BGHSZ at 0.27 s is 920 m/s (Fig. 3.25a), 640 m/s (Fig. 3.25b) and 190 m/s (Fig. 3.25c).

The second degree polynomial through the interval velocity mean from the smooth inversion up to 0.5 s bsf outside the blank zones from Fig. 3.25c is:

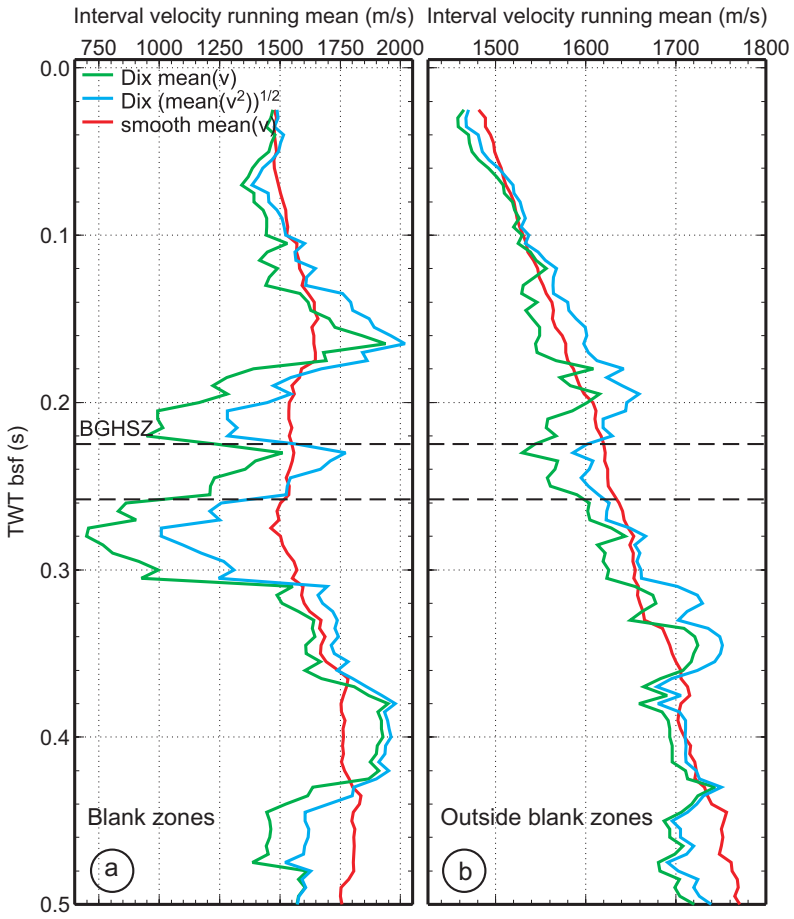

Figure 3.24: Dix interval velocity running mean (green line), square root of the Dix interval velocity squared running mean (blue line), smooth interval velocity running mean (red line): a) inside blank zones; b) outside blank zones.

$$v = 1467.74 + 664.49t - 90.60t^2, \tag{3.21}$$

where t is twt bsf in s.

The second degree polynomial through the interval velocity mean, calculated as the square root of the squared velocity mean up to 2.3 s bsf outside the blank zones, is:

$$v = 1475.07 + 505.40t + 248.22t^2 \tag{3.22}$$

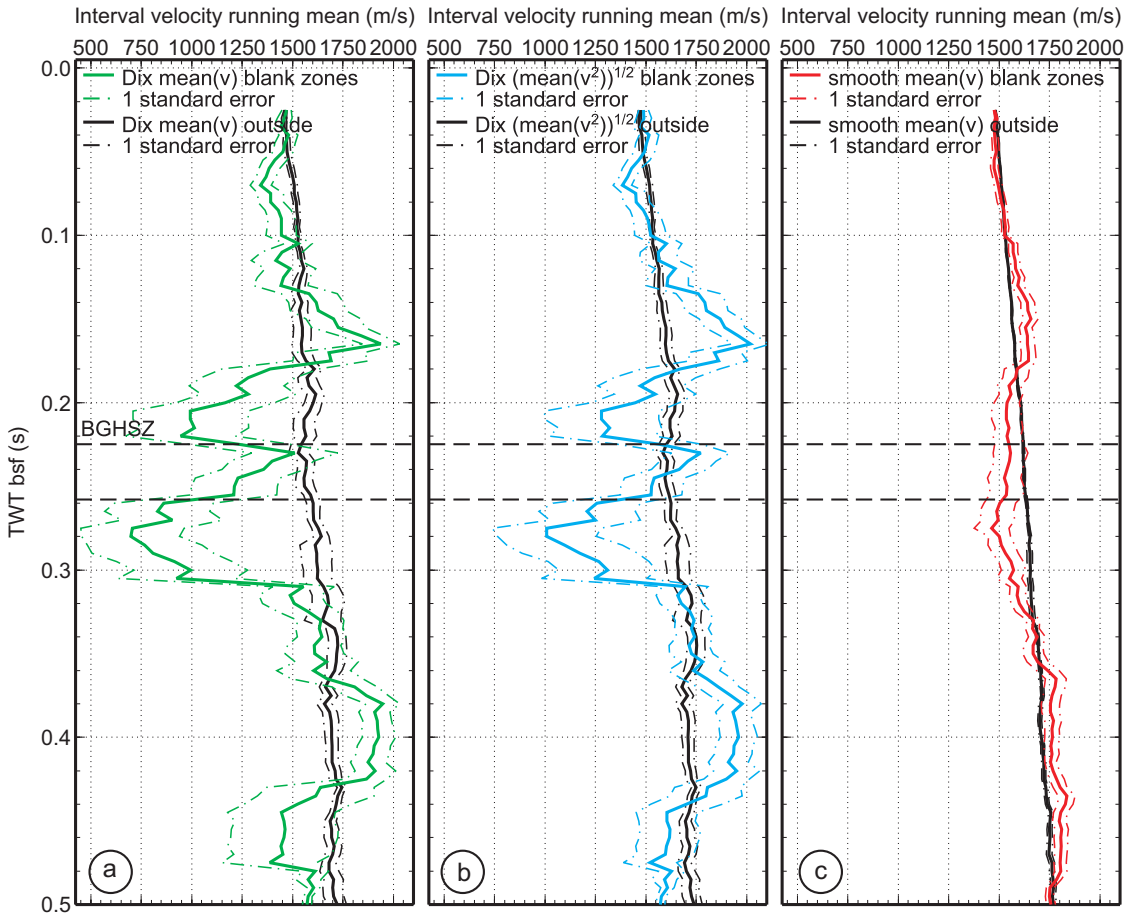

Figure 3.25: Comparison between interval velocity running mean inside and outside the blank zones, with 1 standard error away from the mean for: a) Dix interval velocity mean, b) the square root of the mean squared-Dix-interval velocity; c) smooth interval velocities.

These equations likely characterize best the normal compaction of sediments to greater depths in the area of the line 063. The smooth solution has much lower velocities at greater depths than the other solutions, due to the smoothness constraint and large uncertainties in the stacking velocity; that is why the trend from this solution is derived only up to 0.5 s bsf.

The smooth interval velocities at the location of the blank zones and in the area around them are shown in a gridded plot in Fig. 3.26. The anomalies are not very prominent as a result of the smoothing constraint, also seen from Fig. 3.23.

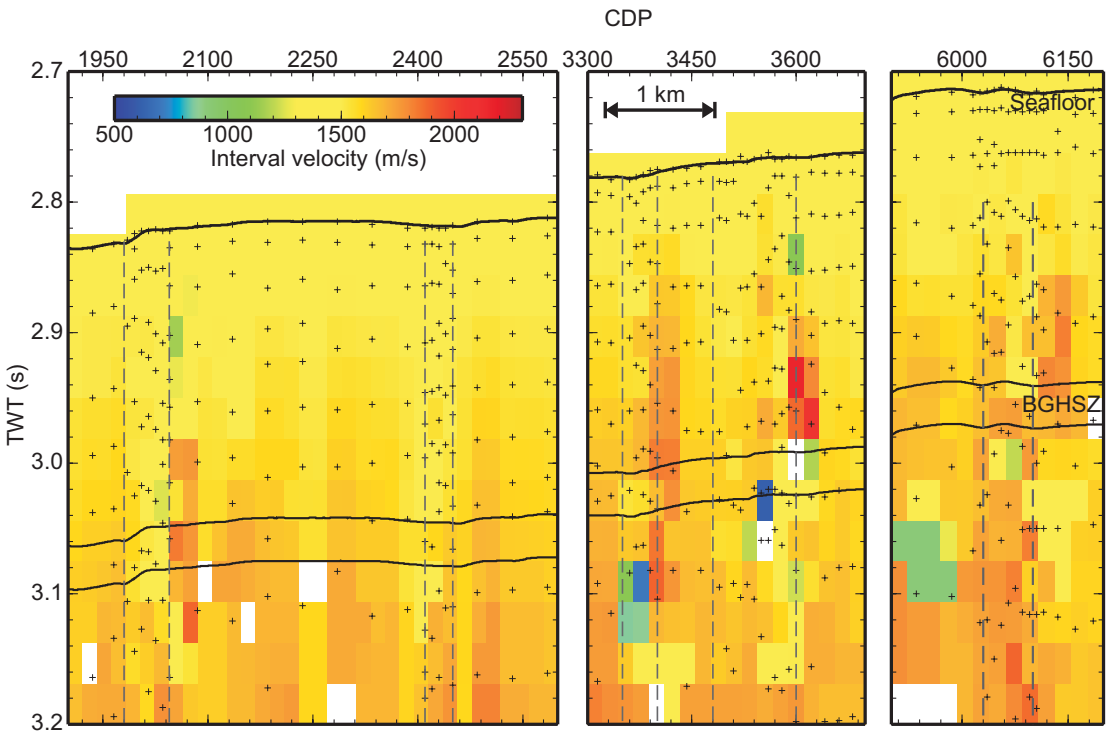

Figure 3.26: Gridded smooth interval velocities around the blank zones. The velocities inside the blank zones are those calculated for case II.

The velocities for the blank zones are separated for each blank zone located at CDP 1985-2045, CDP 3360-3400, CDP 3490-3600, CDP 6015-6115, as shown in Figs. 3.27, 3.28, 3.29, 3.30, respectively. The velocities from CDP 2410-2450, included earlier in the calculations for blank zones, are not shown separately because the area is too narrow and only few velocity profiles were calculated. All the blank zones show a decrease in velocity below the predicted BGHSZ, except for the smooth profile in Fig. 3.27. All the blank zones except for the one in Fig. 3.27 show a positive anomaly above the predicted BGHSZ.

3.2.2 Non-linear Inversion

In this section non-linear Bayesian inversion is used to estimate interval velocities and layer thicknesses from stacking velocities using the Dix equation. The advantage

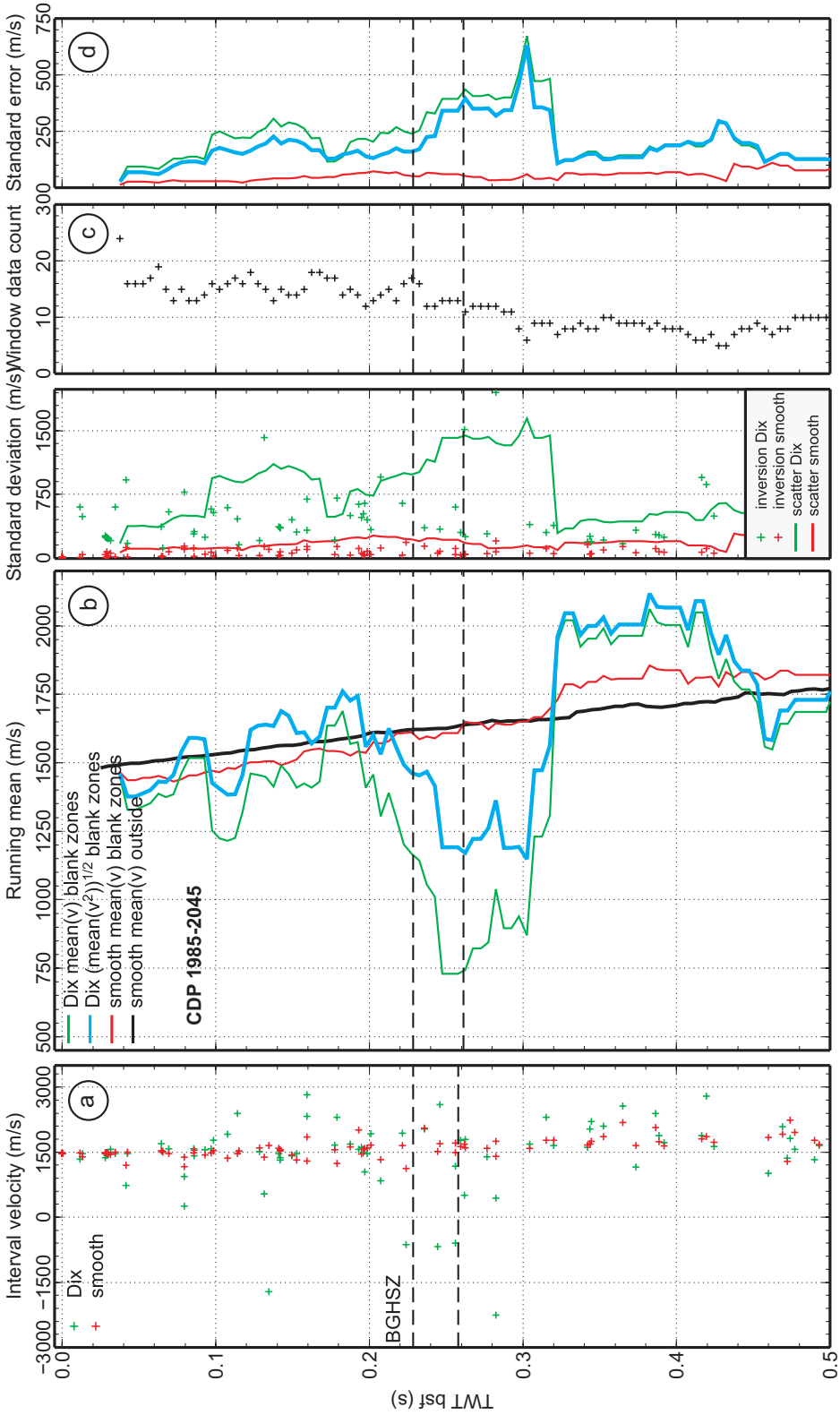

Figure 3.27: a) Comparison between interval velocity from the Dix (green crosses) and smooth model (red crosses) inside blank zone located at CDP 1985-2045 from 10 CDP profiles; b) running mean of the interval velocities in 75 ms long windows calculated every 5 ms; c) standard deviation from the inversion of each velocity profile shown by the crosses; standard deviation of the interval velocity distribution for the running windows with mean shown in b) indicated by the continuous lines; d) window data count; e) standard error of the mean.

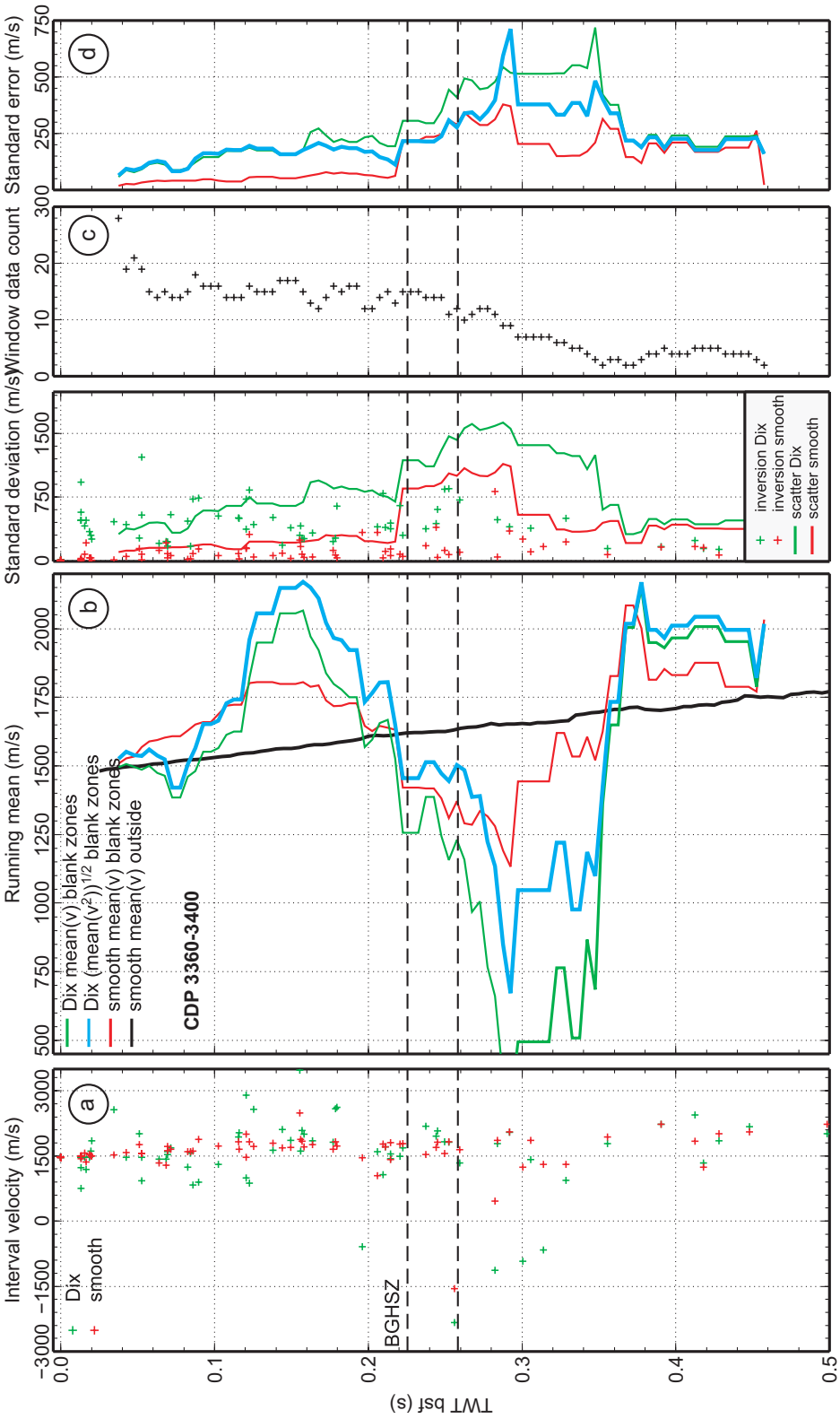

Figure 3.28: a) Comparison between interval velocity from the Dix (green crosses) and smooth model (red crosses) inside blank zone located at CDP 3360-3400 from 9 CDP profiles; b) running mean of the interval velocities in 75 ms long windows calculated every 5 ms; c) standard deviation from the inversion of each velocity profile shown by the crosses; standard deviation of the interval velocity distribution for the running windows with mean shown in b) indicated by the continuous lines; d) window data count; e) standard error of the mean.

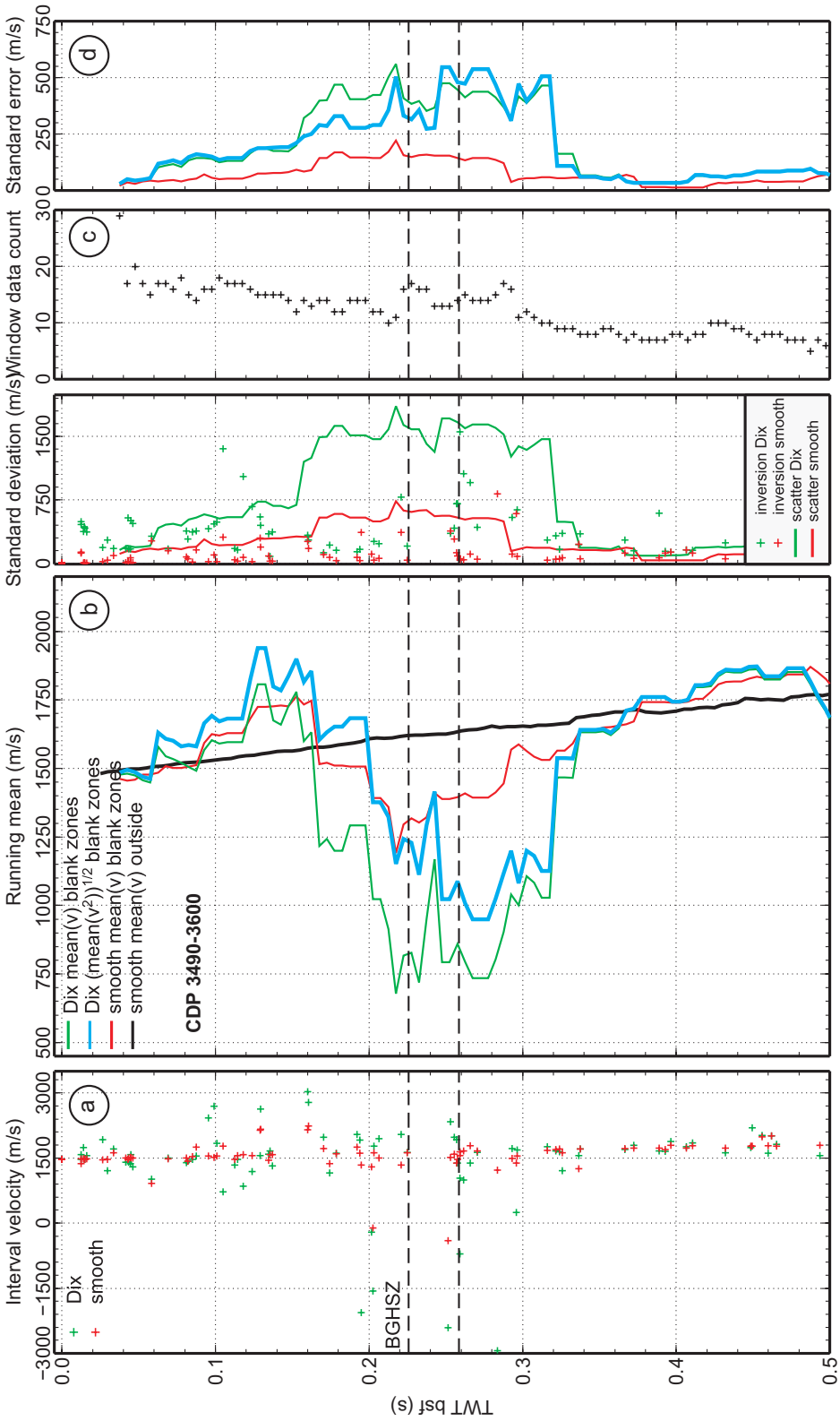

Figure 3.29: a) Comparison between interval velocity from the Dix (green crosses) and smooth model (red crosses) inside blank zone located at CDP 3490-3600 from 12 CDP profiles; b) running mean of the interval velocities in 75 ms long windows calculated every 5 ms; c) standard deviation from the inversion of each velocity profile shown by the crosses; standard deviation of the interval velocity distribution for the running windows with mean shown in b) indicated by the continuous lines; d) window data count; e) standard error of the mean.

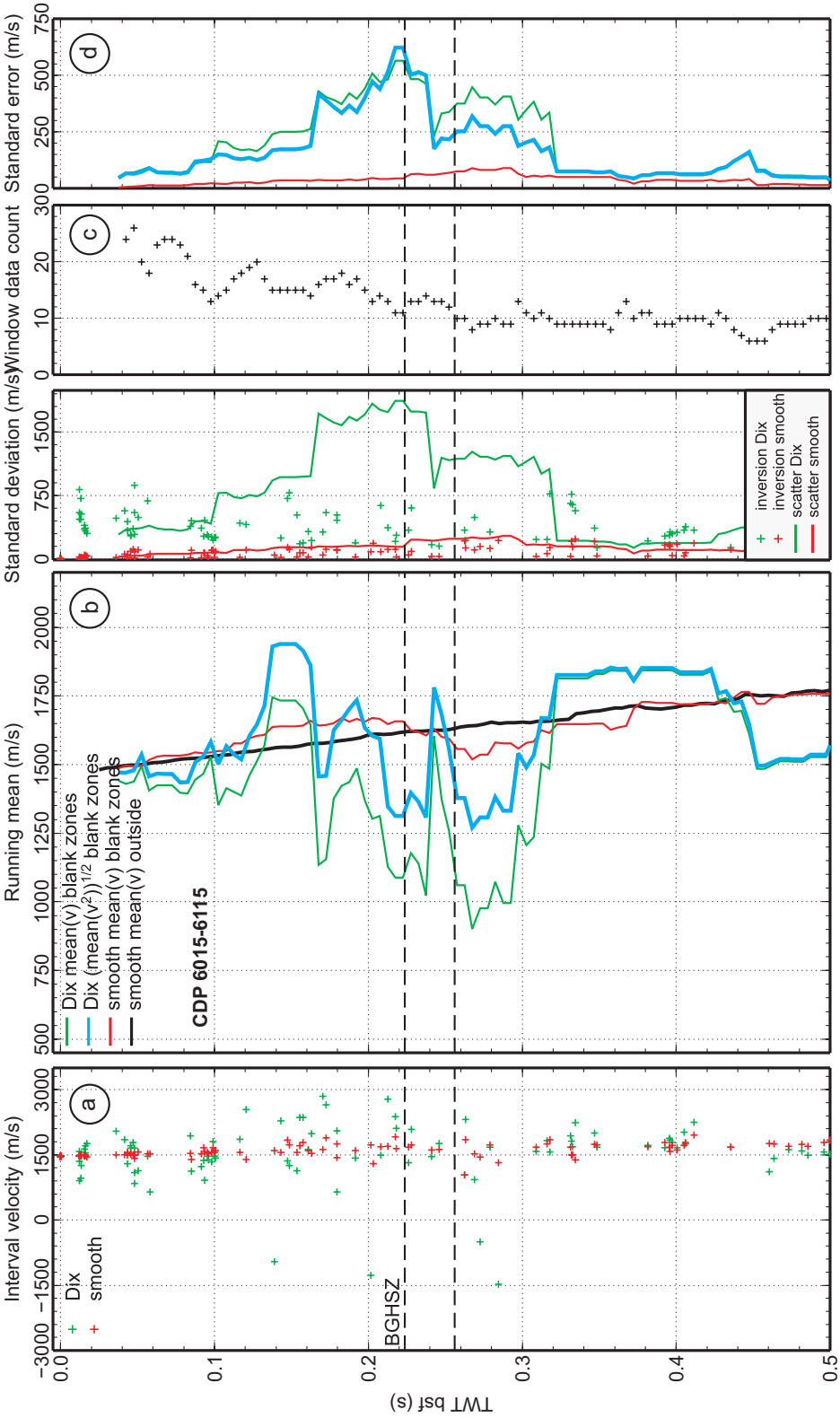

Figure 3.30: a) Comparison between interval velocity from the Dix (green crosses) and smooth model (red crosses) inside blank zone located at CDP 6015-6115 from 11 CDP profiles; b) running mean of the interval velocities in 75 ms long windows calculated every 5 ms; c) standard deviation from the inversion of each velocity profile shown by the crosses; standard deviation of the interval velocity distribution for the running windows with mean shown in b) indicated by the continuous lines; d) window data count; e) standard error of the mean.

of this method over the linear inversion described in Sections 3.1 and 3.2.1 is that the model parameters are determined by taking into account errors in both stacking velocities and traveltime, and they are restricted to realistic values. The Bayesian inversion provides quantitative uncertainty estimates and can include constraints from prior information (e.g., *Tarantola* 1987). *Maliverno and Briggs* (2004) also apply Bayesian inversion to vertical seismic profiling (VSP).

Bayesian Inversion

The stacking velocities at each CDP profile represent the observed data $\mathbf{d} = (v_1, v_2, \cdots v_N)$ and the velocity and thickness of each interval represent the model $\mathbf{m} = (V_1, h_1, V_2, h_2 \cdots V_N, h_N)$. Interval velocities are related to RMS velocities, by a function $\mathbf{d} = \mathbf{d}(\mathbf{m}) + \mathbf{n}$, where $\mathbf{d}(\mathbf{m})$ represents the non-linear relationship between RMS and interval velocity stated through the Dix equation (Eq. 3.4), and $\mathbf{n}$ is assumed to be Gaussian-distributed noise. The interval thickness is calculated as the product between interval velocity and one-way-traveltime. The likelihood function for Gaussian-distributed errors $\mathbf{n}$ with data covariance $\mathbf{C}^{(d)}$ is:

$$L(\mathbf{m}) = \frac{1}{(2\pi)^{N/2}|\mathbf{C}^{(d)}|^{1/2}} exp\left\{-\frac{1}{2}[\mathbf{d}(\mathbf{m}) - \mathbf{d}]^T \mathbf{C}^{(d)-1}[\mathbf{d}(\mathbf{m}) - \mathbf{d}]\right\}. \tag{3.23}$$

In Bayesian inversion, the data ($\mathbf{d}$) and model ($\mathbf{m}$) vectors are considered random variables that obey Bayes' rule, written as:

$$P(\mathbf{m}|\mathbf{d}) \propto P(\mathbf{d}|\mathbf{m})P(\mathbf{m}), \tag{3.24}$$

where $P(\mathbf{m}|\mathbf{d})$ is the posterior probability density (PPD), representing the M-Dimensional probability distribution for the model parameters including both data information $P(\mathbf{d}|\mathbf{m})$ and prior information $P(\mathbf{m})$.

The above equation can also be written in terms of the likelihood function $L(\mathbf{m})$:

$$P(\mathbf{m}|\mathbf{d}^{obs}) \propto L(\mathbf{d}|\mathbf{m})P(\mathbf{m}). \tag{3.25}$$

Since the likelihood $L(\mathbf{m}) \propto exp(-E(\mathbf{m}))$, the PPD can be written as: :

$$P(\mathbf{m}|\mathbf{d}) = \frac{e^{-\phi(\mathbf{m})}}{\int e^{-\phi(\mathbf{m}',\mathbf{d})} d\mathbf{m}'}, \tag{3.26}$$

where $\phi(\mathbf{m}) = E(\mathbf{m}) - lnP(\mathbf{m})$ is the generalized misfit and the domain of integration spans the model space.

The solution of the inverse problem is given by the $P(\mathbf{m}|\mathbf{d})$. However, to interpret the PPD, the distribution properties defining parameter estimates, uncertainties and inter-relationships have to be computed. The parameter estimates are the maximum a posteriori (MAP) model and the mean model, and the parameter uncertainties are the model covariance matrix, 1D and 2D marginal probability distributions, defined, respectively, as

$$\hat{\mathbf{m}} = Arg_{max} P(\mathbf{m}|\mathbf{d}), \tag{3.27}$$

$$\bar{m} = \int \mathbf{m}' P(\mathbf{m}'|\mathbf{d}) d\mathbf{m}', \tag{3.28}$$

$$\mathbf{C}^{(m)} = \int (\mathbf{m}' - \bar{\mathbf{m}})(\mathbf{m}' - \bar{\mathbf{m}})^T P(\mathbf{m}'|\mathbf{d}) d\mathbf{m}', \tag{3.29}$$

$$P(m_i|\mathbf{d}) = \int \delta(m_i' - m_i) P(\mathbf{m}'|\mathbf{d}) d\mathbf{m}', \tag{3.30}$$

$$P(m_i, m_j|\mathbf{d}) = \int \delta(m_i' - m_i)\delta(m_j' - m_j) P(\mathbf{m}'|\mathbf{d}) d\mathbf{m}', \tag{3.31}$$

where δ is the Dirac delta function.

The correlation matrix which quantifies inter-parameter correlations is calculated by normalizing the covariance.

$$R_{ij} = C_{ij}^{(m)} / (C_{ii}^{(m)} C_{jj}^{(m)}). \tag{3.32}$$

Analytical solutions to Eqs. 3.27-3.32 can be found for linear inverse problems with Gaussian-distributed errors and Gaussian prior distributions (*Tarantola* 1987, *Sen and Stoffa* 1996). For non-linear problems, numerical solutions are required. The MAP model involves solving a numerical optimization problem, and the mean and parameter uncertainties are solved by numerical integration. Numerical integration is carried out with a Metropolis Gibbs' sampling (GS) approach. Using the method of importance sampling, samples are drawn from regions that contribute significantly to the integral, and their posterior probability is calculated. The system parameters are repeatedly perturbed and perturbations are accepted if a random number ξ drawn from a uniform distribution on [0,1] satisfies the Metropolis criterion:

$$\xi \leq exp(-\Delta E), \tag{3.33}$$

where ΔE is energy difference between the final and initial state.

Since the choice of parameter perturbations can affect the speed of convergence, the perturbations are drawn from distributions where the parameters have been rotated. The parameter rotation overcomes ineffectual sampling due to correlated parameters. Perturbations are applied in a principal-component parameter space where the axes align with the dominant correlation directions.

Synthetic Studies

The influence of different stacking and traveltime errors on the solution are tested on the synthetic model with positive and negative anomalies used in Sections 3.1.1 and 3.2. Three cases with different standard deviations of the RMS velocities σ_{VRMS} and traveltime σ_t are considered: i) σ_{VRMS} increases linearly from 2 m/s at the seafloor to 15 m/s at 1 s bsf; σ_t increases linearly from 2 ms at the seafloor to 20 ms at 1 s bsf; ii) σ_{VRMS} is a quarter of that used in i); same σ_t as in i); iii) σ_{VRMS} as in i); σ_t a quarter of that in i). The bounds on the parameters are set to 50% and 150% of the true model parameters.

The MAP and mean interval velocity and thickness models, together with the square root of the mean standard error (MSE) and the relative importance of the squared bias and variation are shown in Figs. 3.31 and 3.32. The MAP model is not calculated using numerical optimization, is it the model with the minimum energy from the distribution of models; the mean model is the mean of all models from each

probability distribution. The mean squared error, MSE, of the mean ($\bar{m}$) or MAP ($\hat{m}$) models is defined as:

$$MSE(\bar{m}) = \Sigma(m_i - \bar{m})^2 + \Sigma(\bar{m} - m_{true})^2, \tag{3.34}$$

where the first term represents the variance of all the possible models m_i around the mean and the second term represents the squared bias, which is the difference between the mean and the true model.

The observations with regard to the interval velocity model are: a) the MSE is reduced if σ_{VRMS} is reduced, but not at the same rate; b) the MSE is not reduced if σ_t is reduced; c) the MSE of layers wih anomalously low velocities is larger; d) the MSE increases little with depth; e) the variance of the model contributes more to the MSE than the squared bias. The conclusions with regard to the interval thickness model are: a) the MSE is reduced by similar amounts for deeper thicker layers if either σ_t or σ_{VRMS} are reduced (mean model); b) for only some of the thinner shallower layers, the MSE is reduced if σ_{VRMS} is reduced; c) the reduction of σ_t at shallower depths does not reduce the MSE; d) the MSE increases considerably with depth; e) the variance of the model contributes more to the MSE than the squared bias. For both the interval velocity and thickness estimate, the mean is a better estimate than the MAP, because the latter has a rather unpredictable character (for a non-linear problem, the MAP is not the maximum probability of each model parameter distribution).

The correlations between the model parameters from case i) are shown as the correlation matrix plot in Fig. 3.33 and 2-D marginal probability distributions in Fig.

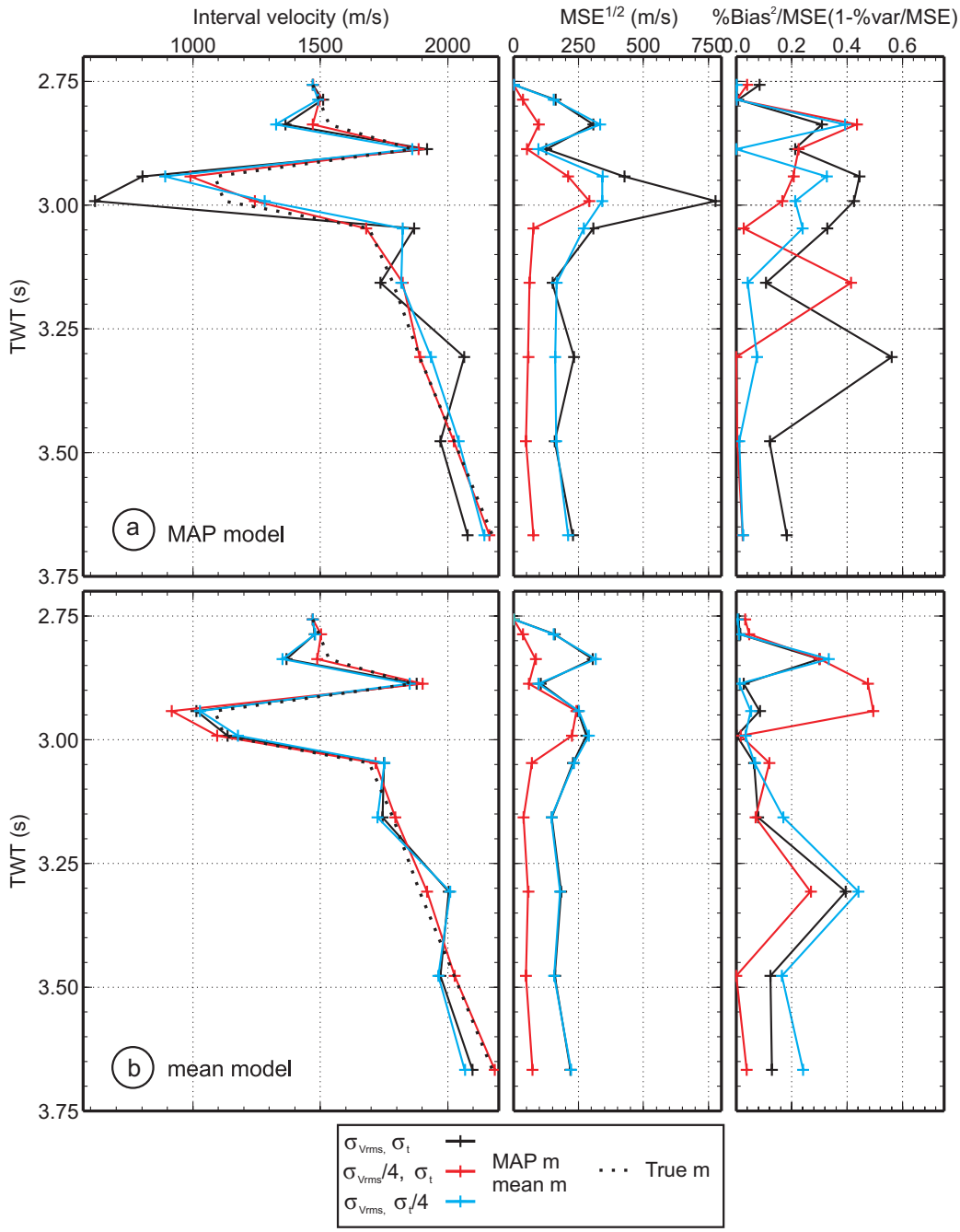

Figure 3.31: a) MAP and b) mean interval velocity model, the square root of the mean squared error (MSE), the percentage of squared bias/variance to MSE. The layers are plotted at the middle of the interval.

3.34. In the layers where the velocity increases with depth, the parameter correlations are the ones one expects: the thickness and velocity of any layer are positively correlated since they are proportional to each other through the time thickness of the

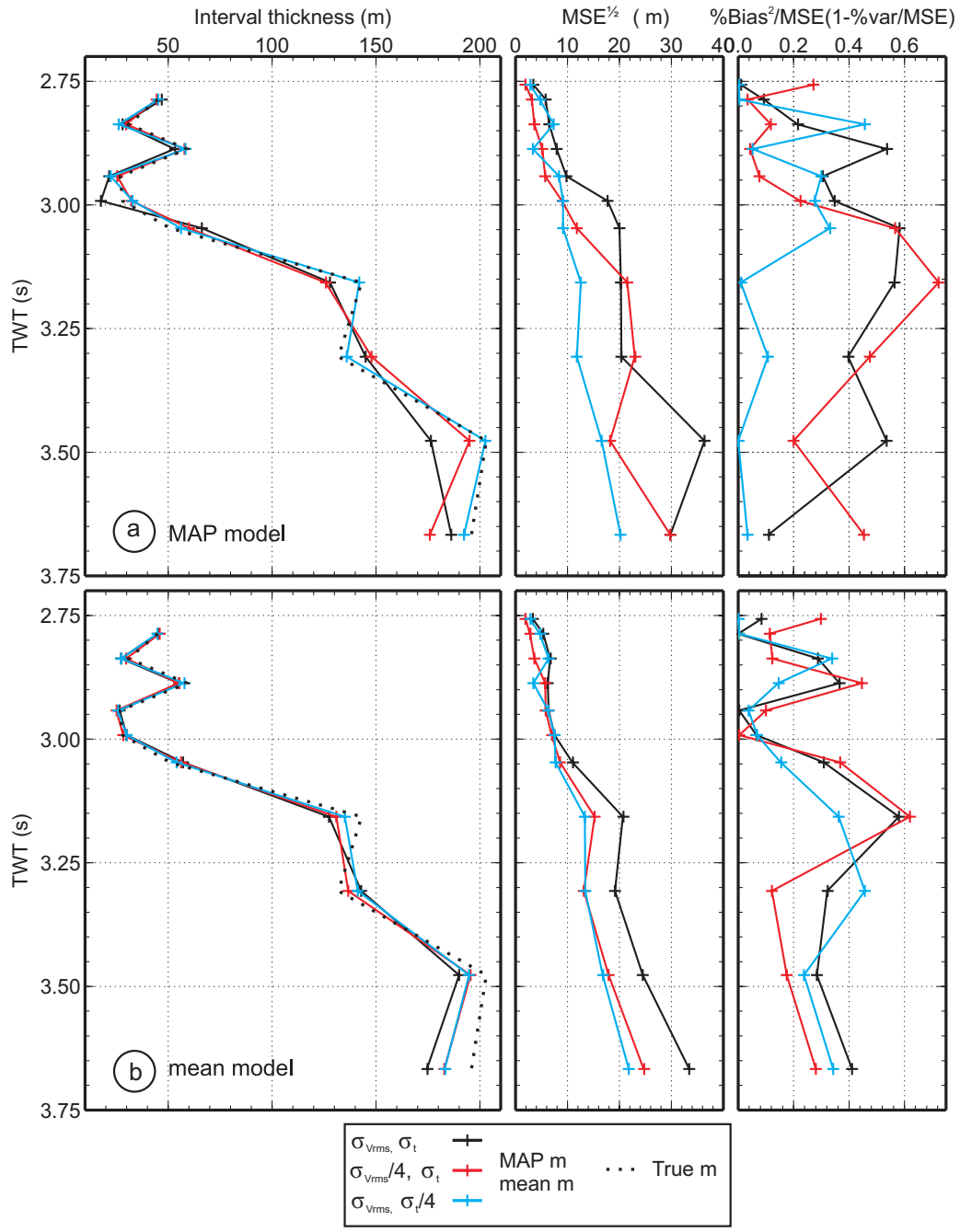

Figure 3.32: a) MAP and b) mean interval thickness model, the square root of the mean squared error (MSE), the percentage of squared bias/variance to MSE. The layers are plotted at the middle of the interval.

layer (Fig. 3.34a, b, f); both the velocity and thickness of neighbouring layers are negatively correlated (Fig. 3.34d), the velocity of one layer is negatively correlated with the thickness of a neighbouring layer (Fig. 3.34c). For the layers with anoma-

lously low velocity values (layer 5 and 6), the relation between the parameters from neighbouring layers is sometimes no longer the one described above, resulting from the wide distribution of the parameters (Fig. 3.34b and e).

The parameter correlations are important to consider when one performs the unconstrained Dix inversion (Sections 3.1 and 3.2.1). There, interval velocities can have non-realistic values (i.e., negative). One cannot exclude only these values, because they are negatively correlated with velocities from the neighbouring layers, so this would bias the results to positive values.

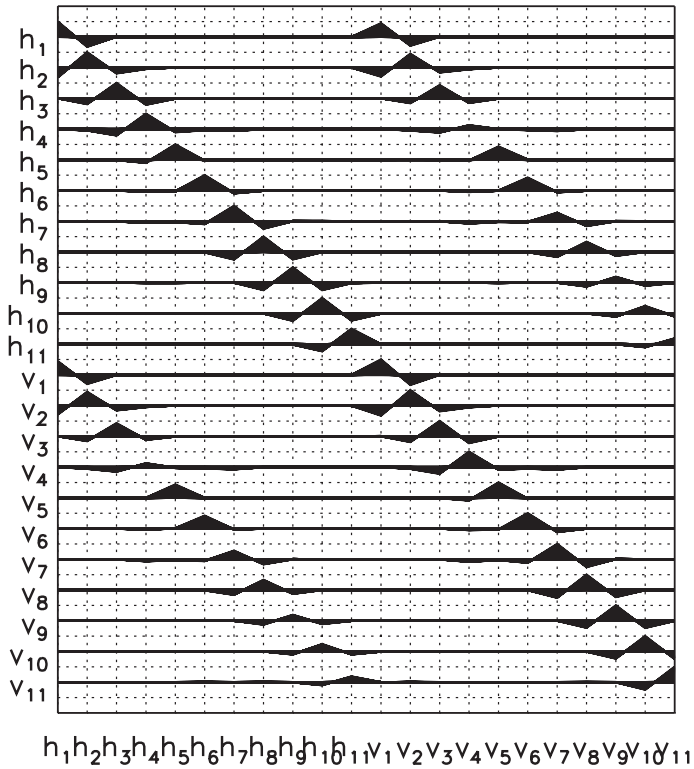

Figure 3.33: a) Correlation matrix plot for case i).

Inversion of Ulleung Basin Data

The data inverted in this section are from two CDP profiles from line 063, with the location indicated in Fig. 3.35: CDP 3463 from outside the blank zones (Fig.

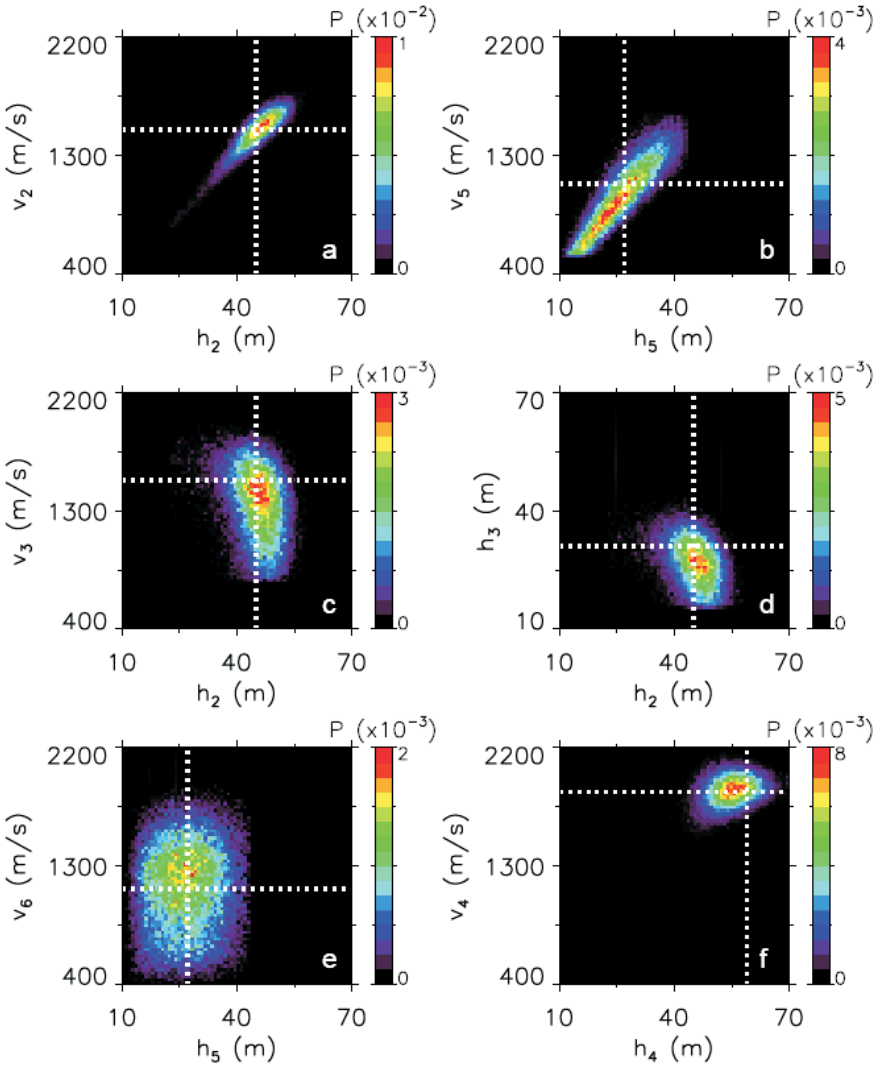

Figure 3.34: a) Joint marginal probability distributions of parameters from the synthetic case i). The colorbar is normalized probability P, and the dashed lines indicate the true parameter values. Layer 4 has a positive velocity anomaly and layers 5 and 6 negative velocity anomalies.

2.4) and CDP 3540 from inside a blank zone (Fig. 2.4). The noise on the data is the same as that given in Section 3.1.3. Since no optimization algorithm was used for the inversion to obtain a starting model, an initial inversion using larger bounds is first carried out, and the model with the smallest energy (MAP model) is used as the starting model for the final inversion. The inversion is not very sensitive to this

starting model. The bounds on the parameters are chosen to be 50% and 150% of the starting model.

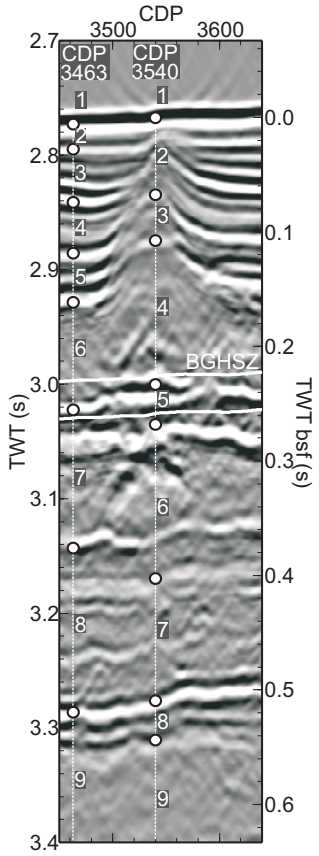

Figure 3.35: Location of the CDP profiles analyzed in Figs. 3.36 and 3.37, where the numbers indicate the layers for which probability distributions are shown.

The inversion results of data from CDP 3463 and CDP 3540 are shown in Figs. 3.36 and 3.37, respectively. The first layer represents the water column. The MAP and mean models are given by the continuous and dashed lines, respectively. The reference velocity from outside the blank zones calculated in Section 3.2.1 is shown for comparison (grey line). The interval velocity distribution at CDP 3540 is very wide when the mean/MAP model decreases considerably with depth (layer 5, 6, 8) and even more when the layers are very thin (layer 8). The interval velocity distribution of layer 4 where the mean/MAP velocity is considerably increased as compared to

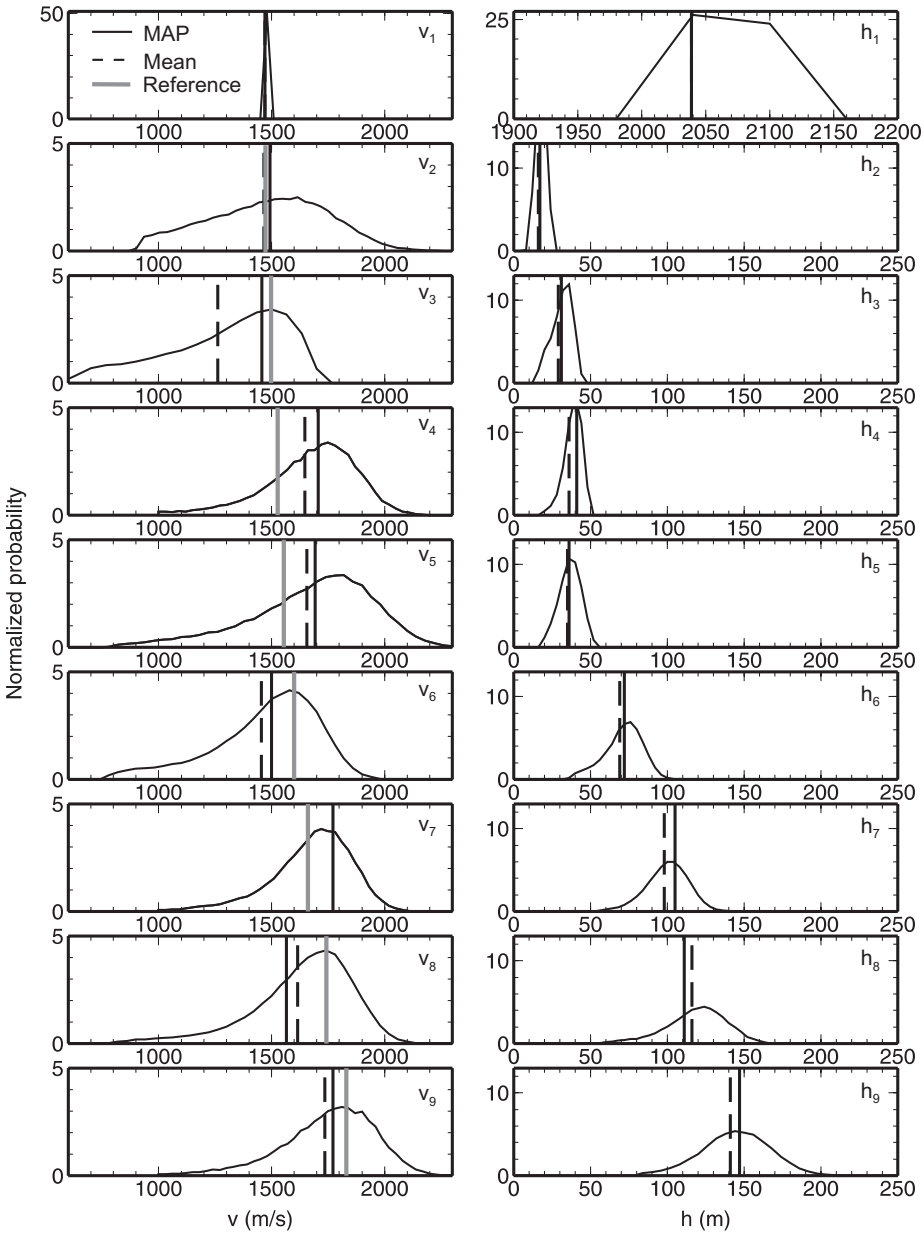

Figure 3.36: Interval velocity and layer thickness 1-D marginal probability distributions of inverted stacking velocities from CDP 3463 located outside the blank zones as shown in Fig. 3.35. Mean model is indicated by the dashed line, MAP model by the solid line and reference velocity from outside the blank zones by grey line.

layer 3 is relatively narrow. The interval velocity distributions at CDP 3463 have a similar width, as the mean/MAP model does not show any large anomalies and the interval thickness increases with depth; the distributions of layer thicknesses become wider with depth, proportional to the mean/MAP model.

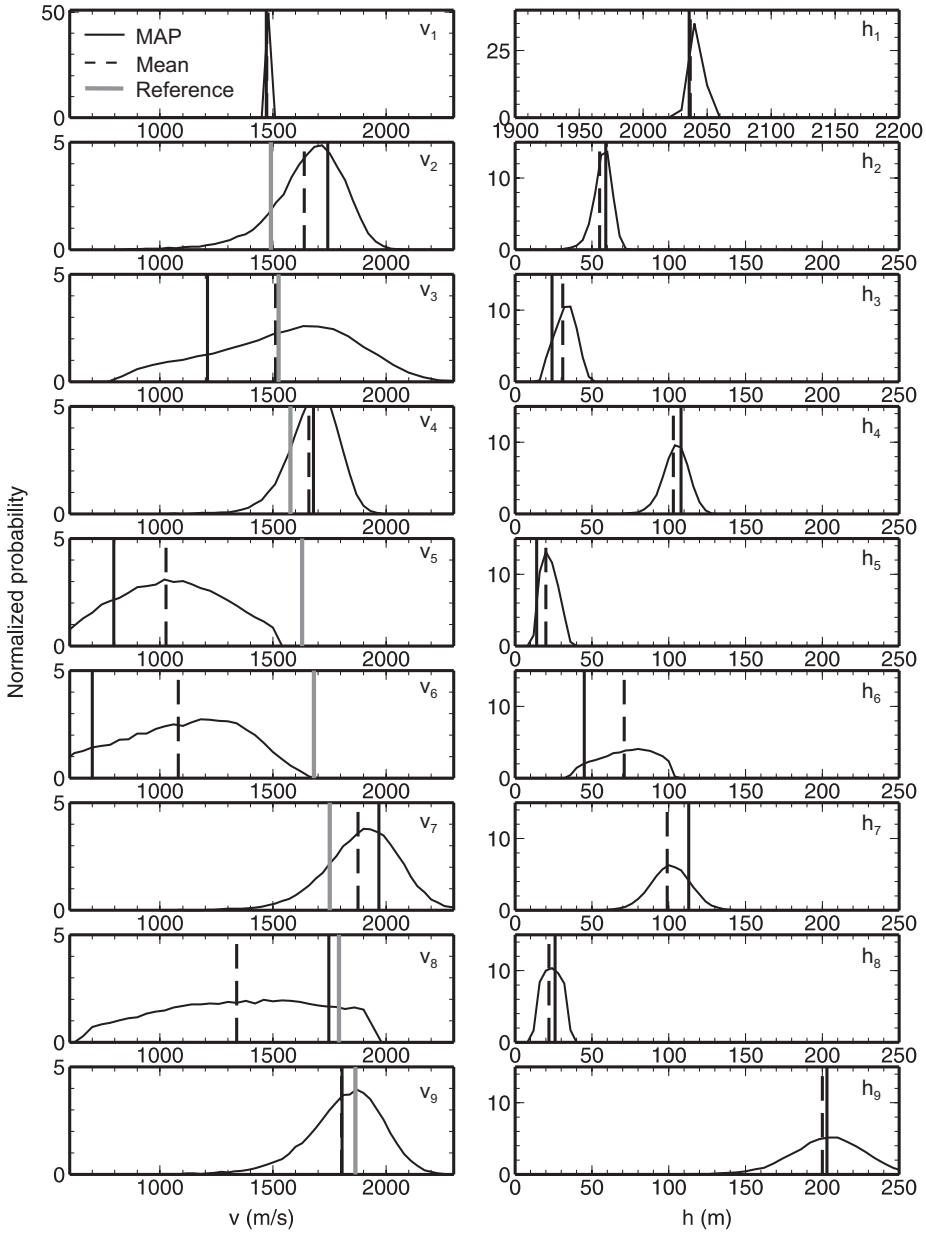

Figure 3.37: Interval velocity and layer thickness 1-D marginal probability distributions of inverted stacking velocities from CDP 3540 located inside a blank zone shown in Fig. 3.35. Mean model is indicated by the dashed line, MAP model by the solid line and reference velocity from outside the blank zones by grey line.

3.3 Interval Velocity from Reflector Pull-up Inside Blank Zones

An independent estimate of interval velocities inside the blank zones is made using the reflector traveltime pull-up compared with the equivalent reflectors outside the

blank zones. These estimates are compared with those derived earlier from the Dix equation. The velocities from the Dix equation have lower uncertainties outside the blank zones, where the velocity is continuously increasing with depth, as compared to higher uncertainties inside the blank zones.

Reflectors in the blank zones are generally bowed up in time-migrated sections, which may result either from high velocity material or from physical bowing of the reflectors. We calculate interval velocities which would be required if the bowing up is entirely due to high velocities compared to outside blank zones. The velocity outside is taken to characterize normal sediments. Interval velocities derived from reflector pull-up are then compared with interval velocities derived from RMS velocities.

The pull-up calculations are done assuming that the true vertical distance between reflectors does not change from outside to inside blank zones. The second assumption is that the rays are vertically incident and straight, such that the distance travelled equals one-way traveltime multiplied by velocity. It is also recognized that the imaging can partially smooth the velocity transition such that a discontinuity at the edge of the structure will appear as a smooth transition. The smooth bowing up rather than than a step up at the edge of the structure could be a result of the imaging horizontal resolution, which in theory after migration should be about a quarter of the dominant wavelength ($\sim$6 m).

The interval velocity from seismic pull-up is calculated for the intervals inside the blank zone centered at CDP 3550 (Fig. 3.38a), which is $\sim$600 m wide. The reflectors are relatively clear and have continuity outside the feature, and they appear bowed upwards both before and after migration, unlike those inside the blank zone centered

at CDP 3380 which appear bowed downwards before migration. The blank zone is wider than other similar features and the rays recorded at almost all offsets have passed through the center of the feature.

The amount of pull-up of each reflector inside the blank zone relative to an average reflection time outside the blank zone is shown in Fig. 3.38b as the distance between the black dashed line and the peak of each reflector. This measure only quantifies the total pull-up, which for deeper reflectors is a a result of the cumulative pull-up of the shallower reflectors. A measure of the relative pull-up for individual intervals is calculated for each interval as the traveltime ratio between the interval thickness outside the blank zones to interval thickness at the center of the blank zone where the maximum bow-up is seen, i.e., where the edge effects of the structure are a minimum as most of the reflections are from rays that travelled inside the blank zones (Fig. 3.38c). Therefore, the velocity estimate is a maximum limit characterizing the central part of the blank zone. A traveltime ratio of 1 means that the interval traveltime is the same outside and inside the blank zone, although it will be an over-estimate if the reflectors do have some physical bowing-up. A ratio larger than 1 indicates a velocity increase inside the blank zones and a ratio less than 1, a velocity decrease. The pull-up and ratio are plotted at the time corresponding to the average reflection time outside the blank zone. The uncertainty of the pull-up and the traveltime ratio are estimated from the error involved in picking the reflectors, given in Table 2.2.

The interval velocity calculated from seismic pull-up inside the blank zone (v_{in}) is proportional to the reference velocity outside the blank zones (v_{out}) and to the ratio shown in 3.38c between the interval thickness outside (dt_{out}) and interval thickness

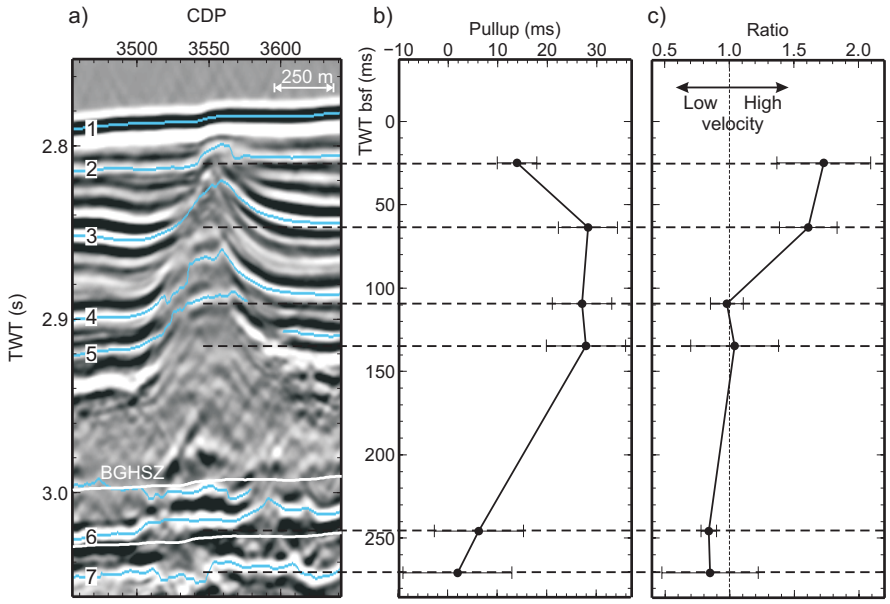

Figure 3.38: a) Blank zone showing the picked reflectors; b) absolute amount of pull-up of the reflectors inside the blank zone as compared to same reflectors outside; c) ratio of interval thickness outside to interval thickness inside.

inside (dt_{in}):

$$v_{in} = v_{out} * \frac{dt_{out}}{dt_{in}} = v_{out} * ratio. \tag{3.35}$$

If the traveltime pull-up of reflectors is real, the gradual decrease in pull-up towards the edges of the blank zone implies a gradual decrease in velocity from a maximum at the center of the blank zone to the reference velocity towards the sides.

The interval velocity from pull-up and stacking velocities inside the blank zones are shown in Fig. 3.39, where the velocities are overlain on the seismic section in Fig. 3.39a and b and compared directly in Fig. 3.39c. The reference velocity outside the blank zone is the profile derived in Section 3.2. The pull-up velocity is calculated using Eq. 3.35, where v_{out} is the reference velocity (Fig. 3.39a and Fig. 3.39c red line). For comparison, interval velocities are calculated directly from averaged stacking velocities from 3 CDP profiles inside the blank zone (Fig. 3.39b and Fig.

3.39c blue line). The uncertainties in the reference velocity and pull-up velocity are not shown because they are very small, unlike the ones derived from the stacking velocities inside the blank zone.

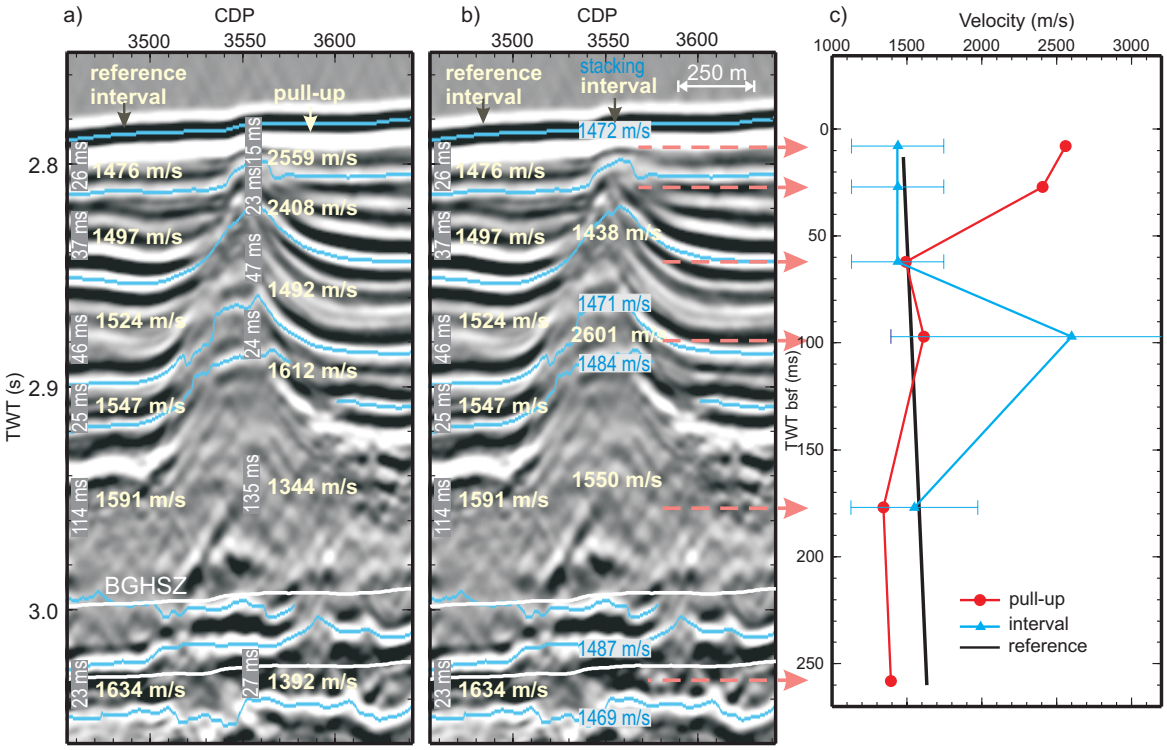

Figure 3.39: a) Interval velocities inside the blank zone (yellow) calculated from the pull-up of reflectors (Eq. 3.35) and reference interval velocity outside; b) reference velocity outside and interval velocity inside the blank zone; c) comparison between the reference velocity (black line) outside the blank zone, pull-up velocity (red line) and interval velocity (blue line) inside the blank zone.

High velocities of about 2550 m/s compared to the reference 1480 m/s are required to account for the thinner near-surface intervals that result from the bowed-up reflectors. The third and fourth interval have almost the same thicknesss outside and inside the blank zone, resulting in similar interval velocity. The large interval through the chaotic zone is 0.8 times thicker inside than outside, which implies a velocity decrease of about 250 m/s. The interval velocities calculated from the reflector pull-up are

compared with those derived from stacking velocities, shown in Fig. 3.39b. Because of the reduced amplitude of the reflectors inside the blank zone, stacking velocities could not be derived from the semblance analysis for all reflectors, such as the shallower ones inside the larger blank zone. Therefore, the interval velocity for these layers is derived as an average velocity of more layers. Because of the large variation in velocities inside the blank zone, the stacking velocities shown in Fig. 3.39b are an average of 3 CDP profiles (∼150 m in width) from the center of the feature. The interval velocity between the seafloor and the top of the fourth layer is 1438 m/s, followed by a high velocity of 2601 m/s in the fourth interval. The velocity in the thick chaotic interval is 1550 m/s.

There is clearly a difference between the interval velocities from these two methods as shown in Fig. 3.39. The pull-up gives high velocities toward the seafloor whereas stacking velocities give high velocities at greater depth. Interval velocities can be as high as 2000 m/s close to the seafloor at some CDP locations, as shown in the gridded plot of interval velocities in Fig. 3.40c, derived from the RMS velocities in Fig. 3.40b. There is a great degree of lateral heterogeneity in the velocity distribution.

Each method for estimating velocity anomalies inside the blank zones relative to outside involves a number of assumptions and results in different errors. The main assumption for the pull-up method, that the pull-up is only a velocity effect, likely involves the largest error. This error is much larger than the computation errors involved in the pull-up velocity estimation. For the pull-up velocity method, the interval velocity and its uncertainty inside the blank zones are dependent on velocities from outside the blank zones. The uncertainty of the reference profile is very small.

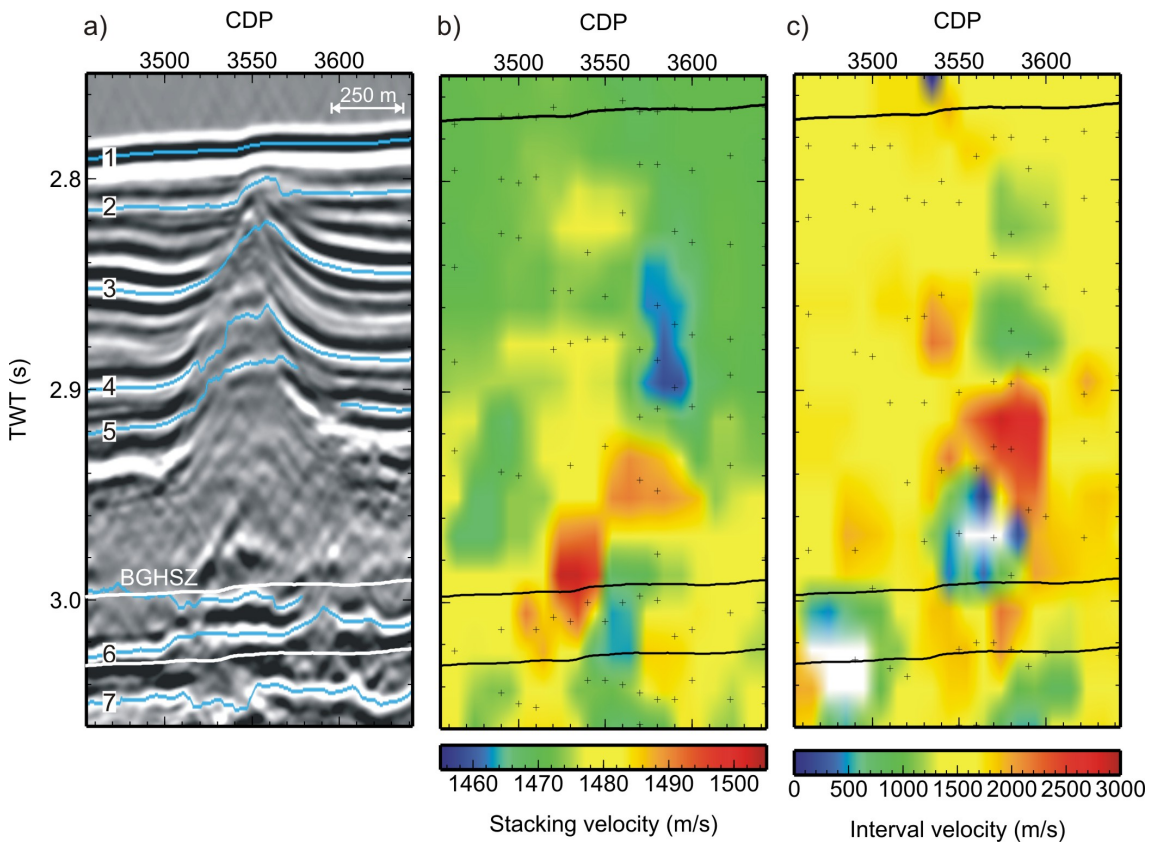

Figure 3.40: a) Blank zone showing the picked reflectors; b) RMS (stacking) velocity; c) interval velocity.

In addition, the velocity from pull-up is a maximum estimate for the central part of the blank zone. Using the same assumptions and calculations, the velocity would be decreasing towards the sides of the blank zones. However, the gradual reduction of pull-up towards the edges could also be an imaging effect, where the edges of the reflectors result from rays that have travelled through both inside and outside of the blank zones.

3.4 Discussion

In this chapter we investigated different ways to calculate interval velocities, to compare the velocities in the blank zones with areas outside of the blank zones. Inter-

val velocities from unconstrained Dix inversion have very scattered values and large estimated uncertanties for individual profiles, especially when the stacking velocities decrease with depth. Values as high as 3000 m/s are obtained above the BGHSZ and unrealistically low velocities below the BGHSZ. The uncertainties can be reduced by adding velocity profiles together to calculate a mean result, assuming little lateral variation in sediments. The mean is considerably closer to the correct model when averaged over at least 20 profiles (without any vertical averaging), but is still biased toward lower velocities due to the non-linear relationship between stacking velocities and interval velocities. This occurs especially at shallower depths where the stacking velocity does not increase rapidly or where it decreases with depth. This situation reflects a small gradient in the stacking velocities with traveltime as compared to a larger standard deviation. One way to reduce the bias to obtain more accurate estimates is to average squared interval velocities and then to take the square root of the mean. The mean of a number of velocity profiles is shown to be more accurate than single profiles. In a synthetic case, where there is no vertical averaging, the accuracy of the mean reaches a plateau after 10 velocity are added. In a real case, where the velocity picks are on an irregular grid and averaged also vertically, at least 15 profiles should likely be added to obtain the same accuracy. There are on average 10 velocity profiles inside the blank zones, since this number is limited by the CDP spacing and the width of the zone. The mean velocity profiles inside the blank zones calculated using the root-mean of squared interval velocity approach has a positive velocity anomaly of 30% above the BGHSZ, and a negative anomaly of 65% below the BGHSZ, as compared to the velocity mean from outside these blank zones. These

anomalies are interpreted as being due to high-velocity hydrate over low-velocity free gas.

An alternative method to obtain interval velocities is regularized inversion, where additional constraints are added to the inversion. The inversion is not used to stabilize an ill-conditioned problem because this can be avoided by using a smaller dataset (i.e., less layers). This approach is different from solving the unconstrained Dix equation, where the data are fit exactly. The stacking velocities are inverted by imposing a smoothness constraint on the squared interval velocities and fitting the observed data to a statistical level determined by the noise on the stacking velocity data. The noise on the stacking velocities is estimated from the lateral scatter along the shotline. Some scatter likely results from real changes in sediment properties above and below the BGHSZ within blank zones due to the presence of gas hydrate and free gas. Therefore, fitting the data to a level of noise which is less than the data scatter, allows for some interval velocities have significant anomalies. The velocity anomalies estimated from the regularized inversion are not as large as those from the unconstrained inversion because the smoothness constraint reduces rapidly oscillating velocities. Inside the blank zones, the individual velocities above the BGHSZ are as high as 2000 m/s, with a mean up to 1800 m/s. Negative and very low interval velocities are avoided below the BGHSZ, and the mean is as low as 1300 m/s. The uncertainty of the regularized solution is greatly improved compared to the unconstrained solution; however, the error values derived from the model covariance matrix should be carefully interpreted, because, like the solution, they depend on the regularization parameter, chosen to give an appropriate misfit to the data.

The Bayesian inversion gives a more accurate uncertainty of the interval velocities and layer thickness by accounting for the uncertainty of both stacking velocity and traveltime. Both this method and the analytical solution of *Hajnal and Sereda* (1981) show that the interval velocity uncertainty increases with increasing uncertainty in stacking velocity and by decreasing the layer thickness. The velocity uncertainty of a layer with a decreasing velocity can be accurately determined with the Bayesian inversion, unlike the analytical solution. The velocity uncertainty of such layers is much larger than where the velocity increases uniformly with depth. Negative velocities are avoided in the Bayesian inversion because the model estimates have pre-defined bounds.

A semi-independent measurement of interval velocity inside the blank zones is calculated from the reflector pull-up compared with sediments outside the blank zones. This results in a 60-70% velocity increase compared to the reference velocity just below the seafloor in the blank zone at CDP 3490-3600. These velocities are higher than those from stacking velocities at these shallow depths. This disagreeement implies that the pull-up is not entirely a result of high velocity material such as gas hydrate. There is likely some physical bowing of reflectors and structural deformation resulting from possible faulting, near the seafloor on this blank zone.

Chapter 4

Gas Hydrate and Free Gas Saturation from Seismic Velocity

Seismic velocities derived in Chapter 3 are used to determine gas hydrate saturations using the effective porosity reduction model and rock-physics model. The time averaging equations are used only for a quick comparison. The effective porosity model is the easiest to apply and does not use as many parameters as the rock physics model. Free gas saturations are derived using the Biot-Gassmann theory. Positive and negative velocity anomalies associated with the blank zones above and below the BGHSZ are interpreted to result from gas hydrate and free gas bearing sediments, respectively, as compared to areas outside them. Thus, the gas hydrate and free gas saturations are a relative estimate; however, as discussed earlier, the areas outside the blank zones are believed to contain only very small amounts of gas-hydrate and free gas.

4.1 Effective porosity reduction model and gas hydrate saturation

In the porosity reduction model, the hydrate effectively reduces the porosity according to a porosity-velocity relation (*Hyndman et al.* 1993, Eq. 1.1). Applying the reference velocity obtained from the inversion with a smoothness constraint for outside the blank zones to this velocity-porosity relation gives the derived porosities shown in Fig. 4.1.

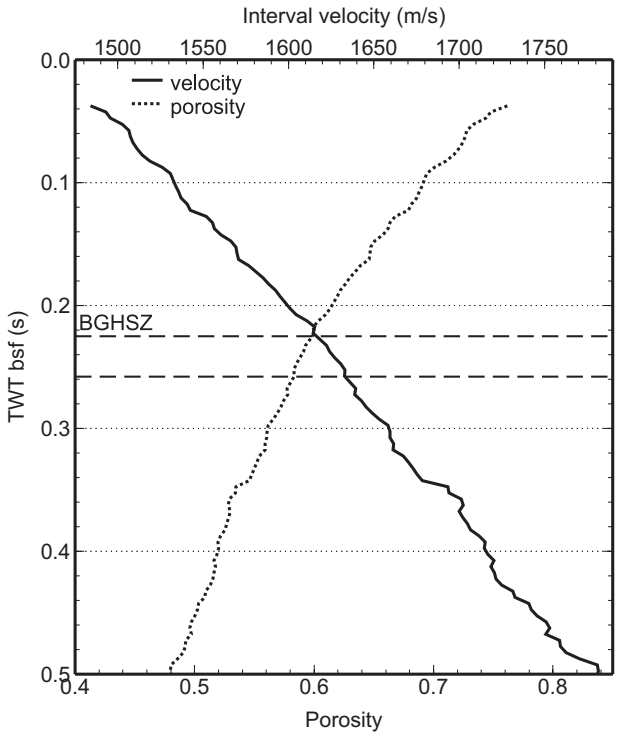

Figure 4.1: Interval velocity outside the blank zones for a smooth model and derived porosity with the *Hyndman et al.* (1993) velocity-porosity relationship (Eq. 1.1).

The gas hydrate saturations shown in Fig. 4.2 are derived from the different mean velocity profiles for blank zones located at CDP 3360-3400, CDP 3490-3600 and CDP 6015-6115 shown in Figs. 3.28, 3.29 and 3.30, respectively. The hydrate saturation

generally increases from zero at ∼50 ms bsf to about 20-40% at ∼150 ms bsf, and then decreases towards the BGHSZ. Due to the resolution of the seismic velocity of the order of tens of meters, compared to the size of gas hydrate veins, nodules and fractures of the order of centimeters, the estimated gas hydrate saturation is only a measure of the bulk average concentration of gas hydrate.

Theoretical curves for gas hydrate saturation as a function of velocity were calculated for different sediment porosities (Fig. 4.3) and compared with results from the blank zones. If the gas hydrate were cementing the grains, the gas hydrate saturations should be lower than indicated by this method, and if gas hydrate were floating inside the pore space, the gas hydrate saturations should be higher.

The velocity estimated from reflector pull-up in Sec. 3.3 is translated into interval velocity using the same approach as above. Gas hydrate saturations are inferred to be 45-60% in the top two layers.

The total uncertainty in the gas hydrate saturation estimate results from the uncertainty in the velocity measurements themselves from inside the blank zones and the reference, the assumption that the sediments are laterally homogeneous and characterized by the reference velocity and the effective medium model itself. The uncertainty of the reference velocity is not accounted for in this study; however, it affects very little the results because it is very small. The minimum and maximum estimates of velocity are shown in Figs. 3.28, 3.29 and 3.30 by the dashed and dotted lines, respectively. The uncertainty of the interval velocity mean is expressed as the standard error of a number of measurements in a vertical window that is sliding down in time. Thus, the standard error quantifies the scatter in the data. In

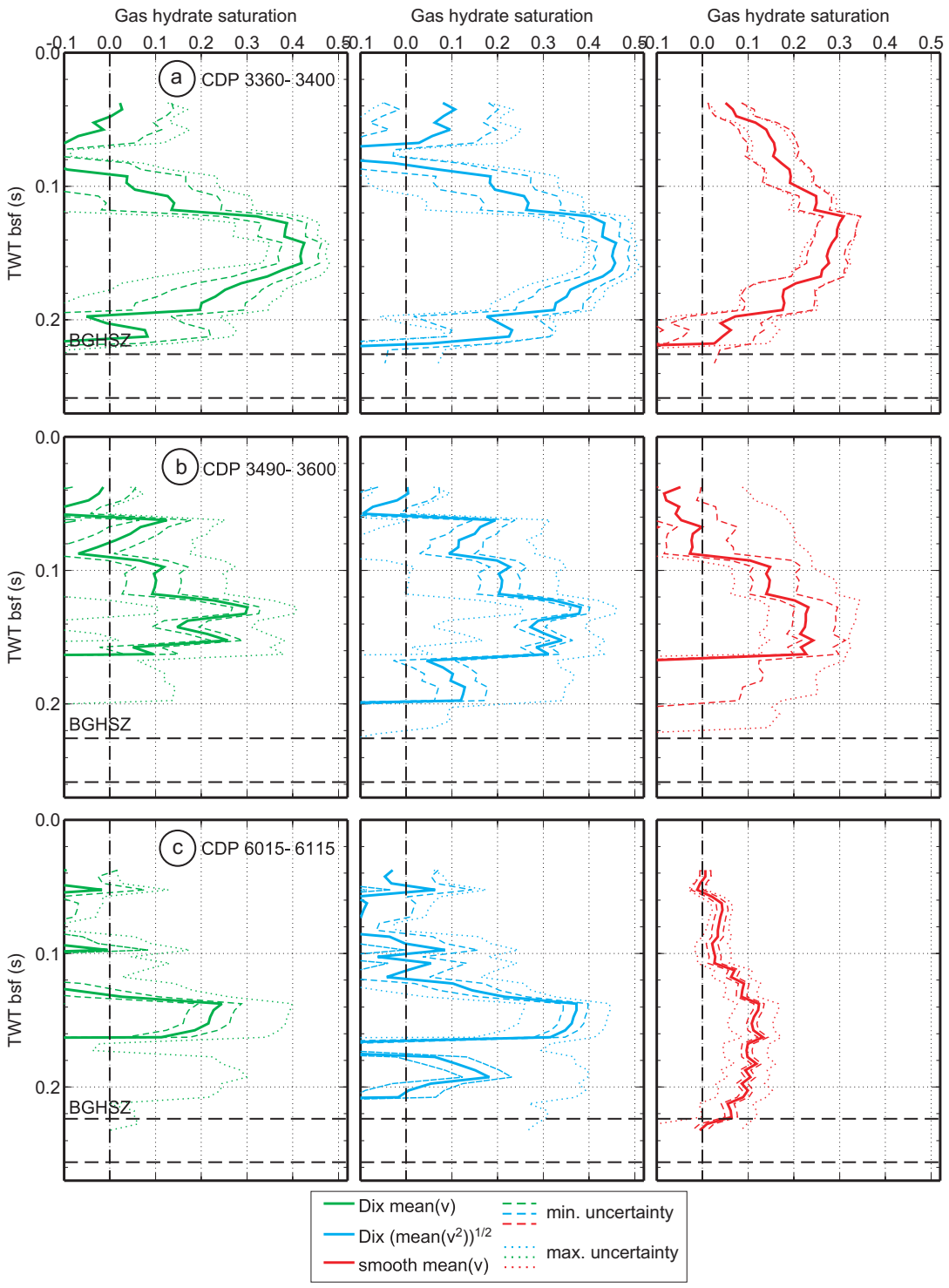

Figure 4.2: Gas hydrate saturations calculated from velocities for blank zones at: a) CDP 3360-3400 shown in Fig. 3.28, b) CDP 3490-3600 shown in Fig. 3.29, c) CDP 6015-6115 shown in Fig. 3.30. Minimum and maximum uncertainty in the estimates derived from the velocity uncertainties are shown by the dashed and dotted lines, respectively.

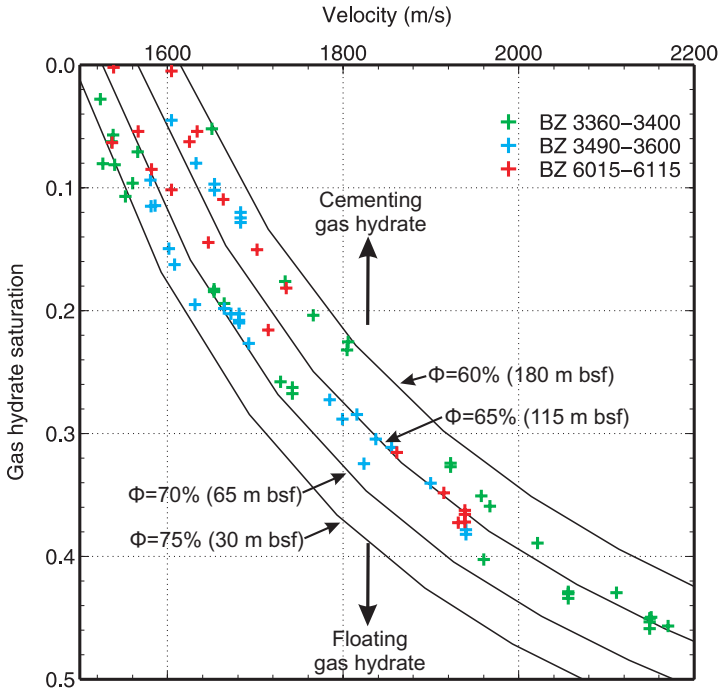

Figure 4.3: Gas hydrate saturation as a function of velocity at different backgroung sediment porosities (ϕ), using the effective porosity reduction model. Crosses indicate the estimates from the blank zones studied.

the blank zones, part of the scatter is likely a result of large variation in physical properties of the sediments, where some velocities are high due to gas hydrate and some are much lower characterizing hydrate-free sediments. Therefore, to exclude the influence of real physical changes from the total standard error, a minimum, more realistic standard error is taken to be linearly increasing with depth, eliminating the larger values around the BGHSZ. The gas hydrate saturation maximum and minimum uncertainty are thus calculated from both the mean velocity standard error (shown in Figs. 3.28, 3.29, 3.30 d)) and its minimum estimate, respectively. There is additional uncertainty due to the velocity-porosity relation, derived for clastic sediments in the Nankai and Cascadia accretionary prisms. The trend is derived from measured sonic velocities and porosities on the range 1.6-2.2 km/s and 35%-60%, respectively. It is

assumed that the sediments in the Ulleung Basin which are similar turbidites, have approximately the same porosity-velocity relation. No mean velocity larger than 2.2 km/s was measured in the blank zones, so the velocity-porosity relation is only extrapolated for depths shallower than the BGHSZ, for sediment velocities between 1470 m/s and 1600 m/s. Variations in lithology would deviate from this velocity-porosity relation and would introduce a degree of uncertainty. However, there is no significant difference between sediments inside and outside blank zones. If carbonates are present in the sediments, they would increase the seismic velocity, and thus the hydrate saturation would be an overestimate. If free gas is present in the sediments above the BGHSZ, it will decrease the velocity, and give an underestimate of the gas hydrate saturation. If hydrate cements the grains, especially at higher saturations, the hydrate saturation estimates should be lower, because the observed high velocity results from an additional increase in the elastic moduli due the stiffening of the frame, along with the hydrate itself.

4.2 Rock physics model and gas hydrate saturation

Constant gas hydrate saturations calculated using the pore-physics model (*Helgerud et al.* 1999) are shown in Fig. 4.4.

Some of the model parameters need to be calibrated such that the calculated liquid-saturated sediment velocity (i.e., hydrate-free) is close to the reference interval velocity from outside the blank zones above the BGHSZ (220 ms bsf/ 170 m bsf). The interval velocity at the surface implies very low surface porosities. The linear increase in interval velocity with depth implies a linear decrease in porosity with depth, which

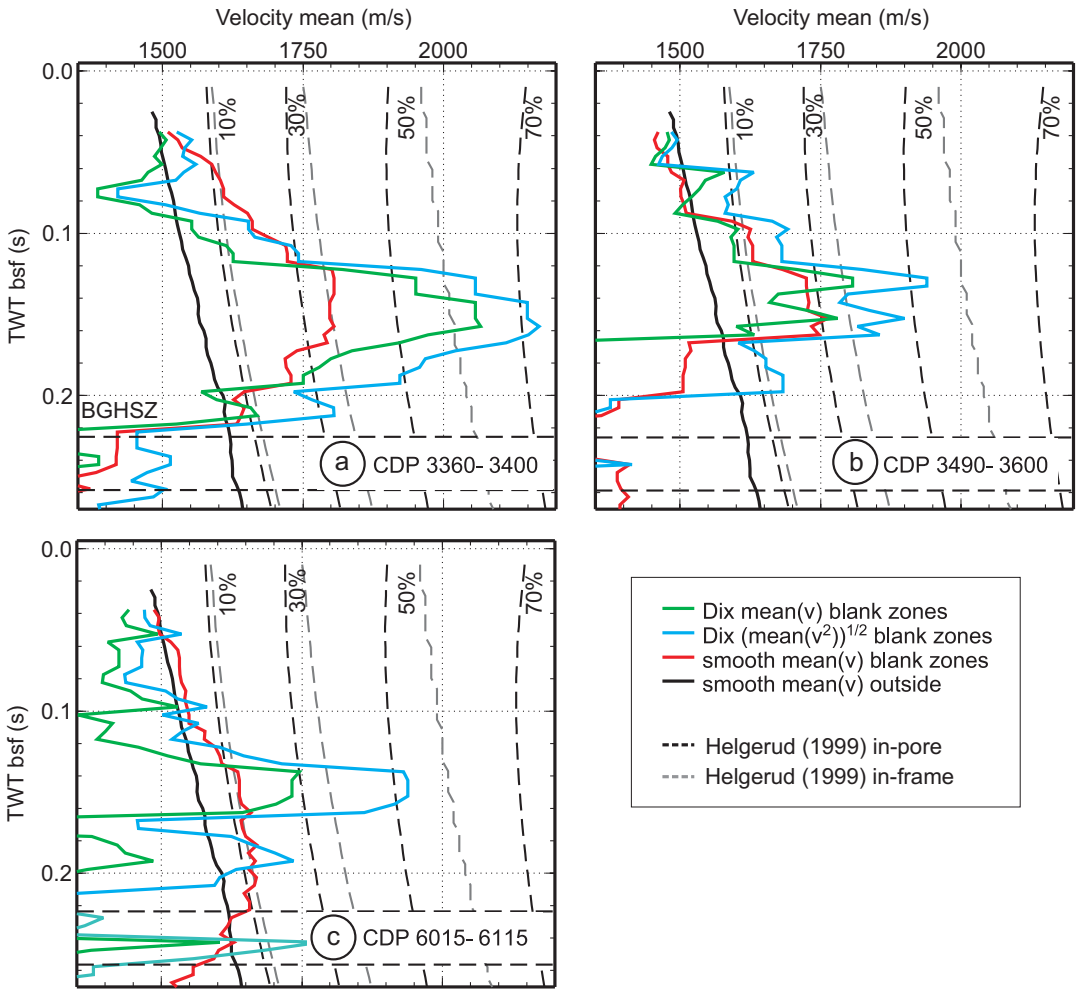

Figure 4.4: Theoretical curves for gas hydrate saturation calculated using the *Helgerud et al.* (1999) rock-physics model.

is difficult to fit using Athy's law (*Athy* 1930), which relates porosity to depth with an exponential. The compressional parameter is calibrated to 500 m^{-1} and surface porosity to 85%. The difference between the calculated hydrate-free velocity and the reference interval velocity decreases from 50 m/s at the surface to 0 m/s at 100 m bsf (130 ms bsf), below which the velocities match. Therefore, gas hydrate saturations are thought to be best estimated at depths below 100 m down to 170 m at the BGHSZ.

The increase in velocity above the BGHSZ inside the blank zones compared to the liquid-saturated sediment velocity from the rock-physics model implies gas hydrate

saturations that are on average 15-20% higher than the ones estimated with the effective porosity reduction model. Gas hydrate saturations estimated from the three-phase weighted equation (*Lee et al.* 1996b) are half as those from the effective porosity model at smaller gas hydrate saturations and 10% smaller at higher gas hydrate saturations.

4.3 Free gas saturations

Free gas saturations have been estimated using the Biot-Gassmann theory (Appendix A).

Fig. 4.5 shows free gas saturations calculated as a function of P-wave velocity for conditions characteristic of the depths immediately below the predicted BGHSZ on line 063.

The shear modulus and matrix compressibility are adjusted to fit the measured P-wave velocity for sediments with no free gas, and its corresponding S-wave velocity calculated with the *Castagna et al.* (1985) relation for clastic sediments ('mud rock line'). The shear modulus μ is calculated from the S-wave velocity equation A.10, using the no-free gas density of sediments below the BGHSZ, $\rho = 1650$ kg/m^3 (*Kim et al.* 2008a). The S-wave velocity is first calculated from the P-wave velocity using the *Castagna et al.* (1985) relation between V_P and V_S:

$$V_P = 1.16V_S + 1360, \tag{4.1}$$

where V_P and V_S are in m/s. The no-free gas P-wave velocity below the BGHSZ, V_P

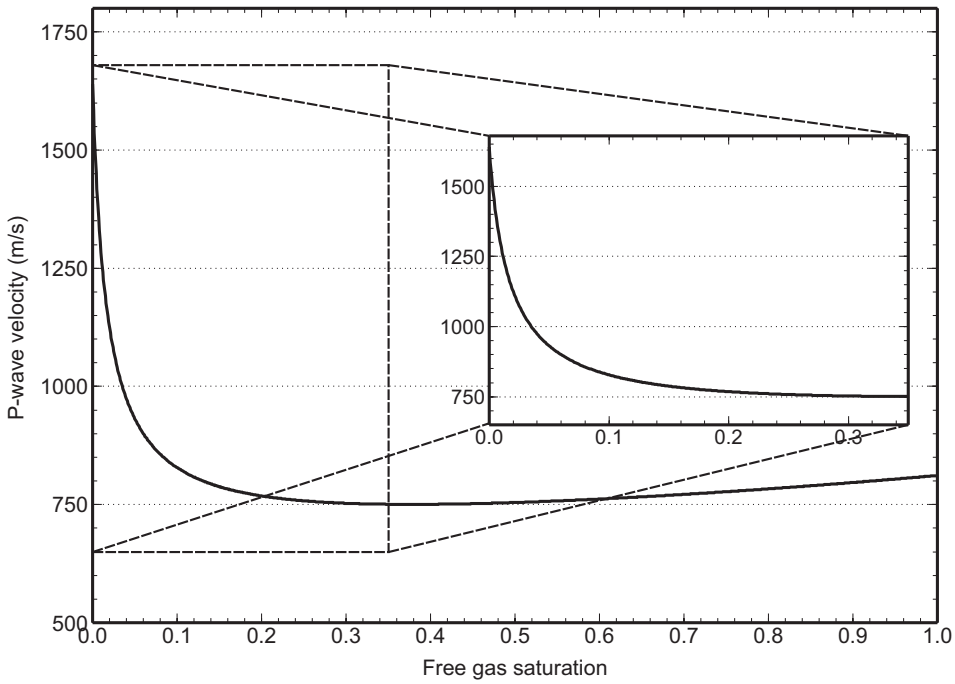

Figure 4.5: Effect of free gas saturation on P-wave velocity using the Biot-Gassmann theory for sediments with a porosity of 58% and density of 1650 kg/m^3 at depths immediately below the predicted BGHSZ for line 063. The expanded inset shows the velocity decrease with increasing free gas saturation up to 35% saturation.

= 1640 m/s corresponds to a S-wave velocity V_S = 241 m/s. The calculated shear modulus is $\mu = 95.8$ MPa. It is recognized that the S-wave velocity and shear modulus are quite low, and this is because the *Castagna et al.* (1985) relation is derived from deeper sediments, and the sediments in this study are much shallower.

The bulk modulus is calculated from V_P for liquid-saturated sediments (Eq. A.9) to give the matrix compressibility C_m (Eq. A.5) of $3.5{\cdot}10^{-11}$ Pa^{-1}.

A continuous velocity decrease to values as low as 750 m/s results from a continuous increase in the free gas saturation up to 30%. At higher free gas saturations, the velocity starts increasing slowly again, due to the decrease in density at a higher rate than the decrease in bulk modulus. Thus, for velocities between 820 m/s and 750 m/s, the gas saturation cannot be determined.

However, very high gas saturations are likely to move upward though the overlying sediments. Velocities lower than 750 m/s are not predicted by the model. In one case, the mean velocity estimate from below the BGHSZ for the Dix model is lower than 750 m/s, reaching 500 m/s. However, as discussed earlier, this velocity estimate is biased to low velocities.

Free gas saturations derived from interval velocities below the BGHSZ from inside the blank zones (Figs. 3.28, 3.29 and 3.30) are shown in Fig. 4.6. The estimates derived from the mean of Dix velocities (green line) are an overestimate, because it was shown that these values tend to be biased to low velocities. The estimates probably lie between the other two estimates (blue and red curves), i.e., saturations less than about 5%.

The uncertainty in the free gas saturation estimates results from the same type of errors as those for the gas hydrate saturations. There is an additional degree of uncertainty introduced by the fixed constants, such as the compressibilities and the calculated shear modulus.

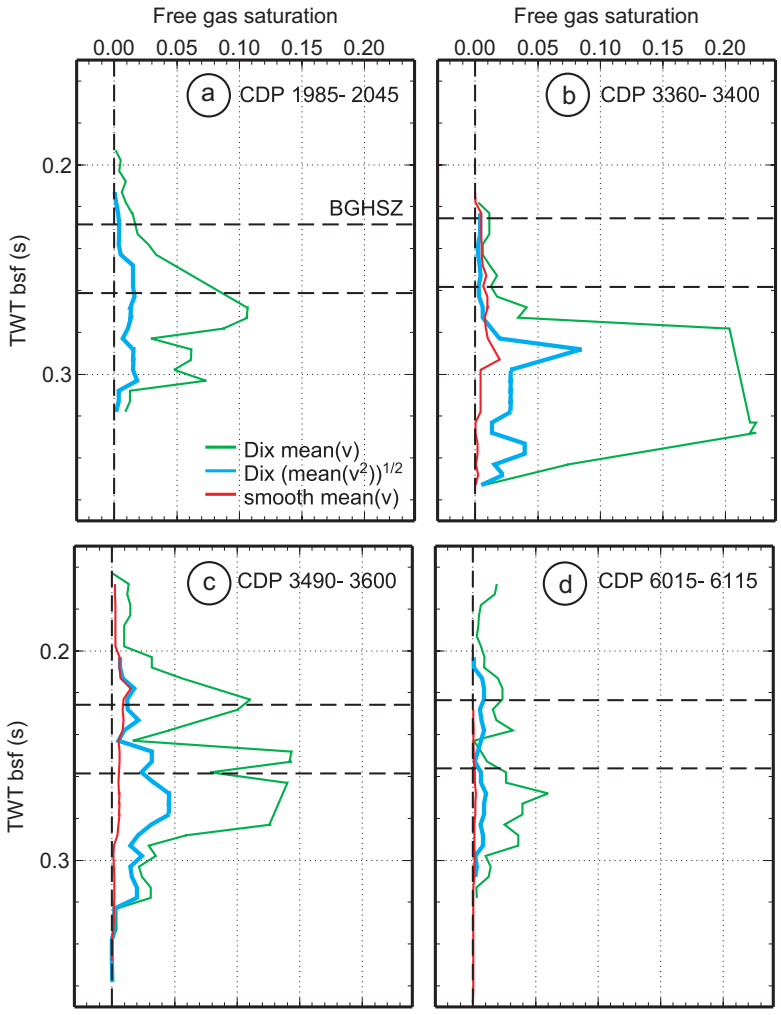

Figure 4.6: Free gas saturation calculated from interval velocities in Figs. 3.28, 3.29 and 3.30, based on the velocity-free gas saturation relationship shown in Fig. 4.5.

Chapter 5

Heat Flow and BGHSZ

The focus in this chapter is to estimate the depth to the BGHSZ on the main study line where there is no BSR. Changes of seismic characteristics with depth across the BGHSZ can thus be examined. For example, high velocities due to hydrate and low velocities due to gas are expected above and below the BGHSZ. Also, changes in seismic attributes are expected at that depth because hydrate and gas affect the seismic wavefield in different ways.

We use the heat flow estimates derived from BSR depths where BSRs are clear in adjacent areas to calibrate our method and input parameters for use in the main study of line 063 in the basin plain. Heat flows are estimated for 3 time-migrated seismic profiles where the BSR can be seen (lines 025, 087, 043 in 1.3). A sensitivity analysis is carried out to investigate the parameters that introduce the largest errors.

In marine gas hydrate areas, the heat flow can be estimated from the depth of the BSR, which represents the BGHSZ (e.g., *Yamano et al.* 1982, *Davis et al.* 1990, *Ganguly et al.* 2000, *He et al.* 2007). Alternatively, as in our study, where a BSR

cannot be seen, the BGHSZ can be predicted if one has knowledge of the regional heat flow (e.g., *Brown et al.* 2006, *Kim et al.* 2008b).

BSRs in the Ulleung Basin are well imaged on the continental slope and are very weak or absent in the basin plain (e.g., *Kang et al.* 2008). *Horozal et al.* (submitted) calculated the regional heat flow from the depth of the BSR identified in a large seismic dataset from the Ulleung Basin. Their heat flow estimates are between 65 and 115 mW/m^2, varying with position in the basin. The heat flow value distribution closely correlates with the bathymetry. Higher heat flow values occur in the deeper northern part of the area in water depths greater than 2000 m where crustal extension is concluded to be greatest, and lower heat flow values occur in the shallower southwestern corner of the area at water depths less than 1000 m, where there has been little recent extension. The reported values are similar to those derived from direct probe measurements, ranging from 63 to 124 mW/m^2 (KORDI, 1993, International Heat Flow Commission, 2006) and 84-130 mW/m^2 (*Kim et al.* 2008b).

5.1 Modeling Paramaters

To determine the heat flow from the depth of the BSR, the following quantities are required: a) seafloor and BSR reflection times; b) velocity-traveltime relationship to convert traveltime to depth; c) thermal conductivity-depth relationship; d) a pressure-temperature relationship that characterizes the conditions for gas hydrate stability; e) seafloor temperature. Conversely, to calculate the depth and traveltime to the BSGHZ from a regional heat flow value, one needs the above mentioned paramaters (except for the BSR reflection time), in addition to a regional value for heat flow.

The way each of these parameters is derived is discussed below.

The thickness of the GHSZ and temperature at the BGHSZ can be derived from: 1. the P-T stability conditions, and 2. the conductive heat flow equation. The thickness of the GHSZ is then converted to traveltime using a velocity-depth relation, and is shown on the seismic section.

The pressure-temperature relation at the BGHSZ assumes methane to be the dominant hydrate-forming gas and pore water salinity of standard ocean water (e.g., *Bouriak et al.* 2000). Methane is found in concentrations of more than 99% in the Ulleung Basin (*Park* 2008). The assumption of seawater salinity is not confirmed by measurements in the area, so it introduces a small degree of uncertainty in the results. The pressure-temperature relationship for the stability of methane hydrate is given by the following equation (e.g., *Bouriak et al.* 2000).

$$P_{GH} = exp((K - 0.0400^2)/(0.0014) + 0.4683), \tag{5.1}$$

where P_{GH} is the pressure at the phase boundary in MPa and K is a constant defined as:

$$K = (0.0007 \cdot T_{GH} + 0.0400)^2, \tag{5.2}$$

where T_{GH} is the temperature at the phase boundary in ${}_oC$.

The depth at the BGHSZ is defined by the intersection of the local geotherm with the hydrate stability curve. A hydrostatic pressure gradient is used in this study to link pressure to depth below the seafloor. A hydrostatic model is preferred since no

substantial overpressures are expected at shallow depths of about 200 m bsf (e.g., *Hyndman et al.* 1993, *Zwart et al.* 1996). The hydrostatic pressure is given by:

$$P_{BGHSZ} = \rho_w g d_{BGHSZ}/10^6, \tag{5.3}$$

where ρ_w is the water density, ρ_w = 1030 kg/m^3, g = 9.81 kg/m^2.

The distance from the seafloor to the predicted depth of the BGHSZ, Δd (in m) is:

$$\Delta d = d_{BGHSZ} - d_w, \tag{5.4}$$

where d_{BGHSZ} is the depth at the BGHSZ from the sea surface and d_w is the water depth. The water depth is calculated from the reflection time of the seafloor picked from the time migrated seismic section at the peak of the zero-phase seafloor reflection:

$$d_w = 0.5 \cdot v_w \cdot TWT_{sf}, \tag{5.5}$$

where v_w is the water velocity, taken as 1485 m/s, and TWT_{sf} is the traveltime at the seafloor.

The thickness of the GHSZ and temperature at the BGHSZ are included in the equation for conductive heat flow transfer assuming a linear increase of temperature with depth:

$$hf = 1000 \cdot k \cdot \frac{t_{BGHSZ} - t_{sf}}{\Delta d}, \tag{5.6}$$

where hf is the heat flow in mW/m^2, k is the thermal conductivity in W/mK,

t_{BGHSZ} and t_{sf} are the temperature at the BGHSZ and seafloor, respectively in ^0C. A constant seafloor temperature of 0.2^{o}C is used (*Kim et al.* 2008b).

An empirical equation derived by (*Davis et al.* 1990) for sediments of the accretionary prism in Northern Cascadia is used in this study to calculate the thermal conductivity as a function of depth. This region has similar turbidite sediments to Ulleung Basin. The thermal conductivity increases slightly with depth as porosity decreases. It is given as a function of depth below the seafloor:

$$k = 1.07 + 5.86 \cdot 10^{-4} \cdot \Delta d - \Delta d^2 \cdot 3.24 \cdot 10^{-7}, \tag{5.7}$$

where k is the thermal conductivity in W/mK (*Davis et al.* 1990).

This equation is used because there are no deep conductivity data available in the Ulleung Basin. Measured thermal conductivities for the upper few meters are on the range of 0.82-0.95 W/mK (*Kim et al.* 2008b). The calculated surface conductivity from Eq. 5.7 is 1.07 W/mK, which is about 20% higher. Measurements of thermal conductivities of sediments of up to about 300 m bsf in the Yamato and Japan basins are about 1.0 W/mK (*Nobes et al.* 1992). *Horozal et al.* (submitted) use this value in their study.

Thermal conductivities are also influenced by the presence of gas hydrate in sediments. Gas hydrate has a thermal conductivity similar to that of water, which is 0.58 W/mK. Hydrate that replaces pore fluid therefore is expected to have only a small effect. However, the presence of considerable saturations of hydrate in sediments can both increase and decrease significantly the bulk thermal conductivity, depending on

the type of sediment (*Santamarina and Ruppel* 2008). Generally, the concentration of of gas hydrate outside of the seismic blank zones is not large enough to significantly affect the thermal conductivity.

The temperature at the BGHSZ and the thickness of the GHSZ can be calculated by solving the equations relating them: Eqs. 5.6 and 5.7 for the regional geotherm and Eqs. 5.1 - 5.5 for the hydrate stability.

The TWT between the seafloor and the BGHSZ (ΔTWT in s) is then calculated:

$$\Delta TWT = 2 \cdot \frac{\Delta d}{V_{BGHSZ}}, \tag{5.8}$$

where V_{BGHSZ} is the average velocity between seafloor and BGHSZ, calculated using the equation from Table 3.2 for sediments outside the blank zones:

$$V_{BGHSZ} = 1450 + 934 \cdot \frac{\Delta TWT}{2}, \tag{5.9}$$

where V_{BGHSZ} is in m/s.

5.2 Results

5.2.1 Heat Flow from the Depth of the BSR

The heat flow is determined from the depth of the BSR identified on limited sections of 3 seismic profiles. The BSR is indicated by the yellow curve for line 043 (Fig. 5.1) and line 087 (Fig. 5.2) from the central basin plain and for line 025 (Fig. 5.3) from the south-western basin slope (see Fig. 1.3 for location). The heat flow

values are similar to those obtained by *Horozal et al.* (submitted). The parameters calculated directly from the depth of the BSR are shown by the blue curves in Fig. 5.4 and the average parameters are shown in Table 5.1. The calculated heat flow deviation from the mean value across each line is approximately ± 5 mW/m^2, which is likely mainly the result of the variability of calculated thermal conductivity, which is very sensitive to small changes in depth. The main changes in depth are due to the error in picking the BSR, which is about ± 5-10 ms, as the error in picking the seafloor is about 1 ms.

Calculated parameters	Line 043 (Fig. 5.4a)	Line 087 (Fig. 5.4b)	Line 025 (Fig. 5.4c)
Heat flow (mW/m^2)	111	119	104
t_{BSR} (^{0}C)	18.32	18.69	15.99
P_{BSR} (MPa)	20.91	21.88	15.83
TWT_{BSR} (s)	2.776	2.906	2.101
ΔTWT (s)	0.236	0.226	0.219
Depth BSR(m)	2069	2165	1567
Δd (m)	183	175	169
k (W/mK)	1.21	1.11	1.12
v (m/s)	1553	1548	1545
$\Delta T/\Delta d$ (^{0}C/km)	100	107	94

Table 5.1: Averaged parameters over limited sections of lines 043, 087, 025, where the BSR can be identifed, calculated directly from the depth of the BSR. The average corresponds to the values shown for every CDP in Fig 5.4 by the blue curve.

The heat flow appears to depend on water depth, as shown in Fig. 5.5 and found by *Horozal et al.* (submitted). There is higher heat flow on lines 043 and 087 from the basin plain, with water depths between 1.75 and 2.05 km, with average values of 111 and 119 mW/m^2, respectively. Lower heat flow with an average of 104 mW/m^2 are found on line 025 from the basin slope, where the water depths are between 1.25

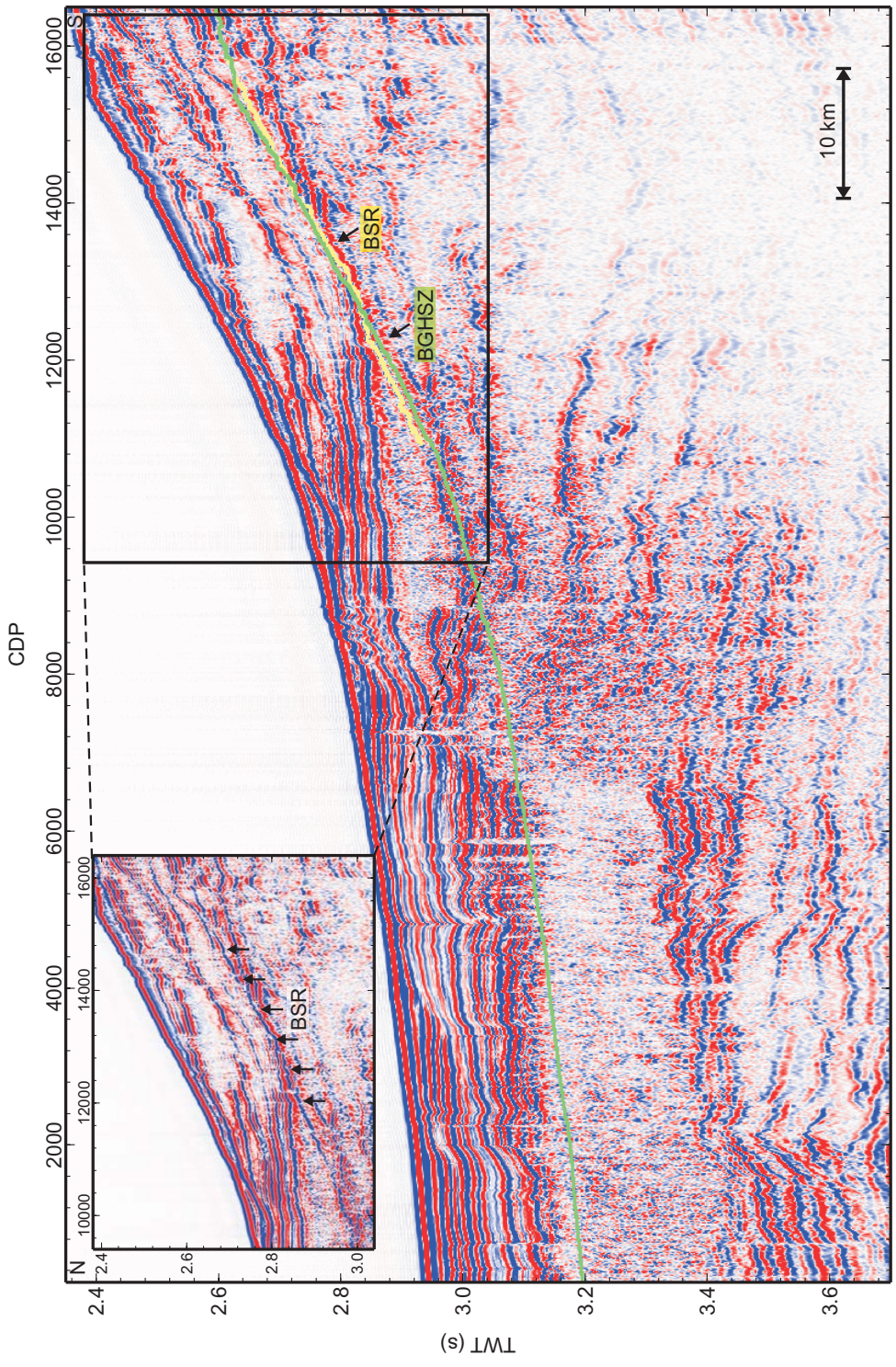

Figure 5.1: Time migrated line 043 from the central basin plain (see Fig. 1.3 for location) with a BSR visible between CDP 11000-15000, marked by the yellow curve. The BGHSZ shown by the green curve is calculated using a constant heat flow of 111 mW/m^2, which is the average heat flow calculated from the depth of the BSR.

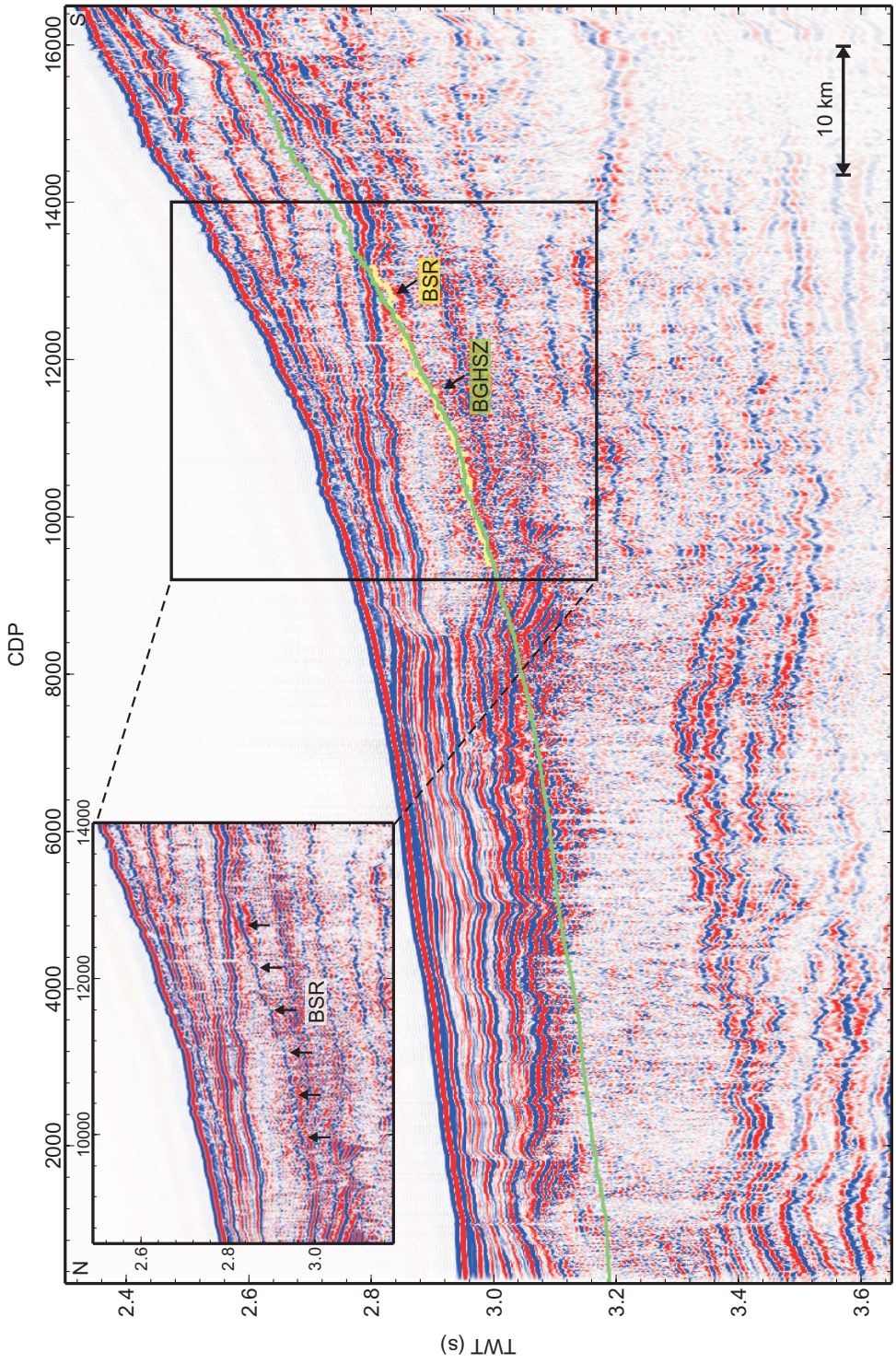

Figure 5.2: Time migrated line 087 from the central basin plain (see Fig. 1.3 for location) with a BSR visible between CDP 9000-13000, marked by the yellow curve. The BGHSZ shown by the green curve is calculated using a constant heat flow of 119 mW/m^2, which is the average heat flow calculated from the depth of the BSR.

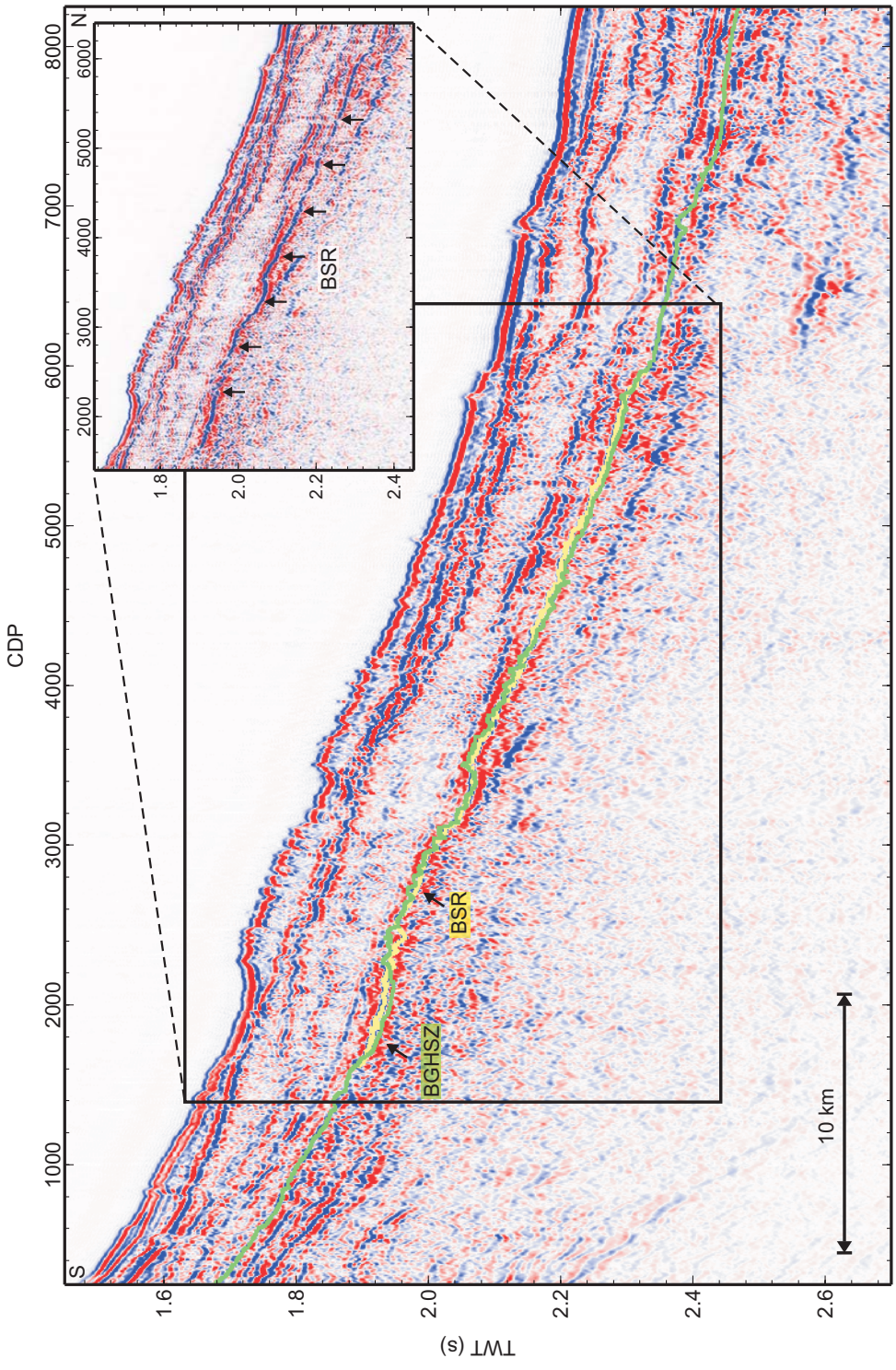

Figure 5.3: Time migrated line 025 from the south-western basin slope (see Fig. 1.3 for location) with a BSR visible between CDP 1500-5500, marked by the yellow curve. The BGHSZ shown by the green curve is calculated using a constant heat flow of 104 mW/m^2, which is the average heat flow calculated from the depth of the BSR.

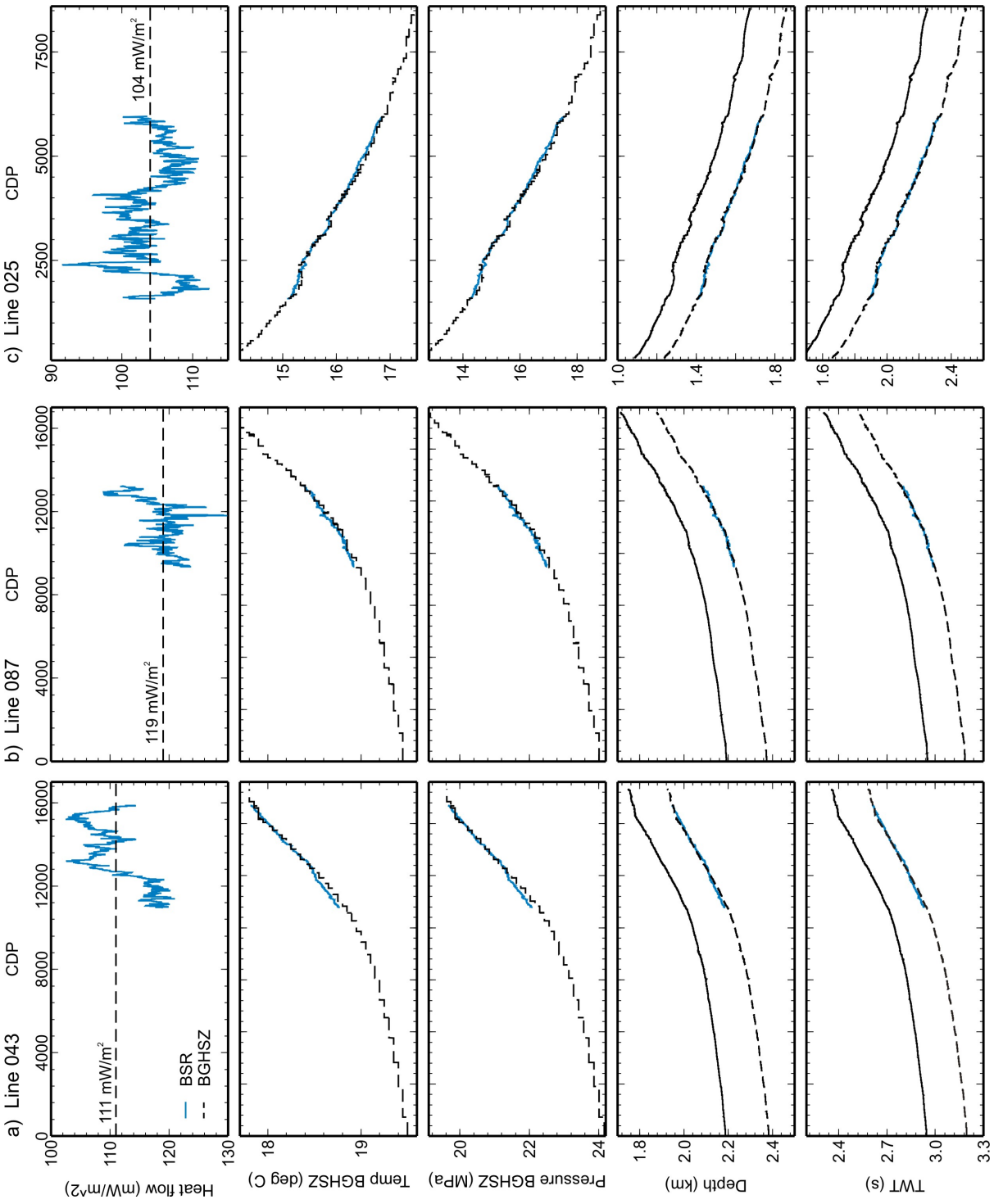

Figure 5.4: Calculated parameters directly from the BSR depth on sections of lines 043, 087 and 025, shown by the blue curves (see Fig. 1.3 for location). Predicted BGHSZ parameters along the entire line shown by the dashed curves, from the corresponding average heat flow shown in top panel.

and 1.55 km. The higher heat flow could be expected in the deep water basin plain, because this is where the maximum basin extension and crustal thinning took place from late Oligocene to early Miocene (*Yoon and Chough* 1995), and, therefore, where the extensional heating is greatest. The lower heat flow on the slope of the basin could be partly the result of the blanket cooling by the greater thickness of sediment deposition on the slope.

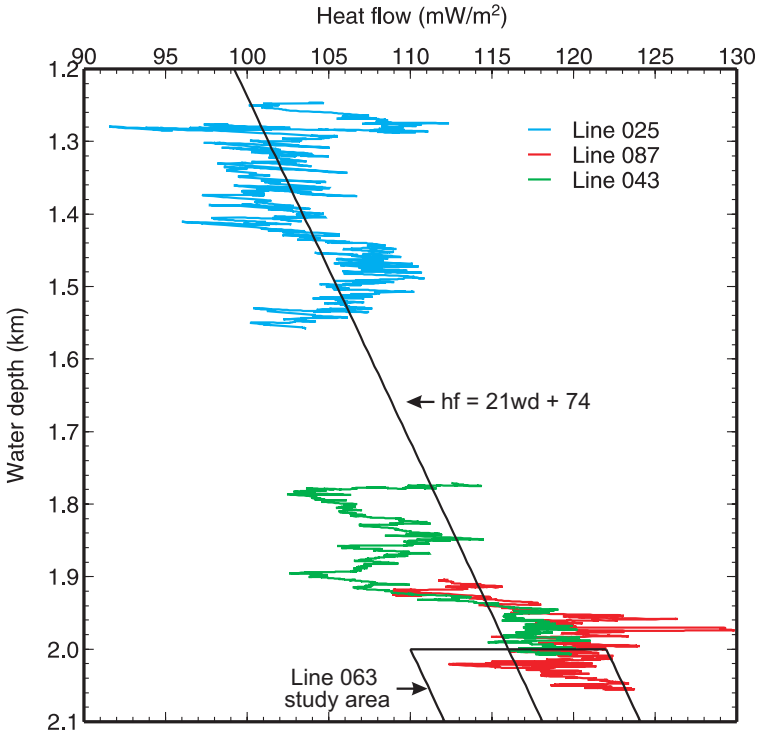

Figure 5.5: Heat flow versus water depth derived from the depth of the BSR on lines 025, 087, 043, used to calibrate the heat flow on study line 063; hf: heat flow, wd: water depth.

The average heat flow for each of the 3 line sections is used to predict the BGHSZ across the entire line. The parameters calculated at the BGHSZ are shown by the dashed black lines in Fig. 5.4, and the traveltimes are shown by the green curves in Fig. 5.1, 5.2, 5.3. The average parameters across the BGHSZ are summarized in Table 5.2.

Calculated parameters	Line 043 (Fig. 5.4a)	Line 087 (Fig. 5.4b)	Line 025 (Fig. 5.4c)
Heat flow (mW/m^2)	111	119	104
t_{BGHSZ} (^{0}C)	18.92	18.86	16.14
P_{BGHSZ} (MPa)	22.53	22.38	16.20
TWT_{BGHSZ} (s)	2.982	2.965	2.144
ΔTWT (s)	0.243	0.227	0.222
Depth BSR(m)	2223	2208	1599
Δd (m)	189	176	171
k (W/mK)	1.16	1.16	1.15
v (m/s)	1556	1548	1546
$\Delta T/\Delta d$ (^{0}C/km)	100	107	94

Table 5.2: Averaged parameters over lines 043, 087, 025, calculated from a constant regional value for the heat flow. The average corresponds to the values shown for every CDP in Fig. 5.4 by the dashed black line.

5.2.2 Estimates and Uncertainties of the BGHSZ from Heat Flow

If the heat flow is related to water depth as shown in Fig. 5.5, then the water depths from line 063, which are 2.0-2.1 km, should correspond with a heat flow between 110 and 125 mW/m^2. *Horozal et al.* (submitted) calculate a heat flow of about 105 $\pm$ 5 mW/m^2 in the area of line 063, from a large seismic dataset. Heat flow estimated in the basin from probe measurements of thermal conductivity and geothermal gradients are in the range of 84-130 mW/m^2, which is similar to the average in the other two basins of the East Sea, Japan and Yamato basins.

The traveltime predicted for a set of initial parameters and conditions for line 063 is shown on all plots in this study for heat flow of 105 and 120 mW/m^2. The depths for the BGHSZ are shown for a comparison for a heat flow of 90, 105 and 120 mW/m^2 in Fig. 6.1 for the main line 063. The thickness of the GHSZ is less at shallower water depth even for a constant heat flow as a result of the lower pressure.

The sources of error in calculating the conditions at the BGHSZ include: i) uncertainties in the velocity profile, including possible lateral velocity variations, which could result mainly if hydrate were present in the sediments; ii) local variations in the heat flow and not accounting for an advective heat flow transfer; iii) uncertainty in the thermal conductivity and ignoring the possible effect of gas hydrate; iv) the use of a hydrostatic increase in pressure with depth; v) error in picking the seafloor; vi) assumption of seawater salinity when calculating the phase boundary condition; vii) constant seafloor temperature. In this section we investigate the influence of some of the most important sources of error. The depth, traveltime, pressure and temperature at the BGHSZ are first calculated from a set of initial parameters (i.e., heat flow and seafloor temperature) and relations (i.e., thermal conductivity-depth, velocity-depth) thought to be representative for the area. The values for the entire profile are indicated by the black line, and the average value across the profile is given in Table 5.3 column a. A realistic degree of uncertainty in each of these parameters and relations is introduced to see how this affects the calculated parameters. The results are shown by the orange and red lines in Fig. 5.6; the average value for each parameter across the line and its error (percentage change from the initial results in Table 5.3 column a) are given in Table 5.3 column b-e.

The initial parameters and relations used are: a heat flow of 105 mW/m^2, average thermal conductivity for sediments up to the depth of the BGHSZ calculated using Eq. 5.7, a velocity-traveltime trend derived from seismic data for line 063, and a constant seafloor temperature of 0.2^{0}C. The heat flow and seafloor temperature remain constant in all cases, except b) and e), whereas the average thermal conductivity and

velocity change each time the depth to the BGHSZ changes. In case c) and d) the thermal conductivity and velocity, respectively are increased to see how they affect the different parameters.

In case a) where the initial parameters are used, the average thermal conductivity is 1.13 W/mK and average seismic velocity is 1563 m/s for sediments in the upper 202 m bsf (or 258 ms bsf). These conditions imply a thermal gradient of 94^0 C/km. In situ measurements of thermal conductivity and geothermal gradient in the Ulleung Basin are 0.82-0.95 W/mK and 103-137 mK/m, respectively (*Kim et al.* 2008b).

The influence of a constant decrease of 5 mW/m^2 on the different parameters is shown by case b) in Table 5.3. The depth of the BGHSZ is 12 m deeper than in case a), associated with a slight increase in pressure and temperature at the BGHSZ, average thermal conductivity and velocity of sediments for a thicker GHSZ.

The largest source of error appears to be introduced from the uncertainty in the thermal conductivity. The thermal conductivity is derived from an empirical relation for sediments from the Cascadia margin. There, the upper 2 km of sediments consists of Pleistocene turbidities (*Davis and Hyndman* 1989), similar to the ones in the Ulleung Basin. Considering the measured thermal conductivities in the Ulleung basin and those predicted by the empirical equation (Eq. 5.7), a possible error in the thermal conductivity is about 10%. A decrease by 10% from an average of 1.13 W/mK to 1.02 W/mK results in 22 m shallower BGHSZ associated with a small decrease in pressure and temperature at the BGHSZ (red line in Fig. 5.6 and Table 5.3c). To maintain the same heat flow of 105 mW/m^2, a thermal conductivity decrease implies a thermal gradient increase from 94^0 C/km up to 105^0 C/km. The average

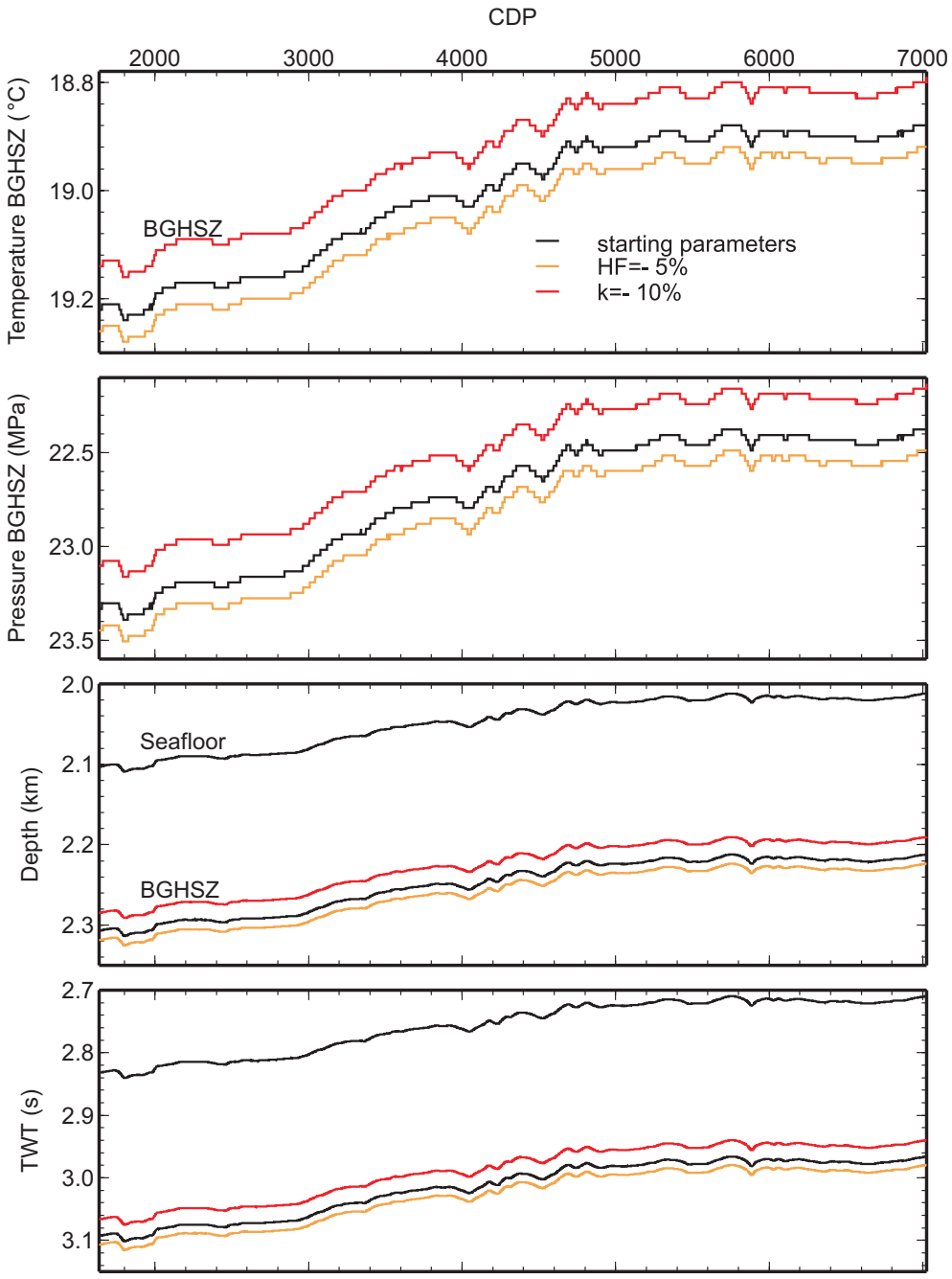

Figure 5.6: Sensitivity of temperature and pressure, depth and traveltime at the BGHSZ to heat flow and thermal conductivity. The black line is calculated with initial parameters: heat flow = 105 mW/m^2, thermal conductivity = 1.13 W/mK, velocity = 1563 m/s, seafloor temperature = 0.2 ^{0}C. The orange and red lines are calculated for a 5% reduced heat flow and 10% reduced thermal conductivity, respectively. The averages for each parameter over the entire line are summarized in Table 5.3.

seismic velocity is slightly decreased to 1551 m/s, because the average is over a thinner interval.

The parameters resulting from an increase in seismic velocity of sediments are summarized in Table 5.3 column d. The seismic velocity does not influence the BGHSZ depth estimated from heat flow. Consequently, the pressure and temperature at the BGHSZ and average thermal conductivity do not change. Only the traveltime is smaller by 11 ms than in the initial case.

A change from 0.2^0 C to 0.5^0 C in the seafloor temperature influences only slightly the results, summarized in Table 5.3 column e.

	a) Initial param	b) Heat flow (mW/m^2)	c) k (W/mK)	d) v (m/s)	e) t_{sf} (^{0}C)
		100 (-5%)	1.02 (-10%)	1636 (+5%)	0.5 (+1.5%)
t_{BGHSZ} (^{0}C)	19.01	19.05 (+0.2%)	18.93 (-0.4%)	19.10 (0%)	19.00 (-0.1%)
P_{BGHSZ} (MPa)	22.74	22.86 (+0.5%)	22.52 (-1.0%)	22.74 (0%)	22.70 (-0.2%)
TWT_{BGHSZ} (s)	3.016	3.029 (+0.4%)	2.989 (-0.9%)	3.004 (-0.4%)	3.011 (-0.1%)
ΔTWT (s)	0.258	0.272 (+5.4%)	0.332 (-10.1%)	0.247 (-4.4%)	0.254 (-1.6%)
Depth (m)	2249	2261 (+0.5%)	2227 (-1.0%)	2249 (0%)	2246 (-0.2%)
Δd (m)	202	213 (+5.8%)	180 (-10.8%)	202 (0%)	198 (-1.7%)
$\Delta T/\Delta d$ (^{0}C/km)	94	89	105	94	96

Table 5.3: Averaged parameter uncertainties over line 063, initial parameters: heat flow = 105 mW/m^2, average thermal conductivity = 1.13 W/mK, average velocity = 1563 m/s, seafloor temperature, $t_{sf} = 0.2^0$ C. The error percentage in the calculated parameters from the initial case is shown in columns b-e in paranthesis.

5.3 Discussion

The heat flow calculated from the depth of the BSR on three seismic lines appears to increase with water depth: it is estimated at 105-125 mW/m^2 on the basin plain and 98-110 mW/m^2 on the slope. This trend can be useful to calibrate the heat

flow and depth to the BGHSZ on the study line 063. The traveltime calculated for a constant heat flow of 105 and 120 mW/m^2 is shown on all velocity profiles and seismic attribute sections.

To determine the different parameters at the BGHSZ, a number of assumptions are made: the heat flow transfer is conductive and the value is constant across the line, the average sediment velocity is constant, the thermal conductivity increases with depth beneath the seafloor without any lateral variations and there is no gas hydrate. The largest errors in these parameters are likely found at the location of chimney/vent-structures where the heat flow, velocity, thermal conductivity and salinity could be different due to the presence of hydrate. There could be a heat flow increase at such features due to the advection of warm fluids migrating upwards through faults and fractures. Gas-dominated effusions would not be able to advect significant heat. As seen from the modeling results in this study (Fig. 5.6), an increase in the heat flow, due to, for example, the advection of warm fluids would result in a shallower BGHSZ. Therefore, gas imaged as bright reflectors could be shallower than the regional depth of the BGHSZ. This could partly explain the pulled-up reflectors around the depth of the BGHSZ. An increased salinity would also result in a shallower BGHSZ, but this effect is not modelled in this study.

Chapter 6

Seismic Attributes and Imaging

In this chapter we examine characteristics of the seismic signal that may provide information on the presence of gas hydrate or free gas. Changes are examined especially at the estimated BGHSZ. The imaging of the seismic profile is done by analyzing attribute displays of a) reflection amplitude, b) instantaneous amplitude and instantaneous frequency. Finite difference time migration is first performed to improve the stack image display. Complex seismic attributes are then computed on zero-offset time-migrated data. These attributes are especially useful to identify areas of increased attenuation or brightened reflectors, which could be associated with variations in the physical properties of sediments. Since gas hydrate and free gas are expected to change the physical properties of bulk sediments, attribute anomalies in the seismic signal could be indicative of their presence.

6.1 Finite Difference Time Migration and Reflectivity Image

The first process is finite difference time migration which, compared to the stack section, improves the horizontal resolution by focusing energy by collapsing diffractions and re-positioning dipping reflectors to their correct geometry. The routine (FDMIG module of Claritas), which is limited to a maximum dip of 45^o, uses an interval velocity model derived from stacking velocity using the Dix equation. The stacking velocities are first smoothed and then converted to interval velocities, because the Dix equation is very sensitive to velocity fluctuations and because the time migration does not perform well with rapid lateral variations in interval velocity, even if they are geologically accurate.

The migrated profile is shown in Fig. 6.1. The image shows more coherent reflectors than the stack. The most prominent features, the acoustic blank zones have clearer reflectors and are narrower. The predicted BGHSZ using a constant heat flow of 105 and 120 mW/m^2 is indicated in the figure (see Chapter 5).

The seafloor amplitude variations are also shown above the section in Fig. 6.1. The red colour marks the location of the blank zones. The seafloor amplitude is lower above the blank zone at CDP 2020, has an average value for the blank zone at CDP 3380 and 6080, both a high and a low at the blank zone at CDP 3550. The blank zone at CDP 6080 does not penetrate upward to the seafloor in the image, so it is not surprising that there is no surface effect. There are several other peaks in amplitude not associated with any blank zone, especially a broad zone between CDP 2800-3000.

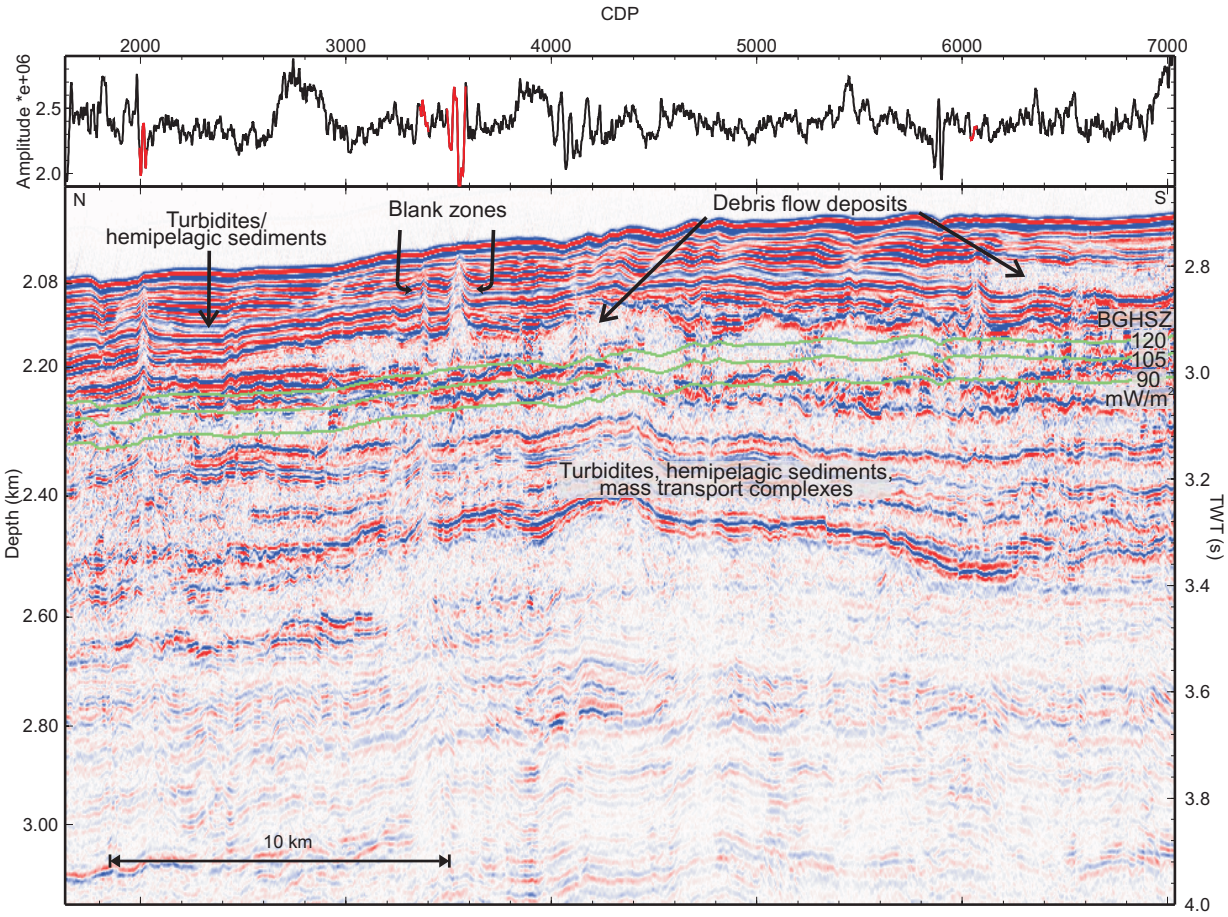

Figure 6.1: Time migrated section 063 in the NE part of the Ulleung Basin as indicated in Figure 1.3. Prominent features are the acoustic blank zones found mainly above the base of gas hydrate stability zone (BGHSZ), calculated using an assumed heat flow of 90, 105 and 120 mW/m^2 (green curves). The seafloor amplitude is shown on top of the section, where the red sections correspond to the location of the blank zones.

The identification of the geological units on our seismic section is done in part by comparing the seismic characters, briefly described in 1.5.3, with those seen over a much larger area in the Ulleung Basin on high resolution and multi-channel reflection profiles interpreted by *Chough et al.* (1997) and *Lee and Suk* (1998). The upper 150 ms bsf of the section generally shows continuous reflectors that follow the undulatory seafloor. This type of reflectivity is interpreted as turbidites and hemipelagic sediments. Horizons with a chaotic internal character and a lens-shape external form are

interpreted as debris flow deposits, found between CDP 2600 and 6000 at around 3 s. The zone between 3.1-3.4 s has variable amplitude reflectors with moderate continuity and some areas with chaotic patterns. This character is likely a result of mixed turbidites/hemipelagic sediments and mass-transport complexes.

The time-migration is an important processing step in improving the image of acoustic blank zones, which have the largest reflector dip. Generally, the reflectors in the blank zones are clearer and the dip angle increases further. The reflectors are shorter than in the unmigrated sections, making the blank zones narrower than in the stack sections. Fig. 6.2 shows the stack and migrated section at several parts of the line where there are blank zones. The reflectors inside the blank zone centered at CDP 2020 appear especially clearer after migration (Fig. 6.2a II), with a well-delineated pull-up for the first reflector below the seafloor as well as for the reflectors close to the BGHSZ. A sub-vertical 'channel' of reduced amplitudes is imaged below the BGHSZ. The reflectors in the blank zone above the BGHSZ centered at CDP 3380 (Fig. 6.2b) appear bowed downwards before migration (Fig. 6.2b I) and bowed upwards after migration (Fig. 6.2b II). This illustrates the importance of migration before interpretation. The reflector at the BGHSZ is visible and appears flat after migration. The reflectors below the BGHSZ can be distinguished after migration, but they have reduced amplitude. After migration, the reflectors above the BGHSZ in the blank zone centered at CDP 3550 (Fig. 6.2b II) are bowed upwards above the BGHSZ, and a number of reflectors around the BGHSZ are very bright and flat. As compared to the narrower blank zone, the reflectors below the BGHSZ have reflection amplitudes as high as adjacent areas. The shape of the reflectors above the BGHSZ

inside the blank zone at CDP 6080 (Fig. 6.2c I) cannot be distinguished in the stack section. After migration (Fig. 6.2c II), the reflectors are slightly clearer and there is a definite bow-up of the reflector at 2.85 s, just below the debris flow deposit seen as an incoherent zone at 2.80-2.85 s. A few short 45^0 dipping reflectors are seen only after migration between 2.9-3.0 s. Below the BGHSZ, the reflectors have good reflectivity and are flat.

The migration process is very sensitive to the accuracy of the velocity field. Since the velocity field from our analysis is very heterogeneous and has extreme values, and the dip of the reflectors is larger (up to 5^0) inside the blank zones, the traveltime errors are likely larger inside these features. Accurate traveltimes of reflectors after time-migration are important for the velocity pull-up calculations discussed in Sec. 3.3.

6.2 Different Offset Stacks

A simple analysis is done to investigate the incidence angles of the rays passing through the blank zones, assuming the rays are straight. The results are schematically shown in Fig. 6.3. The recorded offsets are between 161-3149 m, which results in a maximum incidence angle of 35^0 for rays reflecting from 200 m bsf, corresponding approximately to the BGHSZ. It is useful to know in terms of imaging to what extent the rays corresponding to CDPs inside the blank zones pass through them. Two blank zones imaged between CDP 3360-3400 and CDP 3490-3590 are analyzed in Fig. 6.3 at their central position. For the narrower blank zone, few of the larger offset rays pass through outside the feature, whereas for the wider blank zone, all the recored

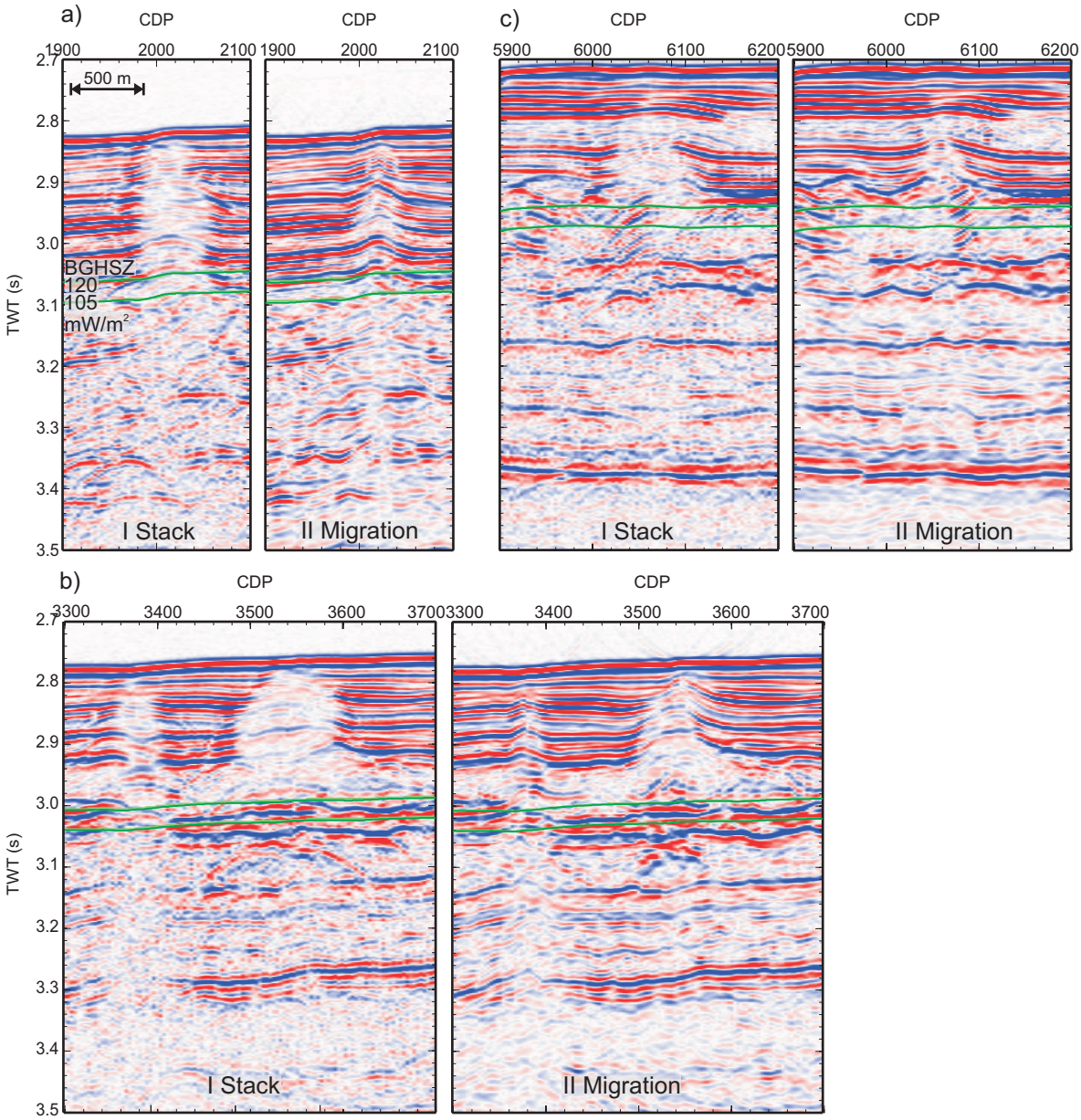

Figure 6.2: Comparison between stack before time-migration (I) and migrated stack (II) for 3 sections of the line 63 with blank zones: a) CDP 1900-2100, b) CDP 3300-3700, c) CDP 5900-6200.

rays pass through the feature.

Traces from different offset ranges are stacked together to see how the image varies. The entire range of offsets (161-3150 m) is divided into five and the traces from each sub-range are stacked and shown in Fig. 6.4 for the blank zones centered at

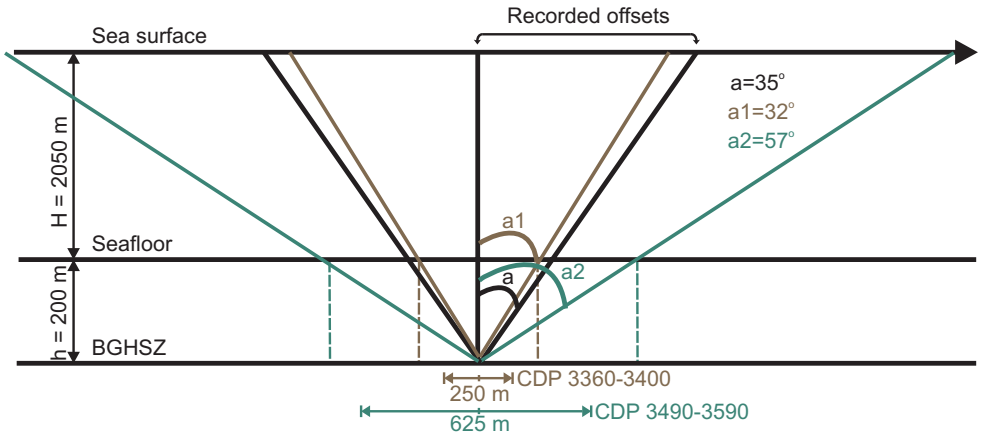

Figure 6.3: Schematic image showing the straight ray paths from the BGHSZ recorded at offsets 161-3149 m. The maximum angle of incidence of rays passing through two of the blank zones is calculated, where the extent of the blank zones is indicated by the dashed lines.

CDP 3380 and CDP 3540. The general patterns are a decrease in amplitude and loss in sharpness of reflectors with increasing offset. This happens because more energy and the high frequency content are lost as the waves travel longer distances. Also, the effect of NMO stretch at long offsets is to reduce the frequency of reflections. Diffractions are also more pronounced at larger offsets and the reflectors around 3.05 s have a wavy structure (Fig. 6.4 o, s) as compared to the flat structure (Fig. 6.4 c) imaged at shorter offsets. The far offset stacks from the narrow blank zone (Fig. 6.4 m, n, q, r) define the reflectors vaguely.

6.3 Complex Trace Analysis

Complex trace analyis is performed on the time-migrated section of line 063. The analysis is a useful way to relate the seismic signal to the physical properties of the sediments, in particular to identify the presence of gas hydrate and gas in sediments (e.g., *Taner et al.* 1979, *Coren et al.* 2001, *Chopra and Marfurt* 2005, *Taylor et al.*

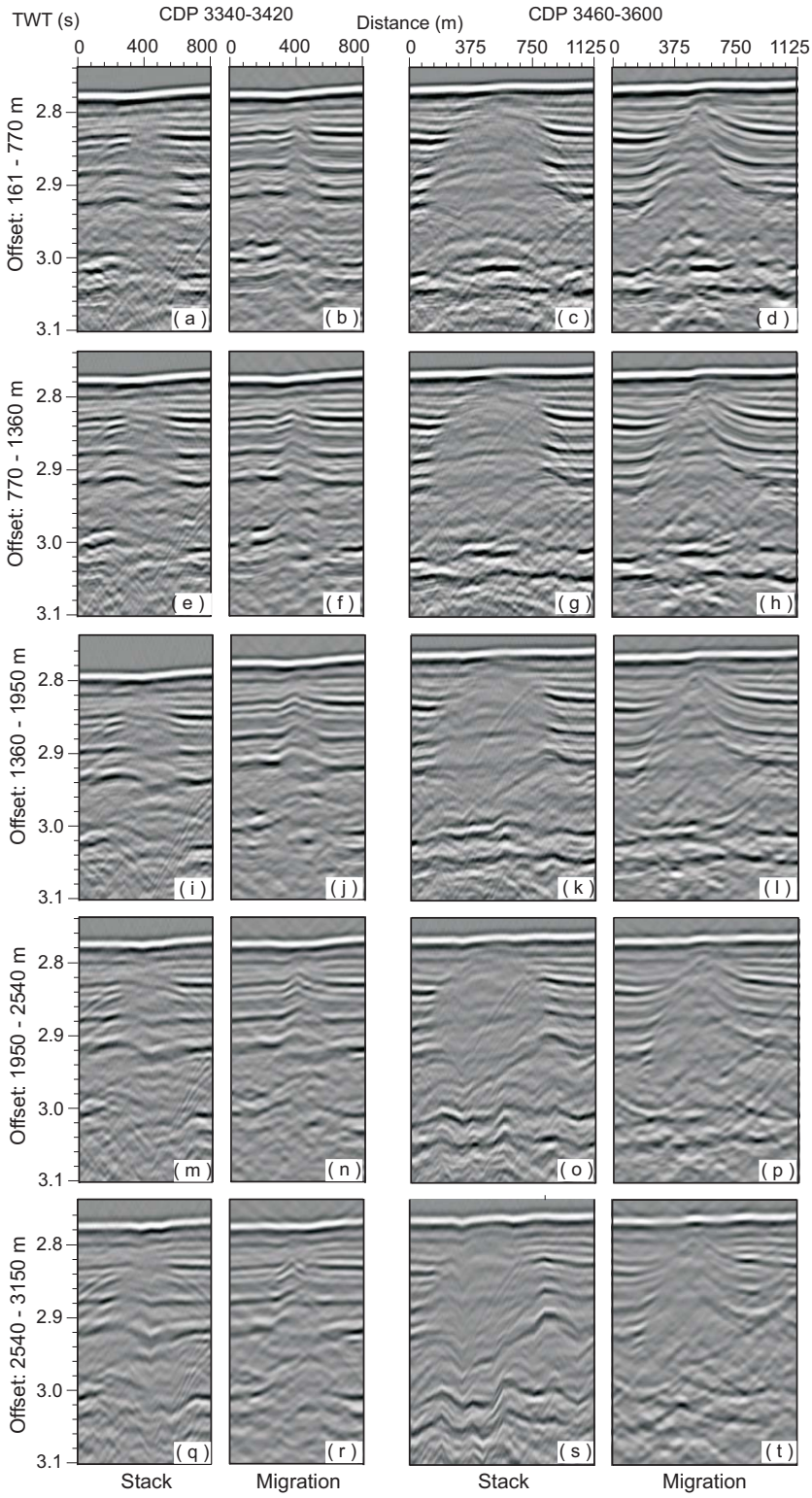

Figure 6.4: Stacks and migrated sections from different offsets for the blank zones centered at CDP 3380 and CDP 3550. a-d) offset: 161-770 m; e-h) offset: 770-1360 m; i-l) offset: 1360-1950 m; m-p) offset: 1950-2540 m; q-t) offset: 2540-3150 m.

2000). The effects of gas hydrate and gas on seismic attributes are described in Sec. 1.3.2. Complex trace analysis involves calculation of the quadrature trace from the seismic trace, using the Hilbert transform and the background of complex trace analysis is summarized in Appendix B.

6.3.1 General applications

Instantaneous amplitude and instantaneous phase are the two fundamental seismic attributes used in the complex seismic trace analysis. Many additional attributes are derived from these two quantities through differentiation, averaging, combination, or transformation. Instantaneous attributes are defined at every point on the seismic trace. Complex seismic attributes are calculated by treating the seismic trace as the real component of a complex waveform. The imaginary component, the quadrature trace, is calculated from the seismic trace using the Hilbert transform. Colour displays of seismic attributes can be used for the interpretation of geologic structures, stratigraphy, and rock/pore fluid properties. Seismic attributes are only in a few cases directly related to a physical property. The best example is the correlation between free gas and high amplitude.

The instantaneous amplitude or trace envelope is a measure of brightness or reflection strength and it is independent of phase and polarity. It is sensitive to changes in acoustic impedance, thus to lithology, porosity, hydrocarbons and thin-bed tuning (*Taner et al.* 1979, *Roberton and Nogami* 1984). High reflection strength is also sometimes associated with gas layers. This is due to the high impedance contrast at the top of a gas-filled layer, which is caused by the low seismic velocity that results

from only a few percent of free gas in the pore space (*Domenico* 1976). These gas layers thus can generate strong reflections, known as 'bright spots'. Gas also can brighten layered reflections by increasing the impedance contrasts between low and high porosity layers that contain more or less gas. Significant thickness of high gas concentrations also can reduce seismic amplitudes through attenuation of the seismic signal. Lateral variations in bed thickness occurring over considerable distances result in changes in the interference of reflectors, seen as lateral changes in reflection strength. Reflection events from one interface can be distinguished from those from more interfaces by looking at the lateral consistency character.

The instantaneous phase is used to track reflector continuity, to detect unconformities, faults and lateral changes in stratigraphy when a coherent reflection event cannot be followed from trace to trace (*Taner et al.* 1979).

Instantaneous frequency can be used to identify abnormal attenuation (*Taner et al.* 1979) and thin bed tuning (*Roberton and Fisher* 1988). Since many reflector events are a composite of individual reflections from closely spaced reflectors or tuning of multiple impedance contrasts, a characteristic reflection frequency pattern is produced. This character of a composite reflection changes gradually as the sequence changes laterally in thickness or lithology.

Another useful application of instantaneous frequency is to identify sediments that are strongly attenuating high frequencies, such as gas sands. Low frequency shadows have been observed on reflections immediately below gas sands, whereas deeper reflections appear normal. Gas hydrates also appear to attenuate energy as discussed in Sec. 1.3.2, but not as much as gas-bearing sediments (e.g., *Taylor et al.*

2000).

Most attributes have a noisy character, since they are derived through differentiation, which introduces less coherent high frequencies and suppresses more coherent low frequencies. Also, because the instantaneous amplitude and phase have inflection points and discontinuities, their differentiation results in spurious spikes. The most anomalous values of instantaneous frequency are most often associated with small amplitudes and are the least reliable, whereas the ones associated with larger amplitudes are more stable (*White* 1991). In order to remove the high frequency noise and the spikes to ease interpretation by emphasising the frequency of stronger reflectors, the instantaneous attributes are filtered. The most common filters are: median filtering, selection of instantaneous attributes at envelope peaks and averaging weighted by the instantaneous power or envelope squared (*Barnes* 2007).

6.3.2 Complex Seismic Attributes on Line 063

Instantaneous amplitude and frequency are calculated from both zero offset traces recorded at the nearest two channels, and the time-migrated section produced from all offsets. By calculating attributes from a zero-offset section, one tries to avoid the reduction of apparent frequency by mis-stacking or emphasizing the larger offsets in the stack, which are NMO-stretched. Some processing mechanisms that reduce the frequency and can be mistaken for characteristics of the formation are mis-stacking due to too coarse velocity picking, non-hyperbolic moveout, locally converted shear-waves, and addition of low frequencies by deconvolution (*Ebrom* 2004).

The attributes (instantaneous amplitude and frequency) are first computed for the

entire profile, after which the areas of interest are zoomed into using the amplitude decay curve option from the XVIEW window in Globe Claritas. A smoothed function of the amplitude of the seismic traces is calculated using a vertically running time-window of 25 ms (20 m) and a horizontally running trace-window of 5 CDPs (33 m). An example calculated from the near half offsets is shown in Fig. 6.5. Lower amplitudes are seen at the location of the blank zones, only above the BGHSZ at the blank zone at CDP 3550, and extending to greater depths at CDP 3380. A bright reflector is seen around the BGHSZ for the blank zone at CDP 3550. The frequencies are reduced around and immediately below the BGHSZ at the blank zone centered at CDP 3550 and also deeper for the blank zone at CDP 3380.

Instantaneous attributes are calculated on selected CDP intervals from time migrated sections, to compare blank zones to the areas outside them. The areas chosen are indicated by the coloured boxes in Fig. 6.6. The instantaneous frequency and amplitude for each zone, scaled by the same factor are shown in Fig. 6.6a and Fig. 6.6b, respectively.

In the reference areas next to the blank zones an arrow indicates a decrease in the instantaneous frequency around the depth of the predicted BGHSZ. In the area CDP 2050-2100, 6110-6200 this decrease is associated with a peak in the instantaneous amplitude ∼25 ms above the BGHSZ. In the areas CDP 3420-3471 and CDP 3582-3630 the decrease in frequency is not associated with a peak in amplitude. Here, the frequency starts decreasing above the predicted BGHSZ. In the blank zones, the instantaneous frequency decreases gradually with depth, and there is no sharp transition near the BGHSZ like in the areas outside.

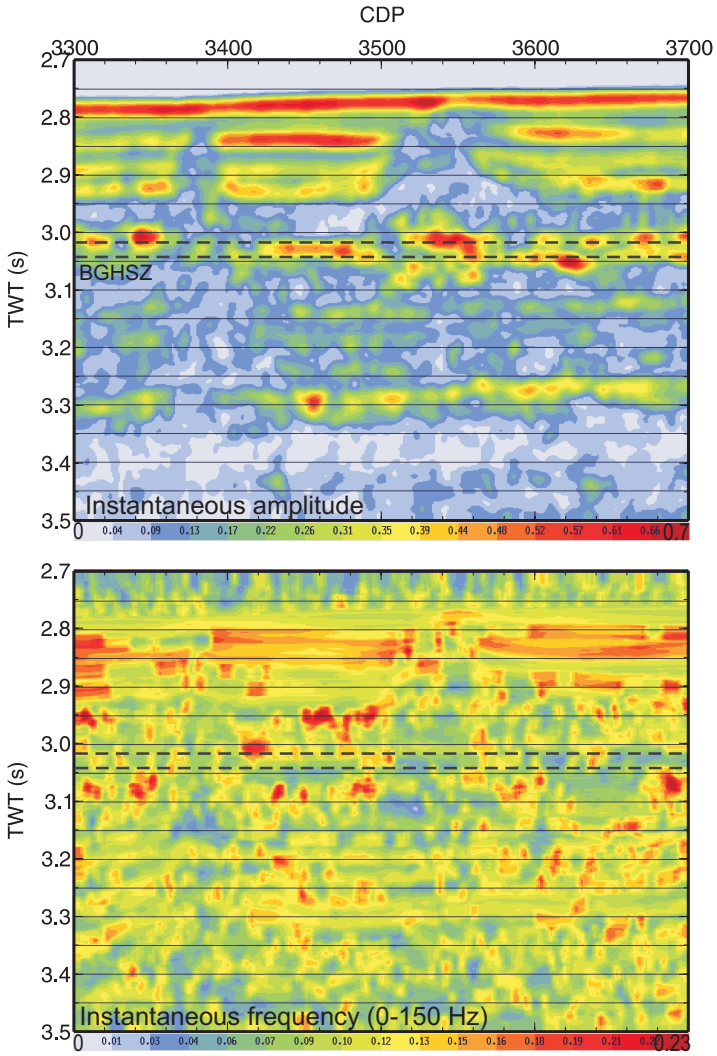

Figure 6.5: Instantaneous amplitude and frequency calculated from the near half offsets from the time-migrated section.

The instantaneous amplitude and frequency for each interval are shown in Fig. 6.7. The colour of the curves corresponds to the location indicated by the same colour boxes in Fig. 6.6. The continuous line represents the attributes from the all-offset section and the dashed line from the zero-offset section. The attributes calculated from the zero-offset section are almost always higher than the ones calculated from the stacked section, as a result of the artifacts introduced by stacking. The zero-offset attributes are used in the interpretation of the results since the mechanisms that

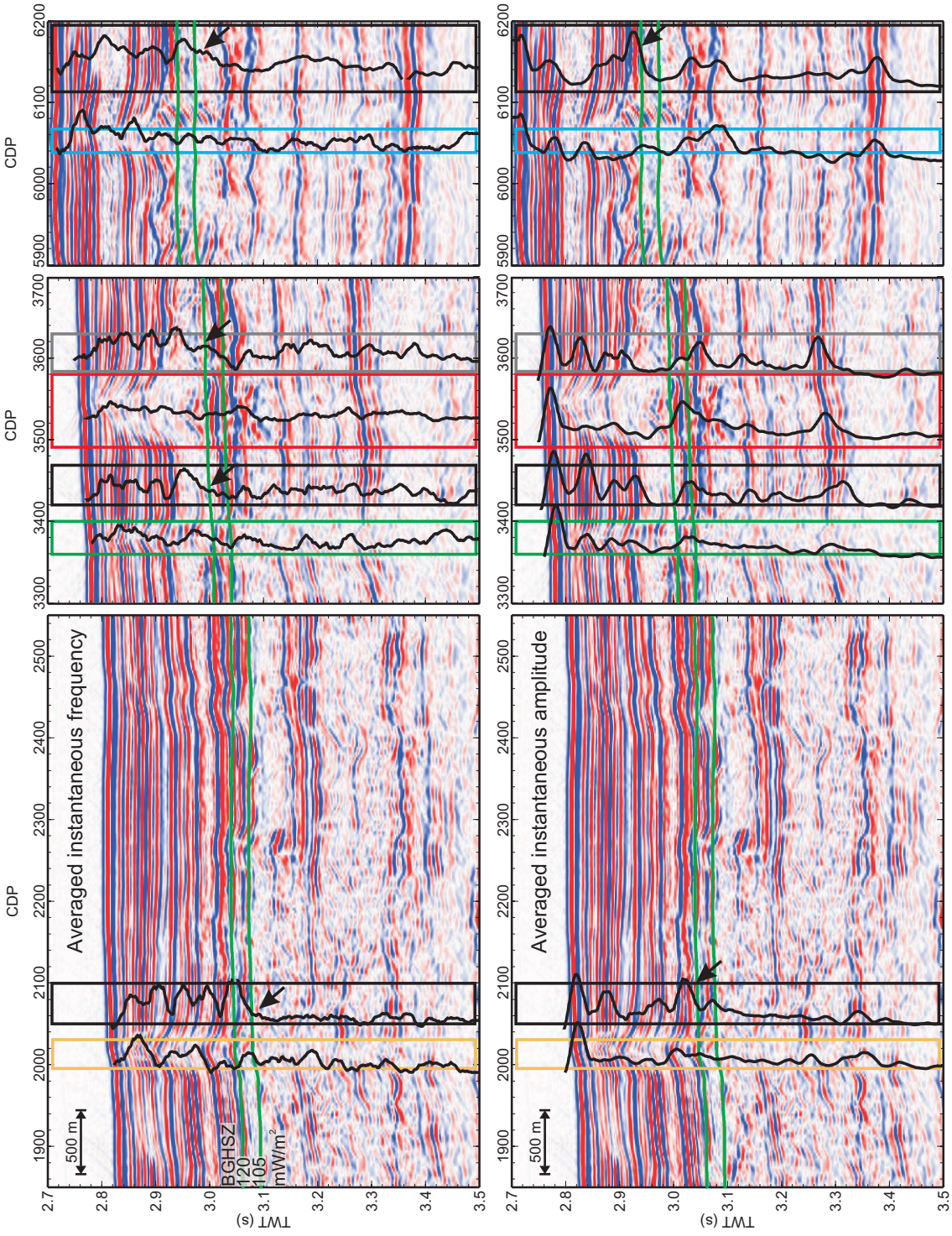

Figure 6.6: Time migrated sections with instantaneous frequency and instantaneous amplitude overlying small sections indicated by boxes over which the attributes are averaged.

would artificially reduce the frequency by stacking are avoided. The instantaneous frequency is more 'wiggly' than the instantaneous amplitude, which reflects the higher degree of susceptibility to noise of the attribute. When the instantaneous amplitude is much reduced, the instantaneous frequency is less reliable, so a more meaningful intepretation should focus on values at stronger reflectors.

The attributes calculated from the zero-offset section from the zones inside and outside adjacent to the blank zones centered at CDP 2010, 3380, 3540 and 6060 are shown in Fig. 6.8 for a direct comparison. The arrows indicate the decrease in instantaneous frequency of about 30-40 Hz for areas outside the blank zones, associated in the cases shown in Fig. 6.8a and d with a peak in instantaneous amplitude. Generally, the attributes inside the blank zones are lower than the ones from the areas outside. The amplitude decrease is pronounced above the BGHSZ for all blank zones, but it is almost as high and sometimes higher for deeper reflectors. The amplitude at 540 ms bsf (Fig. 6.8a) corresponding to the reflector at 3.35 s (Fig. 6.6) is as high inside the blank zone as outside. The reflector at 250 ms bsf inside the blank zone at CDP 3490-3582 (Fig. 6.8b and c) corresponding to 3.02 s (Fig. 6.6) has a slighly higher amplitude than the areas outside the blank zone, at CDP 3420-3471 and CDP 3582-3630. The deeper reflector at 530 ms bsf and 3.26 s shows as high amplitude inside the blank zone as outside at CDP 3420-3471. The reflector at 380 ms bsf inside the blank zone at CDP 6040-6080, corresponding to 3.1 s has a slightly higher amplitude than outside at CDP 6110-6200 and slightly lower for the reflector at 670 ms bsf (3.38 s).

In the blank zone at CDP 1995-2030, there is a more prominent decrease in fre-

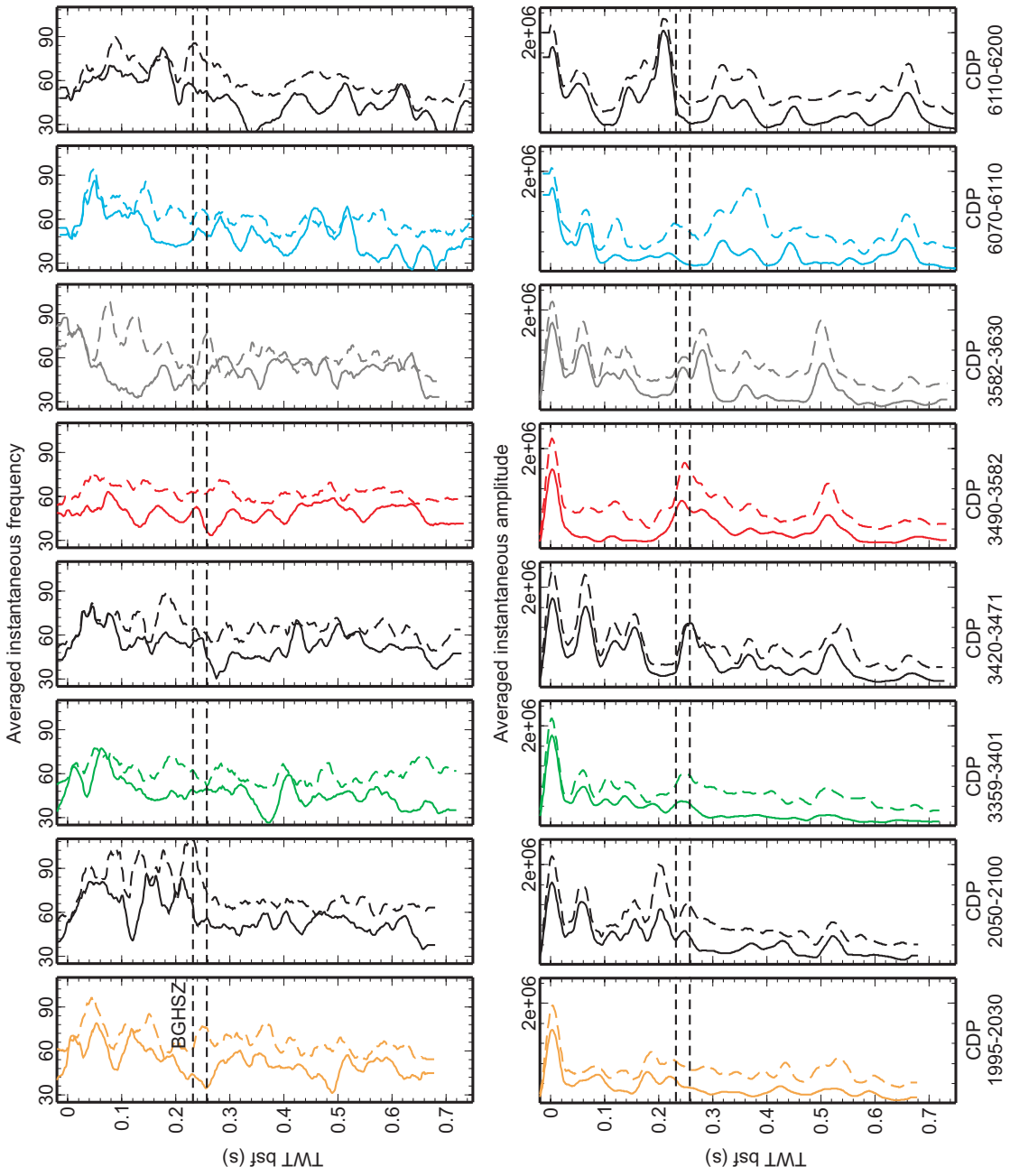

Figure 6.7: Instantaneous amplitude and frequency calculated on selected CDP intervals indicated on the seismic section in Fig. 6.6, where the continuous lines are derived from stacked sections and the dashed lines from a zero-offset section.

quency at 200 ms bsf as compared to the other blank zones (Fig. 6.8a). This is seen on the seismic section at 3.0 s and correponds to the frequency drop at 3.06 s outside the blank zone, at CDP 2050-2100 (Fig. 6.6). The reflectors below which the frequency drops have high amplitude.

6.4 Discussion

Instantaneous amplitude and frequency displays are useful to compare the seismic signal in the blank zones and areas immediately outside. The seismic signal is influenced by both differences in the sediments and the possible presence of gas hydrate and gas, which can physically disturb the layers. The GHSZ for the blank zone at CDP 1995-2030 and area outside it and the top part of the GHSZ for the blank zones and areas outside them between CDP 3300-3700 is found in turbidites (Fig. 6.6), whereas the lower part of the GHSZ is debris flow deposits. The blank zone at CDP 6040-6070 and the area outside it has a debris flow deposit in the middle of the stability zone between turbidite sequences. Debris flows, due to their incoherent character and broken-up layering, reduce the energy likely by scattering. The turbidites and debris flow deposits also may have different permeabilities, which influence the formation of gas hydrate and movement of free gas.

A decreased seafloor amplitude is seen above the blank zone at CDP 1995-2030, and both a decrease and increase at the blank zone at CDP 3490-3582. Higher amplitudes are seen between CDP 2700-2900 but they are not associated with any subsurface feature. The increased amplitudes could be a result of gas hydrate and carbonates on the seafloor, and lower amplitudes from disturbed higher porosity sed-

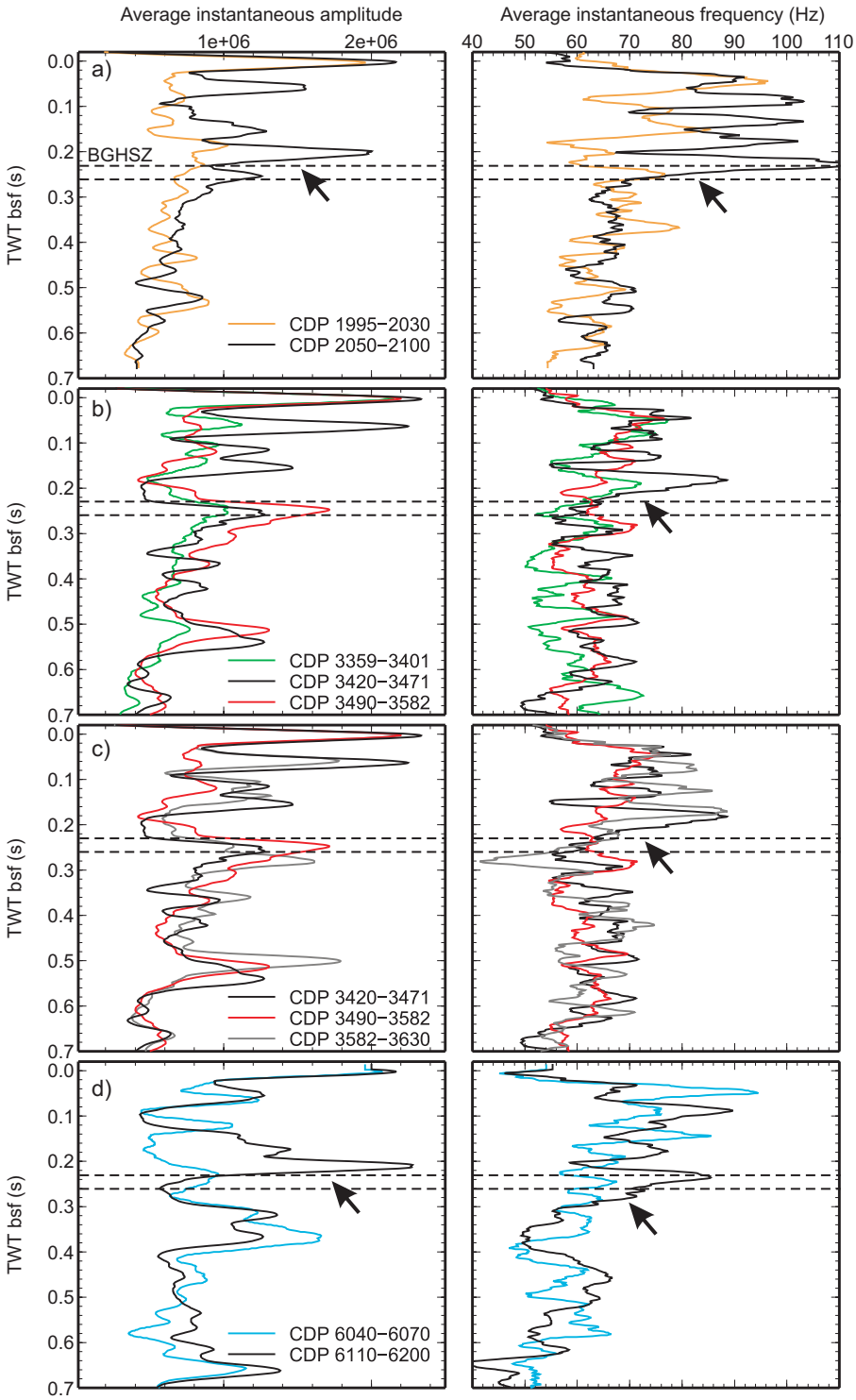

Figure 6.8: Average instantaneous amplitude and frequency for areas inside the blank zones (colour curves) and immediately adjacent to the blank zones (black curves). The arrows indicate a sharp decrease in the instantaneous frequency outside the blank zones, sometimes associated with a peak in instantaneous amplitude.

iments which could be entrained by strong fluxes of upward moving fluids and gases. Since there is no general correlation between the seafloor amplitude and blank zones, it is quite difficult to associate subsurface features such as blank zones to seafloor amplitude.

The decrease in instantaneous frequency at about 200 ms bsf for the areas outside the blank zones (CDP 2050-2100, CDP 6110-6200) associated with a peak in instantaneous amplitude, could result from the presence of gas accumulations below the BGHSZ. The high amplitude could mark the top of the gas accumulation, which generates a higher impedance contrast. The decrease in frequency in some other reference areas at CDP 3420-3471 and CDP 3582-3630 is not associated with a peak in amplitude. The amplitude is lower right above the predicted BGHSZ because of the debris flow, and it is high at the BGHSZ. The high amplitude at this depth, also seen in the blank zone at CDP 3490-3582 is a good indication of gas-charged thin layers.

The frequency inside the blank zones above and below the BGHSZ shows a relatively gradual decrease with depth, with no sharp decrease . Frequency is generally slightly lower inside the blank zones than outside these areas. Both the amplitude and frequency in the blank zone at 3359-3401 are decreased with no peaks in amplitude and suggest no accumulations of gas, but more likely a very heterogeneous distribution of upward-migrating gas, which does not result in brightened reflectors. It is possible that some of the free gas moves into the stability zone without forming hydrate, so the gas would result in the both decreased frequency and amplitude.

The reflector amplitudes in the blank zones are generally lower in the stability zone than beneath. However, the deeper reflectors have higher amplitude than the

shallower reflectors. The similar and sometimes higher amplitude of the deeper reflectors inside the blank zone as compared to outside, suggests that the shallower blanked areas above the BGHSZ are a result of the broken-up reflectivity due to the possible heterogeneous distribution of hydrate. The frequencies are on average ∼5-10 Hz lower inside the blank zones, and sometimes have similar values. Possibly there is some free gas immediately above and below the BGHSZ inside the blank zones, implied from slightly lower observed frequency. Except for the blank zone at CDP 3490-3582, the amplitude around the BGHSZ is never as high as in areas outside, which suggests that the gas does not accumulate at this depth and has a more heterogeneous distribution due to possible migration.

On the amplitude display, channels of reduced amplitude can be identified below some of the blank zones to great depths. There are such channels below the BGHSZ that seem not to be related to the blank zones above the BGHSZ. When these channels are found only below the BGHSZ, they clearly suggest the movement of fluids and free gas upwards. When they appear to feed blank zones in the stability zones, they could be interpreted as a result of the blanking above. However, this possibility is not supported by the lack of amplitude decrease below the blank zone at CDP 3490-3582. Also, the thin channel of reduced amplitudes below the blank zone at CDP 1995-2030 is not vertical below the BGHSZ, suggesting a real conduit, rather than a cumulative effect.

From the above observations, it is quite difficult to give definite and quantitative reasons for the attenuation of the seismic signal. Rather, a few qualitative conclusions can be drawn. Very likely, the presence of gas hydrate in the stability zone in the

blank zones attenuates the signal. This could result from both intrinsic attenuation and from scattering where the reflectors are physically disrupted as a result of hydrate formation. The intrinsic attenuation of the signal inside the blank zones is probably not very large because the average frequency below the BGHSZ is only slightly smaller than that outside the blank zones, and the amplitude of the reflectors is similar. The seismic attributes imply that the blank zones are associated with larger concentrations of gas rich fluids and free gas than the areas outside them. The fluids and free gas migrate upwards, sometimes accumulate in more porous sediments, but also find permeable channels such as fractures and faults to migrate upwards and reach the GHSZ where they form hydrate.

Chapter 7

Summary and Conclusions

MCS seismic data from the basin plain of the Ulleung Basin, collected as part of the 2005 Gas Hydrates 2-D Data Acquisition by KIGAM, were processed to image structures of locally focused upwelling fluids and gases and to obtain seismic velocities, from which gas hydrate and free gas saturations were estimated.

Interval velocities were derived from stacking velocities with the Dix equation using various approaches. Velocity profiles from the blank zones and the areas outside them were averaged into 1-D velocity profiles (e.g., Fig. 7.1). Without applying any constraints to the inversion, the interval velocities have large variations, and their mean is biased to low velocities, when the velocity decreases with depth, as a result of the non-linear relationship between stacking and interval velocities expressed by the Dix equation. An alternative to obtain a more accurate velocity mean by reducing the bias, is to first average squared interval velocities from at least 15 profiles and then take the square root. A minimum-structure solution derived from constrained inversion is preferred when analyzing individual velocity profiles. This solution is

calculated to fit the data to a statistical level and it has a smooth structure that minimizes large oscillations. However, the constraint also smooths out real anomalies inside the blank zones. The preferred solution for the mean velocity across a blank zone would be that obtained from the mean velocity squared if enough velocity profiles were available from the blank zones. There are only about 10 velocity profiles in each blank zone, and so there may still be a small bias in the preferred solution towards the interval velocity mean. Thus, the regularized solution can be taken as a minimum conservative estimate for the effects of hydrate and free gas. Outisde the blank zones, the reference velocity profile is obtained from 110 velocity profiles. The profile that best characterizes the normal compaction of sediments in the area is that obtained from the regularized inversion with a smoothness constraint. This is the preferred solution because the velocity curve was continuously increasing with depth and this type of inversion reduces the uncertainty. Velocity anomalies inside the blank zones as compared to the reference profile are translated into gas hydrate saturations above the BGHSZ and free gas below the BGHSZ, using the porosity-reduction and the Gassmann models, respectively. The seismic velocities indicate only the large scale distribution of gas hydrate in such features, although the gas hydrate is likely distributed heterogeneously.

The unbiased mean velocity is up to 25% higher than the reference above the BGHSZ and up to 40% lower below the BGHSZ inside the blank zones than outside and these anomalies are clearly significant. The velocity anomalies from the regularized inversion are about half those mentioned above. Over most of the depth of the GHSZ inside the blank zone at CDP 1985-2045, the velocity mean is lower than the

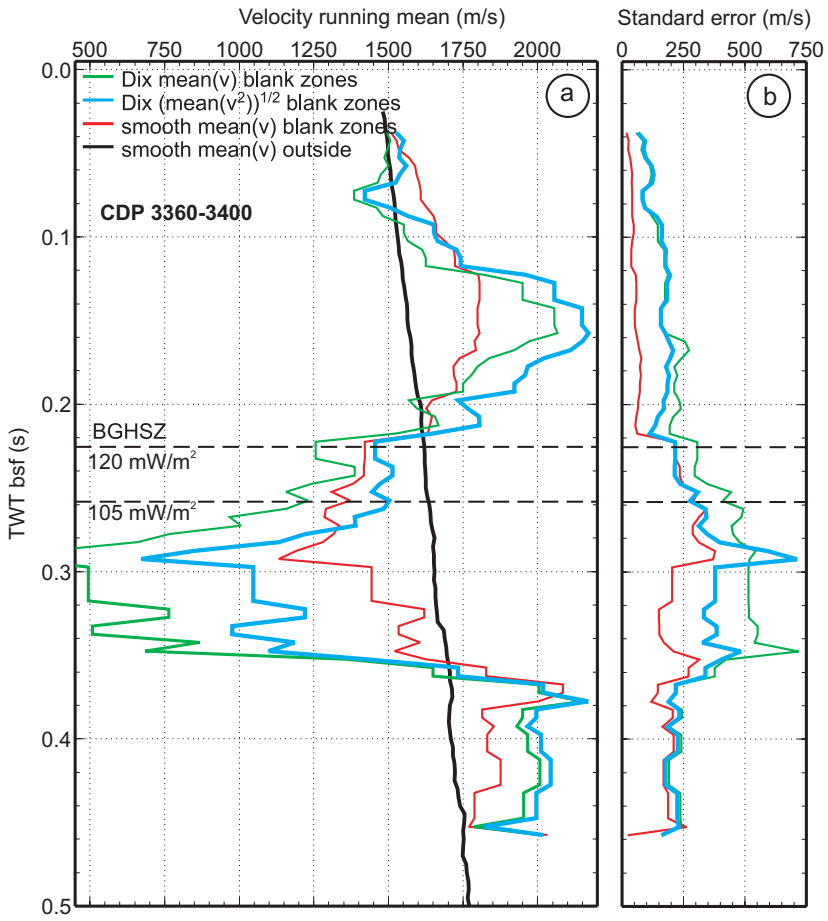

Figure 7.1: Comparison between interval velocity from one blank zone using different methods, as compared to a reference profile.

reference. This implies that there could be free gas that reduces the velocities or that the reference velocity is too high for the type of sediments inside this blank zone. If there were free gas, the reflectors would not appear pulled-up, but rather pulled down. Free gas could exist in the hydrate stability zone if salinities are too high for hydrate to form (*Liu and Flemings* 2007), or if free gas is found inside fractures coated with hydrate and water cannot come into contact with gas (*Riedel et al.* 2006b). There are a few high velocities above the BGHSZ, but when averaged with the rest of velocities, they are no longer significant.

The interval velocity uncertainties are best quantified by the non-linear Bayesian

inversion which takes into account the errors of both the traveltime and the stacking velocity. The uncertainty in velocity remains relatively constant with depth up to 0.5 s bsf for a uniformly increasing velocity with depth and if the thickness of the layers increases with depth. On the contrary, the velocity uncertainty is much larger when the velocity decreases with depth and the intervals are very thin. The interval velocity uncertainty is influenced greatly by the uncertainty in stacking velocity, whereas the interval thickness uncertainty is influenced by both the uncertainty in stacking velocity and traveltime. An important result is that the velocity and the uncertainty of a layer with a velocity decreasing with depth can be accurately determined using the Bayesian inversion, unlike the analytical solution.

Gas hydrate is inferred to exist inside most of the blank zones. For those studied, there is a peak in saturation of 35% at about 30 m above the predicted BGHSZ (Fig. 7.2), distributed over approximately 50 m. Free gas underlying gas hydrate is found in a $\sim$75 m thick layer in saturations of up to 4%. The depth range of gas hydrate and free gas is in good agreement with the stability zone predicted for the BGSHZ from heat flow estimates and sediment properties, where the heat flow was approximately 120 mW/m^2.

An independent velocity estimate inside the blank zones was obtained from the traveltime pull-up of reflectors, assuming that this is entirely a velocity effect. An example was analyzed for the blank zone at CDP 3490-3600. The calculated velocity is increased to 2500 m/s immediately below the seafloor as compared to the reference velocity of 1470 m/s. This high value cannot be reconciled with values obtained from the Dix equation at such shallow depths. This implies that the pull-up is partly a

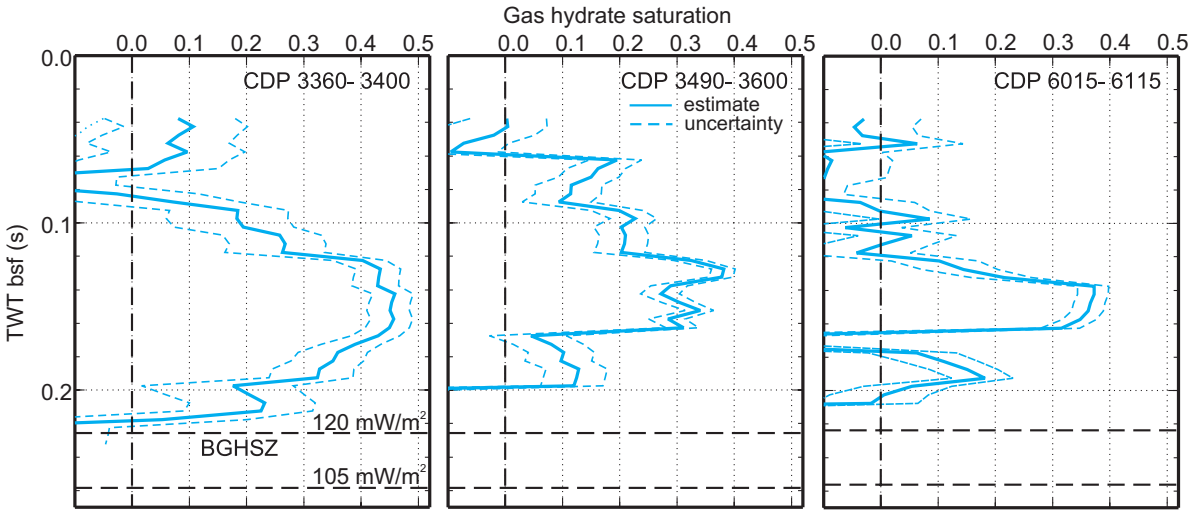

Figure 7.2: Gas hydrate saturation estimated from the unbiased interval velocity mean using the effective porosity reduction model.

velocity effect and partly a structural effect. The relative importance of each effect is difficult to quantify. The heterogeneous formation of hydrate and its possible upward movement due to its low buoyancy (similar to a diapir) likely partially disrupt the layers. However, the reflectors are generally still coherent, unlike those associated with the debris flow deposits.

The seismic signal across the profile is characterized using seismic attributes derived after finite-difference time migration. Some areas immediately adjacent to the blank zones (CDP 2050-2100, CDP 6110-6200) show a sharp decrease in instantaneous frequency associated with a peak in instantaneous amplitude at about 200 ms bsf. A number of velocity profiles from these locations (e.g., CDP 2085, 6160, 6185) also show a reduction in velocity at the same depth. These observations are a strong indication of the presence of free gas. Thus, free gas and gas hydrate likely exist outside the blank zones, but only in small saturations. The averaged velocity profiles (except for the regularized one) capture a velocity decrease of 50 m/s around the

depth of the BGHSZ. Other reference areas that show a decrease in frequency around the depth of the BGHSZ, and no peak in amplitude (CDP 3420-3471, CDP 3582-3630) show no or a very small velocity decrease at the BGHSZ. At these locations, the amplitudes are additionally reduced by the debris flow deposits.

The reflection amplitude below the BGHSZ is reduced for some blank zones, and similar to outside areas for other blank zones. The reflectors around the BGHSZ and below within the blank zone at CDP 3490-3600 have high amplitudes. Since the amplitudes are very low above the BGHSZ, the bright reflectors most likely result from the presence of immobile free gas. Free gas saturations calculated from seismic velocities are 1-4% pore space. There are no bright reflectors around the BGHSZ for the blank zones at CDP 1985-2045, CDP 3360-3400 and CDP 6015-6115; rather, the amplitude and frequency show a continuous decrease from the seafloor to depths below the BGHSZ. The free gas inferred from reduced velocities does not show any large accumulations (except for the peak at CDP 3360-3400, which could be an artifact), but a rather heterogeneous distribution of free gas with saturations of 1-3%. It is possible that at these locations the free gas saturation exceeded a limit and became mobile and started moving upwards. Free gas could also move upwards if entrained by upward advecting fluids. Channels of reduced amplitude are seen extending to great depths below the BGHSZ at the location of the blank zones as well as outside. They are likely permeable migration paths for fluids and free gas.

Our analyses cannot provide a quantitative explanation for the seismic attenuation associated with the blank zones. There is definitely a relation between attenuation and gas hydrate inferred from high seismic velocities. The average frequency below

the BGHSZ inside the blank zones is only slightly smaller than outside the blank zones, implying a small degree of intrinsic attenuation of the signal though the gas hydrate bearing zone. Amplitude blanking is likely result of the energy scattering (*Huang et al.* 2008), resulting from the heterogeneous distribution of hydrate and due to the physical disruption of the reflectors as a result of hydrate formation in groups of sub-parellel veins cross-cutting sedimentary layers, as found at vent sites in the Ulleung Basin (*Holland et al.* 2008).

The different blank zones from line 063, mostly found in turbidite layers, have different seismic character and derived sediment properties. They extend to different depths from the base of the GHSZ upwards and only for some of them the amplitude is reduced to great depths below the stability zone. Gas hydrate is not found to be associated with all the blank zones, unlike free gas, which is always present. This is likely an influence of the formation time of these features, as related to the upward flux of methane rich fluids and gases.

7.1 Recommendation for future work

Seismic velocity derived from the MCS data have proven to be an effective tool in mapping and estimating the distribution of gas hydrate and free gas in localized features of upward moving fluids and gases. Accurate interval velocities require averaging over at least 15-20 velocity profiles, and this should be taken into account in future experiment design and data analysis. Seismic attributes provide additional information but have a less clear pattern and interpretation. A number of suggestions for future work are available.

Borehole logs and VSP from the Ulleung Basin would be very valuable for comparison with these results, especially VSP, which have a similar resolution to our data. Additional constraints from these data can be added to the velocity inversion to provide more accurate velocity estimates and uncertainties. S-wave velocities determined by analysis of data from Ocean Bottom Seismometers or Ocean Bottom Cables would be useful in assesing whether the formation of hydrate cements the grains, and to better constrain the gas hydrate saturation from P-wave velocity.

The regularized inversion can be extended to a 2-D case by adding a second regularization parameter in the horizontal direction. Careful considerations should be given to how the data have to be interpolated to perform this, because the stacking velocities are picked on an irregular grid.

A wide range of seismic attributes, such as coherence and curvature, could be additionally calculated from the seismic data. They could be useful in detecting anomalies in the seismic signal related to gas hydrate and free gas, faults and fractures that represent paths for fluid flow. In addition, seismic attributes may reveal important additional information if calculated from 3-D seismic data. This would provide an excellent opportunity to image the 3-D structure of the blank zones.

Interval velocities obtained with the approach described in this study could be improved if the water layer were much thinner. This could be achieved in a survey where the streamer is deployed closer to the seafloor. The results could be used as a good initial model for curved-ray time migration or depth migration. Pre-stack depth migration would be very useful to image blank zones in depth, as well as faults and fractures that are likely a key player in their formation.

References

Al-Chalabi (1974), An analysis of stacking, rms, average, and interval velocities over a horizontally layered ground, *Geophys. Prosp.*, *22*, 458–475.

Athy, L. (1930), Density, porosity, and compaction of sedimentary rocks, *Am. Ass. Petrol. Geol. Bull*, *14*, 1–24.

Barnes, A. (2007), A tutorial on complex seismic trace analysis, *Geophysics*, *72*(6), W33–W43, doi:10.1190/1.2785048.

Biot, M. (1956), Theory of propagation of elastic waves in a fluid-saturated porous media, I. Low-frequency range and II. High-frequency range, *J. Acoust. Soc. Am.*, *28*, 168–191.

Bouriak, S., M. Vanneste, and A. Saoutkine (2000), Inferred gas hydrates and clay diapirs near the Storegga Slide on the southern edge of the Vøring Plateau, offshore Norway, *Mar. Geol.*, *163*, 125–148.

Brown, H., W. Holbrook, M. Hornbach, and J. Nealon (2006), Slide structure and role of gas hydrate at the northern boundary of Storegga Slide, offshore Norway, *Mar. Geol.*, *229*, 179–186.

Castagna, J., M. Bazle, and R. Eastwood (1985), Relationships between compressional wave and shear-wave velocities in clastic silicate rocks, *Geophysics*, *50*, 571–581.

Chand, S., and T. Minshull (2004), The effect of hydrate content on seismic attenuation: A case study for Mallik 2L-38 well data, Mackenzie Delta, Canada, *Geophys. Res. Lett.*, *31*(L14609), 730–734, doi:10.1029/2004GL020292.

Chapman, N. R., J. F. Gettrust, R. Walia, D. Hannay, G. D. Spence, W. T. Wood, and R. D. Hyndman (2002), High-resolution, deep-towed, multichannel seismic survey of deep-sea gas hydrates off western Canada, *Geophysics*, *67*(4), 1038–1047.

Chopra, S., and K. Marfurt (2005), Seismic attributes - A historical perspective, *Geophysics*, *70*(5), 3SO–28SO, doi:10.1190/1.2098670.

Chough, S., and K. Lee (1992), Multi-stage volcanism in the Ulleung Back-arc Basin, East Sea (Sea of Japan), *The Island Arc*, *1*, 32–39.

Chough, S., S. Lee, J. Kim, S. Park, D. Yoo, H. Han, S. Yoon, S. Oh, Y. Kim, and G. Back (1997), Chirp (2-7 kHz) echo characters in the Ulleung Basin, *Geosc. J.*, *1*, 143–153.

Chough, S., H. Lee, and S. Yoon (2000), *Marine Geology of Korean Seas*, Elsevier.

Chun, J., S. Han, and D. Cheong (1997), Tephrostratigraphy in the Ulleung Basin, East Sea: Late Pleistocene to Holocene, *Geosci. J.*, *1*, 154–166.

Clapp, R., P. Sava, and J. Claerbout (1998), Interval velocity estimation with a null-space, *Stanford Exploration Project*, *97*, 147–157.

Collett, T., M. Riedel, J. Cochran, R. Boswell, P. Kumar, A. Sathe, and the NGHP Expedition 01 Scientific Party (2008), Indian continental margin gas hydrate prospects: results of the Indian national gas hydrate program (NGHP) Expedition 01, in *Proceedings of the 6th International Conference on Gas Hydrates (ICGH 2008)*, Vancouver, BC, Canada.

Cooper, A., and P. Hart (2003), High-resolution seismic investigation of the northern Gulf of Mexico gas hydrate stability zone, *Mar. Petrol. Geol.*, *19*, 1275–1293.

Coren, F., V. Volpi, and U. Tinivella (2001), Gas hydrate physical properties imaging by multi-attribute analysis - Blake Ridge BSR case history, *Mar. Geol.*, *178*, 197–210.

Davie, M., and B. Buffett (2001), A numerical model for the formation of gas hydrate below the seafloor, *J. Geophys. Res.*, *106*, 497–514.

Davis, E. E., and R. D. Hyndman (1989), Accretion and recent deformation of sediments along the northern Cascadia subduction zone, *Geol. Soc. Am. Bull.*, *101*, 1465–1480.

Davis, E. E., R. D. Hyndman, and H. Villinger (1990), Rates of fluid expulsion across the northern Cascadia accretionary prism: constraints from new heat flow and multichannel seismic reflection data, *J. Geophys. Res.*, *95*, 8869–8889.

Desmons, B. (1996), Integrated study of gas hydrates in marine sediments using geophysical and geochemical data, Master's thesis, University of Victoria.

Dix, C. (1955), Seismic velocities from surface measurements, *Geophysics*, *20*, 68–86.

Domenico, S. (1976), Effect of brine-gas mixture on velocity in an unconsolidated sand reservoir, *Geophysics*, *41*, 882–894.

Domenico, S. (1977), Elastic properties of uncosolidated porous sand reservoirs, *Geophysics*, *42*, 1339–1368.

Dubose, J. (1988), A technique for stabilizing interval velocities from the Dix equation, *Geophysics*, *53*, 1241–1243.

Dvorkin, J., and A. Nur (1993), Rock physics for the characterization of gas hydrates, in *The Future of Energy Gases*, USGS Prof. Paper 1570, pp. 293–298.

Dvorkin, J., and R. Uden (2004), Seismic wave attenuation in a methane hydrate reservoir, *The Leading Edge*, *23*, 730–732.

Dvorkin, J., M. Prasad, A. Sakai, and D. Lavoie (1999), Elasticity of marine sediments: rock physics modeling, *Geophys. Res. Lett.*, *26*, 1781–1784.

Ebrom, D. (2004), The low-frequency gas shadow on seismic sections, *The Leading Edge*, *23*(8), 772, doi:10.1190/1.1786898.

Fraser, G. (1989), *Clastic depositional sequences. Processes of evolution and principles of interpretation*, Prentice Hall, Englewood Cliffs, New Jersey.

Ganguly, N., G. Spence, N. Chapman, and R. Hyndman (2000), Heat flow variations from bottom-simulating reflectors on the Cascadia margin, *Mar. Geol.*, *164*, 53–68.

Gassmann, F. (1951), Elastic waves through a packing of spheres, *Geophysics*, *15*, 673–685.

Geertsma, F. (1961), Velocity-log interpretation: The effect of rock bulk compressibility, *Soc. Petrol. Eng. J.*, *1*, 235–248.

Gorman, A., W. Holbrook, M. Hornbach, K. Hackwith, D. Lizarralde, and I. Pecher (2002), Migration of methane gas through the hydrate stability zone in a low-flux hydrate province, *Geology*, *30*(4), 327–330.

Guerin, G., and D. Goldberg (2002), Sonic waveform attenuation in gas hydrate-bearing sediments from the Mallik 2L-38 research well, Mackenzie Delta, Canada, *J. Geophys. Res.*, *107*(B5,2088), doi:10.1029/2001JB000556.

Haacke, R., G. Westbrook, and R. Hyndman (2007), Gas hydrate, fluid flow and free gas: Formation of the bottom-simulating reflector, *Earth and Planetary Science Letters*, *261*, 407–420.

Haacke, R., G. Westbrook, and M. Riley (2008), Controls on the formation and stability of gas hydrate-related bottom-simulating reflectors (BSRs): A case study from the west Svalbard continental slope, *J. Geophys. Res.*, *113*(B05104), doi:10.1029/2007JB005200.

Hajnal, Z., and I. Sereda (1981), Maximum uncertainty of interval velocity estimates, *Geophysics*, *46*(11), 1543–1547.

Hale, D. (1984), Dip-mouveout by fourier transform, *Geophysics*, *49*, 741–757.

Hallam, A. (1981), *Facies interpretation and the stratigraphic record*, W.H. Freeman and Company, Oxford and San Francisco.

Harlan, W. (1999), Constrained dix inversion, *Tech. rep.*, http://billharlan.com/pub/papers/rmsinv.pdf.

He, T., G. Spence, M. Riedel, R. Hyndman, and N. Chapman (2007), Fluid flow and origin of a carbonate mound offshore Vancouver Island: Seismic and heat flow constraints, *Mar. Geol.*, *239*, 83–98.

Heeschen, K., A. Trehu, R. Collier, E. Suess, and G. Rehder (2003), Distribution and height of methane bubble plumes on the Cascadia Margin characterized by acoustic imaging, *Geophys. Res. Lett.*, *30*, 1643.

Helgerud, M. (2001), Wave speeds in gas hydrate and sediments containing gas hydrate: a laboratory and modeling study, Ph.D. thesis, Stanford University.

Helgerud, M., J. Dvorkin, A. Nur, A. Sakai, and T. Collett (1999), Elastic-wave velocity in marine sediments with gas hydrates: effective medium modelling, *Geophysical Research Letters*, *26*, 2021–2024.

Henriet, J., B. D. Mol, M. Vanneste, V. Huvenne, and D. V. Rooij (2001), Carbonate mounds and slope failures in the Porcupine Basin: a development model involving

past fluid venting, in *Petroleum Exploration of Ireland's offshore basins*, edited by P. Shannon, P. Haughton, and D. Corcoran, Special Publication 188, Geological Society of London, pp. 375–383.

Holbrook, W. (2001), Seismic studies of the Blake Ridge: Implications for hydrate distribution, methane expulsion, and free gas dynamics, in *Natural gas hydrates: Occurrence, distribution and detection*, *Geophysical Monograph*, vol. 124, edited by C. Paull and W. Dillon, pp. 235–255, American Geophysical Union.

Holbrook, W., H. Hoskins, W. Wood, R. Stephen, D. Lizarralde, and L. . S. Party (1996), Methane hydrate and free gas on the blake ridge from vertical seismic profiling, *Science*, *273*, 1840–1843.

Holbrook, W., A. Gorman, M. Hornbach, K. Hackwith, J. Nealon, D. Lizarralde, and I. Pecher (2002), Seismic detection of marine methane hydrate, *The Leading Edge*, *21*(686), doi:10.1190/1.1497325.

Holland, M., P. Schultheiss, J. Roberts, and M. Druce (2008), Observed gas hydrate morphologies in marine sediments, in *Proceedings of the 6th International Conference on Gas Hydrates (ICGH 2008)*, Vancouver, BC, Canada.

Horozal, S., G. Lee, D. Yoo, K.-P. Park, H. Lee, and H. Kim (2008), Seismic indicators of gas hydrate and associated gas in the Ulleung Basin, East Sea (Japan Sea) and implications of heat flows derived from depths of the bottom-simulating reflector.

Hovland, M., and O. Gudmestad (2001), Potential influence of gas hydrates on seabed installations, in *Natural gas hydrates: Occurrence, distribution and detection*, edited by C. Paull and W. Dillon, Geophysical Monograph, pp. 307–315, American Geophysical Union.

Huang, J.-W., G. Bellefleur, and B. Milkereit (2008), Seismic modeling of reservoir-scale hererogeneities - an application to the Mallik gas hydrates, Northwest Territories, *Recorder*, pp. 34–41.

Hubral, P. (1976), Interval velocities from surface measurements in the three-dimensional plane layer-case, *Geophysics*, *41*, 233–242.

Hubral, P., and T. Krey (1980), *Interval velocities from seismic reflection time measurements*, SEG, Tulsa, OK, USA.

Hyndman, R., and G. Spence (1992), A seismic study of methane hydrate marine bottom simulating reflectors, *J. Geophys. Res.*, *97*(B5), 6683–6698.

Hyndman, R. D., and E. E. Davis (1992), A mechanism for the formation of methane hydrate and seafloor bottom-simulating reflectors by vertical fluid expulsion, *J. Geophys. Res.*, *97*(B5), 7025–7041.

Hyndman, R. D., K. Wang, T. Yuan, and G. D. Spence (1993), Tectonic sediment thickening, fluid expulsion, and the thermal regime of subduction zone accretionary prisms: The Cascadia margin off Vancouver Island, *J. Geophys. Res.*, *98*(B12), 21,865–21,876.

Jolivet, L., and K. Tamaki (1992), Neogene kinematics in the Japan Sea region and volcanic activity of the northeast Japan arc, in *Proc. ODP, Scientific results 127/128 (part 2)*, pp. 1311–1331, College Station, TX.

Kang, D.-H., D.-G. Yoo, K.-P. Park, N.-H. Koo, W.-S. Kim, K.-S. Park, and H.-Y. Lee (2008), The seismic indicators of gas hydrate in the Ulleung Basin, East Sea off Korea, in *Proceedings of the 6th International Conference on Gas Hydrates (ICGH 2008)*, Vancouver, BC, Canada.

Kastner, M., A. Spivack, M. Torres, E. Solomon, D. Borole, G. Robertson, and H. Das (2008), Gas hydrates in three Indian ocean regions, a comparative study of occurrence and subsurface hydrology, in *Proceedings of the 6th International Conference on Gas Hydrates (ICGH 2008)*, Vancouver, BC, Canada.

Kennet, J., K. Cannariatio, I. Hendy, and R. Behl (2003), *Methane hydrates in Quaternary climate change: The clathrate gun hypothesis*, American Geophysical Union, Washington, D.C., Washington, D.C.

Kim, G., D. Yoo, W. Kim, H. Lee, and K. Park (2008a), Physical properties of gas hydrate-bearing sediments in the Ulleung Basin, the East Sea of Korea: Preliminary result from well-log data, in *Proceedings of the 6th International Conference on Gas Hydrates (ICGH 2008)*, Vancouver, BC, Canada.

Kim, Y.-G., S. Lee, H. Hamamoto, O. Matsubayashi, M. Yamano, and Y.-I. Kwon (2008b), Estimates on the depth of gas hydrate stability zone in the Ulleung Basin, East Sea (Sea of Japan), in *Asia Oceania Geosciences Society Conference Proceedings, Advances in Geosciences*, Busan, Korea.

Klimentos, T., and C. McCann (1990), Relationships among compressional wave attenuation, porosity, clay content, and permeability in sandstones, *Geophysics*, *55*, 998–1014.

Kvenvolden, K., and L. Barnard (1983), Hydrates of Natural Gas in Continental Margins, in *Studies in Continental Margin Geology*, *American Association of Petroleum Engineers Memoirs*, vol. 34, edited by J. Watkins and C. Drake, pp. 631–640.

Kwon, Y., and J. Bahk (2006), Mass failure and mass flow deposits in the Ulleung Basin and Korea Pleateau, East Sea: a brief review, *Tech. rep.*, Thematic session and 2^{nd} international symposium on gas hydrate technology at the 43^{rd} CCOP annual session Yousung Hotel, Korea.

Kwon, Y., B. Ryu, B. Son, C. Jun, D. Sunwoo, H. Kim, H. Lee, I. Hwang, J. Chun, J. Kim, J. Ko, J. Lee, J. Oh, K. Ahn, T. Jung, Y. Lee, and Y. Shin (2006), Sedimentological and geochemical assessment for gas hydrate potential in the East Sea: Preliminary results for a 2006 cruise, *Tech. rep.*, Thematic session and 2^{nd} international symposium on gas hydrate technology at the 43^{rd} CCOP annual session Yousung Hotel, Korea.

Lallemand, S., and L. Jolivet (1985), Japan Sea: a pull apart basin, *Earth Planet. Sci. Lett.*, *76*, 375–389.

Lee, G., and B. Suk (1998), Latest Neogene-Quaternary seismic stratigraphy of the Ulleung Basin, East Sea (Sea of Japan), *Mar. Geol.*, *146*, 205–224.

Lee, H., S. Chough, and S. Yoon (1996a), Slope-stability change from late Pleistocene to Holocene in the Ulleung Basin, East Sea (Japan Sea), *Sed. Geol.*, *104*, 39–51.

Lee, J., Y. Baek, B. Ryu, M. Riedel, and R. Hyndman (2005), A seismic survey to detect natural gas hydrate in the East Sea of Korea, *Mar. Geophys. Res*, *26*, 51–59, doi:10.1007/s11001-005-6975-4.

Lee, K. (1992), Geological structure of Ulleung Back-Arc Basin, East Sea, Master's thesis, Seoul National University.

Lee, M., D. Hutchinson, T. Collett, and W. Dillon (1996b), Seismic velocities for hydrate-bearing sediments using the weighted equation, *J. Geophys. Res.*, *101*(B9), 20,347–20,358.

Lee, M. W., D. R. Hutchinson, W. P. Dillon, J. J. Miller, W. F. Agena, and B. A. Swift (1993), Method of estimating the amount of in situ gas hydrates in deep marine sediments, *Mar. Petrol. Geol.*, *10*, 496–506.

Liu, X., and P. Flemings (2007), Dynamic multiphase flow model of hydrate formation in marine sediments, *J. Geophys. Res.*, *112*(B03101), doi:10.1029/2005JB004227.

MacKay, M., R. Jarrard, G. Westbrook, and R. Hyndman (1994), Origin of bottom-simulating reflectors; geophysical evidence from the Cascadia accretionary prism, *Geology*, *22*(5), 459–462.

Maliverno, A., and V. Briggs (2004), Expanded uncertainty quantification in inverse problems: Hierarchical Bayes and empirical Bayes, *Geophysics*, *69*(4), 1005–1016.

Matsushima, J. (2006), Seismic wave attenuation in methane hydrate-bearing sediments: Vertical seismic profiling data from the Nankai Through exploratory well, offshore Tokai, central Japan, *J. Geophys. Res.*, *111*(B10101), doi:10.1029/2005JB004031.

Mikov, A., G. Dickens, G. Claypool, Y.-J. Lee, W. Borowski, M. Torres, W. Xu, H. Tomaru, A. Trehu, and P. Schultheiss (2004), *Earth Planet. Sci. Letters*, *222*, 829–843.

Milkov, A. (2004), Global estimates of hydrate-bound gas in marine sediments: how much is really out there?, *Earth-Sci. Reviews*, *66*, 183–197.

Minshull, T., C. Singh, and G. Westbrook (1994), Seismic velocity structure at a gas hydrate reflector, offshore western Columbia, full waveform inversion, *J. Geophys. Res.*, *99*, 4715–4734.

Nobes, D., M. Langseth, S. Kuramato, P. Holler, and N. Hirata (1992), Comparison and correlation of physical-property results from Japan Sea basin and rise sites, in *Proc. ODP, Scientific results 127/128, Part 2*, pp. 1275–1296, College Station, TX.

Oldenburg, D., S. Levy, and K. Stinson (1984), Root-mean-square velocities and recovery of the acoustic impedance, *Geophysics*, *49*, 1653–1663.

Otofuji, Y., T. Ytaya, and T. Matsuda (1991), Rapid rotation of southwest Japan paleomagnetism and K-Ar ages of Miocene volcanic rocks of southwest Japan, *Geophys. J. Int.*, *105*, 397–405.

Park, K.-P. (2008), Gas hydrate exploration activities in Korea, in *Proceedings of the 6th International Conference on Gas Hydrates (ICGH 2008)*, Vancouver, BC, Canada.

Park, K.-P., J.-J. Bahk, Y. Kwon, G. Kim, M. Riedel, M. Holland, P. Schultheiss, K. Rose, and the UBGH-1 scientific party (2008), Korean National Program expedition confirms rich gas hydrate deposits in the Ulleung Basin, East Sea, *Fire in the ice*.

Paull, C., W. U. III, W. Borowski, and F. Spiess (1995), Methane-rich plumes on the Carolina continental rise: Associations with gas hydrates, *Geology*, *23*, 89–92.

Pearson, C., P. Halleck, P. McGulre, R. Hermes, and M. Matthews (1983), Natural gas hydrate; a review of in situ properties, *J. Phy. Chem.*, *87*, 4180–4185.

Pecher, I. (2002), Gas hydrates on the brink, *Nature (news and views)*, *420*, 622–623.

Petersen, K., S. Bünz, S. Hustoft, and J. Miniert (2008), 3-D seismic imaging of marine gas hydrates in Arctic sediments of the Vestnesa Ridge off the W-Svalbard Margin, in *Proceedings of the 6th International Conference on Gas Hydrates (ICGH 2008)*, Vancouver, BC, Canada.

Pratt, R., K. Bauer, and M. Weber (2003), Crosshole waveform tomography velocity and attenuation images of arctic gas hydrates, in *SEG 73rd Ann. Mtg.*, Dallas, Texas.

Riedel, M., T. S. Collett, M. J. Malone, and the Expedition 311 Scientists (2006a), Proceedings of the Integrated Ocean Drilling Program, Volume 311, *Tech. rep.*, Integrated Ocean Drilling Program Management International Inc., Washington, DC, doi:10.2204/iodp.proc.311.2006.

Riedel, M., I. Novosel, G. D. Spence, R. D. Hyndman, N. R. Chapman, R. C. Solem, and T. Lewis (2006b), Geophysical and geochemical signatures associated with gas hydraterelated venting in the northern Cascadia margin, *GSA Bull.*, *118*(1-2), 23–38.

Roberton, J., and D. Fisher (1988), Complex seismic trace attributes, *The Leading Edge*, *7*, 22–26.

Roberton, J., and H. Nogami (1984), Complex seismic trace analysis of thin beds, *Geophysics*, *49*(4), 344–352.

Roberts, H. (2001), Fluid and gas expulsion on the northern gulf of mexico continental slope: Mud prone to mineral-prone responses, in *Natural gas hydrates: occurrence, distribution, and detection*, *Geophysical Monograph*, vol. 124, edited by C. Paull and W. Dillon, pp. 145–161, American Geophysical Union.

Roberts, H., B. Hardage, W. Shedd, and J. Hunt (2006), Seafloor reflectivity - an important seismic property for interpreting fluid/gas expulsion geology and the presence of gas hydrate, *The Leading Edge*, *25*, 620–628.

Saeki, T., T. Fujii, T. Inamori, T. Kobayashi, M. Hayashi, S. Nagabuko, and O. Takano (2008), Delineation of methane hydrate concentrated zone using 3D seismic data in the eastern Nankai Trough , in *Proceedings of the 6th International Conference on Gas Hydrates (ICGH 2008)*, Vancouver, BC, Canada.

Sakai, A. (1999), Velocity analysis of vertical seismic profile (vsp) survey at japex/jnoc/gsc mallik 2l-38 gas hydrate research well, and related problems for estimating gas hydrate concentration, in *Scientific results from JAPEX/JNOC/GSC Mallik 2L-38 gas hydrate research well, Mackenzie Delta, Northwest Territories, Canada*, *Bull. Geol. Surv. Can.*, vol. 544, edited by R. Dallimore, T. Uchida, and T. Collett, pp. 323–340.

Santamarina, J., and C. Ruppel (2008), The impact of hydrate saturation on the mechanical, electrical, and thermal properties of hydrate-bearing sand, silts and clay, in *Proceedings of the 6th International Conference on Gas Hydrates (ICGH 2008)*, Vancouver, BC, Canada.

Sassen, R., S. Sweet, A. Milkov, D. DeFreitas, and M. K. II (2001), Thermogenic vent gas and gas hydrate in the Gulf of Mexico slope: Is gas hydrate decomposition significant?, *Geology*, *29*, 107–110.

Schowalter, T. (1979), Mechanics of secondary hydrocarbon migration and entrapment, *Bull. Am. Ass. Petrol. Geol.*, *63*, 723–760.

Sen, M., and P. Stoffa (1996), Bayesian inference, Gibbs' sampler and uncertainty estimation in geophysical inversion, *Geophys. Prosp.*, *44*, 313–350.

Shipley, T., M. Houston, R. Buffler, F. Shaub, K. McMillen, J. Ladd, and J. Worzel (1979), Seismic reflection evidence for the widespread occurrence of possible gas hydrate horizons on continental slopes and rises, *Am. Assoc. Petrol. Geol. Bull.*, *63*, 2204–2213.

Singh, S., T. Minshull, and G. Spence (1993), Velocity structure of a gas hydrate reflector, *Science*, *260*, 204–207.

Sloan, E. (1998), *Clathrate hydrates of natural gases*, Marcel Dekker, 2^{nd} Edition.

Tamaki, K., K. Suyehiro, J. Allan, J. J. Ingle, and K. Pisciotto (1992), Proceedings of the Ocean Drilling Program, Sci. Res., 127/128, Pt. 2, *Tech. rep.*, Integrated Ocean Drilling Program Management International Inc.

Taner, M., and R. Sheriff (1977), Application of amplitude, frequency, and other attributes to stratigraphic and hydrocarbon determination, in *Applications to hydrocarbon exploration*, *Am. Ass. Petrol. Geol. Memoir*, vol. 26, pp. 301–327.

Taner, M., F. Koehler, and R. Sheriff (1979), Complex seismic trace analysis, *Geophysics*, *44*(6), 1041–1063.

Tarantola, A. (1987), *Inverse Problem Theory: Methods for Data Fitting and Model Parameter Estimation*, 613 pp., Elsevier, Amsterdam.

Taylor, M., W. Dillon, and I. Pecher (2000), Trapping and migration of methane associated with the gas hydrate stability zone at the Blake Ridge Diapir: new insights from seismic data, *Mar. Geol.*, *164*, 79–89.

Valenciano, A., M. Brown, A. Guitton, and M. Sacchi (2004), Interval velocity estimation using edge-preserving regularization, in *SEG Int'l Exposition and 74th Ann. Mtg.*, Denver, Colorado.

Vanneste, M., M. D. Batist, W. Versteeg, A. Golmshtok, and A. Kremlev (2001), Multi-frequency seismic study of gas hydrate-bearing sediments in Lake Baikal, *Mar. Geol.*, *172*, 1–21.

Waite, W. F., M. B. Helgerud, A. Nur, J. Pinkston, L. A. Stern, S. H. Kirby, and W. B. Durham (2000), First laboratory measurements of compressional and shear wave speeds through pure methane hydrate at in situ conditions, in *Gas Hydrates: Challenges for the Future*, vol. 912, edited by G. D. Holder and P. R. Bishnoi, pp. 1003–1010, Ann. N. Y. Acad. Sci.

White, R. (1991), Properties of instanatanoues seismic attributes, *The Leading Edge*, *10*, 26–32.

Wood, A. (1941), *A text book of sound*, 235-248 pp., Macmillan.

Wood, W., W. Holbrook, and H. Hoskins (2000), In situ measurements of P-wave attenuation in methane hydrate and gas bearing sediments on the Blake Ridge, in *Proceedings of the Ocean Drilling Program, Scientific Results, 164*, edited by C. Paull, R. Matsumoto, R. Wallace, et al., Ocean Drilling Program, pp. 265–272, College Station, Texas.

Wood, W., J. Gettrust, N. Chapman, G. Spence, and R. Hyndman (2002), Decreased stability of methane hydrates in marine sediments owing to phase-boundary roughness, *Nature*, *420*, 656–660.

Wyllie, M., A. Gregory, and G. Gardner (1958), An experimental investigation of factors affecting elastic wave velocities in porous media, *Geophysics*, *23*, 459–493.

Wyman, R. (1982), Petrogeophysics, the relationships of petrophysics, geology and geophysics, in *Stratigraphic interpretation of seismic data*, pp. 1–106, Am. Ass. Petrol. Geol., Continuing education.

Yamano, M., S. Uyeda, Y. Aoki, and T. Shipley (1982), Estimates of heat flow derived from gas hydrates, *Geology*, *10*, 339–343.

Yilmaz, O. (2001), *Seismic data analysis: processing, inversion and interpretation of seismic data*, Society of Exploration Geophysicists, 2^{nd} Edition.

Yoo, D., D. Kang, W. Kim, N. Koo, G. Kim, K.-P. Park, H. Lee, and G. Lee (2008), Geophysical evidence for gas hydrate in the Ulleung Basin, East Sea (Sea of Japan), in *Proceedings of the 6th International Conference on Gas Hydrates (ICGH 2008)*, Vancouver, BC, Canada.

Yoon, S., and S. Chough (1995), Regional strike slip in the eastern continental margin of Korea and its tectonic implications for the evolution of Ulleung Basin, East Sea (Sea of Japan), *Geol. Soc. Am. Bull.*, *107*, 83–87.

Yuan, T., R. D. Hyndman, G. D. Spence, and B. Desmons (1996), Seismic velocity increase and deep-sea gas hydrate concentration above a bottom-simulating reflector on the northern Cascadia continental slope, *J. Geophys. Res.*, *101*(B6), 13,655–13,672.

Zwart, G., J. Moore, and G. Cochrane (1996), Variations in temperature gradients identify active faults in the oregon accretionary prism, *Earth Planet. Sci. Lett.*, *139*, 485–495.

Appendix A

Elastic properties of free gas sediments

This section provides the theoretical background for estimating P- and S-wave velocities as a function of free gas concentration, applied in Section 4. The Biot-Gassmann theory (*Biot* 1956, *Gassmann* 1951) can be used to estimate physical properties of rocks with partial gas saturations. The mixture of free gas and pore water in the sediment pore space is approximated by a single-phase effective fluid. The properties of the effective fluid are calculated by volume averages of density, viscosity, and compressibility of the separate phases. This method is commonly used to estimate seismic velocities in gas-bearing sediments (e.g., *Domenico* 1977, *Desmons* 1996).

The bulk density of a partially saturated gas sediment can be calculated using the equation:

$$\rho = \phi S_w \rho_w + \phi(1 - S_w)\rho_g + (1 - \phi)\rho_m, \tag{A.1}$$

where ρ is the bulk density, ρ_w is the water density (1030 kg/m^3), ρ_m is the solid matrix density, ϕ is the sediment porosity, S_w is the fractional water saturation, S_w = 1 - S_g, and S_g is the free gas saturation. The solid matrix density is calculated from an average porosity ϕ = 58% in a 100 ms interval below the BGHSZ and an average density ρ_{av} = 1650 kg/m^3 (*Kim et al.* 2008a) to give ρ_m = 2506 kg/m^3. The bulk porosity is derived from the velocity profile, shown in Fig. 4.1, and the porosity-velocity relationship of *Hyndman et al.* (1993). The density of gas at standard temperature depends on pressure P, and can be calculated from the density of methane at standard pressure P_0 = 1 atm, ρ_0 = 0.714 kg/m^3:

$$\rho_g(P) = \frac{P}{P_0}\frac{T}{T_0}\rho_{g0}. \tag{A.2}$$

The pressure at the depth of the BGHSZ, 180 m below the seafloor at a water depth

of 2030 m is 22 MPa, assuming hydrostatic pressure, and the temperature is 19 ^oC.

The fluid compressibility is calculated as an average of water and gas compressibility:

$$C_f = S_w C_w + (1 - S_w) C_g, \tag{A.3}$$

where C_f is the fluid compressibility, C_w is the water compressibility, C_w=4.2·10^{-10} Pa^{-1} and C_g is the gas compressibility. If there is no gas, the fluid compressibility equals the water compressibility. The gas compressibility is dependent on pressure and temperature and it is calculated using a measured compressibility C_{g_1} at pressure P_1:

$$C_g = C_{g_1} \frac{T}{T_1} \left(\frac{P_1}{P} \right)^2, \tag{A.4}$$

with C_{g_1} = 7.74·10^{-8} Pa^{-1} at P_1 = 155 atm and T_1 = 287.3 K characteristic at ODP Site 889, calculated by *Desmons* (1996), starting from measured methane compressibilities by *Wyman* (1982). The estimated temperature at the BGHSZ is 292 K (Table 5.3, Chapter 5).

The bulk modulus of the saturated sediment can be calculated using the *Geertsma* (1961) theory:

$$K = \frac{C_m / C_b}{C_m} + \frac{(1 - (C_m / C_b))^2}{(1 - \phi - C_m / C_b) C_m + \phi C_f}, \tag{A.5}$$

where C_m is the compressibility of the solid matrix material (individual solid grains) and C_b is the compressibility of the frame (dry bulk sediment). The choice of C_m in our calculations is described in Section 4.3. The compressibility of the frame is a function of the pore and matrix compressibility:

$$C_b = \phi C_p + C_m, \tag{A.6}$$

where C_p is the pore compressibility. The pore compressibility is a function of differential pressure, expressed as:

$$C_p = C_{p_0} + m P_d, \tag{A.7}$$

where C_{p_0} is the compressibility at zero differential pressure, C_{p_0} = 2.96·10^{-9} Pa^{-1}, m is the pore compressibility gradient with pressure, m = -7.5·10^{-17} Pa^{-2}, the negative sign suggesting a decrease in pore compressibility with increasing pressure. P_d is the differential pressure, which is the difference between lithostatic and hydrostatic

pressure:

$$P_d = (\rho_{av} - \rho_w)gz, \tag{A.8}$$

where ρ_{av} is the average sediment density above the BGHSZ, g is the gravitational acceleration, g = 9.81 m/s^2 and z is the distance from the seafloor to the BGHSZ in m. The average thickness of the GHSZ estimated from a constant heat flow of 120 mW/m^2 is 180 m, at a water depth of 2030 m. The average density ρ_{av} is taken to be 1500 g/cm^3.

The P- and S- wave velocities can be calculated using the following equations, respectively:

$$v_P = \sqrt{\frac{K + \frac{4}{3}\mu}{\rho}}, \tag{A.9}$$

$$v_S = \sqrt{\frac{\mu}{\rho}}, \tag{A.10}$$

where μ is the shear modulus. The shear modulus is calculated from an estimated S-wave velocity for water-saturated sediments with density corresponding to the free gas zone. A constant shear modulus value is used when calculating velocity as a function of free gas saturation, assuming no significant change in shear modulus with free gas saturation. The reference no-gas velocity for a 100 ms thick zone below the BGHSZ corresponding to a density of 1650 kg/m^3, is 1640 m/s.

Appendix B

Complex trace analysis

The conventional seismic trace $x(t)$ can be represented as the real component of a complex seismic trace $z(t)$:

$$z(t) = x(t) + i \cdot y(t), \tag{B.1}$$

where $y(t)$ is called the quadrature trace. The seismic trace, as a solution of the wave equation, can be written as:

$$x(t) = a(t) \cos \phi(t), \tag{B.2}$$

where $a(t)$ is a slowly varying function, the envelope, and the phase, $\phi(t) = 2\pi f t$, and f is frequency in Hz.

The quadrature trace is determined from x(t) by convolution with the Hilbert tranform or quadrature filter h(t), such that:

$$y(t) = h(t) \star x(t), \tag{B.3}$$

where

$$h(t) = 1/(\pi t) \tag{B.4}$$

The Fourier tranform of h(t) is defined as:

$$H(f) \; = \; \begin{cases} -i & , \quad f > 0, \\ +i & , \quad f < 0, \\ 0 & , \quad f = 0. \end{cases} \tag{B.5}$$

The rotated trace under a phase rotation of 90^o is the Hilbert transform, resulting in a quadrature trace (*Taner et al.* 1979):

$$\bar{x}(t) = y(t) = -a(t) \sin \phi(t). \tag{B.6}$$

The quadrature trace does not have any physical meaning. Peaks and troughs on the quadrature trace correspond to zero crossings on the seismic trace (*Taner and Sheriff* 1977). The trace envelope a(t) is defined as the maximum value that a seismic trace can have under a constant phase rotation, which makes it independent of phase. The trace envelope can be described as a function that connects the waveform peaks, as well as troughs, since it is independent of polarity.

The complex trace can be thus written as:

$$z(t) = a(t)\cos\phi(t) - a(t)\sin\phi(t) = a(t)exp(-i\phi(t)) \tag{B.7}$$

The envelope amplitude is:

$$a(t) = (x^2(t) + y^2(t))^{1/2} \tag{B.8}$$

The angle that rotates the trace to a maximum, or instantaneous phase is:

$$\phi = arctan\frac{y(t)}{x(t)} \tag{B.9}$$

The instantaneous phase has a sawtooth appearance and its values range from (-π, π]. They refer to the apparent position along the seismic trace, such that peaks have 0^o phase, troughs have 180^o phase, downward zero crossings have -90^o phase.

The instantaneous frequency represents the rate of change with time of the instantaneous phase divided by 2π (*Taner et al.* 1979):

$$f(t) = \frac{1}{2\pi}\frac{d\phi}{dt} \tag{B.10}$$

It has units of Hz, but it is not a frequency in the physical sense, as it has negative values at inflection points of the trace and can also exceed the maximum frequency in the seismic signal when the trace is close to zero and crosses it for one or two samples.